Simplified Template Cross Section measurements of associated VH production in the $H \to b\bar{b}$ decay channel with $\sqrt{s} = 13$ TeV proton-proton collisions at the ATLAS experiment

by

Ryan Justin Atkin
Supervisor: Assoc. Prof. Sahal Yacoob
Co-Supervisor: Dr. James Keaveney

A thesis submitted for the
degree of Doctor of Philosophy

in the
UCT-CERN Group
Department of Physics
Faculty of Science
University of Cape Town

November 2024

University of Cape Town

The copyright of this thesis vests in the author. No quotation from it or information derived from it is to be published without full acknowledgement of the source. The thesis is to be used for private study or non-commercial research purposes only.

Published by the University of Cape Town (UCT) in terms of the non-exclusive license granted to UCT by the author.

University of Cape Town

Declaration of Authorship

I, Ryan Justin Atkin, declare that this thesis titled, *Simplified Template Cross Section measurements of associated VH production in the $H \to b\bar{b}$ decay channel with $\sqrt{s} = 13$ TeV proton-proton collisions at the ATLAS experiment* and the work presented in it are my own. I confirm that:

- This work was done wholly or mainly while in candidature for a research degree at the university of Cape Town.
- The work presented in this thesis was part of an ATLAS analysis, which consisted of around 40 people contributing to entire analysis. Therefore, my work on certain aspects of Chapters 5 and 6 is clearly labelled throughout, and Chapter 7 is fully of my own, independent work.
- Where any part of this thesis has previously been submitted for a degree or any other qualification at this University or any other institution, this has been clearly stated.
- Where I have consulted the published work of others, this is always clearly attributed.
- Where I have quoted from the work of others, the source is always given. With the exception of such quotations, this thesis is entirely my own work.
- I have acknowledged all main sources of help.
- Where the thesis is based on work done by myself jointly with others, I have made clear exactly what was done by others and what I have contributed myself.

Signed by candidate

Signed:

Date: 1 November 2024

UNIVERSITY OF CAPE TOWN

Abstract

Department of Physics
Faculty of Science

Doctor of Philosophy

by Ryan Justin Atkin

This thesis presents a Simplified Template Cross-Section (STXS) measurement of the production of the SM Higgs boson in association with a W or Z boson, where the Higgs boson decays to $b\bar{b}$ and the W/Z boson (V) decays leptonically. The data used is the full Run-2 ATLAS dataset, corresponding to 140 fb^{-1} of integrated luminosity, which was collected in proton-proton collisions at a centre of mass energy of $\sqrt{s} = 13$ TeV. This process was previously observed by both the ATLAS collaboration in 2021, and the CMS collaboration in 2023, measuring the signal strength to be $\mu_{VH}^{bb} = 1.02^{+0.18}_{-0.17}$ and $\mu_{VH}^{bb} = 1.15^{+0.22}_{-0.20}$ respectively.
The measurement in this thesis expands the STXS regions to 10 by splitting each region by the number of jets additional to the Higgs decay products. Some of these regions have not been studied yet and so this measurement acts a feasibility study for those regions. All 10 of the STXS regions studied have a signal strength which agrees well with the standard model expectation. While some signal strengths are negative, their uncertainties were large enough to still agree with a value of 1. Increasing the minimum requirement on the transverse momentum of the additional jets was found to decrease the uncertainties on the signal strengths for the regions with at least one additional jet. However, this reduction was not enough to obtain statistically significant results in some of the additional jets STXS regions.

Acknowledgements

Firstly, I would like to express my gratitude to SA-CERN and the University of Cape Town for their financial support toward my PhD, funded largely through the National Research Foundation (NRF). I am also immensely grateful to my family, particularly my mother and brother, for their unwavering emotional support and encouragement throughout the many ups and downs of this journey. To my father, who unfortunately passed away during my studies and didnt get to see the end product this work is dedicated to his memory.

I would like to extend my sincere thanks to my co-supervisor, James Keaveney, for his invaluable guidance in helping deepen my understanding of the physics involved and refining my thesis writing. I am also deeply appreciative of my colleagues in the ATLAS $VH \to b\bar{b}$ analysis group, from whom I have learned so much and who made this analysis possible. Special thanks go to the analysis contacts Hannah Arnold, Yanhui Ma, and Elisabeth Schopf whose support and insights were indispensable, often serving almost as co-supervisors themselves.

Lastly, and by no means least, I am profoundly grateful to my supervisor, Sahal Yacoob, for his vital mentorship, guidance, and patience. His assistance in times of financial or personal difficulty has been invaluable. This December marks a decade since I first began working with Sahal, from my Honours through to my MSc and now my PhD. His support and influence over these past 10 years have been instrumental in shaping both my academic and personal growth.

Contents

Chapter 1

Introduction

The most successful theory at describing the fundamental particles and forces of the universe (except for only gravity) is the Standard Model (SM) of particle physics [1–4]. At the core of the SM is the concept of symmetry and gauge invariance. The first Quantum Field Theory (QFT), known as Quantum Electrodynamics (QED) [5–7], was expanded upon to include quarks, the strong and weak forces and spontaneous symmetry breaking, resulting in the SM. The SM describes three of the four fundamental forces of nature, and how all the known fundamantal particles interact via those forces. With the discovery of the Higgs boson in 2012 by the ATLAS [8] and CMS [9] collaborations at the Large Hadron Collider (LHC) [10], all the particles predicted by the SM have been discovered. To date, there have been no significant results that disagree with the SM [11], even with increasingly precise measurements.

Despite the successes of the SM, experimental observations and theoretical insights, mostly from outside of particle physics, suggest that the SM is an approximation of a more fundamental theory of nature [12]. Now that all the pieces of the current SM have been found, the goal of particle physics is to discover this more fundamental theory. Areas of study include the nature of neutrinos, the origin of dark matter [13], the reason for the baryon asymmetry in the universe [14], and attempts at describing gravity on the quantum scale [15]. There are also some questions about the Higgs boson: is it a fundamental scalar boson or a complex object? why is its mass so much lower than the naive expectation? and why do the fundamental particles have the masses that they do? More on the Higgs in Section 2.2.

One of the most promising approaches to finding deviations from the SM is to perform precision measurements of the Higgs boson. Of the 19 free parameters in the SM, 15 of them are related to the Higgs [16][17]. Therefore, many extensions of the SM have properties significantly different to the SM Higgs boson properties. Precision measurements of the Higgs boson's properties thus may be a very promising way of finding new physics.

The search for possible theories beyond the SM (BSM) at the LHC can be done either directly by searching for new particle productions, or indirectly by looking for discrepancies between

the SM predictions and the experimental data. The direct searches use specific BSM models to search for any of the particles they predict, for example supersymmetry [18][19] or the two-Higgs-doublet model [20]. Indirect approaches perform precision measurements of the cross-sections to find discrepancies with the SM predictions. Effective Field Theories (EFTs) are a common method to parametrise the LHC data in this case, assuming some higher energy theory that exists beyond the scale of the LHC. The benefit of the indirect method is that there are far less assumptions of the new physics, whereas direct searches usually have many assumptions based on the particular properties of the new particle.

This thesis presents a measurement of the Higgs boson (H) production rate in association with a W/Z boson (collectively called vector bosons, V). The decay channel involves the leptonic decays of the vector bosons, and the Higgs boson decaying to two b-quarks. The measurement is performed within the Simplified Template Cross-Section (STXS) framework [21][22], using a multivariate approach to maximally discriminate between signal and background events. The data studied is the full Run-2 dataset of proton-proton (pp) collisions, corresponding to a luminosity of 140 fb^{-1}, at a centre-of-mass energy of $\sqrt{s} = 13$ TeV, and collected by the ATLAS experiment at the LHC. For the presented measurement, the b-quarks were at low enough momenta such that they could be individually reconstructed, or resolved. At higher energies, the two b-quarks become too collimated to each other, or boosted, that they cannot be individually resolved. So while the analysis presented in this thesis is an independent measurement, it is heavily based on the ATLAS analysis [23] that combines the previous $VHb\bar{b}$ resolved [24], $VHb\bar{b}$ boosted [25] and $VHc\bar{c}$ resolved [26] analyses.

This thesis is structured as follows:

- Chapter 2 introduces the theoretical and phenomenological context of this thesis, with a short overview of the SM of particle physics. There will also be a focus on the Higgs mechanism and cross-sections, both fundamental aspects of the analysis.
- Chapter 3 gives an overview of the LHC and the ATLAS experiment, along with the methods used to simulate theoretical models and produce Monte Carlo data.
- Chapter 4 describes the algorithms used within the ATLAS collaboration for the reconstruction and identification of the particle four-momenta from raw detector information.
- Chapter 5 introduces the VH process, as well as the object and event definitions used by this analysis and the Monte Carlo samples used. Additionally, the statistical methods and final measurement techniques are described.

- Chapter 6 describes the experimental and modelling systematic uncertainties used in this analysis.
- Chapter 7 presents the results of the study on increasing the transverse momentum selection applied to the additional jets in the event, in terms of a likelihood fit within the STXS framework with finer binning. While these changes were implemented by the ATLAS combination analysis mentioned above, the results shown in this thesis are independent to their analysis.
- Chapter 8 provides a brief summary and conclusion of the thesis.

Chapter 2

Theoretical background

This chapter introduces the theory that describes our current knowledge of particle physics, the SM, and follows mostly from what is in References [27][28]. A focus is put on the Higgs mechanism and a summary of Higgs processes studied at the Large Hadron Collider. The SM has proven time and again to agree with experimental observations, however there are several aspects of the natural world that the SM is unable to explain. One way to test new theories or their effects on the SM is to use EFTs. The benefit of EFTs is that they are less model dependent than other methods, and allow the study of theories whose energy scales are beyond the reach of the LHC.

2.1 The Standard Model

The SM is the current theoretical framework that describes all the known elementary particles and their interactions with three of the fundamental forces of nature. The SM describes the electromagnetic, weak and strong interactions via their quantised force mediators, or gauge bosons, and how they interact with the fundamental matter particles, known as fermions. The fermions, all spin-$\frac{1}{2}$, comprise of six quarks, six leptons and all their anti-particles. The gauge bosons, spin-1 particles, comprise of one electromagnetic force carrier (photon, γ), three weak force carriers ($W^{\pm}$, Z^0) and eight colored strong force carriers (gluons, g). Additionally, there is a spin-0 (scalar) boson responsible for the masses of the massive fundamental particles (Higgs boson, H).

The leptons are composed of the unit charged electron, muon and tau lepton (e,μ,τ) that interact via the weak and electromagnetic forces, and their corresponding chargeless neutrinos (ν_e,ν_μ,ν_τ) that only interact via the weak force. The six quarks are comprised of the up, charm and top quarks (u, c, t, known as up-type quarks), and the down, strange and bottom quarks (d, s, b, known as down-type quarks). The up-type and down-type quarks have electric charges

of $+\frac{2}{3}|e|$ and $-\frac{1}{3}|e|$ respectively, and are able to interact with the weak, electromagnetic and strong forces. In a somewhat similar manner to electromagnetism, the quarks and gluons carry an additional form of charge known as color charge, through which the strong force interacts. Unlike the electromagnetic force which has positive or negative charges however, the strong force has three color charges, namely blue, green and red, and their anti-color equivalents. A quark only carries one of these colors at a time, which is switched to another color via a gluon exchange, while the gluons carry two color charges: one color and one different anti-color charge (e.g., blue anti-green). Due to color confinement, only colorless particles are allowed to exist freely in nature, as a color-anti-color pair, or a combination of all three colors. The result of this is that an individual quark or gluon cannot exist by itself but has to be combined into a colorless composite particle (hadron), such as a meson (two quarks) or baryon (three quarks). There are some more exotic combinations possible, for example a tetraquark (four quarks) [29] or a pentaquark (five quarks) [30]. A diagram summarising the fundamental particles of the SM is given in Figure 2.1. All of the stable matter in the universe is comprised of the first generation of fermions: the up and down quarks, and the electron and electron neutrino. The second and third generations of fermions are unstable and decay to the lighter particles in the first generation via the weak force.

The SM is a relativistic QFT, built on the lagrangian formalism and the principles of local gauge invariance, i.e., the lagrangian and the dynamics of the system do not change under local phase transformations of the fields. The fermions obey the Fermi-Dirac [32] statistics, and a free fermion follows the Dirac Lagrangian:

$$\mathcal{L}_{Dirac} = \bar{\psi}(i\gamma^{\mu}\partial_{\mu} - m)\psi. \tag{2.1}$$

Here, m is the mass of the particle, ψ is the Dirac field spinor, γ^{μ} represents the Dirac-γ matrices and ∂_{μ} is the partial four-derivative. The Einstein summation is used whereby the up and down μ indices are summed over the four co-ordinates (0,1,2,3) of time and space. This spinor field transforms under a local $U(1)$ phase transformation, such that:

$$\psi(x) \rightarrow \psi'(x) = e^{iq\theta(x)}\psi(x), \tag{2.2}$$

where $\theta(x)$ is the phase shift and q is the elementary charge. Ensuring the Lagrangian remains invariant under this transformation, a new degree of freedom is added to the partial derivative such that:

$$D_{\mu} = (\partial_{\mu} + ig_E A_{\mu}), \tag{2.3}$$

where A_{μ} transforms as:

$$A_{\mu} \rightarrow A'_{\mu} = A_{\mu} - \partial_{\mu}\theta(x). \tag{2.4}$$

Here, A_{μ} is considered the gauge field for the electromagnetic interaction, representing the

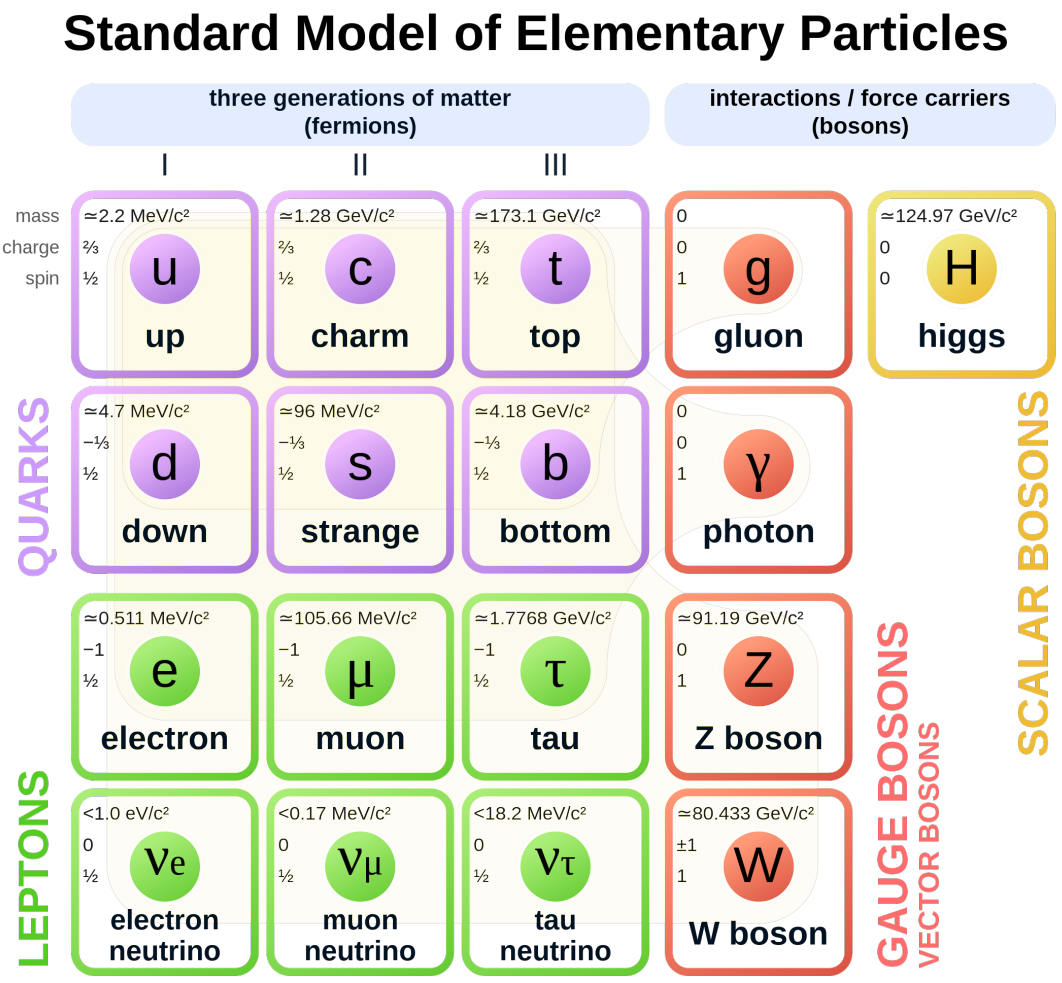

FIGURE 2.1: Diagram of the 12 fundamental fermions and 5 fundamental bosons of the Standard Model of particle physics [31]. Brown loops show which of the gauge bosons (red) couple to which fermions, split by quarks (purple) and leptons (green). The Higgs boson couples to all particles with mass.

photon, and g_E is the electromagnetic interaction strength. Following this, the QED Lagrangian can be written as:

$$\mathcal{L}_{QED} = \bar{\psi}(i\gamma^\mu D_\mu - m)\psi - \frac{1}{4}F_{\mu\nu}F^{\mu\nu}, \tag{2.5}$$

where $F_{\mu\nu} = \partial_\mu A_\nu - \partial_\nu A_\mu$ is the electromagnetic field strength tensor and $F_{\mu\nu}F^{\mu\nu}$ represents the kinetic energy term of the photon. The QED Lagrangian describes the interaction between all electrically charged fermions and photons.

Extending the unitary group of dimension one ($U(1)$) to the special unitary group of dimension three ($SU(3)$), we move into the realm of Quantum Chromodynamics (QCD) [33–35]. This results in the expansion from one mediator (photon) in QED, to eight mediators (gluons) in QCD, corresponding to the eight generators of the $SU(3)$ local gauge symmetry. Additionally, the number of charges increases from one to three color charges. The only particles that carry

the color charge are the quarks and the gluons, and collectively are often referred to as partons. Unlike photons, the gluons are able to self-interact. One of the results of this self-interaction is that the strong force does not weaken as the distance between two colored objects increases, and so the potential energy of the interaction increases linearly as the distance is increased. At some point it becomes energetically favourable for new quarks to be created from this energy as opposed to increasing the energy further, confining the colored quarks into colorless composite particles. Another important aspect of QCD is known as asymptotic freedom and is related to the variation of the strong coupling constant, α_s, as the energy scale Q^2 varies. This is evident in the following equation:

$$\alpha_s(Q^2) \propto \frac{1}{\ln(Q^2/\Lambda^2_{QCD})}, \tag{2.6}$$

where Λ_{QCD} is the QCD energy scale on the order of 200-300 MeV [11]. For smaller energy scales (larger distances) below Λ_{QCD}, α_s becomes larger than 1 and the theory enters the non-perturbative regime. At higher energy scales (shorter distances) above Λ_{QCD}, α_s decreases below 1 which allows for perturbative calculations to be used.

Within the SM framework, the electromagnetic and weak forces are combined into an electro-weak (EW) interaction. The charged-current weak interaction relating to the W bosons, are associated with the special unitary group of two dimensions $SU(2)_L$. The L indicates that this interaction only couples with the left-handed (right-handed) particle (anti-particle) states. The generators of this $SU(2)_L$ gauge symmetry are the weak isospin $\mathbf{T}$, which can be written in terms of the Pauli spin matrices $\boldsymbol{\sigma}$ as $\boldsymbol{T} = \frac{1}{2}\boldsymbol{\sigma}$. Using this description, the left-handed particles and right-handed anti-particles are represented by weak isospin doublets with total isospin $I_W = \frac{1}{2}$, while the right-handed particles and left-handed anti-particles are represented by weak isospin singlets with $I_W = 0$. In order to conserve the local gauge symmetry of the Lagrangian, three gauge fields W^k_μ, with $k = 1, 2, 3$, are introduced, acting in a similar manner to A_μ. The weak charged-currents can be expressed as linear combinations of W^1_μ and W^2_μ as:

$$W^\pm_\mu = \frac{1}{\sqrt{2}}(W^1_\mu \pm W^2_\mu). \tag{2.7}$$

Since the W bosons have integer electric charge, they can only interact between fermions that differ in charge by ± 1, resulting in quark and lepton doublets of the form, e.g.:

$$q_L = \begin{pmatrix} u \\ d \end{pmatrix}_L, l_L = \begin{pmatrix} \nu_e \\ e^- \end{pmatrix}_L. \tag{2.8}$$

Under the $SU(2)_L$ transformation, the two components of the doublet mix, allowing the weak force to change, e.g., a left-handed e^- to a left-handed ν_e via a W boson. However, only left-handed fermions can mix under the weak force $SU(2)_L$ transformations. Since there is no experimental evidence for a right-handed gauge group $SU(2)_R$ [11], the right-handed electron singlet, e^-_R, does not participate in weak interactions and cannot mix with other particles under

weak force transformations.

From experimental observations, the Z boson interacts with both left- and right-handed particles, and so cannot be associated with the W^3 gauge field. However, in the electroweak model of Glashow [1], Salam [2] and Weinberg [3], a $U(1)_Y$ local gauge symmetry is used instead of the $U(1)$ symmetry, which introduces the weak hypercharge $Y = 2Q - 2I_W$, where Q is the electromagnetic charge. There is also a new gauge field B_μ, charged in terms of the weak hypercharge Y. The combination of $SU(2)_L \otimes U(1)_Y$ generates four gauge fields of the electroweak interaction with two being the $W^\pm$ bosons introduced earlier. The other two, Z_μ and A_μ, correspond to the Z boson and photon respectively and are created via the combination of the B_μ and W^3_μ fields, as:

$$\begin{aligned} A_\mu &= +B_\mu \cos\theta_W + W^3_\mu \sin\theta_W, \\ Z_\mu &= -B_\mu \sin\theta_W + W^3_\mu \cos\theta_W, \end{aligned} \tag{2.9}$$

where θ_W is the weak mixing angle. The weak mixing angle and the couplings of the weak (g_W, g_Z) and electromagnetic forces are related as:

$$g_E = g_W \sin\theta_W = g_Z \sin\theta_W \cos\theta_W. \tag{2.10}$$

The EW and QCD theories are unified within the SM framework under the symmetry group $SU(3)_C \otimes SU(2)_L \otimes U(1)_Y$. For the local gauge symmetry to be satisfied, all the particles are required to be massless, since the mass term would break the symmetry. As an example, the Dirac mass term for fermions, written as $m\psi\bar{\psi} = m(\bar{\psi}_L + \bar{\psi}_R)(\psi_L + \psi_R) = m(\bar{\psi}_L\psi_R + \bar{\psi}_R\psi_L)$, has both right- and left-handed couplings. The left-handed doublets and right-handed singlets have different transformation properties under $SU(2)_L$ and so aren't invariant under $SU(2)_L$ gauge transformations. However, from experiment, it is known that these particles have mass, which is a contradiction. An additional mechanism is thus required to provide the masses of the particles.

2.2 The Higgs mechanism

In order to obtain masses for the fundamental particles of the SM whilst maintaining gauge invariance, the Brout-Englert-Higgs mechanism [4][36][37], shortened to the Higgs mechanism, is used. The Higgs mechanism introduces a scalar field with which the massless particles interact, and it is through this interaction that the particles acquire their mass. The Higgs field transforms as a doublet under $SU(2)_L$ and is part of the $SU(2)_L \otimes U(1)_Y$ electroweak sector. It also introduces an additional scalar Higgs term in the Lagrangian:

$$\mathcal{L}_{Higgs} = (D^\mu\phi)^\dagger(D_\mu\phi) - V(\phi). \tag{2.11}$$

As such, this new field is associated with a weak isospin doublet of complex scalar fields with four degrees of freedom:

$$\phi = \begin{pmatrix} \phi^+ \\ \phi^0 \end{pmatrix} = \frac{1}{\sqrt{2}} \begin{pmatrix} \phi_1 + i\phi_2 \\ \phi_3 + i\phi_4 \end{pmatrix}. \tag{2.12}$$

The covariant derivative of ϕ follows as:

$$D_\mu \phi = (\partial_\mu + i g_W \frac{\boldsymbol{\sigma}}{2} \cdot \boldsymbol{W_\mu} + i \frac{1}{2} g' B_\mu)\phi, \tag{2.13}$$

where W_μ and B_μ are the gauge fields related to $SU(2)_L$ and $U(1)_Y$ respectively. The g_W and $g' = g_Z \sin(\theta_W)$ terms are the gauge couplings introduced at the end of Section 2.1. This covariant derivative ensures invariance of ϕ under local $SU(2)_L \otimes U(1)_Y$ transformations. Referring back to Equation 2.11, the first term represents the kinetic energy, and the second term is the Higgs potential, defined as:

$$V(\phi) = \mu^2 \phi^\dagger \phi + \lambda (\phi^\dagger \phi)^2, \tag{2.14}$$

with μ and λ being scalar constants. The first term in Equation 2.14 is the mass term while the second term is the self-interaction term. To obtain a minimum of this potential, λ is required to be positive. If the sign of μ^2 is positive, the potential has a unique minimum at $\phi = 0$. For this case, the Lagrangian of Equation 2.11 represents a scalar particle of mass μ which obeys the $SU(2)$ symmetry. If the sign of μ^2 is negative, the potential has an infinite set of minima defined by the circumference corresponding to:

$$\phi^\dagger \phi = \frac{1}{2}(\phi_1^2 + \phi_2^2 + \phi_3^2 + \phi_4^2) = \frac{v^2}{2} = -\frac{\mu^2}{2\lambda}, \tag{2.15}$$

where v is the vacuum expectation value (VEV). All the minima are equivalent under the $SU(2)$ transformation. A diagram illustrating the potentials for the $\mu^2 > 0$ and $\mu^2 < 0$ cases are shown in Figure 2.2. As can be seen, for the case where μ^2 is negative, a non-zero value of v breaks the initial symmetry of the Lagrangian, causing what is known as spontaneous symmetry breaking.

Assuming the field is at a minimum when $\phi_1 = \phi_2 = \phi_4 = 0$ and $\phi_3 = v$, and using Equation 2.12, the result is:

$$< 0|\phi|0 >= \frac{1}{\sqrt{2}} \begin{pmatrix} 0 \\ v \end{pmatrix}, \tag{2.16}$$

where the Higgs field, after the unitary gauge transformation, is then given by:

$$\phi = \frac{1}{\sqrt{2}} \begin{pmatrix} 0 \\ v + h \end{pmatrix}. \tag{2.17}$$

Here, v is a real constant and h is a real scalar field, hereby referred to as the Higgs boson field. Writing the Lagrangian in Equation 2.11 such that it respects the $SU(2)_L \otimes U(1)_Y$ local gauge symmetry, the mass terms for the gauge bosons can be obtained. In this case, ϕ_1, ϕ_2 and ϕ_4 of

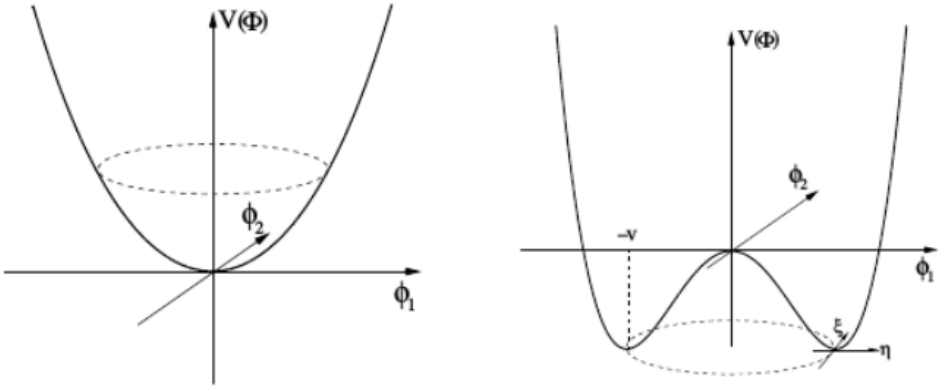

FIGURE 2.2: Diagram illustrating the potential $V(\phi)$ of a complex scalar field for $\mu^2 > 0$ (left) and $\mu^2 < 0$ (right) [38]. These are simplified diagrams, only showing two of the four components of the Higgs field as defined in Equation 2.12. After symmetry breaking, the vacuum expectation value acquires the value of v. The angular fluctuations of the field, ξ, correspond to the Goldstone bosons, while the radial fluctuations, η, correspond to the Higss boson.

Equation 2.12 represent the massless Goldstone fields that are "absorbed" by the $W^{\pm}$ and Z bosons, while ϕ_3 represents the massive Higgs boson. The masses are found to be:

$$\begin{aligned} m_W &= \frac{g_W v}{2} \\ m_Z = \frac{v}{2}\sqrt{g_W^2 + g'^2} &= \frac{m_W}{\cos\theta_W} \\ m_H = \sqrt{-2\mu^2} &= \sqrt{2\lambda v^2} \\ m_\gamma &= 0. \end{aligned} \tag{2.18}$$

The results show that we end up with masses for three bosons (W, Z, H), and the one boson that is massless (γ). The photon remains massless since the spontaneous symmetry breaking reduces the electro-weak symmetry $SU(2)_L \otimes U(1)_Y$ to the electromagnetic symmetry $U(1)_{em}$ [39].

For the Higgs field to provide the masses of the fermions, an additional Yukawa term is added to the Lagrangian. Taking the electron as an example, with left-handed doublets ψ_L (of the form given in Equation 2.8) and right-handed singlets ψ_R, their interaction with the Higgs field ϕ, written as $\bar{\psi_L}\phi\psi_R$, is invariant under $SU(2)_L \otimes U(1)_Y$ gauge transformations. It is therefore possible to construct a gauge invariant Lagrangian term as:

$$\mathcal{L}_{Yukawa,e} = g_e(\bar{\psi_L}\phi\psi_R + \bar{\psi_R}\phi^\dagger\psi_L), \tag{2.19}$$

where g_e is the Yukawa coupling constant between the Higgs field and the electron [3]. Using the Higgs field as described in Equation 2.17, and after symmetry breaking, $\mathcal{L}_{Yukawa,e}$ becomes:

$$\mathcal{L}_{Yukawa,e} = \frac{g_e v}{\sqrt{2}}(\bar{\psi_L}\psi_R + \bar{\psi_R}\psi_L) - \frac{g_e h}{\sqrt{2}}(\bar{\psi_L}\psi_R + \bar{\psi_R}\psi_L). \tag{2.20}$$

The value of the Yukawa coupling is not determined by the Higgs mechanism, but for convenience, is chosen to be defined in terms of the electron mass as:

$$g_e = \sqrt{2}\frac{m_e}{v}. \tag{2.21}$$

Using this and the fact that $\psi = \psi_L + \psi_R$, Equation 2.20 becomes:

$$\mathcal{L}_{Yukawa,e} = -m_e\bar{\psi}\psi - \frac{m_e}{v}\bar{\psi}\psi h. \tag{2.22}$$

Here, the first term contains the electron mass, and the second term represents the coupling of the electron to the Higgs field.

While the same process can be used to obtain the masses of the quarks, it must be noted that since only the lower component of the Higgs doublet contains the non-zero VEV (Equation 2.17), and comparing to the fermion doublets in Equation 2.8, only the down-type quarks and charged leptons would obtain a mass. For the up-type quarks to obtain a mass, the conjugate Higgs doublet must be used, defined as:

$$\begin{aligned}\tilde{\phi} \equiv i\sigma^2\phi^* &= i\begin{pmatrix}0 & -i\\ i & 0\end{pmatrix}\begin{pmatrix}\phi^{+*}\\ \phi^{0*}\end{pmatrix} = \begin{pmatrix}\phi^{0*}\\ -\phi^-\end{pmatrix}\\ &= \frac{1}{\sqrt{2}}\begin{pmatrix}\phi_3 - i\phi_4\\ -\phi_1 + i\phi_2\end{pmatrix} = \frac{1}{\sqrt{2}}\begin{pmatrix}v + h\\ 0\end{pmatrix}.\end{aligned} \tag{2.23}$$

Due to the properties of $SU(2)$, the conjugate doublet transforms in the same manner as the doublet. The Lagrangian for the up-type quarks would then look like Equation 2.19, but using $\tilde{\phi}$ instead of ϕ and g_u instead of g_e, and following the procedure as above for the electron, the masses of the up-type quarks can be obtained.

The above formalism works fine for one generation of quarks. However, in the SM there are three generations of quarks which have a slight mismatch between the mass/flavour eigenstates and the weak interaction eigenstates. Since the Yukawa couplings of the quarks are defined in the weak eigenstate basis, an additional matrix is required to transform these weak eigenstates into the mass eigenstates. So instead of the quarks' weak force interactions occurring within a simple doublet like in Equation 2.8, they occur within doublets of the form:

$$\begin{pmatrix}u\\ d'\end{pmatrix}, \begin{pmatrix}c\\ s'\end{pmatrix}, \begin{pmatrix}t\\ b'\end{pmatrix}, \tag{2.24}$$

where the weak eigenstates d', s' and b' are a combination of the down-type quarks' mass eigenstates. The weak eigenstates are obtained via the 3×3 unitary Cabibbo-Kobayashi-Maskawa (CKM) matrix [40][41], as follows:

$$\begin{pmatrix} d' \\ s' \\ b' \end{pmatrix} = \begin{pmatrix} V_{ud} & V_{us} & V_{ub} \\ V_{cd} & V_{cs} & V_{cb} \\ V_{td} & V_{ts} & V_{tb} \end{pmatrix} \begin{pmatrix} d \\ s \\ b \end{pmatrix} \tag{2.25}$$

It is the non-diagonality of the CKM matrix that allows the quarks of different generations to interact with each other, producing generation-changing (flavor-changing) charged-current interactions. The parameters of this matrix have to be obtained through experimental measurements, and is observed to be a highly diagonal matrix. This means the quarks strongly favour decaying to the other quark within its generation, e.g., $c \to s$, while they decay to quarks of the opposite type in other generations at much lower rates.

2.3 Beyond the Standard Model

While the SM introduced in the previous sections has described many aspects of nature, with many successful experimental results backing these predictions, there are some things the SM is unable to explain. Some of the issues the SM is unable to explain are:

- Dark matter: Through astronomical observations, it has been observed that about 85% of the "stuff" in the universe that interacts with gravity is made up dark matter [42]. Unfortunately, almost nothing is known about dark matter since the only evidence for it is from its gravitational effects on large astronomical scales, e.g., the rotation of galaxies [43] indicates that there is more mass than what we can see, and the amount that light is bent around galaxies (gravitational lensing) [44] also suggests more mass than what is observed. It is unknown whether dark matter interacts via any other force and, as to date, there is nothing in the SM that is capable of describing it.

- Dark energy: It was expected that due to the attractive nature of gravity, the expansion of the universe should slow down over time. However, through cosmological observations, the expansion of the universe was found to be accelerating [45]. There is nothing in the SM that is able to describe this rate of acceleration.

- Matter-antimatter asymmetry: Assuming that there were equal amounts of matter and anti-matter produced in the early universe, they should have all annihilated each other and left only photons. And given that observations of the universe indicate that all the observable "stuff" is matter, why did this dominate over anti-matter. The amount of CP violation described in the SM does not explain this discrepancy [46].

- Parameters of the SM: Many of the parameters of the SM are not explained by the theory, but are determined from experiments. The 19 free parameters include the nine masses of the fermions, the three coupling constants of the forces, the four parameters that define the CKM matrix, the mass of the Higgs boson and the VEV of the Higgs field, and the strong CP phase. Some parameters also need to be fine-tuned, e.g., the bare Higgs mass has to be fine-tuned in order to cancel the large quantum corrections to the Higgs mass. The arbitrariness of some of the parameters and the fine-tuning required for some of the parameters in the SM suggest that the SM is incomplete.

- Neutrino oscillations: Within the SM, neutrinos can only be left-handed, ruling out a mechanism capable of producing neutrino masses. However, the discovery of neutrino oscillations implies that the neutrinos do have mass [47]. While there is a way to expand the SM to allow this to happen [48], exactly what needs to be added depends on whether the neutrinos have separate anti-particles or if they are their own anti-particles, which is unknown. This would also add at least seven additional free parameters to the 19 already existing free parameters of the SM.

- Gravity: While there is a very successful theory of gravity in the General Theory of Relativity [49], it does not work well on the small scales of particle physics or in regions of very strong gravitational fields. Attempts to create a quantum theory of gravity [15] have struggled for various reasons, one of which is that describing gravity in the framework of QFT leads to non-renormalizable infinities. Another is that since the effects of quantum gravity are only important at scales several orders of magnitude above what experiments are capable of currently, there is no experimental evidence to help guide the quantum theory of gravity.

There are some additional theories that attempt to solve these problems, e.g., Supersymmmetry (SUSY) models [18][19] and string theory [50][51]. These theories can be studied via analyses targeting specific aspects of these theories. This is more of a test for those theories specifically rather than a test to see if any deviation from the SM can be found. A better way to search for deviations from the SM is to use a model-independent approach, with little to no assumptions from any BSM models. This approach usually takes the form of adding extra terms to the SM Lagrangian, acting as an EFT.

2.3.1 Effective Field Theory

In nature, physical processes occur at a wide range of different energies, which while dominant in one energy range, may be negligible in another. However, sometimes a particular theory at a higher energy scale may exhibit small residual effects at a lower energy scale that is under study. According to the decoupling theorem [52], if the mass of a new particle is much larger

than the energy of the process under study ($M \gg E$), the effects of that particle can become suppressed. This "decouples" the heavy particle from the lower energy theory. Therefore, not all the degrees of freedom of the full theory are required at lower energies, and so there is now an effective theory, or EFT. These effects enter into the lower energy theory via higher order perturbative effects, without explicitly including the new particle. In this manner, a physical theory can be thought of as an approximation of some theory at higher energy scales. An example of this is the Fermi theory of the weak interaction which effectively describes the weak theory at energies much lower than the mass of the W and Z bosons.

From this, it would be reasonable to assume that the SM may be an approximation of a larger theory at some higher energy scale [12]. The electroweak scale is of the order of ~ 100 GeV. The scale of the larger theories can vary from ~ 1 TeV for SUSY [53], all the way up to the Planck scale ($\sim 10^{19}$ GeV) for theories of Quantum Gravity [54].

An effective field theory for the SM is known as the Standard Model Effective Field Theory, or SMEFT. In SMEFT, the four dimensions of the SM are extended by a set of local, higher dimensional operators, each suppressed by an increasingly larger power of the energy scale of the new physics. The SMEFT Lagrangian can be written as:

$$\mathcal{L}_{SMEFT} = \mathcal{L}_{SM} + \sum_i \frac{c_i^{(5)}}{\Lambda}\mathcal{O}_i^{(5)} + \sum_i \frac{c_i^{(6)}}{\Lambda^2}\mathcal{O}_i^{(6)} + \sum_i \frac{c_i^{(7)}}{\Lambda^3}\mathcal{O}_i^{(7)} + \dots . \tag{2.26}$$

Here, $\mathcal{O}_i^{(D)}$ are $SU(3)_C \otimes SU(2)_L \otimes U(1)_Y$ invariant operators of dimension D, c_i are the coupling constants known as Wilson Coefficients, and Λ is the energy scale of the new physics. Due to the symmetries of the SM, the dimension five operators violate lepton number [55] and the dimension seven operators violate baryon minus lepton number [56]. As such, the leading-order BSM effects are from the dimension six operators $\mathcal{O}_i^{(6)}$, while effects from dimension eight and above are generally too suppressed and are considered negligible.

The effect of the SMEFT Lagrangian is to change the cross-section of the process of interest. STXS measurements (Section 2.5.1) have the cross-section calculations split into different kinematic regions, with the higher energy regions being more sensitive to BSM effects. It is therefore advantageous to do SMEFT studies in conjunction with the STXS measurements, where the more sensitive regions can be exploited to optimise the studies.

2.4 Event generation

In order to test the SM and any of the BSM theories, those theories need to be modelled in terms of the collisions that will be tested, e.g., pp collisions at the LHC. Monte Carlo (MC) methods are used to achieve this, modelling everything from the matrix element to the hadronisation. Depending on the process being modelled, there may be one MC generator dedicated to the

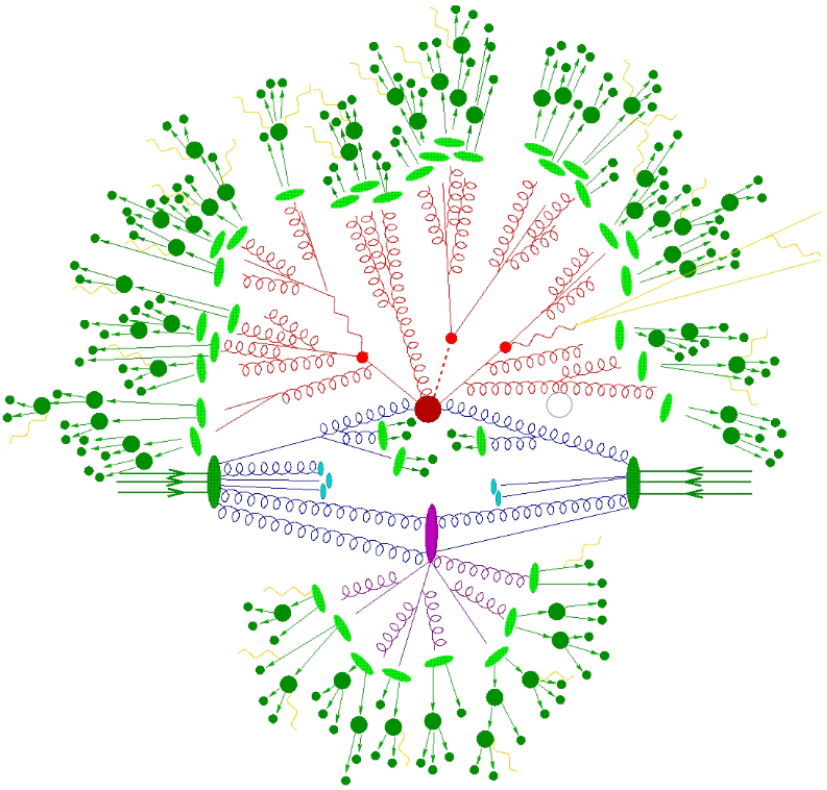

FIGURE 2.3: Diagram illustrating the steps and components of the simulation of a proton-proton collision [57]. The three parallel green lines on the left and right are the quarks in the incoming protons. The blue lines show the initial interactions from the partons in the protons. The red represents the hard collision and the subsequent parton showering. The initial hadrons produced from hadronisation are shown in light green ovals, which then decay to lighter hadrons in the dark green. The purple represents additional interactions from the same proton collision, known as the underlying event. The hadrons formed just before the hard collision are from initial state radiation, while the cyan ovals represent the beam remnants. The yellow curvy lines are from the electromagnetic radiation given off during the decays of the hadrons.

matrix element and another dedicated to the parton shower and hadronisation. In some cases, just one MC generator is used to do both steps. An illustration of the processes modelled by the MC generators in pp collisions is given in Figure 2.3. The stable particles (who typically travel further than $c\tau = 1\text{cm}$) produced through hadronisation are then sent through a simulation of the detector in order to get MC data in the same format as the raw data obtained from the actual detector. This detector simulation process is described in Section 3.2.5.

2.4.1 Hard Process

When describing protons, at low energy they can be approximated as a bound state of three quarks and are dominated by non-perturbative QCD effects. At higher energies, a sea of virtual partons existing from vacuum fluctuations, becomes more dominant. When two protons "collide" at the LHC, it is the partons in the protons that are interacting. Using this partonic

model of hadrons, when two hadrons scatter, the hard collision (large momentum transfer) occurs between parton a and b, represented by the maroon circle in Figure 2.3. Each parton carries a certain fraction of the hadrons momentum, x_1 and x_2, known as the Bjorken-x [58] of each parton. At a given energy scale, Parton Distribution Functions (PDFs) tell us the probability of finding a parton with a particular Bjorken-x inside a hadron. The probability of the interaction between the partons a and b producing some final state X is given by the cross-section $\hat{\sigma}_{ab\to X}$. This cross-section is calculated from the interaction Lagrangian. The inclusive cross-section for two hadrons interacting and creating a final state X is then given as, by the QCD Factorisation Theorem [59],:

$$\sigma_{pp\to X} = \sum_{a,b} \int_0^1 dx_1 dx_2 f_1(x_1, \mu_F^2) f_2(x_2, \mu_F^2) \otimes d\hat{\sigma}_{ab\to X}(x_1 P_1, x_2 P_2, \mu_R, \mu_F), \tag{2.27}$$

where for this case the hadrons are protons p. The probability of a parton with momentum $x_i P_i$, within a proton of momentum P_i, to be involved in the hard scatter, can be represented by the PDFs $f_i(x_i, \mu_F)$. According to the QCD Factorisation Theorem, the low energy scale (soft), non-perturbative structure of the proton can be factored out into the PDFs, separating it from the perturbative, high energy (hard) processes. This separation is controlled by the factorisation scale μ_F, which essentially determines at what point the corrections to the mediating particle fall under the PDF calculations, or the hard scatter process. This factorisation helps to deal with infra-red (IR) divergences that arise from large amounts of low energy emissions.
The perturbative hard scatter calculations make use of Feynman diagrams that assist in visualising the different interactions, as well as simplifying the mathematics. Feynman diagrams consist of "external" lines that represent the incoming and outgoing particles, "internal" lines that represent the mediators of the process, and vertices where different lines may meet, representing the interactions occurring in that process. Examples of some Feynman diagrams are shown in Figure 2.4. If any of the internal lines form a closed loop, it is called a "loop" diagram, otherwise it is known as a "tree-level" diagram. The order of the calculation is defined by the number of vertices. The "tree-level" diagrams are the leading-order calculations for a process. Adding extra vertices to a simple process, particularly via loops, results in higher-order corrections to that process.
Another form of divergence that needs to be dealt with are ultra-violet (UV) divergences. The UV divergences originate from large momenta loop corrections and can be fixed via a process known as renormalisation, which introduces a renormalisation scale μ_R [60]. Renormalisation allows us to redefine certain bare quantities in the theory, e.g., the masses and coupling constants before any quantum effects are considered, in terms of measurable finite quantities. The value of μ_R determines the energy at which the renormalisation occurs. The parameters in the theory are thus dependent on this parameter, and results in running coupling constants. This means the strength of the interactions, for example those between partons governed by the

strong coupling constant α_s, are dependent on the value of μ_R.
The impact of the μ_F and μ_R scales on the cross-section decreases as the order of the perturbation increases. This is due to the higher-order terms providing corrections that account for variations due to these scales.
Due to the limited phase space accessible to detectors used in particle physics, total cross-sections of a process cannot be directly measured. Instead, by restricting theoretical calculations to match the phase space observed by the detector, we can measure the fiducial cross-section. A more fine grained measurement with respect to some parameter or angle Ω provides the differential cross-section $\frac{d\sigma}{d\Omega}$. Instead of measuring the inclusive cross-section of a process $pp \to X$, it is often better to measure the exclusive cross-section, studying a specific decay of X into some final state Y, $pp \to X \to Y$. Exclusive measurements have reduced background contributions, and because they provide more precise information on a specific process, they rely on fewer theoretical assumptions. The probability for a state X to decay to a state Y is given by the branching ratio $\mathrm{BR}(X \to Y) = \Gamma_{X\to Y}/\Gamma_X$, where $\Gamma_{X\to Y}$ is the partial decay width for the decay $X \to Y$ and Γ_X is the total decay width of X. Precise knowledge of the decay widths is important for accurately determining the exclusive production cross-sections. For this thesis, $pp \to X \to Y$ would be $pp \to VH \to \text{leptons} + b\bar{b}$.

2.4.2 Parton shower and hadronisation

The partons that undergo the hard collision, and the subsequent partons resulting from that, can produce further parton emissions. If the incoming partons radiate, it is known as initial state radiation (ISR), while the emission from the outgoing partons is known as final state radiation (FSR). Depending on the choice of μ_F, some of these emissions will be calculated in the matrix element calculation, while the others are modelled approximately by parton shower algorithms. The showering starts with the most energetic emissions and moves to the lower energy emissions until it gets to a point where α_s becomes too large (~ 1 GeV) and the partons become confined into hadrons through the process of hadronisation. Looking back at Figure 2.3, the red represents to the parton showering, while the light green ovals are the original hadrons produced from hadronisation.
At the scale that hadronisation occurs, perturbation theory breaks down. Therefore, non-perturbative hadronisation models, known as fragmentation functions [61], are used to describe how the colored partons are confined into the colorless hadrons. Hadronisation is not described directly by QCD but is rather more like a phenomenological process. Fortunately, to a good approximation, the hadronisation process is independent of the initial conditions, and can be applied to different collisions.
Most of the hadrons produced by the initial hadronisation are unstable. Models are used to

simulate their decay to lighter, more stable particles that live long enough to make it through the detector without decaying to some lighter state.

2.4.3 Underlying event and pileup

The hard collision will mostly involve the interaction of just one parton from each proton. Often, the remaining partons will travel down the beam pipe and not enter the sensitive parts of the detector. Sometimes, however, the other partons will also interact with each other, undergoing the same steps as described for the hard scatter, and forming hadrons. The emissions and hadrons from this chain could interact with the hard collision chain, and so also need to be modelled. This extra contribution is known as the underlying event, and is represented by the dark purple oval in Figure 2.3.

Contributions from the other pp collisions that occur at the same time as the hard-scatter (in-time pileup) and from residual effects of collisions happening shortly before or after the hard-scatter (out-of-time pileup) also need to be taken into account. This is done by overlaying simulated minimum bias events to the simulated process [62]. After all these steps, the particles are run through a simulation of the detector, as described in Section 3.2.5.

2.5 Higgs production and decay at the LHC

Since the Higgs couples to fermions and bosons with a strength that is proportional to the mass of those fermions and bosons, there is a preference for the Higgs boson to be produced in processes with heavy particles and to decay into heavy particles, so long as they are kinematically accessible.

The dominant production mechanisms for the Higgs boson are the gluon-gluon fusion (ggF), vector boson fusion (VBF), associated vector boson production (VH), and associated di-top production (ttH) [11] . The leading-order Feynman diagrams for these processes are shown in Figure 2.4. The dominant production is ggF, occurring about 88.2% of the time in pp collisions at $\sqrt{s} = 13$ TeV. Since the Higgs boson only couples to massive particles, the ggF process is only allowed through loop diagrams, where loops with non-top quarks are suppressed due to how strong the coupling between the Higgs boson and the top quark is. Although this production is dominant in pp collisions, it also has a large background from QCD processes that naturally occur in pp collisions. These QCD processes make the study of any physics process with partons in the final state challenging. The second dominant production is VBF, with a fraction of about 6.9%. VBF occurs via the scattering of two quarks with each emitting a vector boson V, and the vector bosons then annihilate to create the Higgs boson. A characteristic of this production is that the Higgs boson is produced at a large angle with respect to the direction of either quark. The next production mode is VH, which can be split into the WH and ZH productions. The

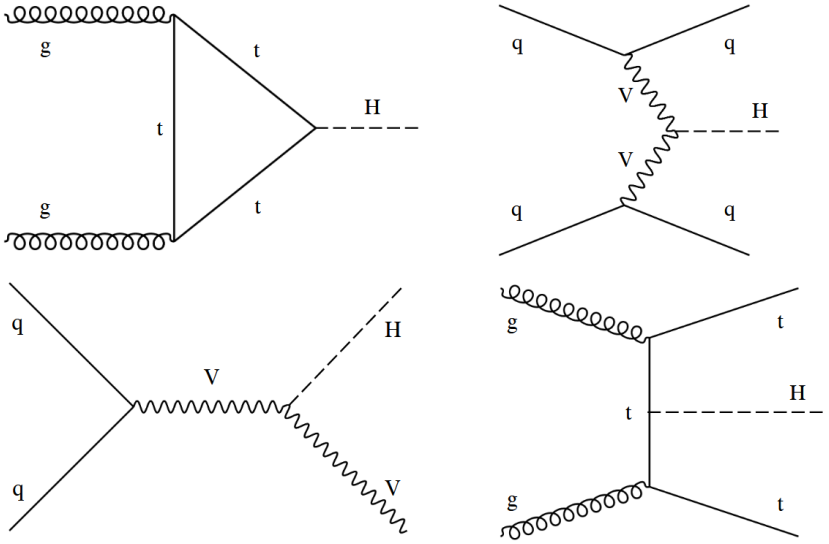

FIGURE 2.4: The leading-order Feynman diagrams for the four dominant Higgs production mechanisms: top left is gluon-gluon fusion (ggF), top right is vector boson fusion (VBF), bottom left is associated vector boson production (VH), and bottom right is associated top production (ttH) [63].

WH production occurs about 2.5% of the time, while ZH occurs about 1.6% of the time. Since this process involves a vector boson radiating a Higgs boson, it is also known as Higgs-strahlung. The addition of the vector boson decaying to leptons provides additional objects to select on that reduce the large background that the ggF process suffers from. This is the production mode studied in this thesis and is discussed in more detail in Chapter 5. The other production process is ttH, with a fraction of 0.9%. This process is similar to ggF, however instead of a top loop, the two top quarks are final state objects, and the Higgs boson is produced from the top quark mediator. The radiation of the Higgs off the top quarks provides a direct probe of the top-Higgs Yukawa coupling. Shown in Figure 2.5 are the cross-sections of the mentioned production modes as a function of the centre-of-mass energy.

The lifetime of the Higgs boson is on the order of 10^{-22}s, and so will decay to other particles quickly; either directly for massive particles, or indirectly to massless particles via a loop of massive particles. The fraction of the Higgs boson decaying to different states relative to the total Higgs boson decay rate, known as the branching ratio (BR), is shown in Figure 2.5. The dominant decay of the Higgs boson is to two bottom quarks, with a BR of about 58.2% at a Higgs boson mass of 125 GeV. This is the decay mode studied in this thesis and is explained more in Chapter 5. The other dominant decays are to two W bosons at $\sim 21.4\%$, two τ-leptons at about $\sim 6.3\%$, two charm quarks at $\sim 2.9\%$, two Z bosons at $\sim 2.6\%$ and to two photons at $\sim 2.3\%$. Despite top-quarks having the largest Yukawa coupling to the Higgs, the Higgs boson does not decay to two top quarks since the mass of just one top quark is already larger than the mass of the Higgs boson. For a similar reason, this is why the $H \to WW$ and $H \to ZZ$ branching ratios are smaller than the $H \to b\bar{b}$ branching ratios despite the vector bosons having

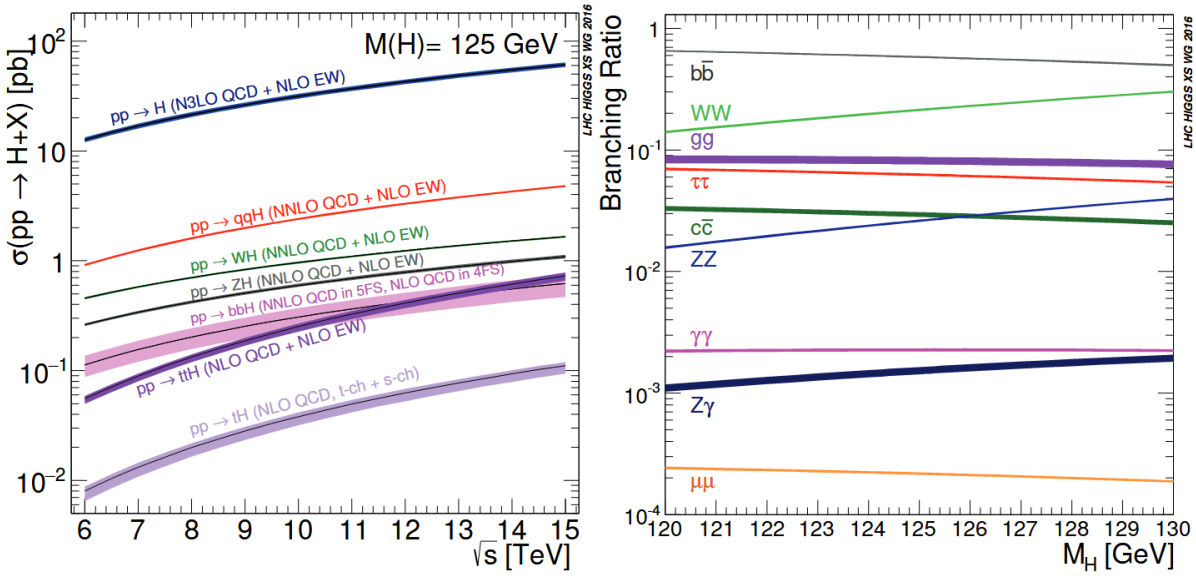

FIGURE 2.5: (Left) The SM Higgs production cross-sections as a function of the centre-of-mass energy $\sqrt{s}$, for pp collisions [11]. The qqH production here represents the VBF production, and the bands indicate the theoretical uncertainties. (Right) Branching ratios for the main decay modes of the Higgs boson in the mass range around 125 GeV with the theoretical uncertainties indicated by the bands [11].

a larger mass than b-quarks. However, since one W or Z boson is lighter than the Higgs boson, it is possible for the Higgs to decay to one on-shell vector boson, and one off-shell. This allows these decays to occur and is also the reason why the $H \to ZZ$ BR is smaller than the $H \to WW$ BR since the off-shell Z is more off-shell than the off-shell W.

Given the decay products of the Higgs boson, to study the couplings of the bottom type quarks to the Higgs field, we have a choice of $H \to b\bar{b}$ or $H \to c\bar{c}$. However, since the BR of $H \to c\bar{c}$ is almost 20 times less than $H \to b\bar{b}$, and that c-quarks are more difficult to reconstruct than b-quarks, $H \to b\bar{b}$ is the best decay mode to study for this. Since the final state of $H \to b\bar{b}$ contains quarks, there is a large background that comes from the QCD processes. So even though the ggF production of the Higgs boson occurs around 20 times more than the VH production, the VH is chosen as it provides extra vector bosons to select on. Searching for the leptonic decays of the vector bosons reduce this large amount of QCD background at the LHC.

2.5.1 Overview of the Simplified Template Cross-Section framework

This section provides an overview of the theoretical background of the STXS framework [21][64]. The STXS measurements are an evolution of the standard cross-section measurements. The focus of the first Higgs boson measurements was to simply observe the Higgs boson for the first time, so the focus was on maximising the sensitivity of the Higgs signal. Now that the Higgs boson has been discovered and with the large increase in data, instead of measuring a single

cross-section, the STXS framework allows the measurement of multiple cross-sections in different kinematic regions. These smaller regions, called STXS bins, also reduce the theoretical uncertainties folded into the measurements. In fully fiducial cross-section measurements, an extrapolation is required from the phase space used to perform the measurement, into a larger phase space used to do the theoretical calculations. Instead, a predefined phase space close in definition to the phase space used by the experiments can be defined to calculate the cross-sections. These smaller phase spaces are defined in terms of observables directly measured by experiments, e.g., the transverse momentum of one of the particles being studied. This reduces the amount of extrapolation that is required from the measured phase space to the theoretical phase space, and some of the uncertainties get absorbed into the cross-section calculations and separated from the measurement. Additionally, since these regions have their own cross-sections, each region has the possibility of showing deviations from the SM. As an example, there may be a BSM effect that is too small to have a noticeable impact on the total cross-section, but since this BSM effect targets events at higher energies, the deviation becomes noticeable in the bins with very high transverse momentum.
There are various goals that are considered when defining the STXS bins. The kinematic selections that define the bins are simplified compared to the fiducial volumes of the different analyses in the different Higgs decay channels. Defining the bins inclusively in the Higgs boson decay allows the combination of measurements from different decay channels and experiments. The bin definitions are still kept as close as possible to what the usual experimental kinematic selections would be. This allows the use of multivariate techniques to maximise the sensitivity, especially in decay channels plagued by larger backgrounds, i.e., $H \to b\bar{b}$, while keeping the unfolding uncertainties small. The STXS measurements are defined independently for the different production modes, reducing the model dependence for example on the relative fractions of the different production modes predicted by the SM.
The main goals when determining what exactly the STXS bins will be, can be summarised as the following:

- Minimise the dependence on the theoretical uncertainties
- Isolate any possible BSM effects
- Maximise the experimental sensitivity
- Limit the number of bins to match the experimental sensitivity

For the results of an analysis to be combined with other analyses, a full split at the theoretical level needs to be applied, independent on the number of bins that were actually measured. Therefore, ensuring that there aren't too many STXS bins is important to help with the implementation of the STXS framework, despite this often contradicting with the first three points

in the list above.

The STXS framework is not a rigid one and can adapt to the increasing datasets that are available by changing the number of bins available. This allows for an increase in the granularity to be accessible for combinations of decay channels, but still allows individual analyses to merge some bins depending on their sensitivity. In this thesis, the STXS stage 1.2 binning is used, albeit in a reduced state. The bins used and how the STXS framework is implemented in this thesis is explained with more detail in Section 5.5.

Chapter 3

Experimental apparatus

3.1 CERN and LHC

The Organisation for European Nuclear Research (CERN) is a European research organisation located on the Franco-Swiss border in Geneva, Switzerland, and was founded in 1954 [65]. CERN is the largest particle physics research facility in the world, with just over 100 countries involved in some manner. Some of the notable achievements in physics at CERN include the discovery of the W and Z bosons in 1983 by the UA1 [66][67] and UA2 [68][69] collaborations, the first production of anti-atoms, anti-hydrogen [70], in 1995, and the discovery of the Higgs boson in 2012 by the ATLAS [8] and CMS [9] collaborations. The information under the ATLAS section comes from Reference [71], unless otherwise stated.

3.1.1 LHC

The Large Hadron Collider (LHC) is a circular particle accelerator located at CERN and was completed in 2008 [10]. It is the largest machine in the world, with a circumference of 26.7 km, and crosses under the border between France and Switzerland. The tunnel the LHC is located in was built for the Large Electron Positron (LEP) [72] machine, and lies between 45 m and 170 m below the surface. The LHC is a double-ring synchrotron accelerator, using radio-frequency cavities to accelerate the charged particles, and liquid helium cooled, superconducting magnets to bend the path of the particles (dipole magnets) and focus the beam (multipole magnets). It was designed to accelerate protons and heavy ions, e.g., lead atoms, in opposite directions around the ring, colliding the particles at four points in the ring. The shape is actually an octant instead of a circle, containing eight straight sections where the detectors are and where the particles are injected and accelerated, and eight curved sections where the magnets to curve the beam are.

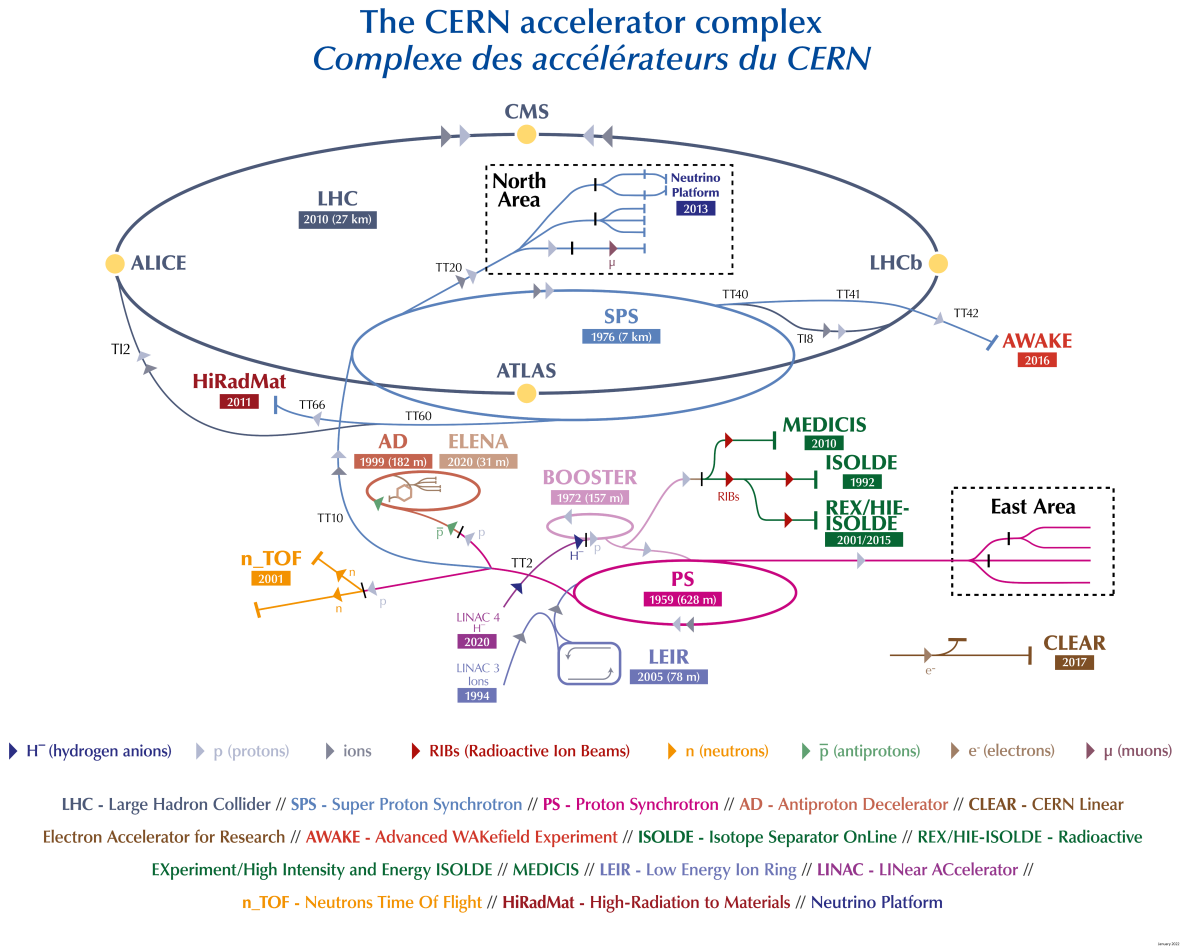

FIGURE 3.1: An illustration of the accelerator complex at CERN[73].

The original design was to accelerate protons up to a centre-of-mass energy of $\sqrt{s} = 14$ TeV, and at an instantaneous luminosity of 10^{34} cm^{-2}.s^{-1}. However, due to complications in the early days of the LHC, the energy started at a lower value and was slowly increased over the years. For Run-1 in 2009 to 2012, the centre-of-mass energies were $\sqrt{s} = 7$ and 8 TeV. For Run-2 in 2015 to 2018, $\sqrt{s} = 13$ TeV and now during Run-3, planned from 2022 till 2026, it is running at $\sqrt{s} = 13.6$ TeV. The results presented in this thesis use the full Run 2 dataset, with a luminosity of around 140 fb^{-1}.

The various accelerators situated at CERN are shown in Figure 3.1. The protons start off in the LINAC4 and then travel through the Proton Synchrotron Booster (PSB), the Proton Synchrotron (PS), the Super Proton Synchrotron (SPS) and lastly get injected into the LHC. At each new accelerator, the particles are accelerated to higher speeds and injected into the LHC at 450 GeV. The particles in the LHC are accelerated in bunches, due to the use of the radio-frequency cavities, with a temporal space between each bunch of 25 ns, providing a potential bunch crossing rate of 40 MHz.

The four main experiments at the LHC, located where the particle beams cross, are the ALICE (A Large Ion Collider Experiment) [74], ATLAS [71], CMS (Compact Muon Spectrometer) [75] and LHCb (LHC beauty) [76] experiments. The ATLAS experiment is discussed in Section 3.2.

3.1.2 Luminosity measurement

The rate of events occurring in the LHC is given by the following relation:

$$\frac{d}{dt}N_{event} = \mathscr{L}_{ins}\sigma_{event}, \tag{3.1}$$

where $\mathscr{L}_{ins}$ is the instantaneous machine luminosity and σ_{event} is the cross-section of the event under study [77]. It is therefore important to have accurate luminosity measurements to calculate the cross-sections of the different events. The delivered luminosity can be defined using the accelerator parameters, and is given by [77]:

$$\mathscr{L}_{ins} = \frac{n_b f_r n_1 n_2}{2\pi\Sigma_x\Sigma_y}. \tag{3.2}$$

Here, n_b is the number of bunches per beam, f_r is the revolution frequency, n_1 and n_2 are the number of protons per colliding bunch and Σ_x and Σ_y characterise the horizontal and vertical convolved beam widths respectively. The measurement of these beam parameters are performed using van der Meer (vdM) scans [78]. For Run-2 of the LHC, the main bunch-to-bunch luminosity measurement for ATLAS was performed using the LUCID2 detector [79]. The LUCID2 detectors are photomultiplier tubes placed $\sim \pm 17$ m from the interaction point and use Cherenkov light to measure the luminosity.

In ATLAS, the basic time interval over which to measure the luminosity is known as a luminosity block (LB) [80]. The time duration of one LB is about one minute, and the experimental conditions are assumed to be constant during this time. The $\mathscr{L}_{ins}$ is calculated using the visible interaction rate per bunch crossing, measured by the luminosity detectors per LB. The integrated luminosity of the LB is then the $\mathscr{L}_{ins}$ multiplied by the duration of that LB. The total luminosity of a dataset is then the sum of the integrated luminosities of each LB used in that dataset. The integrated luminosity delivered to and measured by ATLAS for the full Run-2 data taking period is shown in Figure 3.2. In the figure, there are three different luminosity measurements. In green, is the amount of data the LHC delivered to the ATLAS detector. The yellow is the amount of data ATLAS managed to record, which is less than the delivered due to the data-acquisition inefficiencies and due to the ATLAS warm-up before data can be taken. The blue is the amount of data designated good for physics analysis, after removing the LBs that had data taking issues, e.g., some detector components weren't working.

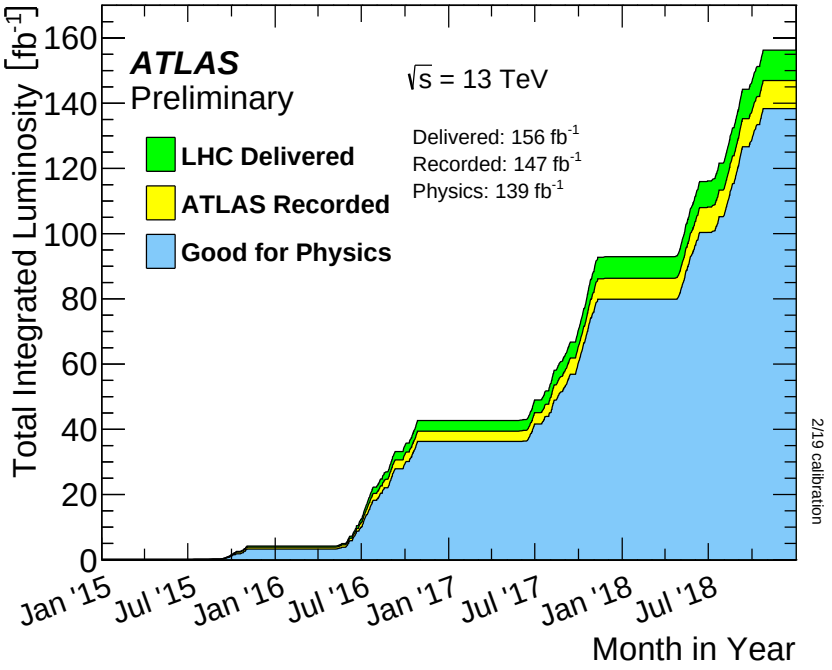

FIGURE 3.2: The cumulative luminosity delivered by the LHC (green), recorded by ATLAS (yellow), and that which is good for physics (blue) during stable beams for pp collisions at 13 TeV centre-of-mass energy for the full Run-2 data taking period [81]. The delivered luminosity was delivered from the start of stable beams until the LHC requests ATLAS to put the detector in a safe standby mode. The recorded luminosity is less due to the data-acquisition inefficiencies and due to the ATLAS warm-up before data can be taken. The luminosity good for physics is after removing data taken when not all the necessary components of the ATLAS detector were working.

3.1.3 Pileup

In the LHC, there are many pp collisions per bunch crossing to help achieve the high luminosities. However, this adds large amounts of extra radiation from other pp collisions not involved in the high p_T event of interest, referred to as pileup [62]. There are two types of pileup. In-time pileup is the extra pp collisions that occur in the same bunch crossing as the event of interest. In-time pileup also has a smaller subset of radiation known as the underlying event. The underlying event is the extra radiation that originates from the same pp collision of interest that provides the hard (high p_T) event. Out-of-time pileup is the radiation due to pp collisions occurring in the other bunch crossings other than the one of interest. The reason for this radiation is due to the sensitivity window of some of the ATLAS subdetectors being longer than the 25 ns spacing between bunch crossings.

The number of pp collisions per bunch crossing is determined by a Poisson distribution with a mean value of:

$$\mu = \frac{\mathscr{L}_{ins}\sigma_{pp}}{n_b f_r}. \tag{3.3}$$

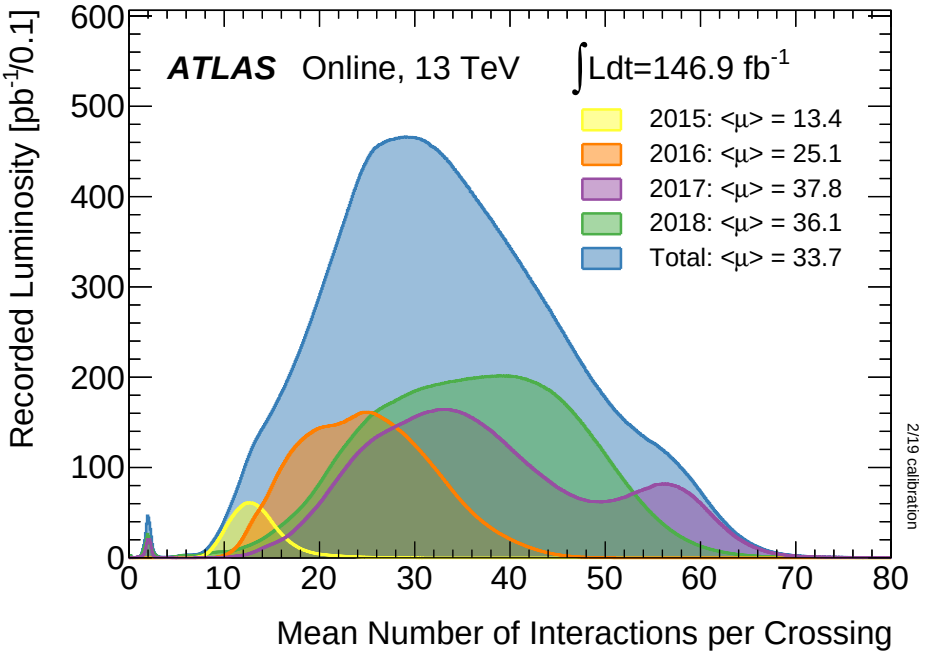

FIGURE 3.3: Shown is the luminosity-weighted distribution of the mean number of interactions per bunch crossing for the full Run-2 ATLAS pp collision data at 13 TeV centre-of-mass energy, corresponding to a recorded luminosity of 146.9 fb^{-1} [81]. The mean number of interactions per crossing corresponds to the mean of the Poisson distribution of the number of interactions per crossing calculated for each bunch.

$\mathscr{L}_{ins}$ is the instantaneous luminosity and σ_{pp} is the inelastic pp cross-section, assumed to be 80 mb for the $\sqrt{s} = 13$ TeV data. The number of protons per bunch is given by n_b, and f_r is the LHC revolution frequency. The number of interactions averaged over all bunch crossings and the analysed data is defined as $\langle\mu\rangle$. Figure 3.3 shows the mean number of interactions for the full Run-2 data.

3.2 ATLAS overview

The ATLAS detector [71] is a multipurpose detector located at the LHC, with a large focus on studying pp collisions. ATLAS is nominally forward-backward symmetric with respect to the centre of the detector and covers a full 2π angle around the beam and a nearly full 2π angle parallel to the beam. The main purpose of this almost full 4π coverage is to be able to more accurately calculate the missing energy in an event, which is used to determine whether there were any particles that escaped undetected, like SM neutrinos or unknown particles that are non-interacting. The ATLAS detector consists of four main subdetectors: the Inner Detector (ID) closest to the beam, the calorimeters, the Muon Spectrometer (MS) and the solenoid and toroid magnets. A diagram of the ATLAS detector is shown in Figure 3.4.

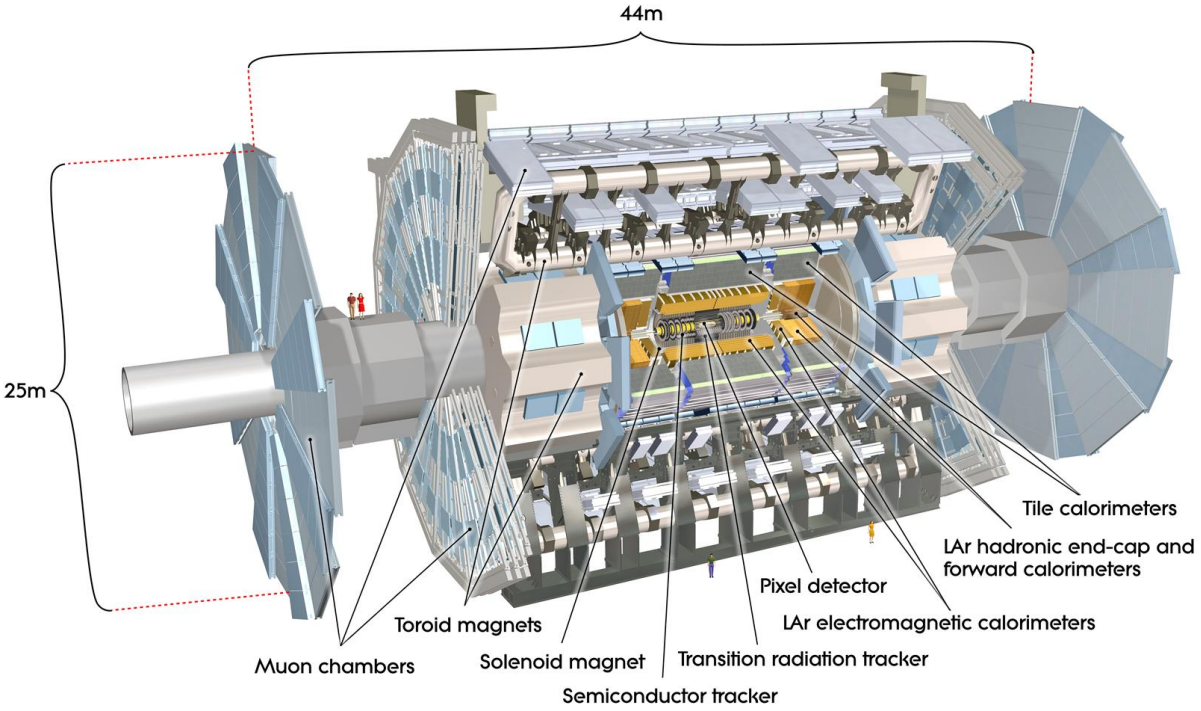

FIGURE 3.4: Cut away 3-dimensional view of the ATLAS Detector showing the several sub-detectors [71].

The Cartesian axes in ATLAS are defined such that the origin is at the point of interaction, with positive $\hat{z}$ in the anticlockwise direction of the LHC, $\hat{y}$ pointing up and $\hat{x}$ directed to the centre of the LHC ring. The positive $\hat{z}$ section of ATLAS is sometimes called the A side (anticlockwise), while the negative $\hat{z}$ is the C side (clockwise). A cylindrical co-ordinate system, however, is preferred, with z defined as already mentioned, the azimuthal angle ϕ around the beam pipe ($x-y$ plane), and the angle θ defined as the angle between the beam pipe and the detection point in the detector. Instead of using θ as is, a preferred co-ordinate used is the rapidity:

$$\mathcal{Y} = \frac{1}{2}\ln\left[\frac{E+p_z}{E-p_z}\right], \tag{3.4}$$

where E is the energy of the particle and p_z is the z-component of the particle's momentum. For high-energy low-mass particles, i.e. essentially massless particles, rapidity reduces to pseudorapidity:

$$\eta = -\ln\left[\tan(\frac{\theta}{2})\right], \tag{3.5}$$

where θ is defined as before. Rapidity is used due to the momentum distribution of the partons in the protons being complex and possibly leading to boosts in collisions. Rapidity has a nice trait where the differences in rapidity are Lorentz invariant and are thus unaffected by these boosts, also resulting in a roughly constant distribution in pseudorapidity. Another complication with

the momenta of the partons is that longitudinal momentum conservation cannot be used, as the partons within the proton each carry a different fraction of the proton's momentum and these fractions are unknown at the time of the collision. However, due to there being negligible if not non-existent momentum in the transverse plane ($x-y$ plane) before a collision, the transverse momentum $p_T = |\vec{p}|\sin(\theta) = \frac{|\vec{p}|}{\cosh(\eta)}$ and transverse energy $E_T = E\sin(\theta) = \frac{E}{\cosh(\eta)}$ are widely used variables. The values for $|\vec{p}|$ and E are obtained from the tracks and the particle showers respectively. The distance between two points in pseudorapidity-azimuthal space is defined as $\Delta R = \sqrt{\eta^2 + \phi^2}$.

3.2.1 Inner Detector

The closest subdetector to the beam pipe, the Inner Detector (ID) is important for particle identification, and momentum and vertex measurements of charged particles. It is 2.1 m in diameter and 6.2 m in length, also making it the smallest subdetector. Measurements are possible for particles within the range $|\eta| \leq 2.5$ and usually above a threshold p_T of 0.5 GeV. The ID is situated within a large solenoid magnet, 5.3 m in length and with a diameter of 2.5 m. The solenoid produces a 2 T, near uniform magnetic field in the $\hat{z}$ direction, bending charged particle tracks in the transverse $R-\phi$ plane. The particle momenta and charge sign are measured using the bending of the tracks. The direction of the curve gives the charge sign while the greater the momentum of the particle, the less it bends in the magnetic field. The relative resolution in momentum increases as the momentum of the particle increases and is given by the following equation [82][71]:

$$\frac{\sigma_{p_T}}{p_T} = \frac{p_T \sigma_x}{0.3BL^2}\sqrt{\frac{720}{N+4}} \approx 0.05 p_T \oplus 1\%. \tag{3.6}$$

Here, σ_{p_T} is the uncertainty in p_T, σ_x is the track measurement error, assumed to be constant for each point, and $\oplus$ means summed in quadrature. The magnetic field B is measured in tesla, the chord length L of the arc from the first to the last point is in metres and p_T is given in GeV/c. The number of equally distributed points over the arc is defined as N. A requirement of the ID is to be able to accurately reconstruct vertices, showing which reconstructed objects are linked to the same process. B-hadrons have a longer lifetime than the lighter quarks and can travel $c\tau$ ~0.5 mm [11] before decaying, forming a secondary vertex displaced from the primary vertex. Reconstructing this secondary vertex is therefore important for finding b-jets.
There are three sections to the ID, going from the innermost outward and also descending in granularity, they are the Pixel, SemiConductor Tracker (SCT) and the Transition Radiation Tracker (TRT), and shown in Figure 3.5. The decrease in granularity and efficiency is due in most part to costs, as well as the amount of readout cables, power cables and cooling pipes that would be required for a full pixel ID. Since the ID is before the calorimeters which measure the

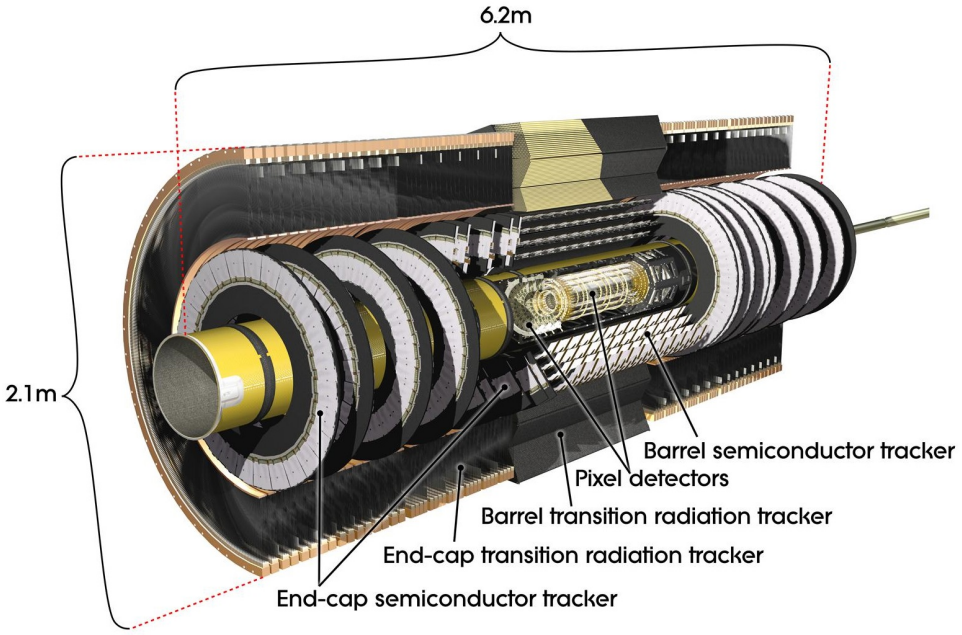

FIGURE 3.5: Cut away view of the ATLAS Inner Detector showing the three subsections [71].

energy of the particles, the ID is designed to interact with the particles as little as possible so that accurate energy measurements can be performed.

3.2.1.1 Pixel detector

The pixel detector is the closest section to the beam pipe and thus requires the highest granularity and resolution. The pixel sensors are silicon semiconductors and are 250μm thick with each pixel having an area of $50 \times 400\mu\text{m}^2$. There are 47 232 pixels per sensor, and a total of 1744, 19×63 mm^2 sensors in the pixel detector, resulting in around 80.4 million readout channels. In the pixel barrel, the sensors are placed on staves arranged in three layers. In the end-cap region, the sensors are placed on disks with three disks per side. The inner most layer (B-layer) was intended to be replaced every three years due to the high radiation dose it receives, while the other two layers were designed to withstand a 1 MeV neutron equivalent radiant energy per unit area of up to $\sim 8 \times 10^{14}$ $\text{n}_{\text{eq}}/\text{cm}^{-2}$.
In 2014 during Long Shutdown 1 (LS1), the beam pipe's diameter within the ATLAS detector was reduced to allow for the insertion of the Insertable B-Layer (IBL) [83]. The inclusion of the IBL was in preparation for the increase in luminosity the LHC would be running at in Run-2. It was inserted 1 mm from the beam pipe (at $r = 33$ mm in Figure 3.6), adding a fourth layer for improved tracking efficiencies and allowed the B-layer to remain in the ID instead of being replaced. IBL pixel sizes are smaller than the other pixels at 50×250 μm^2 with a sensor thickness of 200 μm [83]. A new cooling system based on CO_2 evaporative cooling was implemented for the IBL as well, instead of the C_3F_8 used in other parts of the ID.

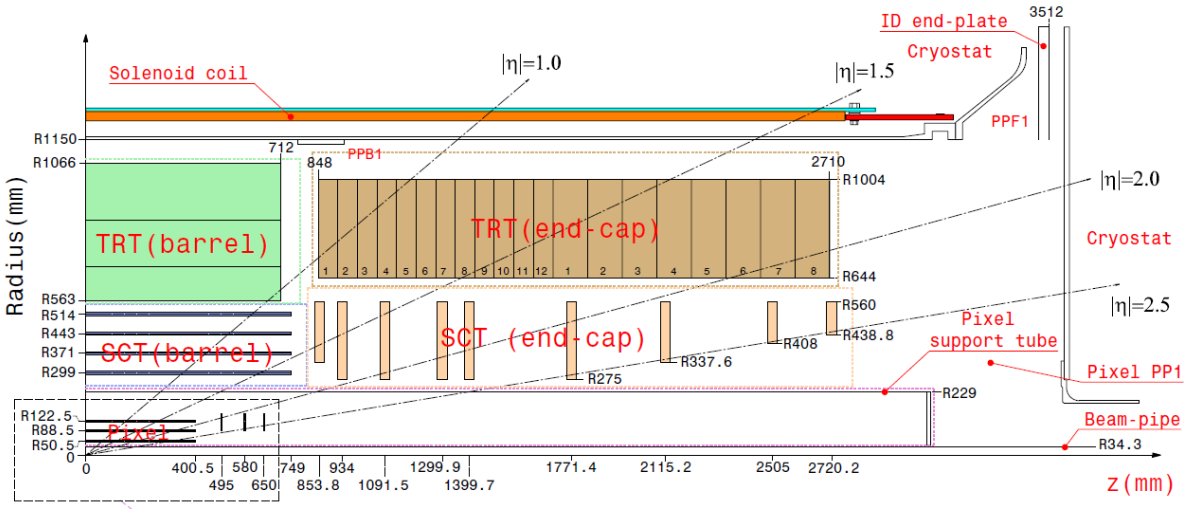

FIGURE 3.6: A quadrant of the ATLAS ID without the IBL [71].

3.2.1.2 Semiconductor Tracker

The SCT surrounds the pixel detector and has 15 912 sensors that are $285 \pm 15\mu$m thick. Each sensor has 12 cm long active strips with a pitch (distance between each strip) of 80 μm, giving the SCT 6.3 million readout channels. The strips in the barrel are parallel to the beam while those in the end-cap are orthogonal to and focus on the beam pipe. As the SCT is further from the interaction point than the pixel detector, it was designed to withstand a 1 MeV neutron equivalent radiant energy per unit area of up to $\sim 2 \times 10^{14}$ n_{eq}/cm^{-2}.
The strip sensors are arranged on staves in four layers in the barrel section, and on disks in the end-cap region with nine disks either side. Since the strips are elongated, they are only capable of 1D position measurements. Therefore, the staves and disks are double sided with the strips on each side placed at a slight angle to the other side (a stereo angle). In the barrel region, one side of the stave has the strips running parallel to the beam while the strips on the opposite side are rotated off this direction by a stereo angle of 40 mrad. The end-caps have a similar situation, though the direction is orthogonal to the beam. The second dimension of the position is then taken as the points where the strips on either side of the stave overlap.

3.2.1.3 Transition Radiation Tracker

The TRT is the final section of the ID, surrounding the SCT and consists of gas filled drift (straw) tubes instead of semiconductors. The 4mm diameter tubes act as the cathodes while 31 μm thick tungsten wires coated in gold act as the anodes. The barrel tubes are 1440 mm long and the end-cap tubes are 370 mm in length. The barrel tubes are aligned parallel to the beam while the tubes in the end-cap are aligned radially, focusing on the beam pipe. There are 73 straw planes in the barrel and 160 straw planes in the end-cap providing a total of 351 000

readout channels in the TRT.

The TRT provides track finding in the range $|\eta| = 2.0$ and only provides information in the $R-\phi$ plane for the barrel, and $z-\phi$ in the end-caps. The TRT provides a large number of hits per track (~ 36) which contribute significantly to the momentum measurements of the particles, making up for the reduced accuracy of the individual measurements. The Xenon based gas mixture of the TRT provides improved electron identification through the detection of transition-radiation photons absorbed by the gas. This provides larger signals than the minimum ionising charged particles, helping distinguish between electrons and pions. The transition radiation is produced by the polypropylene fibres in between the tubes, which as a secondary purpose, act as a polymoderator, protecting the ID by absorbing neutrons radiated from the calorimeters.

3.2.2 Calorimeters

The calorimeters are the subdetectors after the ID and solenoid, and whose purpose is to measure the energy of the particles. The calorimeter system consists of three sections, namely the Electromagnetic Calorimeter (ECal), the Hadronic Calorimeter (HCal) and the Forward Calorimeter (FCal), which are shown in Figure 3.7. The calorimeters cover a pseudorapidity range of $|\eta| < 4.9$ as well as a full 2π azimuthal coverage. The large coverage of the calorimeters is important in the measurement of the missing transverse energy, which is important for studies involving SM neutrinos or undiscovered non-interacting particles.

The calorimeters operate through the use of alternating layers of active sampling media and dense absorber materials which promote and sustain the showers. The exact materials used depend on each calorimeter and what those calorimeters are targeting. To get accurate energy measurements and prevent energy leakage, the particle showers must be contained within the calorimeters as much as possible. This also helps to prevent non-muon particles from entering the muon spectrometer and creating fake muon signals.

The energy resolution of the calorimeters is given by:

$$\frac{\sigma_E}{E} \approx \frac{a}{\sqrt{E}} \oplus \frac{b}{E} \oplus c, \tag{3.7}$$

where a is the statistical stochastic term, b is the noise term, and c is a constant. So, unlike the ID, the resolution of the calorimeters improves with higher energy particles. The energy resolution approximates to the following for the ECal and HCal separately [84]:

$$\begin{aligned} \frac{\sigma_E}{E} &\approx \frac{10\%}{\sqrt{E}} \oplus \frac{170\ \text{MeV}}{E} \oplus 0.7\% \qquad \text{(ECal)} \\ \frac{\sigma_E}{E} &\approx \frac{52.9\%}{\sqrt{E}} \oplus 5.7\% \qquad \text{(HCal)} \end{aligned} \tag{3.8}$$

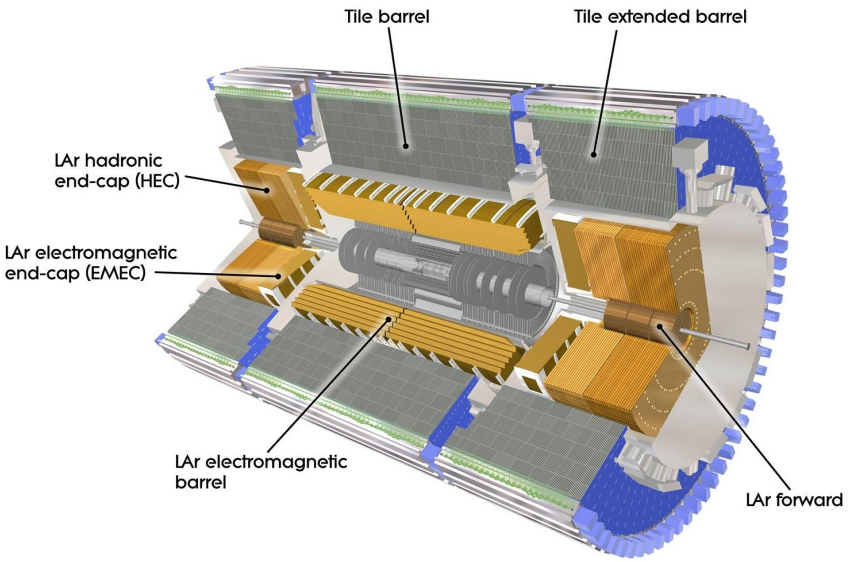

FIGURE 3.7: Cut away view of the ATLAS Calorimeter system showing the three subsections [71].

Due to the complexity of the hadronic showers, the HCal has a worse resolution, but because the electronic noise term is negligible, it is not shown in the approximation. In the ECal, particles predominantly give off energy via bremsstrahlung radiation. The amount of energy lost is determined by the radiation length (X_0) of the material, where one X_0 is the distance over which an electron will be left with $\frac{1}{e}$ of its energy after bremsstrahlung. The ECal in ATLAS has a total radiation length of $\sim 22X_0$. In the HCal, the dominant energy transfer is due to ionisation and nuclear interactions. In this case the nuclear interaction length (λ) is used, which is the mean distance travelled by a hadron before interacting with a nucleus. The HCal has a total width of $\sim 7.5\lambda$, while the ECal is $\sim 1.5\lambda$.

3.2.2.1 Electromagnetic calorimeter

The ECal uses Liquid Argon (LAr), along with kapton electrodes, as the active detecting material and lead plates as the absorber material. LAr is the main active detector medium due to its response stability over time and intrinsic radiation hardness. The barrel ECal consists of two cylinders separated by a small distance at $\eta = 0$, each with a length of about 3.2 m, and a radius from 1.4 m to 2 m. They cover the central region up to $|\eta| \leq 1.475$. The electrodes and lead plates are arranged in an accordion geometry, with the sheets in a radial direction and the lines of the folds in the beam direction. This guarantees a full azimuthal symmetry with no azimuthal cracks.

The readout in the barrel is segmented in $\eta - \phi$ to provide shape information on the showers. They are also split into three layers. The inner layer has the finest granularity of $\Delta\eta \times \Delta\phi = 0.003 \times 0.025$, useful in identifying $\pi^0 \to \gamma\gamma$ decays and photon direction measurements, and

has a depth of 4.3 X_0. The second layer is the thickest layer, at 16 X_0, intended to contain most of the EM shower. It has a segmentation of $\Delta\eta \times \Delta\phi = 0.025 \times 0.025$. The third and thinnest layer, with a depth of 2 X_0, and largest granularity at $\Delta\eta \times \Delta\phi = 0.05 \times 0.025$, is used to estimate leakage into the hadronic calorimeter.
In each end-cap, there is an ECal wheel, covering the region $1.375 < |\eta| < 3.2$ and is ~ 0.63 m thick. The geometry of the end-cap wheels is very similar to the barrel ECal, but with the sheet and fold lines opposite to the design of the barrel. In various regions of the barrel and end-caps, thin pre-sampler layers are placed between the solenoid magnet and the calorimeter, which has fine resolution and is used to estimate the energy lost to the material before the calorimeters.

3.2.2.2 Hadronic calorimeter

The HCal is positioned after the ECal and uses different sampling technologies depending on the required physics performance. There is a 5.8 m long barrel section and two extended barrels on either side of the barrel, each 2.6 m long. They both have a radius from ~ 2.3 m to ~ 4.3 m and cover the region $|\eta| < 1.0$ and $0.8 < |\eta| < 1.7$ respectively.
The tile calorimeter (TileCal) uses layers of plastic scintillating tiles as active material and steel plates as the absorber and makes up the barrel and extended barrel. The tiles are wedge shaped and placed radially and perpendicular to the beam, with photomultiplier tubes used to read the signal from the scintillators. The TileCal is also split into three layers like the ECal, with a reduced granularity compared to the ECal of $\Delta\eta \times \Delta\phi = 0.1 \times 0.1$. The reduced granularity is compensated for since hadronic showers are wider than electromagnetic showers.
The hadronic end-cap uses LAr as the active material with copperplates as the absorber. They are located after the ECal end-caps, consisting of two wheels each side that are 0.8 and 1.0 m thick, and cover the region $1.5 < |\eta| < 3.2$. LAr is used in these forward regions due to its intrinsic radiation hardness.

3.2.2.3 Forward calorimeter

The forward calorimeter (FCal) consists of three modules, each 0.45 m thick, and lies within the gaps between the beam and the end-cap calorimeters, covering the region $3.1 < |\eta| < 4.9$. The first module uses copper as the absorber material while the outer two use tungsten, and the active material for all three is LAr. The difference in metals is because the first module is designed to measure electromagnetic showers, and the other two measure hadronic showers. Due to the high radiation environment in the very forward region, the design is different to the other calorimeters. Each module has a metal matrix with regularly spaced holes that hold cylindrical electrodes parallel to the beam. The electrodes have a tube (cathode) within which is a rod (anode) and in the gap between these two is the LAr medium.

3.2.3 Muon Spectrometer

Muons are far heavier than electrons, and so do not lose much energy through bremsstrahlung. On top of this, since they are leptons, they do not interact via the strong force. With a lifetime of around 2.2 μs, muons decay outside the ATLAS detector, so they will pass through the entire detector with little interaction. It is for this reason that the Muon Spectrometer (MS) is the final layer of the ATLAS detector, where almost all the particles penetrating this far will be solely muons. Unfortunately, there are some highly energetic hadronic showers that manage to leak into the MS, or punch-through as it is often called, creating fake backgrounds for muons. An illustration of the ATLAS MS is shown in Figure 3.8.
The defining feature of the ATLAS detector is the large air-core toroidal magnet, which dominates the design of the MS. In the barrel region there are eight large superconducting coils, which are capped off at either end by two smaller end-cap toroidal magnets. The barrel toroid provides a magnetic field for the $|\eta| < 1.4$ region, the end-cap toroids cover the $1.6 < |\eta| < 2.7$ region and the $1.4 < |\eta| < 1.6$ region has a contribution from both. The average strength of the magnetic field provided by the toroidal magnets is 4 T. The choice of the additional toroidal magnet was to maximise the bending volume of the magnetic field, and to allow precise momentum measurements of forward particles. The precision with which the muon momenta can be measured varies from around 3% for lower p_T muons ($2 < p_T < 250$ GeV) and 10% for higher p_T muons ($p_T > 250$ GeV). The MS barrel has components in and around the toroidal magnets, while the three end-cap wheels are either in front (muon small wheel) or behind (the two muon big wheels) the toroidal end-cap magnets. The detectors in the MS can be split into two functions, one for triggering and the other for precision tracking.

3.2.3.1 Tracking chambers

The detectors used the most for the tracking are the Monitored Drift Tubes (MDTs), gas filled aluminium drift tubes with an anode wire in the middle. The MDT chambers are arranged in three layers in the barrel, at radii of 5 m, 7.5 m and 10 m from the the beam. In the end-cap, the MDTS are placed on four wheels/disks at distances of 7.4, 10.8, 14 and 21.5 m along the beam pipe from the interaction point. The disk at 10.8 m isn't one of the three main muon wheels as it is a disk that surrounds the end-cap toroidal magnets. The roughly 3 cm wide tubes are in the $\hat{\phi}$ direction in the barrel, since the muons bend in the $\hat{\eta}$ direction. For the end-caps, the barrels are placed perpendicular to the beam pipe. Overall, the MDTs cover the region $|\eta| < 2.7$.
In the forward regions, $2.0 < |\eta| < 2.7$, additional Cathode Strip Chambers (CSCs) are used, which have a faster readout time compared to the MDTs. CSCs are multiwire proportional chambers, with wires orthogonal to the beam pipe, and cathode planes segmented into strips

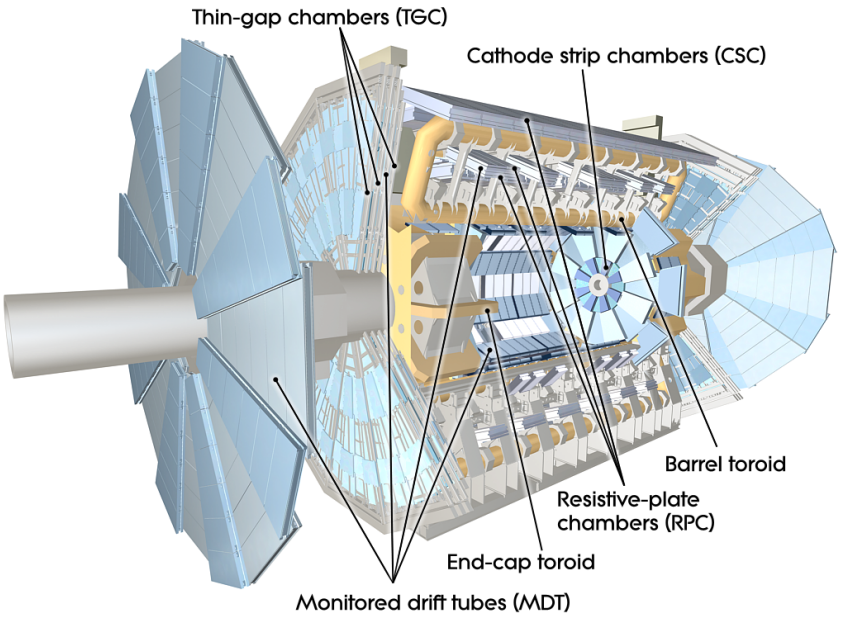

FIGURE 3.8: Cut away view of the ATLAS muon spectrometer showing the four different detector technologies [71].

orthogonal to the wires, providing a 2D measurement. Both the MDTs and CSCs have a spatial resolution of around 50 μm.

3.2.3.2 Triggering chambers

Given that most of the tracking chambers have a slow readout, dedicated fast triggering chambers are added to provide fast signals that can be triggered on. In the barrel, and installed between the MDT layers, are the Resistive Plate Chambers (RPCs). The RPCs are two high voltage electrode plates with a thin gas-filled gap. In the end-caps, Thin Gap Chambers (TGCs) are installed, which are multiwire proportional chambers with short distances between the anodes and cathodes. While the signal rate is higher in these chambers, their tracking precision is reduced, with $\mathcal{O}$(mm) precision, so provide a slight assistance with muon trajectory measurements. Additionally, the triggering chambers provide a second co-ordinate measurement for the track reconstruction. The triggering chambers do not cover the full muon range, but rather only the $|\eta| < 2.4$ region.

3.2.4 Trigger and data acquisition

The LHC is designed to provide as much data as possible, in order to maximise the statistical power of the analyses, since processes are probabilistic. However, there is a limit to the amount of information that can be transferred and stored. With the LHC capable of producing a bunch

crossing every 25 ns (40 MHz), there is about 60 TB of information produced every second. Fortunately, most of these events do not contain any hard collisions and so can be rejected, reducing the pressure on the bandwidth.

The Trigger and Data AcQuisition (TDAQ) [85] systems are comprised of smaller subsystems, usually based on the subdetectors. The Front-End (FE) systems of the detectors are used to convert the charge depositions in the sensors to an analogue or digital signal which is used to reconstruct the objects. The triggers are used to determine whether an event has any interesting objects that are worth studying. The trigger system is split into two main parts to help reduce the amount of data. The hardware based L1 trigger searches for high p_T events using the muon and calorimeter information, reducing the rate down to 100 kHz. At the L1 stage, smaller $\eta - \phi$ regions of the detector where these interesting features were found, known as Regions of Interest (RoI), are created and passed on to the next stage. While the L1 trigger is making a decision, the event info is stored in the FE buffers on the detector and are then passed to the Readout Drivers (RODs) off detector once accepted. An illustration of the ATLAS TDAQ system, used during Run-2, is shown in Figure 3.9.

After the L1 trigger is the software based High Level Trigger (HLT), which runs on a dedicated computing farm. The HLT uses offline-like algorithms to reconstruct the event within the RoI, reducing the rate further down to around 1.5 kHz. The events that pass the HLT are permanently stored in the CERN T0 computing sites for offline reconstruction.

The different object triggers used at each step are combined into trigger chains, which are themselves collected into trigger menus, defining which object triggers are used. Some necessary triggers, e.g., lower p_T triggers, could lead to very large rates. To overcome this, only a randomly selected fraction of events that pass these triggers are actually selected, in a process known as pre-scaling. The trigger menus used are determined before each ATLAS run, depending on what physics processes want to be prioritised. During a single run, as the luminosity decreases, the pre-scales will be changed.

3.2.5 Detector simulation

So far, this chapter has described the experimental apparatus used to study the real life nature of hadron collisions. The data that is obtained from these experiments provide the true distributions of the different physics processes, within statistical limitations. However, for that data to be understood, it needs to be compared to some theoretical model of what our best understanding of the natural world is. In Section 2.4, the methods used to go from the matrix element calculations of a pp collision to the formation of stable particles is introduced. This section will describe the simulation of those stable particles, how they would interact with the ATLAS detector and how that information is converted into a form that matches what we get from the physical detector.

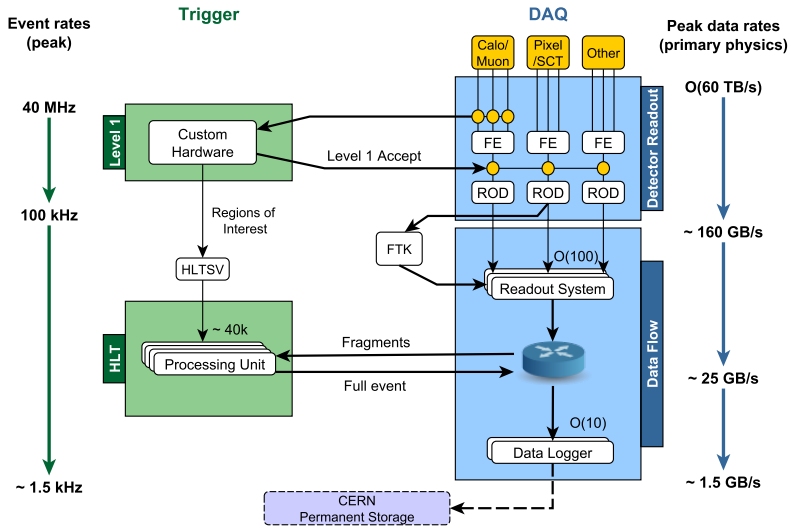

FIGURE 3.9: Illustration of the ATLAS Trigger and Data Acquisition system during Run 2 of the LHC data taking [86]. Also shown are the expected peak rates and bandwidths through each component.

The stable particles obtained from the event generation are passed through a Geant4 [87] based simulation of the detector. The interaction of the particles with the matter within the ATLAS detector volume is modelled, accounting for electromagnetic and hadronic interactions, as well as secondary particle production. The interaction points within the sensitive detector volumes and the amount of energy deposited at each of those points is stored. These energy deposits undergo a digitisation process which aims to mimic how the front-end electronics of the ATLAS experiment would collect and store the same signal. Each subdetector has its own digitisation process specific to what their readouts output. At this point, the simulation and experimental data are essentially the same and both are run through the same reconstruction chain using the ATLAS reconstruction software [88], and described in Chapter 4. This allows the data from the physical detector to be directly compared to our theoretical expectations. While this full simulation is very accurate, it is unfortunately computationally expensive. Instead, a parameterised simulation can be used to reduce the simulation time while maintaining a reasonable level of accuracy. Within ATLAS, this is performed using the Atlfast-II software [89], which uses the full detector simulation for the ID and MS, but replaces the calorimeters with a parameterised simulation called FastCaloSim [90]. Here the particle showers are parameterised in terms of their lateral and longitudinal energy profiles. There is also the Atlfast-IIF software [89] that replaces the ID and MS in Atlfast-II with the Fast ATLAS Tracking Simulation (Fatras) [91]. The computational time is reduced by an order of magnitude with Atlfast-II, and by up to a further order of magnitude with Atlfast-IIF. Another commonly used method to reduce the time spent on detector simulation is to only simulate those events that are most likely to pass

an analysis chain. This is done by including MC filters between the generation and detector simulation that apply selections, e.g., events with exactly two charged leptons or events within a specified range of missing transverse energy.
With the simulation, the information of the particles' path and decay chain are also kept, providing a truth record of the event. These truth particles can then be geometrically matched to the particles inferred from the reconstruction so that the true origin of the reconstructed objects in simulation is known.

Chapter 4

Physics object reconstruction

After a pp collision, all the produced particles travel through the ATLAS detector leaving different electronic signals throughout depending on what the particle is and the physics process of the interaction. Those raw electronic signals, either from the detector or after the digitisation process in simulation, are fed into reconstruction algorithms to identify the physics objects (particles) that left those signatures. Once reconstructed, those objects are then corrected (calibrated) for detector effects.
This chapter will describe the methods and algorithms used to reconstruct and identify the physics objects in the ATLAS detector.

4.1 Primary vertices and tracks

4.1.1 Charged particle reconstruction in the ID

The magnetic field within the ID, produced by the solenoid magnet, is directed along the z-axis and bends the charged particles produced in the beam collisions in the transverse plane. They are bent in order to calculate their momentum and charge.
In order to reconstruct the tracks of the charged particles, the charge deposited by these particles in the layers of the ID are used [92]. The pixels (Pixel), strips (SCT) and tubes (TRT) that had depositions are geometrically clustered to form "hits". A fit is performed on these "hits" to find the tracks that are most likely from particles. These potential tracks are then required to pass several criteria: $p_T > 400$ MeV, at least 7 hits in the silicon layers of the ID and small impact parameters with low uncertainties. Due to the size of the ID, tracks can only be reconstructed in the pseudorapidity range $|\eta| < 2.5$.
One of the most fundamental parts of any analysis is correctly determining the position where the hard scatter occurred, in otherwords, the pp interaction we are interested in. This is known

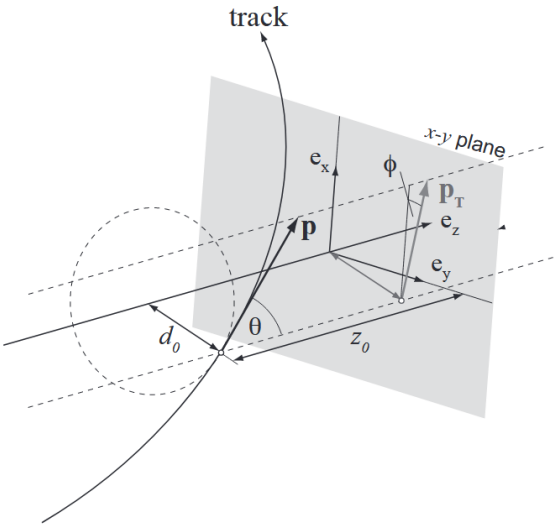

FIGURE 4.1: A diagram of the impact parameters used in ATLAS[95]. The transverse impact parameter (d_0) is defined as the distance of closest approach of the track to the beam line in the transverse plane ($x-y$ plane). The longitudinal impact parameter (z_0) is the z distance between the vertex and the point on the track that defines d_0.

as the "Primary Vertex" [93] [94], and matchong tracks to this vertex separates the process of interest from the pileup collisions. An iterative procedure is used to find and fit the vertices, using the tracks as input along with a seed position, and a χ^2 minimisation. Once the vertices have been found, the one with the highest sum of the squared transverse momenta of the tracks, Σp_T^2, is considered the primary vertex and the rest are the pileup vertices. The resolution on the primary vertex position improves as the number of fitted tracks increases. The transverse resolution varies from around 100 μm to 20 μm while the longitudinal resolution varies from around 150 μm to 30 μm [93].

Two important quantities used in the reconstruction of the vertices and afterwards are the transverse impact parameter (d_0) and the longitudinal impact parameter (z_0). These are distances of the point of closest approach on the track (perigee) in the transverse and longitudinal planes respectively. A diagram illustrating the impact parameters is shown in Figure 4.1.

4.2 Leptons and photons

In this section, the reconstruction and identification of electrons and muons are described, both being important signatures of the W and Z boson decays in the VH analysis presented in this thesis. Although photons are not used in this thesis, they are discussed here to differentiate them from electrons, given how similar their signatures are. The τ-leptons are not included in this section since they are not used as separate objects in this analysis but are rather classified as jets not originating from a b-quark.

4.2.1 Electron and photon reconstruction

Electrons and photons both leave a signature in the ECal of the ATLAS detector through a showering process. The signatures are so similar that the reconstruction of the electrons and photons are performed in parallel. The main difference between the electron and photon is that since the photon has no charge, it has a very small interaction with the ID and thus has no reconstructed track. The electron, however, will have a reconstructed track pointing to the shower it produced in the ECal.
To reconstruct the deposits (clusters) in the ECal, the ECal is divided into a grid of unit size $\Delta\eta \times \Delta\phi = 0.025 \times 0.025$ which corresponds to the granularity of the middle layer of the ECal. A sliding-window algorithm [96], of size 3×5 grid units in $\eta - \phi$ space, is then used to identify cluster seeds within $|\eta| \leq 2.5$. All cells within the window and the longitudinal layers of the ECal are summed to create a tower energy, and if the energy of the tower is greater than 2.5 GeV, then the tower is considered a seed. Cells within a predefined $\eta - \phi$ distance from the seed, dependent on the layer, are then clustered to the seed cluster to form the final cluster.
Once ECal clusters have been found, tracks in the ID are matched to the clusters if the distance between the position of the track in the middle layer of the ECal and the barycentre of the clusters is $\Delta\eta < 0.05$ and $\Delta\phi < 0.1$. These matched tracks are then refitted using a Gaussian Sum Filter [97] that takes into account the energy lost via non-linear Bremsstrahlung. The clusters with the matched tracks are the electron candidates, while the clusters with no matched tracks are photon candidates.

4.2.2 Electron and photon identification

Electrons are identified by using 3 identification criteria, each one more stringent than the previous and called *loose*, *medium* and *tight* [98]. All electrons passing the *tight* criterion also pass the *medium*, and all passing the *medium* pass the *loose*. The tighter criteria improve the rejection of non-prompt electrons and electrons originating from photon conversions but reduce the efficiency of electron identification. These criteria are briefly summarised:

- *loose*: simple shower-shape cuts are used and the matching between the cluster and the track is lenient.
- *medium*: the cuts from the *loose* selection are made more stringent with an added lenient selection on the transverse impact parameter for the track and the number of hits in the TRT. To discriminate from photon conversions in the ID, a hit in the innermost layer of the pixel detector is required.

- *tight*: the cuts from the *medium* selection are made more stringent, any photon conversion vertices associated with the cluster are vetoed, and an additional selection on the ratio between the cluster energy and the matching track momentum is added.

Cuts applied to the shower-shape also help separate electron clusters from clusters originating from light hadrons interacting with the ECal. Ligh hadron showers in the ECal are usually smaller than electron showers and tend to be closer to the HCal. A likelihood-based method [99] is used to help identify electrons. The multivariate technique considers the shower shapes, track quality, matching between the clusters and tracks, and a high threshold signal in the TRT that is indicative of transition radiation from an electron.
For electrons that have $E_T > 15$ GeV, the efficiency to reconstruct them in the central region of the detector is roughly 92%, 87% and 77% for the *loose*, *medium* and *tight* selections respectively. Plots of the electron efficiency as a function of transverse energy and pseudorapidity are given in Figures 4.2(a),4.2(b). The efficiency improves as the energy of the electron increases, and the efficiency drops as the electrons become more forward.
To further improve the efficiency of prompt electrons and reduce the backgrounds, certain isolation and quality selections are applied. The electron tracks need to pass cuts on the longitudinal and transverse impact parameters, removing tracks that may not originate from the vertex that the prompt electron comes from. There are two isolation requirements, loose and tight. For the loose isolation, the scalar sum of the track p_T within a variable cone with $\Delta R_{max} = 0.2$ around the electron track, divided by the p_T of the electron, must be less than 0.15 [99]. For the *tight* electrons, an extra isolation is applied where the sum of the transverse energy of the clusters in the calorimeter within a cone with $\Delta R = 0.2$, and not associated to the electron, must be less than 3.5 GeV.
When it comes to identifying photons, the tracks play a major role. Sometimes photons will convert to an e^+e^- pair in the ID, creating a conversion vertex which will point to the clusters in the ECal. These are known as *converted* photons, while those photons that make it to the ECal without pair producing are called *unconverted* photons. The unconverted photons will have no track associated with the ECal cluster. To differentiate between prompt photons and background photons (usually originating from jets), the shape of the cluster is used, as well as information from the first ECal layer. Prompt photons tend to have narrower showers due to their higher energies.

4.2.3 Muon reconstruction

Muons are primarily reconstructed using a combination of the MS and ID, with a small contribution from the calorimeters [101]. Tracks are reconstructed independently in the ID and MS first, and then combined following an outside-in method to form the muon candidate track (combined muons). Due to the limited size of the ID, combined muons can only be reconstructed

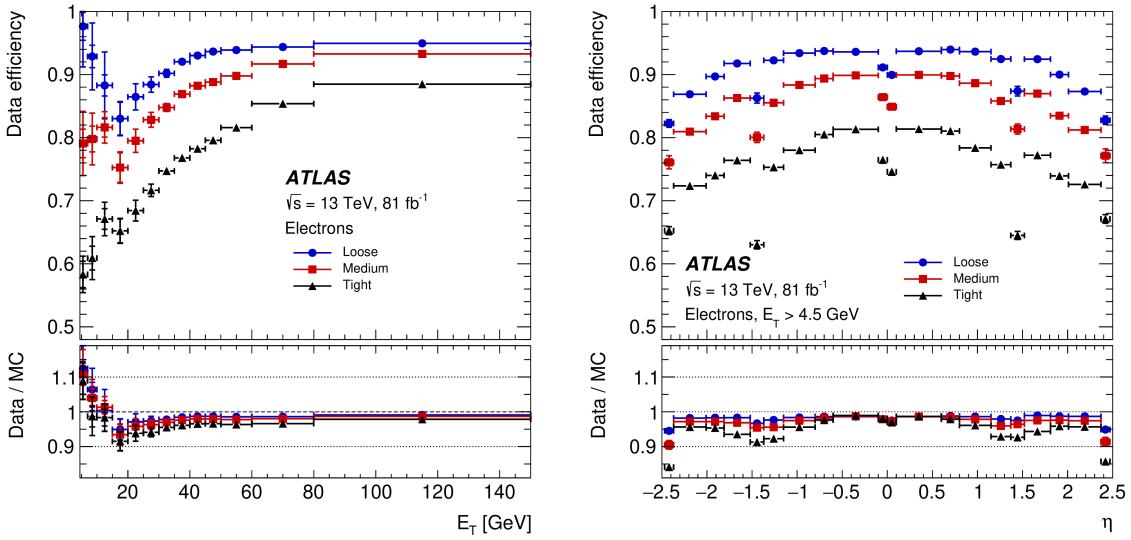

(a) (b)

FIGURE 4.2: The measured electron-identification efficiencies in $Z \to ee$ events as a function of E_T (a) and η (b) for the *loose* (blue), *medium* (red) and *tight* (black) definitions [100]. The vertical bars represent the uncertainties, for statistical (inner bars) and total (outer bars). The data efficiencies are obtained by applying data-to-simulation efficiencies measured in $J/\psi \to ee$ and $Z \to ee$ events to $Z \to ee$ simulation. In both plots, the bottom panel shows the ratio of data to simulation.

in the region $|\eta| < 2.5$.

A less common muon reconstruction uses just the information from the MS, and is used mostly in the $2.5 < |\eta| < 2.7$ region, which is not covered by the ID. These are known as extrapolated muons. Another method is the calorimeter-tagged muons. This is when a track in the MS is missing, and is mostly used in the $|\eta| < 0.1$ region where the MS has reduced acceptance due to making space for the ID and calorimeter services. The track in the ID is matched to an energy deposit in the calorimeter with an energy around the expected value to be deposited by a muon.

4.2.4 Muon identification

Similar to the electrons, the muons are required to pass different identification criteria depending on the analysis requirements, namely *loose*, *medium* and *tight*. They are defined as:

- *medium*: Only uses combined and extrapolated muons. The combined must have ≥ 3 hits in at least two MDT layers, except in the $|\eta| < 0.1$ region where at least one layer is needed. The extrapolated muons require at least three MDT or CSC layers and occur in the $2.5 < |\eta| < 2.7$ region. For the combined muons, a loose compatibility between the ID and MS tracks is applied, based on the relative differences in the momentum of the tracks.

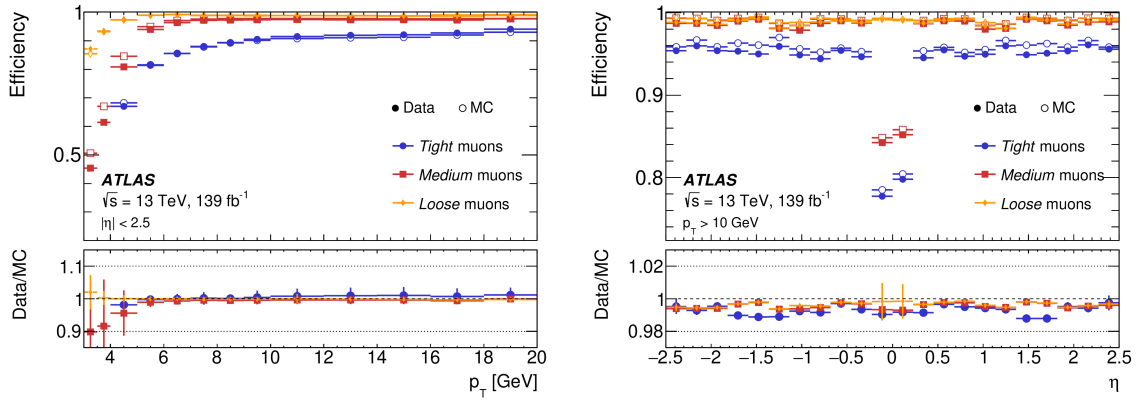

(a) (b)

FIGURE 4.3: The measured muon-identification efficiencies as a function of p_T (a) and η (b) for the *loose* (yellow), *medium* (red) and *tight* (blue) definitions [102]. The plot in (a) used $J/\psi \to \mu\mu$ events while (b) used $Z \to \mu\mu$ events and muons with $p_T > 10$ GeV. The vertical bars represent the uncertainties, for statistical (inner bars) and total (outer bars). In the upper panels of both plots, the open markers are from simulation while the filled markers are from data. In both plots, the bottom panel shows the ratio of data to simulation.

- *loose*: This uses all the muon types discussed in Section 4.2.3. All the combined and extrapolated muons must pass the *medium* selection, and the calorimeter-tagged muons are restricted to the $|\eta| < 0.1$ region.

- *tight*: Only combined muons passing the medium selection are used, which then have a tighter selection on the compatibility between the ID and MS tracks.

Plots of the muon identification efficiency as a function of p_T and η are given in Figures 4.3(a),4.3(b). The muon efficiencies are more constant compared to the electron efficiencies due to their cleaner signals.
Similar requirements on the transverse and longitudinal impact parameters that are applied to the electrons are also applied to the muon tracks. For all muons, an isolation requirement is applied where the scalar sum of the track p_T within a variable cone of $\Delta R = \min(10 \text{ GeV}/p_T^\mu, 0.3)$ around the muon track, must be less than 15% of the muon transverse momentum p_T^μ. The *tight* muons have an additional isolation where the sum of the p_T of the tracks around the muon track, and excluding the muon track, in a cone with $\Delta R = 0.2$ must be less than 1.25 GeV.

4.3 Jets

In high-energy hadron collisions, the majority of the particles produced are quarks and gluons. Unfortunately, due to QCD color confinement (see Chapter 2), these particles immediately undergo fragmentation and hadronisation, resulting in a collimated stream of particles stable

enough to travel through the detector. These streams, known as jets, deposit large amounts of energy in the calorimeters, producing a "shower" of lighter particles which are primarily electrons and photons. This makes jets complicated to reconstruct, but ideally, they are capable of providing information about the original partons [103].

4.3.1 Jet reconstruction

There are several ways to reconstruct jets in ATLAS, but for the jets used in this thesis, the Electromagnetic Particle Flow (EMPFlow) algorithm [104] is used. This uses the information from both the calorimeters and the ID. The cells in the calorimeters with sufficient energy depositions (to avoid noise) are grouped together into 3-dimensional clusters known as topological clusters (topo-clusters) via an iterative algorithm [105]. These topo-clusters, along with the tracks in the ID that are not associated to leptons, are input to the EMPFlow algorithm where overlaps between the tracks and the topo-clusters are removed via a cell-based subtraction. First, tracks are matched to the topo-cluster with the smallest $\Delta R' = \sqrt{(\frac{\eta_t - \eta_c}{\sigma_\eta})^2 + (\frac{\phi_t - \phi_c}{\sigma_\phi})^2}$, where (η_c, ϕ_c) and (η_t, ϕ_t) are the (η, ϕ) co-ordinates of the topo-cluster and track respectively, and σ_η and σ_ϕ are the angular topo-cluster widths. Tracks with $\Delta R' > 1.64$ to the nearest topo-cluster are considered unmatched and left as tracks. Additionally, the energy of the matched topo-cluster must be at least 10% of the momentum of the track. Sometimes a particle may deposit energy into multiple topo-clusters, so to distinguish between single and multiple topo-cluster depositions, the significance of the difference between the matched topo-cluster energy and the expected deposited energy is used, defined as follows:

$$S(E^{\text{clus}}) = \frac{E^{\text{clus}} - \langle E_{\text{dep}} \rangle}{\sigma(E_{\text{dep}})}. \tag{4.1}$$

Here, E^{clus} is the energy of the topo-cluster while $\langle E_{\text{dep}} \rangle = p^{\text{trk}} \langle E^{\text{clus}}_{\text{ref}} / p^{\text{trk}}_{\text{ref}} \rangle$ is the expected energy to be deposited in the calorimeter for a track with momentum p^{trk}. The expectation value $\langle E^{\text{clus}}_{\text{ref}} / p^{\text{trk}}_{\text{ref}} \rangle$ is determined using single-pion samples with no pileup [104]. $\sigma(E_{\text{dep}})$ is then the spread of the expected energy. If the energy of a topo-cluster is more than $1\sigma(E_{\text{dep}})$ below the expected energy deposited by the track, i.e., $S(E^{\text{clus}}) < -1$, a split-shower recovery is performed where topo-clusters within $\Delta R = 0.2$ of the track are labelled as matched to the track. If the total energy of all the topo-clusters matched to the track is less than the expected energy, $E^{\text{clus}} < \langle E_{\text{dep}} \rangle$, then those topo-clusters are removed. Otherwise, the energy in the cells of all the topo-clusters matched to the track are removed one-by-one, moving from more energy dense regions to less energy dense regions, until the total energy of the removed topo-clusters matches the expected deposited energy of the track. If the energy in the remaining cells is consistent with the width of the expected energy, or specifically if less than $1.5\sigma(E_{\text{dep}})$, it's assumed that these cells are due to a single particle depositing energy in these topo-clusters.

These extra cells likely originate from shower fluctuations and so are removed. If the remaining energy is above $1.5\sigma(E_{\text{dep}})$, the extra energy is likely deposited from multiple particles, and so those topo-clusters are kept. The tracks, along with the modified and unmodified topo-clusters enter the jet reconstruction algorithms.
This reconstruction of jets differs from the previous published paper [24] which used only the topo-clusters in the jet reconstruction, and are known as EMTopo jets.

4.3.1.1 Reconstruction algorithms

Jet reconstruction algorithms are designed in such a way as to allow for reconstruction using any four-momentum object as the input, be it a calorimeter cell, charged particle track or MC truth object. Due to its excellent performance at reconstructing jets, the anti-k$_T$ algorithm [106] is the method used for jet reconstruction of small-R jets in the ATLAS collaboration.
There are two distance measures in the algorithm, namely the distance between two objects i and j (d_{ij}) and the distance between object i and the beam (d_{iB}):

$$d_{ij} = \min\left(\frac{1}{p_{Ti}^2}, \frac{1}{p_{Tj}^2}\right)\frac{\Delta R_{ij}^2}{R^2}, d_{iB} = \frac{1}{p_{Ti}^2} \tag{4.2}$$

where $\Delta R_{ij}^2 = (\eta_i - \eta_j)^2 + (\phi_i - \phi_j)^2$ is the angular distance between the two objects i and j; p_{Ti}, η_i, ϕ_i are the transverse momentum, pseudorapidity and azimuth of object i, and R is the distance parameter.
The clustering is performed sequentially by comparing all objects and finding the smallest distance measure. If d_{ij} is the smallest, the objects i and j are combined and the 4-momentum of the object recalculated. If d_{iB} is the smallest, object i is classified as a jet and removed from the list. The distances are all recalculated and the procedure is repeated until all objects have been classified as jets.
Due to the inverse squared momenta in the algorithm, the anti-k$_T$ algorithm favours hard particles over soft particles. Soft objects are thus clustered to hard objects long before they start clustering with themselves. This results in jets that are resilient to soft particles which is important since jets should be resilient to final state radiation and unwanted background. The distance parameter R determines the maximum size of the jet, and for small-R jets takes the value of 0.4. Small-R jets are used to reconstruct individual quarks/gluons while large-R jets (typically $R = 1.0$) are used to reconstruct boosted objects whose decay particles begin to merge and struggle to be resolved.

4.3.2 Small-R jet calibration and selection

The reconstruction of jets unfortunately is not perfect, and so corrections are required. These corrections, Jet Energy Scale (JES), calibrate the energy scale of the jets to account for several effects, namely the different responses of the electromagnetic and hadronic calorimeters (calorimeter non-compensation), dead material, out-of-cone energy and pileup contamination [107]. The JES corrections aim to restore the energy of the jets to the scale of the truth jets. There are several steps to this correction, which occur in the following order [108]:

- **Origin correction:** The direction of the jet is corrected to point towards the hard-scatter primary vertex, since when they are reconstructed they originally point to the centre of the detector.
- **Pileup corrections:** The expected pileup contamination is removed from the jets by subtracting the expected p_T due to the soft contributions and is dependent on the area of the jet. The residual pileup dependence is removed via corrections dependent on the number of primary vertices in the event (for in-time pileup) and the average number of bunch crossings (for out-of-time pileup).
- **Absolute JES correction:** MC samples are used to compare the pileup corrected reconstructed jets to the jets at truth level. Both the energy and η of the jets are corrected, altering the 4-momentum of the jets. The η calibration accounts for the transition between the calorimeters.
- **Global Sequential Calibration (GSC):** Reduces the dependence of the jet energy on the shape of the shower in the calorimeters, including possible energy leakages. Information from the ID, calorimeters and the MS is used. The correction improves the identification of quark- versus gluon-initiated jets, since quark jets have harder hadrons that elongate the shower, while gluons have more soft particles which give a wider shower shape.
- ***In-situ* calibration:** Applied only to data and accounts for the imperfect detector description in simulation. The corrections are calculated by balancing the p_T of jets to other well measured reference objects using γ+jets, Z+jets and multijet samples.

Another correction is the Jet Energy Resolution (JER) and is defined as σ_{p_T}/p_T [109]. It is obtained in-situ and applied to the Monte Carlo by smearing the jet energies with a gaussian function that has a width equal to the JER uncertainty in data. The JES and JER corrections are applied as scale factors to each jet in an event, scaling the magnitude and resolution of their energies respectively. After these corrections are applied, there still may be some pileup jets left in the event. The number of pileup jets are reduced by applying a cut on a discriminant, the

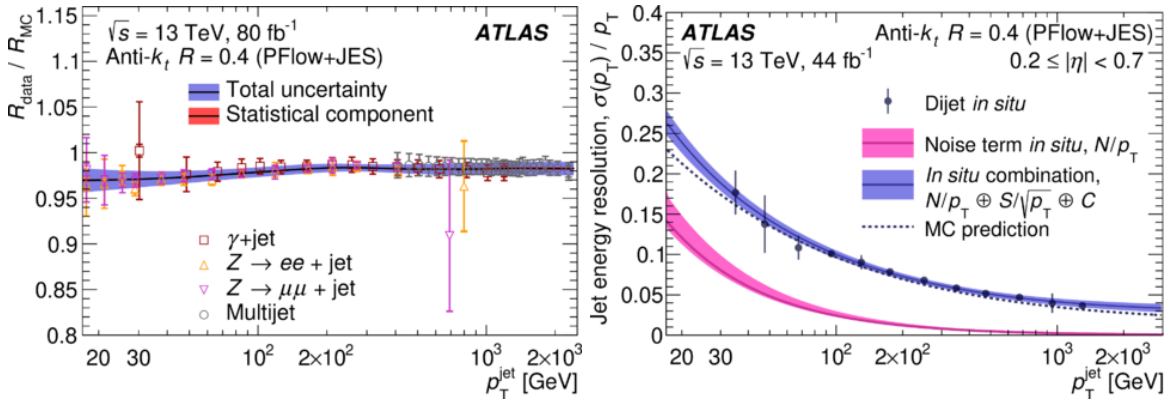

(a) (b)

FIGURE 4.4: (a) The ratio of data to simulation of the PFlow+JES jet response as a function of jet p_T for Z+jet, γ+jet and multijet in-situ calibrations [111]. The vertical bars represent the uncertainties, for statistical (inner bars) and total (outer bars). The final correction and its uncertainty bands are also shown. (b) The relative jet energy resolution as a function of p_T for PFlow+JES jets. [111] The vertical bars on the points represent the total uncertainties on the relative resolution in dijet events.

Jet Vertex Tagger (JVT) [110]. The JVT is built using information on the tracks and vertices to separate between pileup and hard-scatter jets. A plot of the PFlow+JES jet response as a function of p_T is shown in Figure 4.4(a), and the relative jet energy resolution of PFlow+JES jets as a function of p_T is shown in Figure 4.4(b).

4.3.3 B-Jet reconstruction and identification

Determining the origin of a jet is important in physics analyses in order to be able to reconstruct the hard collision correctly and know if it is a process we are interested in. The jets most important to identify are the jets originating from b-quarks, particularly for this analysis. To identify a jet as a b-jet, or "to tag a jet", a b-tagging algorithm is used that takes the tracks in the jet as input. The lifetime of b-hadrons is of the order 1.5 ps [11], so a b-hadron with an energy in the tens of GeV is able to travel a few mm before decaying. This is a sweet spot for our detectors as top quarks decay too quickly to even form hadrons, while up, down and strange hadrons have too long a lifetime and often make it to the calorimeters. Charm hadrons have a slightly longer lifetime than b-hadrons, but not too long that they reach the calorimeters, so they can be tagged but with a lower efficiency-to-rejection factor than b-hadrons. The slightly longer lifetime of the b-hadron results in a secondary vertex that is slightly offset from the primary vertex. A diagram illustrating the secondary vertex (SV) being produced a distance L_{xy} from the primary vertex (PV) is shown in Figure 4.5. Since the b-hadron decays via electroweak interactions, b-quarks prefer to decay to c-quarks ($|V_{cb}|^2 \gg |V_{ub}|^2$), and so b-jets often contain

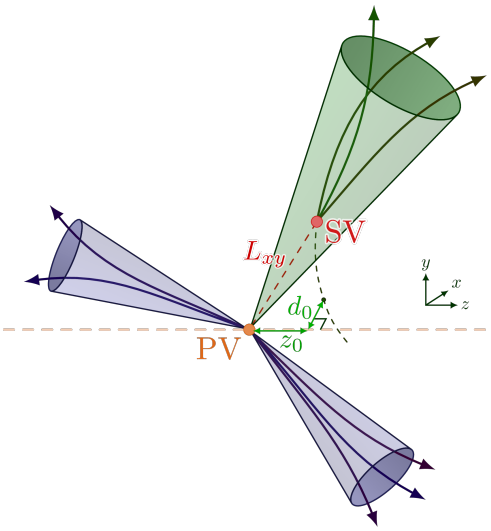

FIGURE 4.5: Diagram illustrating the characteristics of a b-hadron decay [113]. PV is the primary vertex, while SV is the secondary vertex created by the decay of the b-hadron, after it has travelled a distance L_{xy} due to its particular lifetime.

c-hadrons with their own displaced vertex [112]. This offset, along with the large mass of b-hadrons (~ 5 GeV) producing more tracks than light hadrons when it decays, can be exploited with the b-tagging algorithms.

Within ATLAS, there are two levels of b-tagging algorithms. The low-level algorithms are designed to discriminate between b- and non-b-jets on specific aspects. The outputs of these are then fed into a high-level multivariate algorithm to maximise the b-tagging performance. The low-level taggers are as follows [114]:

- **IP2D and IP3D:** These algorithms use the longitudinal and transverse impact parameter significances. They look to see if the point of closest approach is in front or behind the primary vertex with respect to the direction of the jet, with b-hadrons likely being in front.
- **SV1:** Reconstructs the secondary vertex using track pairs associated to the jet and far enough from the primary vertex. The new vertex has to pass a fit quality requirement where poorly fitted tracks are removed. A cut on the mass is performed and then properties of the secondary vertex and a momentum comparison between the tracks associated to the secondary vertex and all the tracks within the jet is performed.
- **JetFitter:** Uses a Kalman filter to find a common line in 3D space on which the primary, b- and c-vertices lie, providing an approximate flight path of the b-hadron. Takes into account the flight lengths of the particles.
- **RNNIP:** A recurrent neural network that takes as input track-based variables, e.g., impact parameters, track p_T and ΔR between track and jet axis [115].

The high-level tagger used in this analysis is the DL1r algorithm [116], which is the same as the DL1 algorithm [117] with the additional input of the RNNIP algorithm. The DL1r algorithm is an artificial deep neural network that takes the output of the low-level taggers as input. The DL1r algorithm has three outputs that correspond to the probabilities that the jet is a b-, c- or light-flavour jet. The three outputs (p_b, p_c, p_u) are combined into a function with a tuneable parameter f_c (the fraction of c-jets) which can be varied depending on the analysis' needs (set to 0.018 in this analysis). The output of this function is the final discriminant for b-tagging, and is defined as:

$$D = \log\left(\frac{p_b}{f_c p_c + (1 - f_c) p_u}\right) \tag{4.3}$$

The DL1r algorithm is trained on $t\bar{t}$ events (due to the $\sim 100\%$ decay of top quarks to bottom quarks) and a cut on D is applied depending on the efficiency working point which is specific to each analysis. ATLAS has four default working points to choose from, which is an average b-tagging efficiency of 60%, 70%, 77% and 85%. The higher the b-tag efficiency, the lower the c- and light-tag rejection. This can be seen in Figures 4.6(a),4.6(b). While the 60% working point will find the least amount of b-jets, the fraction of those jets that are real b-jets will be the highest. For each operating point, data-to-simulation scale factors are computed as a function of the b-jet p_T, defined as the ratio of the efficiency in collision data to the efficiency in simulation. Also shown in Figures 4.6(a),4.6(b) is a comparison of the DL1r algorithm to the MV2c10 [118] algorithm that was used in the previous round of the analysis. The DL1r and MV2c10 algorithms use the same inputs, except for the RNNIP which is only used by the DL1r, but the major difference is that the MV2c10 algorithm is based on a boosted decision tree, as opposed to a deep neural network that the DL1r uses. A description of boosted decision trees and deep neural networks is given in Section 5.2.2.

For the simulation, the true flavour of a jet is found by matching the reconstructed jet with truth particles. A jet is labelled as a true b-jet if a weakly decaying b-hadron with $p_T > 5$ GeV lies within $\Delta R = 0.3$ of the jet axis. If no b-hadron is found, c-hadrons and τ-leptons are searched for. If none of these are found, the jet is labelled as a light-jet.

4.3.3.1 Pseudo-Continuous b-Tagging (PCBT)

The tagging scheme used in this analysis is known as Pseudo-Continuous b-Tagging (PCBT), which splits the classification of the b-jets into 5 bins with the edges defined by the four working points (i.e., [100-85], [85-77],[77-70],[70-60],[60-0]). Since this analysis uses the working point of 70%, PCBT splits the b-tagged jets into two categories of different "purity", instead of just having them all labelled as passing the 70% working point. The tagged binning is then also used in the training of the final MVA discriminant used in this analysis to separate VH signal from the background processes.

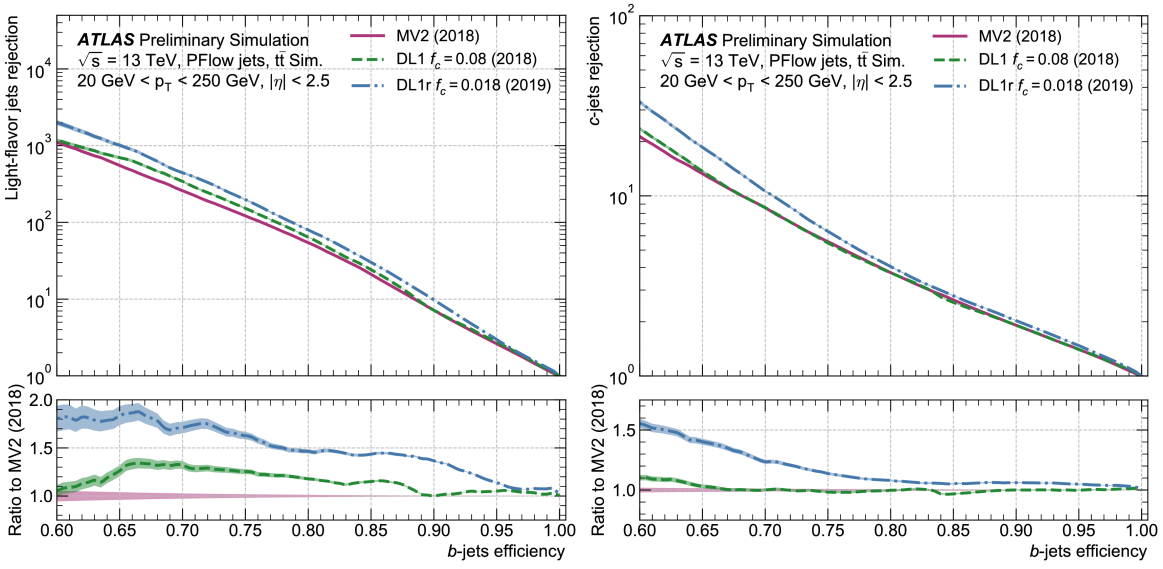

(a) (b)

FIGURE 4.6: The ROC curves of several ATLAS b-tagging algorithms showing the light-flavour rejection ($\frac{1}{\epsilon_u}$) vs b-jet efficiency (ϵ_b) (a) and c-jet rejection ($\frac{1}{\epsilon_c}$) vs b-jet efficiency (b) [119]. The DL1r algorithm used in this analysis is the blue dashed line, while the algorithm used in the previous round of the analysis is the solid line in maroon. The performance was evaluated using simulated $t\bar{t}$ events with PFlow jets reconstructed using the anti-K$_T$ algorithm with $R = 0.4$ and with $20 < p_T < 250$ GeV and $|\eta| < 2.5$. The shaded bands show the statistical uncertainty.

4.3.3.2 Corrections to b-tagged jets

Once the b-jets are found, energy corrections are applied to them since they have unique features that make the GSC calibrations sub-optimal. These corrections are applied to improve the signal mass resolution and sensitivity. The corrections are as follows:

- **Muon-in-Jet:** Due to the weak decays of the b- and c-hadrons within a b-jet, about 10% of the time there will be a muon within the jet. The correction is applied if a muon with $p_T > 4$ GeV is found within a variable distance from the jet centre, maxing out at $\Delta R = 0.4$ for low p_T muons. If more than one muon passes this, the one with the smallest ΔR is used. The 4-momentum of the selected muon is added to the jet after the expected energy deposited by the muon is subtracted from the calorimeter. This improves the jet p_T and direction since the muon deposits a small amount of energy in the calorimeter.

- **PtReco:** b-jets can suffer from out-of-cone effects due to the secondary vertex and the heavy b-hadron mass. This is when some of the energy is not captured by the reconstruction algorithm. To correct this, a scale factor is applied to the p_T of the jets that is calculated as the ratio between the true p_T of the jet and the reconstructed p_T after the muon-in-jet correction has been applied. The scale factor is derived separately for b-jets with or without a lepton, with the difference most likely due to the neutrino from

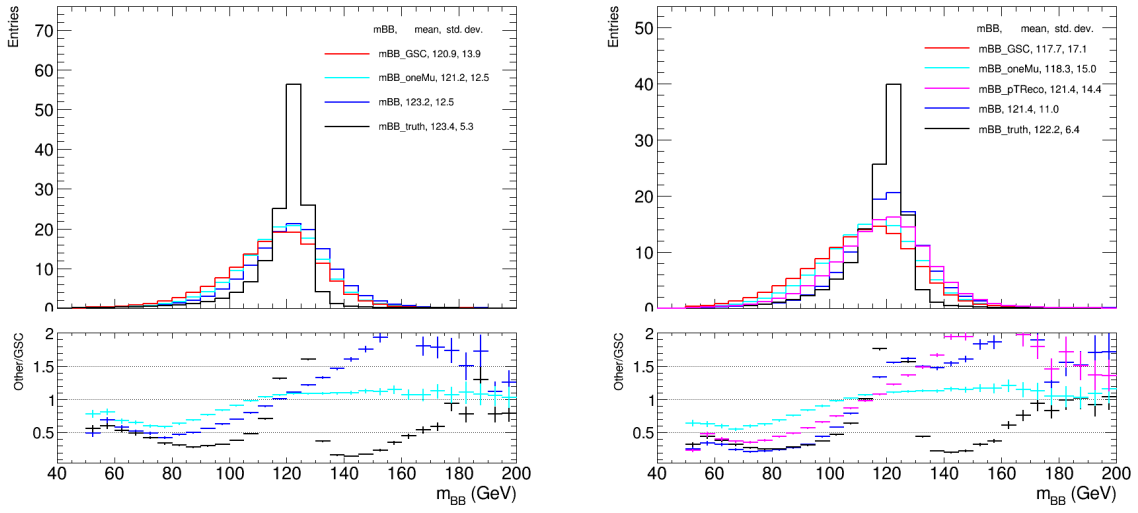

(a) (b)

FIGURE 4.7: The invariant mass distributions of the two Higgs boson candidate jets in the 2-jet region, with CRs & SR combined, for the 1-lepton $WH \to l\nu b\bar{b}$ 150 GeV $<p_T^V<$400 GeV (a) and 2-lepton $ZH \to llb\bar{b}$ 75 GeV $<p_T^V<$400 GeV (b). The red lines are for the uncorrected jets (mBB_GSC), the cyan lines are the jets with the muon-in-jet corrections (mBB_oneMu), the magenta lines have an additional PtReco correction applied (mBB_pTReco). The blue lines are the fully corrected jets, which in the 0- and 1-lepton are the PtReco jets, while in 2-lepton they are the jets after the kinematic fit has been applied. Finally, the black lines (mBB_truth) is the invariant mass of the truth jets matched to the Higgs candidate reconstruction jets. In the legend are the mean and standard deviation of the distributions, obtained from fitting a Bukin function. In the 2-lepton plot, the PtReco correction is shown just for direct comparison with the kinematic fit.

the semi-leptonic decays. The correction is applied as a function of p_T, with larger scale factors at lower p_T.

- **Kinematic Fit:** The Kinematic Fit (KF) replaces the PtReco correction in the 2-lepton channel of this analysis (see Section 5.1), since it is possible to take advantage of the well measured $Z \to \ell\ell$ process. Here, a likelihood fit is performed to constrain the final state objects to be balanced in the transverse plane, thereby improving the b-jet energy. No improvement was found in the $n_{jets} > 3$ region and so the KF is only applied to the 2- and 3–jet regions.

As can be seen in Figure 4.7, each successive correction both shifts the peak of the invariant mass distribution up towards the true value, and also reduces the width of the distribution.

4.4 Missing transverse energy

The missing transverse energy, E_T^{miss}, needs to be measured as accurately as possible as it is an important observable used to estimate the amount of energy carried by weakly interacting particles, e.g., neutrinos or dark matter candidates. Since they are not observed, they create a momentum imbalance in the transverse plane of an event. This is due to the colliding beams having close to zero transverse momentum, so if the observed total transverse momentum in the detector is not close to zero it is possible that an undetected particle was produced. E_T^{miss} is calculated using two contributions, the hard term which comes from the reconstructed objects in the event matched to the hard collision, and the soft term which is all the charged tracks matched to the hard collision but not to any of the reconstructed objects [120]. The missing transverse energy is defined as the negative vectorial sum of transverse momenta of the hard and soft terms, or in other words:

$$\mathbf{E}_T^{miss} = -\left(\sum_{electrons} \mathbf{p}_T^e + \sum_{photons} \mathbf{p}_T^\gamma + \sum_{muons} \mathbf{p}_T^\mu + \sum_{\tau-leptons} \mathbf{p}_T^{\tau_{had}} + \sum_{jets} \mathbf{p}_T^{jet} + \sum_{soft} \mathbf{p}_T^{soft} \right) \quad (4.4)$$

Since the reconstruction of the hard objects are done independently of each other, there is a chance that some of the detector signal may be shared between different objects, e.g., calorimeter signals shared between jets and electrons. This may introduce double counting of energy when calculating the E_T^{miss} term, so a signal ambiguity resolution procedure is used that rejects already used signal contributions [120]. It works in an order starting with electrons, then photons, τ-leptons and finally jets. A separate procedure is used to remove jets when overlapping with muons that is dependent on the momenta of the muons and jets, and the number of tracks associated to the jets.

Chapter 5

Event selection and statistical treatment of the $VH \to b\bar{b}$ resolved analysis

This chapter will introduce the $VH \to b\bar{b}$ resolved STXS measurement, outlining the strategy used to calculate the signal strengths of this process within the framework of the Simplified Template Cross-Section (STXS) measurements.
The work in this thesis is part of the larger and final Run-2 VH to $b\bar{b} + c\bar{c}$ resolved+boosted analysis [23] which combines the $VH \to b\bar{b}$ resolved, $VH \to b\bar{b}$ boosted and $VH \to c\bar{c}$ resolved analyses. As such, only a very brief introduction to the $VH \to b\bar{b}$ boosted and $VH \to c\bar{c}$ resolved analyses will be given.
For the sake of the work presented in this thesis, the analysis methods were frozen before the Run-2 combined analysis had decided on what the final analysis methods would be. Therefore, this chapter does not describe the completed version of the Run-2 combined analysis, but rather only describes the outline of the analysis methods used for this thesis alone.

5.1 Overview

From Chapter 2, we know the most sensitive decay channel to study the Higgs coupling to down type quarks is the $H \to b\bar{b}$ decay. However, since the final state particles form jets, the signal is dominated by the large multijet backgrounds at the LHC. To overcome this, studying the $H \to b\bar{b}$ decay in the associated vector boson (W/Z) production channel allows the selection of the leptons produced in the leptonic decays of the vector bosons to reduce the large jet backgrounds. This results in three channels that can be studied, based on the number of leptons from the vector boson decay, namely the 0-lepton ($ZH \to \nu\nu b\bar{b}$), 1-lepton ($WH \to l\nu b\bar{b}$)

and 2-lepton ($ZH \to llb\bar{b}$) channels.
In the case of the resolved $VH \to b\bar{b}$ analysis, the transverse momentum of the Higgs boson is low enough such that the b-quarks from the Higgs are reconstructed individually using small-R jets (described in Section 4.3.1.1). For the boosted $VH \to b\bar{b}$ analysis, the transverse momentum of the Higgs boson is high enough such that the b-quarks are boosted, and thus too close to each other to be reconstructed individually. Instead, a single large-R jet is used to reconstruct the merging of the resultant showering of the two b-quarks. The boundary between the resolved and boosted analyses is where the transverse momentum of the vector boson (p_T^V) is equal to 400 GeV, with the resolved regime being below 400 GeV. The p_T^V approximates the p_T of the Higgs boson (p_T^H) well, assuming a tree-level process with no extra radiation, since the Higgs boson recoils off the vector boson. The p_T^V is used over p_T^H since the resolution of lepton measurements is better than those of jets. For the $VH \to c\bar{c}$ resolved analysis, a similar approach as to the $VH \to b\bar{b}$ resolved analysis is used, however instead of searching for b-quarks, the search is for c-quarks.
While there are some strategies used in this thesis based on the ATLAS analysis that combines the three different strategies mentioned above, the calculations and measurements are done independently.

5.2 $V(H \to b\bar{b})$ resolved

The $V(H \to b\bar{b})$ production can be split into three modes. These are the quark-induced production of either a W or Z boson ($qqVH$), and the gluon-induced production of a Z boson ($ggZH$). Leading-order Feynman diagrams of these processes can be seen in Figure 5.1. Gluon-induced production only occurs for the Z boson as the Z boson has zero charge, and the W production has contributions from both the W^+ and the W^-. Due to the additional loop in the $ggZH$ process, its cross-section is lower than the $qqZH$ process. The final state objects are the leptons from the leptonic decays of the Z and W bosons, and the b-jets from the Higgs decay. While VH processes with the Higgs boson decaying to charm quarks are also used in this thesis, they are treated as backgrounds to the $V(H \to b\bar{b})$ signal process. They have the same Feynman diagrams as the bottom quark decays but with the Higgs boson decaying to two charm quarks instead. Unfortunately, the $VH \to b\bar{b}$ process is not the only process that has leptons and b-jets in the final state. These other processes are the backgrounds for this analysis and can be separated into reducible and irreducible backgrounds.
The irreducible background processes have the exact same final state objects as the signal process, which in this thesis, are the diboson and V+jets processes. The diboson processes have one of the vector bosons decaying to leptons, while the other decays to quarks. The VZ processes are particularly similar to the signal as the hadronic decays of the Z boson results in a peak in the invariant mass distribution of the jets close enough to the Higgs boson mass peak such

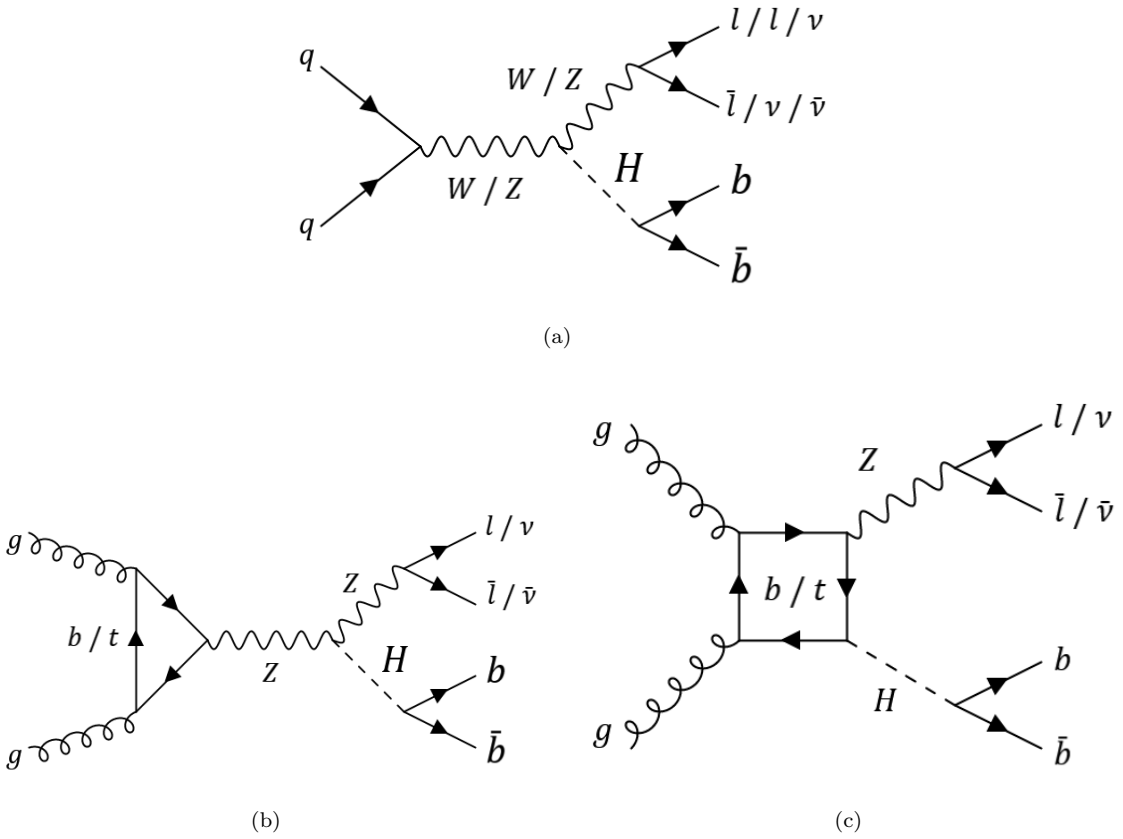

FIGURE 5.1: The leading-order quark-induced (a) and gluon-induced (b)(c) contributions to the production of VH process.

that the tails overlap. The leading-order quark- and gluon-induced diboson Feynman diagrams are shown in Figure 5.2. The V+jets processes have the vector bosons decay leptonically, while the b-jets come from the additional gluon radiation in the production. The leading-order quark- and gluon-induced V+jets Feynman diagrams are shown in Figure 5.3.

The reducible backgrounds have more final state objects than the signal, so can only pass the event selection due to some of these objects falling outside the fiducial volume or being misreconstructed. For this analysis, the reducible backgrounds are the $t\bar{t}$, single-top and the QCD multijet processes. In the following, all the top quarks decay to a W boson and a b-quark almost 100% of the time. The $t\bar{t}$ processes have two top quarks, resulting in the most final state objects of the modelled background processes in this analysis. At a centre-of-mass energy of $\sqrt{s} = 13$ TeV at the LHC, top quark pairs are produced around 90% of the time via gluon-induced processes [11]. The $t\bar{t}$ process becomes more signal like when only one of the top quarks falls fully inside the detector acceptance, or the other top quark is poorly reconstructed. The leading-order $t\bar{t}$ Feynman diagrams are shown in Figure 5.4. The single-top processes can be split into three production modes, namely the s-channel, t-channel and Wt-channel. The s-channel has a b-quark and a top-quark, while the t-channel has a top-quark and another quark that can be any flavour. The Wt process has a W boson and a top quark, and in this analysis,

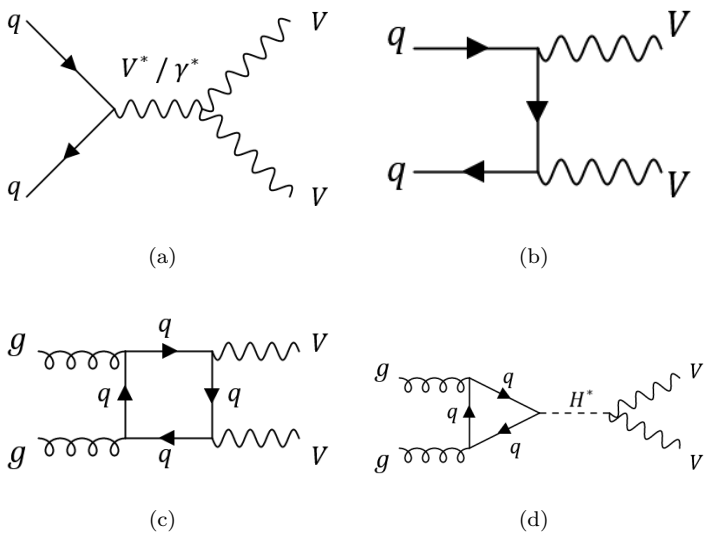

FIGURE 5.2: The leading-order quark-induced (a)(b) and gluon-induced (c)(d) contributions to the production of diboson processes.

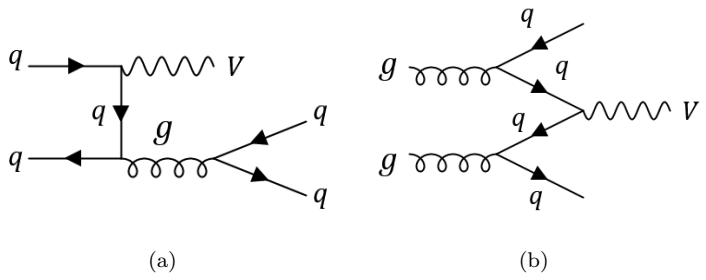

FIGURE 5.3: The leading-order quark-induced (a) and gluon-induced (b) contributions to the production of the V+jets processes.

is the dominant single-top process. The leading-order single-top Feynman diagrams are shown in Figure 5.5. The QCD multijet background originates from the large amount of parton-parton interactions in pp collisions. Despite not being a genuine source of prompt leptons and E_T^{miss}, due to the large cross-section of this background at the LHC, it can potentially contribute a non-negligible amount. Some of the many Feynman diagrams of the QCD multijet background is shown in Figure 5.6.

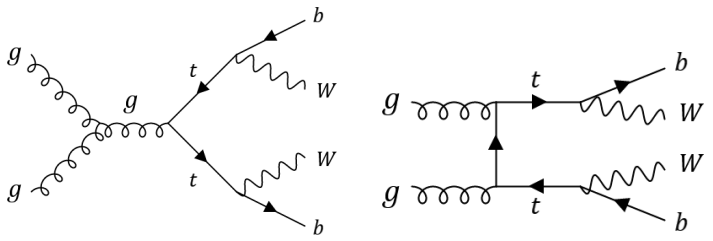

(a) (b)

FIGURE 5.4: The leading-order gluon-induced contributions to the top quark pair production. The gluon fusion production is in (a) and the t-channel production is in (b).

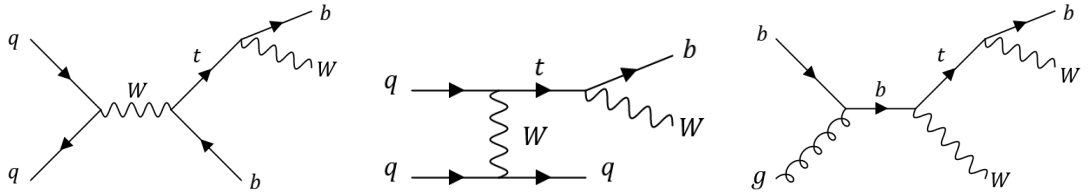

(a) (b) (c)

FIGURE 5.5: The leading-order contributions to the s-channel (a), t-channel (b) and Wt channel (c) single-top productions.

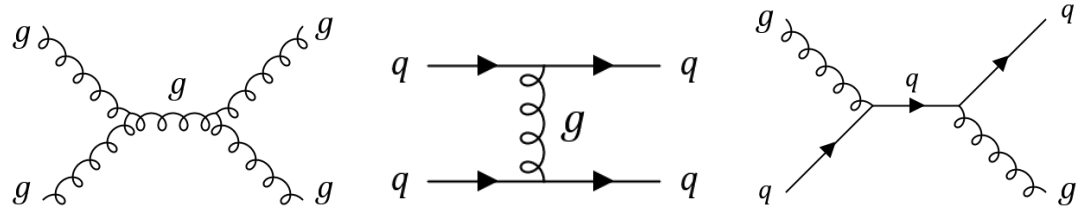

(a) (b) (c)

FIGURE 5.6: Some of the leading-order contributions to the QCD multijet background.

5.2.1 Event selections

The physics objects used in this analysis are those defined in Chapter 4. However, before they are used, they have to pass an overlap removal procedure. The overlap removal ensures there is no sharing of signals in the detector between two or more physics objects, and is the final stage of object reconstruction before the analysis specific selections are applied. The overlap removal procedure is applied to each event, in a sequential manner, with the objects that fail at each step removed before proceeding. The objects that fail are more likely to be fake reconstructions. While hadronically decaying τ-leptons are not used in this thesis, they are used in the overlap removal procedure. The overlap removal proceeds as follows:

- tau-electron: If the ΔR between the hadronically decaying τ-lepton and the electron is less than 0.2, the τ-lepton is removed
- tau-muon: If the ΔR between the hadronically decaying τ-lepton and the muon is less than 0.2, the τ-lepton is removed
- electron-muon: If a muon and an electron share a track in the ID, the electron is removed if the muon is a combined muon, whereas the muon is removed if the muon is a calorimeter-tagged muon.
- electron-jet: If the ΔR between the electron and the jet is less than 0.2, the jet is removed. However, the electron is removed if the ΔR is between 0.2 and the lesser of 0.4 and $0.04 + 10/p_T^e$. Here, p_T^e is the transverse momentum of the electron in GeV.
- muon-jet: If the ΔR between the jet and the muon is less than 0.2, the jet is removed if the jet has less than three associated tracks each with $p_T > 500$ MeV or the muon carries more than half of the jet p_T. For the jets that remain, if the ΔR is smaller than the lesser of 0.4 and $0.04 + 10/p_T^\mu$, the muon is removed. Here p_T^μ is the transverse momentum of the muon in GeV.
- tau-jet: If the ΔR between the jet and the hadronically decaying τ-lepton is less than 0.2, the jet is removed. Since this thesis doesn't use specifically use τ-leptons, the jets from the surviving hadronically decaying τ-leptons are classified as normal jets.

The selections for the jets are common between the three lepton channels. For the 0- and 1-lepton channels, either exactly two or exactly three jets are required, while the 2-lepton channel requires either exactly two or ≥ 3 jets. Henceforth, the number of these reconstruction level jets will be denoted as n_{jets}. The higher jet multiplicity in the 2-lepton channel takes advantage of the reduced top background due to requiring two leptons, increasing the sensitivity to the signal. This is unlike in the 0- and 1-lepton channels where the top backgrounds become larger

at higher jet multiplicities. Of these jets, at least two must be central jets ($|\eta| < 2.5$) and exactly two of those central jets have to pass the 70% working point of the DL1r b-tagging algorithm. From here on, the number of jets that are b-tagged is denoted as n^b_{jets}. The central jets must have $p_T > 20$ GeV while the forward jets ($2.5 < |\eta| < 4.5$) have $p_T > 30$ GeV. Additionally, the leading (highest p_T) b-tagged jet must have $p_T > 45$ GeV. The 4-vectors of the two b-tagged jets are added together, forming a new 4-vector that represents the Higgs boson candidate. Due to the data being mismodelled by the simulated events at low values of the invariant mass of the Higgs boson candidate (m_{BB}), a selection of $m_{BB} > 50$ GeV is applied. The selections on the jets are all applied using the GSC jets before the b-jet corrections are applied, as described in Section 4.3.

While what is described in the rest of this paragraph is fully explained in Section 7.1, it is important to briefly introduce it here since it involves an additional selection on the jets that will be discussed in the coming sections. Specifically, the STXS regions are split by the number of truth jets to increase the granularity of the STXS measurement. However, due to reconstruction effects and analysis region selections, this splitting results in correlations between these STXS regions. A major focus of this thesis is studying the impact of applying a tighter selection of $p_T > 30$ GeV to the non-b-tagged central jets. This tighter selection is intended to better align the selections applied at the STXS level with the analysis level and, ideally, reduce the correlations between the STXS regions that differ by the number of jets. As a result, this thesis will often compare two scenarios: one where the non-b-tagged central jets have a minimum p_T of 20 GeV, and another where the minimum p_T is set to 30 GeV.

The vector boson candidate is formed from summing the 4-vectors of the leptons and/or neutrinos in the event, which must pass the selections described in the following subsections. The selections differ per channel due to the different leptonic decays of the vector bosons, and the different backgrounds that need to be suppressed. The definitions of the leptons used in the selections are summarised in Table 5.1. The analysis regions are defined by p_T^V, such that the analysis regions match with the STXS regions, as described in Section 5.5. Due to the requirement that the resolved and boosted analyses be orthogonal, all three leptonic channels require $p_T^V < 400$ GeV. A summary of all the event selections used in this thesis is given in Table 5.3

5.2.1.1 Event selections in the 0-lepton channel

Events were selected that fired the lowest non-prescaled E_T^{miss} triggers available during each data taking period, which varied from E_T^{miss} >70 GeV to E_T^{miss} >110 GeV. Due to the lower efficiencies of the E_T^{miss} triggers around these threshold values, only events with $E_T^{miss} > 150$ GeV are used in this analysis. This provides an efficiency between 85% and 90% around 150 GeV and essentially 100% above 200 GeV [121]. This results in two p_T^V regions, $150 < p_T^V < 250$ GeV and $250 < p_T^V < 400$ GeV. There are required to be exactly zero VH-loose leptons, and

TABLE 5.1: Definitions of the electrons and muons used in the selections. The identification criteria are defined in Section 4.2, along with their corresponding isolation requirements.

	Lepton Selection	p_T **(GeV)**	$\lvert\eta\rvert$	**ID**	d_0^{sig}	$\lvert\Delta z_0 \mathbf{sin}\theta\rvert$ **(mm)**
Electrons	VH-loose	> 7	< 2.47	Loose	< 5	< 0.5
	ZH-signal	> 27	< 2.47	Loose	< 5	< 0.5
	WH-signal	> 27	< 2.47	Tight	< 5	< 0.5
Muons	VH-loose	> 7	< 2.7	Loose	< 3	< 0.5
	ZH-signal	> 27	< 2.5	Loose	< 3	< 0.5
	WH-signal	> 25	< 2.5	Medium	< 3	< 0.5

the candidate Z-boson is defined by the E_T^{miss} 2-vector of the event. Therefore, only in the 0-lepton channel is the p_T^V defined as E_T^{miss}.
Due to a slight dependence of the trigger efficiency on the jet activity in an event, a selection on the scalar sum of the p_T of the jets (S_T) is used to remove the regions with lower jet activity where the mismodelling occurs. These cuts are $S_T > 120$ (150) GeV in the 2- (3-) jet events respectively. To suppress the multijet background in this channel, which is present due to large E_T^{miss} coming from mostly mismeasured jets, several angular selections have been applied. These selections take into account the topology of the signal process:

- $\min[\Delta\phi(\mathbf{E}_T^{miss}, \mathbf{jets})] > 20°(30°)$ for 2 (3) jet events: A minimum is required on the azimuthal separation between E_T^{miss} and the set of all jets in the event.
- $\Delta\phi(\mathbf{E}_T^{miss}, \mathbf{H}_{cand}) > 120°$: A minimum is required on the azimuthal separation between E_T^{miss} and the Higgs candidate.
- $\Delta\phi(\mathbf{b}_1, \mathbf{b}_2) < 140°$: A maximum is required on the azimuthal separation between the two b-tagged jets used to create the Higgs candidate.
- $\Delta\phi(\mathbf{E}_T^{miss}, \mathbf{p}_T^{miss}) < 90°$: A maximum is required on the azimuthal separation between E_T^{miss} and the missing transverse momentum (p_T^{miss}) calculated only using tracks, and only those tracks associated to the primary vertex.

5.2.1.2 Event selections in the 1-lepton channel

In the 1-lepton channel, there are two sub-channels, one for the electron and one for the muon decays of the W bosons. In the electron sub-channel, a single electron trigger with loose ID quality is applied that requires the electron to have $p_T > 24$ GeV in 2015 data, and $p_T > 26$ GeV in the 2016 to 2018 data. At the analysis level, the electrons are required to satisfy the WH-signal electron selection, and exactly zero additional VH loose leptons are allowed in the event. An extra cut of $E_T^{miss} > 30$ GeV is applied in this sub-channel to reduce the amount of

multijet backgrounds. For the muon sub-channel, the event must pass the same E_T^{miss} triggers used in the 0-lepton channel. A single muon trigger is not used since the E_T^{miss} trigger was found to have a higher efficiency due to the limited coverage of the muon spectrometer, and there is significant E_T^{miss} in the event due to the neutrino produced along with the muon. The muon is then required to satisfy the WH-signal muon criteria, with exactly zero additional VH-loose leptons in the event. The 4-vector of the W boson candidate is formed via the summation of the lepton 4-vectors and the E_T^{miss} 2-vector in the event. There are two p_T^V regions, $150 < p_T^V < 250$ GeV and $250 < p_T^V < 400$ GeV. Currently, the backgrounds are found to be too large in the $75 < p_T^V < 150$ GeV region to still be sensitive to the signal and so it is not used in this thesis.

5.2.1.3 Event selections in the 2-lepton channel

Similar to the 1-lepton channel, there are two sub-channels based on the flavour of the charged leptons. In the electron sub-channel, the same trigger selections used in the 1-lepton channel are applied. In the muon sub-channel, a single muon trigger with loose isolation requirements is used which requires the muon to have a p_T that varies from 20 to 26 GeV depending on the year of data taking. The E_T^{miss} trigger is not used since there is expected to be very little E_T^{miss} in this lepton channel. Both electron and muon sub-channels must have exactly two same-flavour VH-loose leptons, with the leading lepton having $p_T > 27$ GeV. In the muon sub-channel, the muons must have opposite charges which is not required in the electron sub-channel since the charge misidentification is significantly larger for electrons. The 4-vector of the Z-boson candidate is formed by the summation of the 4-vectors of the two leptons in the event, and a selection on the invariant mass of the two leptons is applied such that $81 < m_{ll} < 101$ GeV. These selections suppress the multijet background to negligible values. Due to the larger signal-to-background ratio in the 2-lepton channel, the $75 < p_T^V < 150$ GeV region is also studied along with the $150 < p_T^V < 250$ GeV and $250 < p_T^V < 400$ GeV regions, giving three p_T^V regions.

5.2.1.4 Signal and control region definitions

The work in this section was done by the author.

All the analysis regions defined by the number of leptons, n_{jets} and p_T^V provide 14 analysis regions (summarised in Table 5.3). Each analysis region is then split into one signal region and two control regions, resulting in 14 signal regions and 28 control regions. The control regions are defined using a 2-dimensional cut on the distance between the two b-tagged jets $\Delta R(b_1, b_2)$ and the p_T^V of the event. The cuts are dependent on the number of jets and are defined such that the low control region (CRLow) contains 10% of the diboson events, while the high control region (CRHigh) contains 5% (15%) of the signal events in the 2 (3/3+) jet regions respectively.

TABLE 5.2: The values of the parameters for the function $f(p_T^V) = a + e^{b-c\times p_T^V}$ used to classify an event as a signal region event, or one of the control regions. For the CRLow, $\Delta R(b_1, b_2) < f(p_T^V)$, while for CRHigh $\Delta R(b_1, b_2) > f(p_T^V)$. The values for the different jet p_T selections are shown as well, namely the 20 GeV and 30 GeV selections.

	20 GeV parameters			**30 GeV parameters**		
	a	**b**	**c**	**a**	**b**	**c**
2-jet CRLow	0.400	0.788	-0.010230	0.389	0.836	-0.010011
2-jet CRHigh	0.870	1.379	-0.007953	0.815	1.391	-0.007221
3-jet CRLow	0.421	0.268	-0.008089	0.402	0.270	-0.007558
3-jet CRHigh	0.763	1.332	-0.007304	0.674	1.293	-0.005880

While the 3-jet CRHigh contains more signal than in the 2-jet regions, the ratio of signal-to-background is roughly the same between the 2- and 3-jet regions. Per p_T^V bin, the values of $\Delta R(b_1, b_2)$ that satisfy these requirements are found, and the following function is fit to these points across the p_T^V range:

$$dR = a + \exp(b + c * p_T^V). \tag{5.1}$$

The 2-dimensional histograms of the signal sample, along with the resultant functions (red lines), are shown in Figure 5.7 for both the 20 GeV and 30 GeV additional jet p_T selections. The values of the parameters in Equation 5.1 are given in Table 5.2. The sharp cut of the distribution at $\Delta R(b_1, b_2) = 0.4$ is due to the jets being reconstructed with a radius of $R = 0.4$. The SR lies between the two functions, CRLow is in the lower $\Delta R(b_1, b_2)$ values, while CRHigh is in the higher $\Delta R(b_1, b_2)$ values. The CRLow is enriched in W+jets events while the CRHigh is enriched in top and Z+jets events. These are the three dominant backgrounds in the analysis. The requirement on the diboson background in the CRLow is to ensure there are enough diboson events left in the SR for the VZ fits. These VZ fits are usually used as cross checks for the VH fit, but are not used in this thesis. The signal and control regions are defined in the 1-lepton channel and applied to the other lepton channels, with a minimal effect on the sensitivities in the other lepton channels. While the 1-lepton channel doesn't have $p_T^V < 150$ GeV in this thesis, events with $75 < p_T^V < 150$ GeV are used to fit these functions since the 2-lepton channel does have $75 < p_T^V < 150$ GeV events.

The main difference between the signal and control region definitions between the 20 GeV and 30 GeV jet p_T selections is that the function defining CRHigh is slightly higher in $\Delta R(b_1, b_2)$ for the 30 GeV selections, and so it lets a bit more background into the SR. This is likely due to the migrated signal events having lower energy and so the b-jets from the Higgs decay are more separated. What the distributions of the signal in the other lepton channels look like relative to these functions are shown in Figure 5.9. While the functions obtained from the 1-lepton channel describe the 0-lepton channel very well, they do not describe the 2-lepton channel as well. In

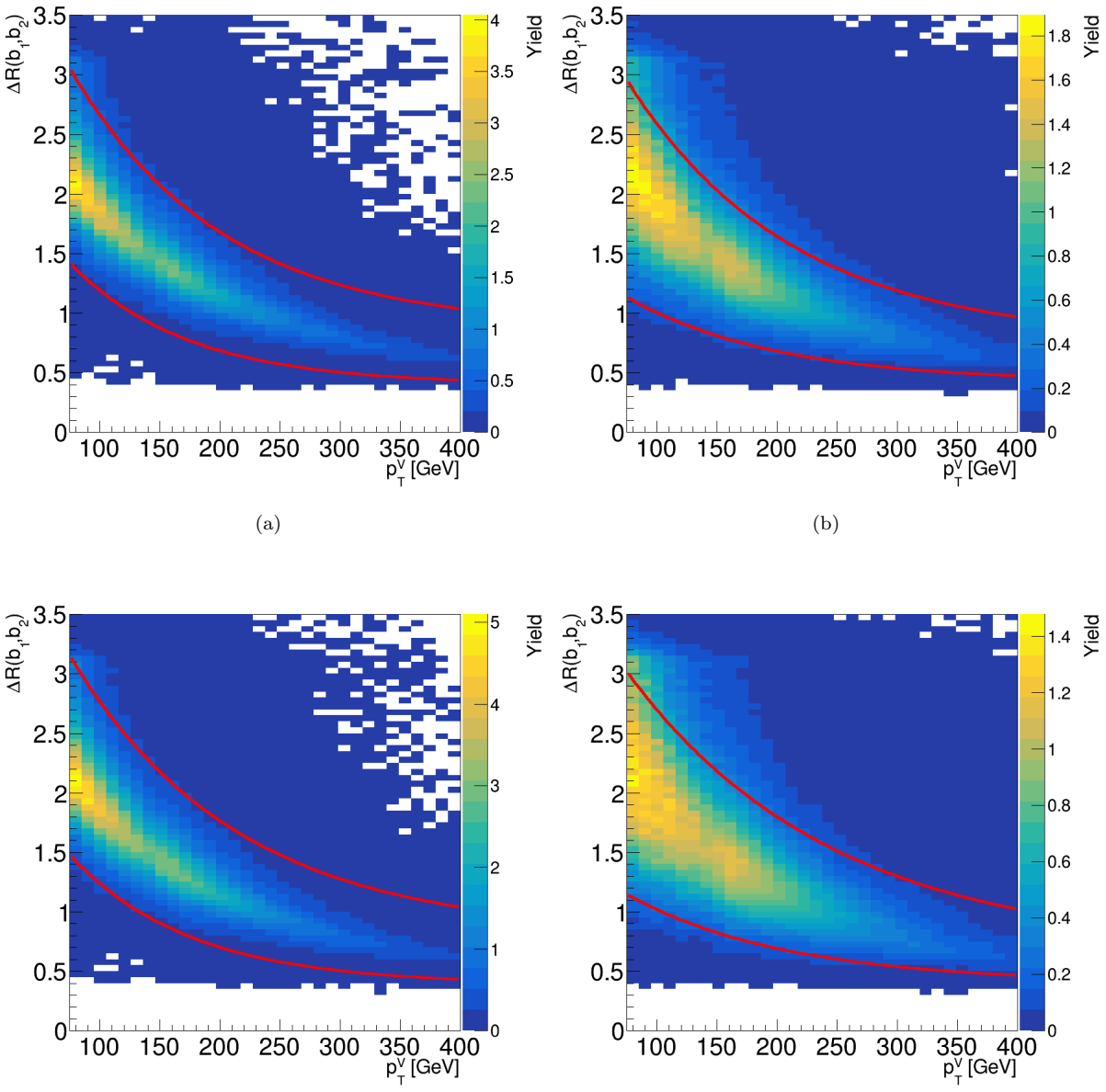

FIGURE 5.7: Shown are the two dimensional $\Delta R(b_1, b_2)$ and p_T^V plots of the signal samples in the 1-lepton channel at 140 fb^{-1}. Figures (a) and (b) are the 2- and 3-jet regions for the jet p_T selections of 20 GeV, while (c) and (d) are the 2- and 3-jet regions for the jet p_T selections of 30 GeV. Also shown are the functions obtained from the fit of $f(p_T^V) = a + e^{b-c\times p_T^V}$ to obtain the CRHigh selection (upper red line) and the CRLow selection (lower red line). The SR lies between the two red lines. The colours in the axis on the right represent the yields.

the 2-lepton, 2-jet regions, the CRLow boundary is slightly low, resulting in only about 5% of the diboson events falling in the CRLow. But in the ≥3-jet regions, the CRHigh boundary is slightly low, getting worse as the p_T^V increases, resulting in almost 30% of the signal events falling in the CRHigh for the 250< p_T^V < 400 GeV region. A comparison of the CR and SR yields is given Appendix A.2.

To get an idea of what some of the backgrounds look like for this two-dimensional distribution, they are shown in Figure 5.8 for the 1-lepton, 2-jet events with the jet p_T selection of 30 GeV. The single-top backgrounds are not shown as they look very similar to the $t\bar{t}$ background distributions. As can be seen, the top backgrounds tend to have larger $\Delta R(b_1, b_2)$ values, while the diboson background on average has $\Delta R(b_1, b_2)$ values even smaller than the signal. The W+jets background tends to lower values of $\Delta R(b_1, b_2)$, while the Z+jets background tends to larger values.

The 42 signal and control regions are all used as inputs to the final likelihood fit, as described in Section 5.4. This is done to create a signal region enriched in the VH events, while keeping additional regions enriched in the backgrounds to help constrain the background normalisations in the final likelihood fit.

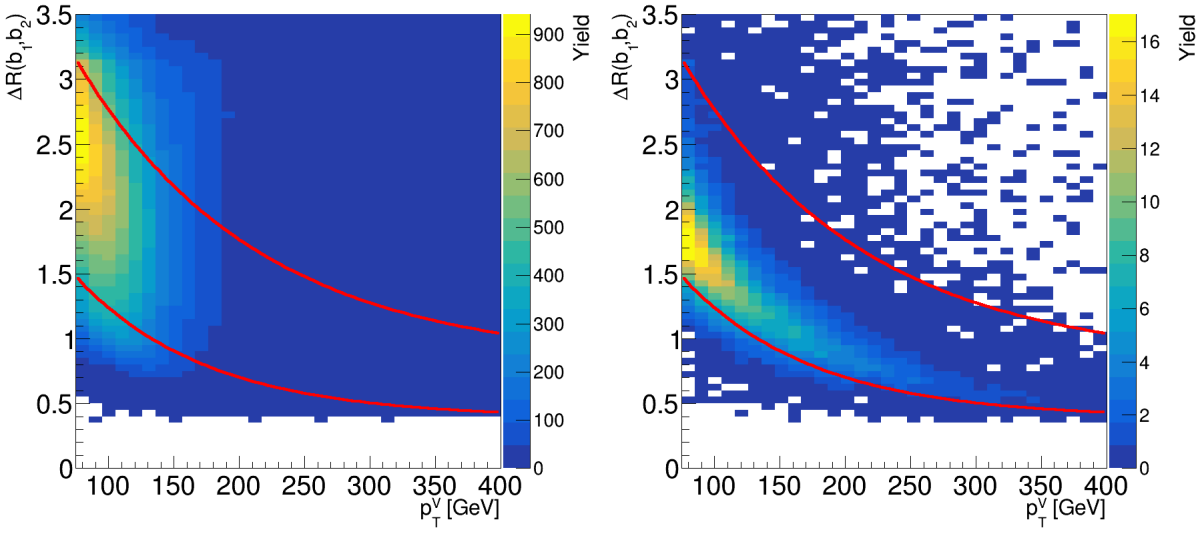

(a)

(b)

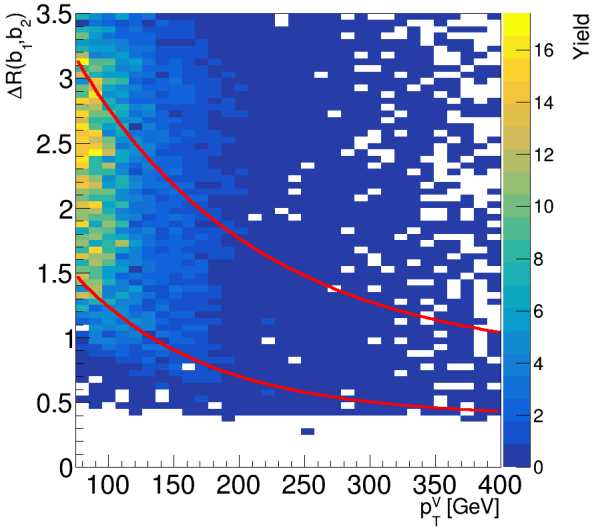

(c)

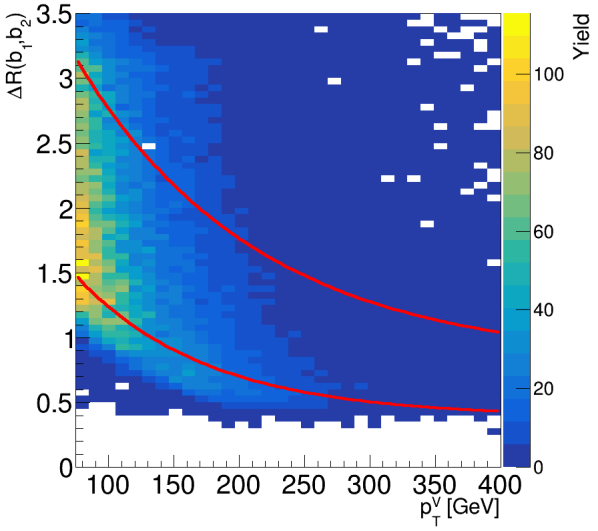

(d)

FIGURE 5.8: The two dimensional $\Delta R(b_1, b_2)$ and p_T^V plots in the 1-lepton channel, showing the distribution of several backgrounds at 140 fb^{-1} and the functions of the form $f(p_T^V) = a + e^{b - c \times p_T^V}$ used to define the CRHigh (upper red line) and the CRLow (lower red line). These plots are of 2-jet events, with the additional jet p_T selection of 30 GeV. The samples shown in these figures are $t\bar{t}$ in (a), diboson in (b), Z+jets in (c) and W+jets in (d).

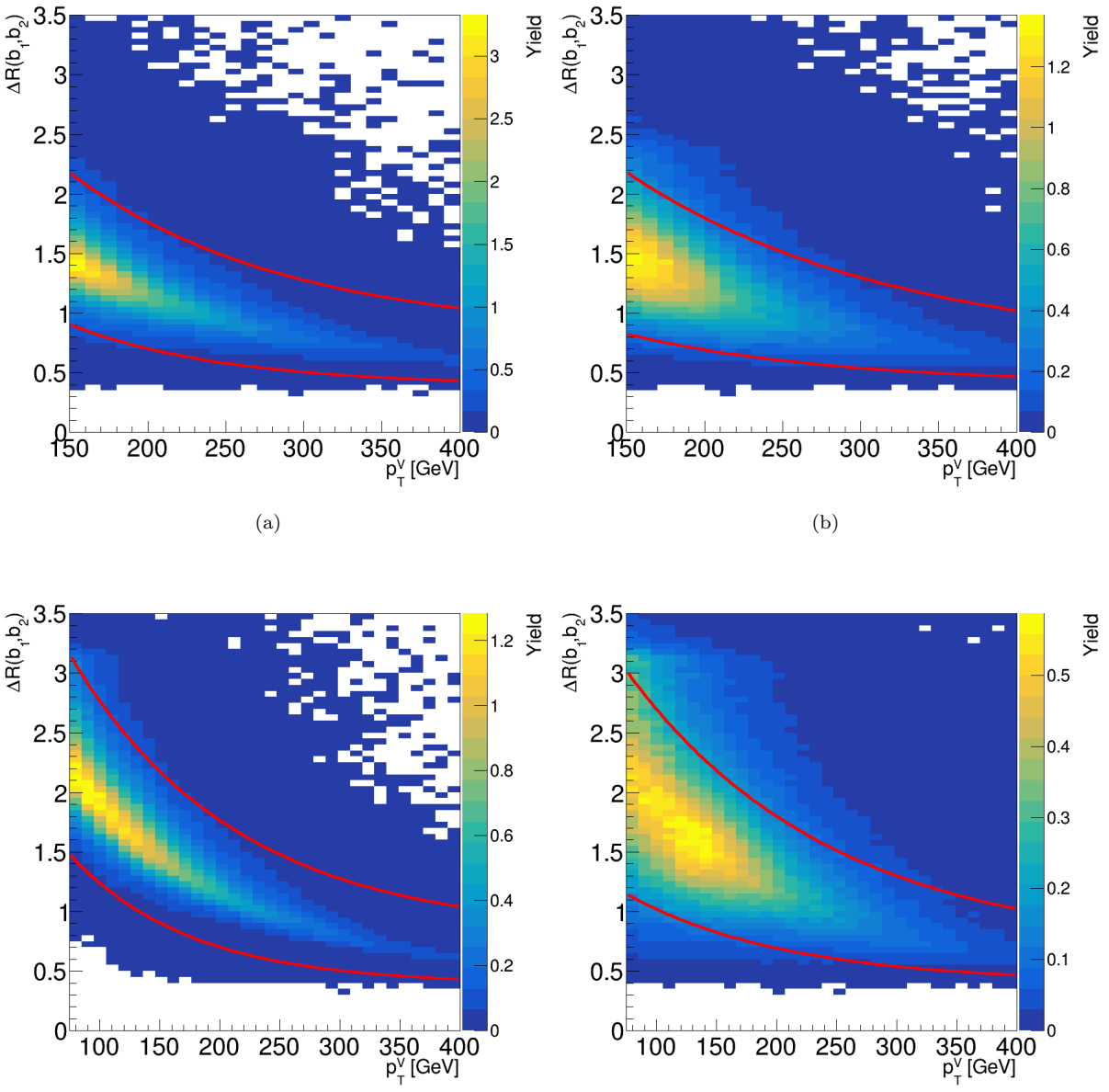

FIGURE 5.9: The two dimensional $\Delta R(b_1, b_2)$ and p_T^V plots showing the distribution of the signal samples at 140 fb^{-1} and the functions of the form $f(p_T^V) = a + e^{b-c\times p_T^V}$ used to define the CRHigh (upper red line) and the CRLow (lower red line). Figures (a) and (b) are the 2- and 3-jet regions for the 0-lepton channel, while (c) and (d) are the 2- and ≥3-jet regions for the 2-lepton channel. All four plots are using the additional jet p_T selection of 30 GeV. As a reminder, the p_T^V in the 0-lepton channel is defined as the E_T^{miss} .

TABLE 5.3: Summary of the event selections and categorisations in the 0-, 1- and 2-lepton channels.

Selection	**0-lepton**	**1-lepton**		**2-lepton**
		e **sub-channel**	μ **sub-channel**	
Trigger	E_T^{miss}	Single Lepton	E_T^{miss}	Single Lepton
Leptons	0 loose leptons	Exactly 1 tight electron 0 additional loose leptons $p_T > 27$ GeV	Exactly 1 tight muon 0 additional loose leptons $p_T > 25$ GeV	Exactly 2 loose leptons Leading $p_T > 27$ GeV Same-flavour Opposite-sign charges ($\mu\mu$)
E_T^{miss}	> 150 GeV	> 30 GeV	-	-
m_{ll}	-	-	-	81 GeV $< m_{ll} <$ 101 GeV
Jet regions	Exactly 2 or exactly 3 jets			Exactly 2 or ≥ 3 jets
Jet p_T	> 30 GeV for $2.5 < \lvert\eta\rvert < 4.5$. For non-tagged jets in $\lvert\eta\rvert < 2.5$, two separate selections of 20 GeV and 30 GeV are used			
b-jets	Exactly 2 b-jets passing the 70% DL1r working point			
Leading b-tagged jet p_T	> 45 GeV			
m_{BB}	> 50 GeV			
S_T	> 120 GeV (2-jet), > 150 GeV (3-jet)	-		-
$\min[\Delta\phi(\mathbf{E}_T^{miss}, \mathbf{jets})]$	$> 20°$ (2-jet), $> 30°$ (3-jet)	-		-
$\Delta\phi(\mathbf{E}_T^{miss}, H_{cand})$	$> 120°$	-		-
$\Delta\phi(\mathbf{b}_1, \mathbf{b}_2)$	$< 140°$	-		-
$\Delta\phi(\mathbf{E}_T^{miss}, \mathbf{p}_T^{miss})$	$< 90°$	-		-
p_T^V regions	-	-		75 GeV $< p_T^V <$ 150 GeV
	150 GeV $< p_T^V <$ 250 GeV	150 GeV $< p_T^V <$ 250 GeV		150 GeV $< p_T^V <$ 250 GeV
	250 GeV $< p_T^V <$ 400 GeV	250 GeV $< p_T^V <$ 400 GeV		250 GeV $< p_T^V <$ 400 GeV
Signal regions	p_T^V dependent $\Delta R(\mathbf{b}_1, \mathbf{b}_2)$ signal selection			
Control regions	p_T^V dependent $\Delta R(\mathbf{b}_1, \mathbf{b}_2)$ high and low side-bands			

5.2.2 Multivariate approach to classification

A conventional method for performing analyses is using a cut-based approach whereby selections are applied on individual kinematic variables to provide a region with as much signal and as little background as possible. A simple cut-based approach however does not fully exploit all the information in an event. Instead, a Multivariate Analysis (MVA) strategy is used to improve the signal purity and background rejection. This method takes several observables as input, and using a machine learning technique, outputs a one-dimensional discriminant optimising the separation between signal and background. In this analysis, the machine learning technique used is a Boosted Decision Tree (BDT) [122], using the TMVA package of ROOT [123]. While BDTs don't always model complex systems as well as Artificial Neural Networks (ANNs), they are generally simpler and easier to interpret.

5.2.2.1 Boosted Decision Trees

Several observables of an event are fed into a decision tree, which begins at the root node. At each node, a binary decision is made based on one of the observables, aiming to classify the event into one of two classes. This process continues, branching at each decision point, until a specified maximum depth is reached, defined as the longest path from the root to a leaf node. The choice of the decision applied at each node is based on maximising the separation gain between nodes, defined as

$$\Delta G = G_{parent} - (G_{duaghter1} + G_{daughter2}) \tag{5.2}$$

A common way to calculate the gain is the Gini index:

$$G = p(1-p), \tag{5.3}$$

whereby $p = \frac{s}{s+b}$ is the purity. The final nodes of the tree give the probability of the event to be classified as either signal or background. An example of a single tree can be seen on the left of Figure 5.10. The dots in the dashed box are the data to be trained on, and the black dots in the tree are the nodes at which each single binary decision is made.
A single tree can be unstable with a small change in the inputs. Instead, a boosting method can be used whereby the weights of the misclassified events are increased (boosted) and a new tree is formed. Again, referring to Figure 5.10, the second box from the left shows the events that had their weights boosted (blue dots) after the first tree. This is repeated on each new tree until a maximum number of trees has been reached, which creates a "forest" of trees. The outputs of all these "weak" classifiers are combined to give a strong classifier. The boosting is controlled by a loss function which resembles the residual between the actual value and the predicted value.

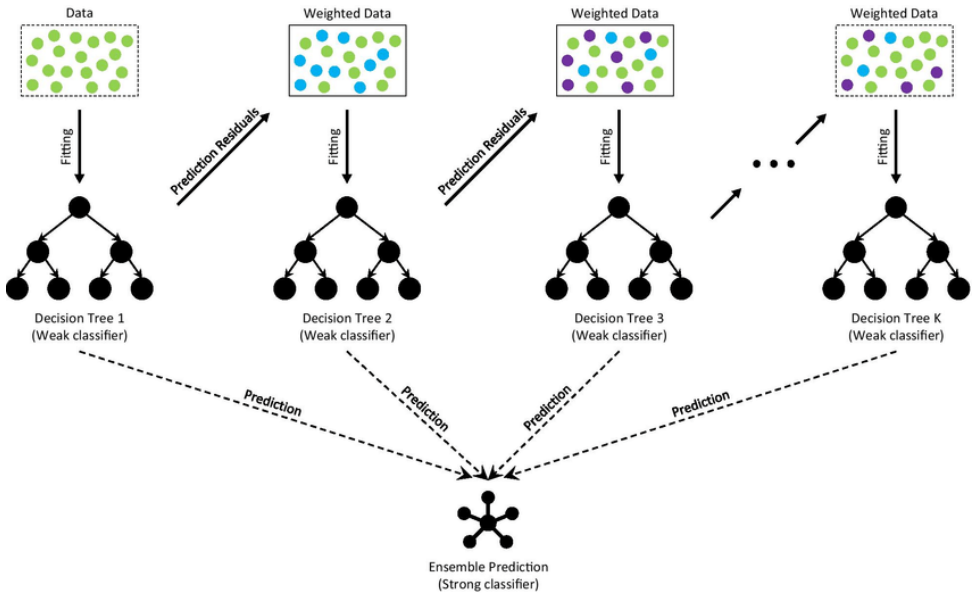

FIGURE 5.10: Diagram illustrating the architecture of a Boosted Decision Tree (BDT) [125]. The coloured dots in the dashed box represent the data to be trained on, while the black dots in the tree diagram are the nodes at which a single decision is made.

The goal is to minimise the loss function. The learning rate is a parameter that determines the size of the step taken to minimise the loss function at each iteration of the boosting. An example of a boosting algorithm, such as the one used in this analysis, is the GradBoost [124] algorithm, or gradient boosting. Here, after increasing the weights of the events with larger residuals, the outputs of the weak learners are combined as a weighted sum to represent the model response. A gradient descent procedure is then used to determine the steps taken to reduce the loss function by calculating the steps proportionally to the negative gradient of the loss function. A problem that machine learning algorithms face is known as overtraining. This is when the machine learning algorithm over-fits to the training data, predicting the results very well in the training set but when evaluated on a different set, performs poorly. One way to check if this has happened is to evaluate the performance of the algorithm using the Receiver Operator Curve (ROC). This curve is created by plotting the signal acceptance against the background rejection while various thresholds are applied to the algorithm's discriminant score. One of the ways to estimate the performance of the ROC is to use the area under the curve. If the area of the curve is 1, there is perfect background rejection independent of what the signal efficiency is, which is the best outcome to have. An area of 0.5 means the algorithm can't differentiate between background and signal, which is the worst outcome. Comparing the ROC curves of a machine learning algorithm evaluated on the training set and the test set, if the area under the curve is very similar then there is no overtraining. However, if the area for the test set is significantly smaller, this usually implies overtraining has occurred. Typically, a dataset would be split in half, with one half being used for the training of the machine learning algorithm, and the other half is used as the dataset that is being studied. Of the training dataset, about 80%

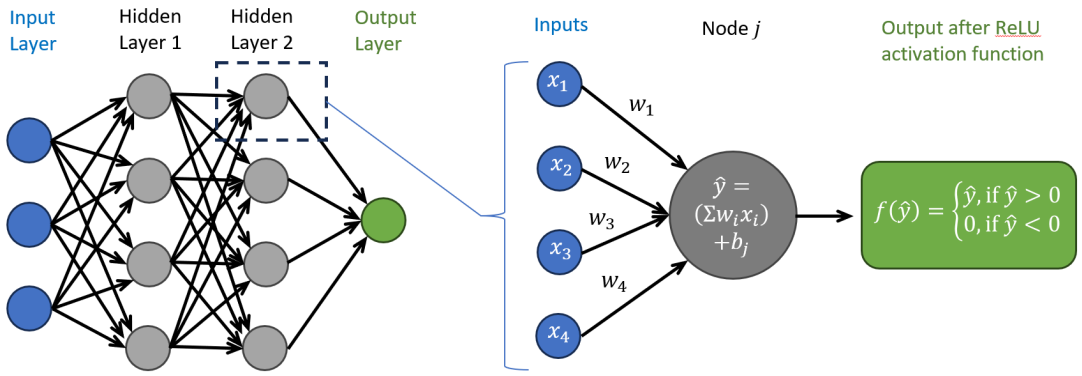

FIGURE 5.11: Diagram illustrating the architecture of a Deep Neural Network (DNN). On the left is the structure of the entire neural network. On the right is a zoomed in view of one of the nodes to show how the weights, biases and activation functions are applied.

is used to do the training, while the other 20% is used to test the algorithm. Since only half the dataset is being evaluated with this method, two algorithms are trained. One algorithm is trained on the first half and evaluated on the second half of the dataset, while the other algorithm is trained on second half and evaluated on the first half of the dataset.

5.2.2.2 Deep Neural Networks

The use of a Deep Neural Network (DNN) in this thesis is for classifying nominal samples from alternative samples when calculating systematic uncertainties, as described in Section 6.2.3.1. Instead of applying multiple binary cuts on different variables like a BDT, DNNs (a type of ANN) use a brain-inspired architecture, allowing them to model more complex patterns in the data. There are multiple layers of nodes, with each node connected to every node in the previous and following layers. A diagram illustrating a DNN is shown in Figure 5.11. The input layer is the first layer and takes in the features that are used to classify the events. The next layer is called the hidden layer, and may consist of multiple layers, with the Deep in DNN referring to multiple hidden layers. Each node j per layer receives the output x_i from each of the nodes i in the previous layer, multiplied by a weight w_{ij} specific to the connection between node i and node j. Those weighted values are then summed and a bias value b_j, specific to node j, is added to that sum, producing a new value $\hat{y_j} = \sum(w_i x_i) + b_j$. To introduce non-linearity into the matrix defining the neural network, this weighted sum is passed to a non-linear activation function. In the case of the Rectified Linear Unit (ReLU) function [126], the output will be a value of 0 if $\hat{y_j} < 0$ and $\hat{y_j}$ if $\hat{y_j} > 0$. The output of the activation function is the input to the nodes in the next layer. The number of nodes in the output layer will depend on how many categories are being differentiated. As an example, for the DL1r flavour tagging algorithm introduced in Section 4.3.3, there are three outputs for the three flavours that a jet can be tagged as. The output of the final layers are passed to an additional activation function, e.g., the softmax

function $p_c = e^{z_c}/\Sigma e^{z_c}$ [127], where the outputs z_c are converted to probabilities p_c for each category c. When training the DNN, supervised learning is performed, and a cross-entropy loss function is used to measure how far off the neural network's guess is compared to the actual value. A back-propagation algorithm is then used to optimise the neural networks weights and biases by minimising the loss function.

5.2.3 Input variables to signal vs background BDT classifier

To ensure an unbiased result, the BDT used for the MVA is trained and evaluated on separate simulated events. One training is performed using odd (even) event-numbered MC events and then evaluated on the even (odd) events respectively. The final BDT distribution is then addition of the odd and even event distributions. Due to the different kinematics and background compositions in the different signal regions, different MVAs are trained in separate regions depending on the lepton channel and number of jets. Additionally, in the 2-lepton channel, separate BDTs are trained for the 75 GeV$< p_T^V <$ 150 GeV and $p_T^V >$ 150 GeV regions. Although the BDTs are only applied in the signal regions, they are trained inclusively of the signal regions and the low and high control regions to increase the statistics. This gives 8 BDTs for the 14 signal regions.

The input variables used for the BDTs are slightly different between each lepton channel and are summarised in Table 5.4. The variables common to all three lepton channels are: The invariant mass of the two b-tagged jets m_{bb}, the $(\eta - \phi)$ distance between the two b-tagged jets $\Delta R(b_1, b_2)$, the transverse momentum of the leading (sub-leading) b-tagged jets $p_T^{b_1}$ ($p_T^{b_2}$), the transverse momentum of the vector boson candidate p_T^V, the ϕ distance between the vector boson candidate and the Higgs boson candidate $\Delta\phi(V, H)$, the binned distribution of the DL1r b-tagging score of the leading (sub-leading) b-tagged jets, named binned DL1r(b_1) (binned DL1r(b_2)), as defined by the pseudo-continuous tagging. The common variables that are only used in 3-jet events are: The transverse momentum of the third jet $p_T^{j_3}$, the invariant mass of the two b-tagged jets and the third jet m_{bbj}.

The 0-lepton specific variables are: The η distance between the two b-tagged jets $|\Delta\eta(b_1, b_2)|$, scalar sum of E_T^{miss} and the p_T of the jets M_{eff}, the vectorial sum of the p_T of all the tracks associated to the primary vertex but not associated to any reconstructed object is the track based soft E_T^{miss} term. The 1-lepton specific variables are: missing transverse momentum E_T^{miss}, the minimum ϕ distance between the charged lepton and the b-tagged jets $\min[\Delta\phi(\ell, b_i)]$, the transverse mass of the W boson candidate $m_T^W = \sqrt{2p_T^\ell E_T^{miss}(1 - \cos(\Delta\phi(\ell, E_T^{miss})))}$, the distance in rapidity between the W boson candidate and the Higgs boson candidate $\Delta Y(W, H)$, the reconstructed mass of the leptonically decaying top quark m_{top}. The 2-lepton specific variables are: The quasi-significance of E_T^{miss} defined as $E_T^{miss}/\sqrt{S_T}$ (with S_T being the scalar p_T sum of the charged leptons and jets) is E_T^{miss} significance, the pseudo-rapidity distance between the

TABLE 5.4: Summary of the variables used to train the BDT MVA per lepton channel

Variable	**0-Lepton**	**1-Lepton**	**2-Lepton**
m_{bb}	✓	✓	✓
$\Delta R(b_1, b_2)$	✓	✓	✓
$p_T^{b_1}$	✓	✓	✓
$p_T^{b_2}$	✓	✓	✓
p_T^V	✓	✓	✓
$\Delta\phi(V, H)$	✓	✓	✓
binned DL1r(b_1)	✓	✓	✓
binned DL1r(b_2)	✓	✓	✓
$\lvert\Delta\eta(b_1, b_2)\rvert$	✓		
M_{eff}	✓		
track based soft E_T^{miss} term	✓		
E_T^{miss}	$\equiv p_T^V$	✓	
$\min[\Delta\phi(\ell, b_i)]$		✓	
m_T^W		✓	
$\Delta Y(W, H)$		✓	
m_{top}		✓	
E_T^{miss} significance			✓
$\Delta\eta(V, H)$			✓
$m_{\ell\ell}$			✓
$\cos\theta(l^-, Z)$			✓
Only in 3-jet events			
$p_T^{j_3}$	✓	✓	✓
m_{bbj}	✓	✓	✓

Z boson candidate and the Higgs boson candidate $\Delta\eta(V, H)$, the invariant mass of the two charged leptons $m_{\ell\ell}$, the Z boson polarisation defined as the cosine of the polar angle between the negative lepton direction in the rest frame of the Z boson and the direction of the Z boson in the laboratory frame is $\cos\theta(l^-, Z)$.

The variables $\Delta Y(W, H)$ and m_{top} are calculated assuming the transverse component of the neutrino is defined by E_T^{miss} and the longitudinal component is defined by applying a W-mass constraint on the lepton-neutrino system. The m_{top} variable is then calculated assuming a top quark decay and calculating the invariant mass of the lepton, reconstructed neutrino and the b-tagged jet that gives the lowest mass value.

The hyper-parameters used in the training of the BDTs used in this analysis are summarised in Table 5.5.

TABLE 5.5: Hyper-parameters used for the BDT MVA trainings

TMVA Setting (definition)	**Value and definition**
BoostType (Boost procedure)	GradBoost
Shrinkage (Learning rate)	0.5
SeparationType (Node separation gain)	Gini index
PruneMethod (Pruning method)	None
NTrees (Number of trees)	200 (600 for 1-lepton)
MaxDepth (Maximum tree depth)	4
nCuts (Number of cuts tested per variable per node)	100
nEventsMin (Minimum percentage of total events in a node)	5%

5.2.4 BDT bin optimisiation

Since the distributions of the signal and background BDT scores are binned, the choice of binning will affect the amount of separation between signal and background. It is possible to exploit the fact that the bins with the lower BDT scores are dominated by background and deplete in signal, and the bins with the higher BDT scores have a large signal to background ratio. The binning of the BDT distributions can be altered using a method known as Transformation D. The defining equation for this transformation is:

$$Z = z_s \frac{n_s}{N_s} + z_b \frac{n_b}{N_b} \tag{5.4}$$

The values for z_s and z_b can be varied, and they define the number of new "signal" and "background" bins, with the total number of new bins being $z_s + z_b$. The values for this analysis, chosen to keep the MC statistical uncertainty below 20%, are $z_s = 10$ and $z_b = 5$ for the $p_T^V < 250$ GeV regions, and $z_s = 5$ and $z_b = 3$ for the $250 < p_T^V < 400$ GeV regions. Larger values for z_s provide finer binning at larger BDT values where the signal-to-background ratio is higher. The variables N_s (N_b) are the total number of signal (background) in the distribution, while n_s (n_b) are the number of signal (background) in a given interval I. The transformation is an iterative process and proceeds as follows, starting with many narrow, equidistant bins: Starting at the bin with the largest BDT score, increase the interval I by adding one after the other the next bin on the left, and recalculate Z after the addition of each bin. Once $Z > 1$ and the statistical uncertainty is $< 20\%$, combine all the bins in I into one bin. Then repeat this process, starting with the first bin to the left of the new merged bin until all the bins have been merged into new bins. Although the bins will be of varying widths, for illustrative purposes they are plotted as bins of equal widths. This means the bins no longer represent the BDT scores shown on the plots, but this has no impact on the likelihood fit since it doesn't care what the exact values of the bins are. An example of this transformation before and after using bins of equal widths is given in Figure 5.12.

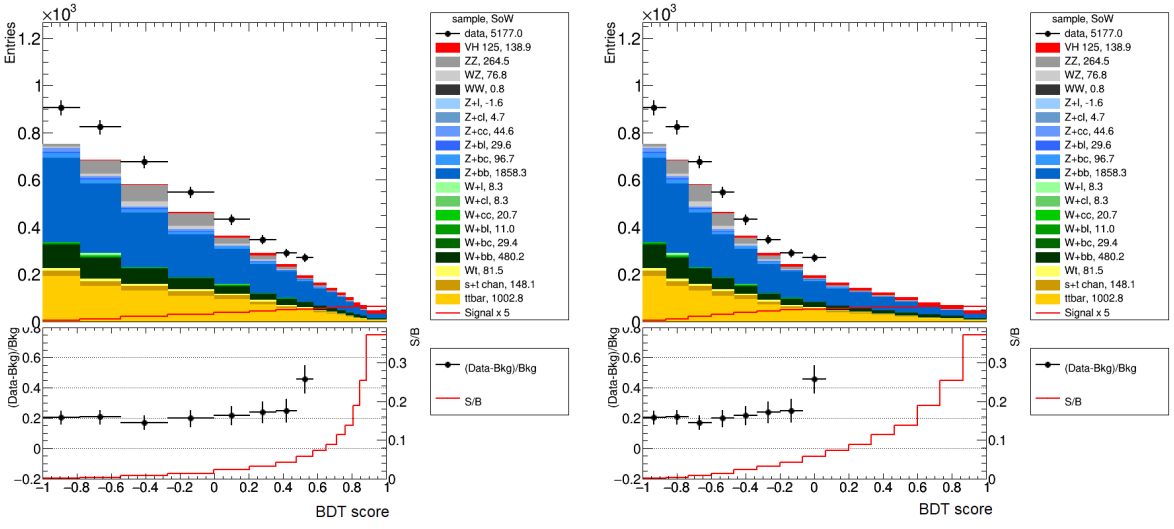

(a) (b)

FIGURE 5.12: An example of the BDT distribution from the 0-lepton, 2-jet, 150 GeV$< p_T^V <$ 250 GeV signal region immediately after the BDT transformation (a) and after the BDT transformation but with equidistant binning (b). Both plots are using pre-fit data. The upper legend shows the different samples with their corresponding yield, or some-of-weights (SoW).

5.3 Data and simulated samples

The data used in this analysis corresponds to pp collisions at a centre-of-mass energy of $\sqrt{s} = 13$ TeV. The data were collected by the ATLAS experiment at the LHC during the data taking periods of 2015-2018 and correspond to the full Run-2 dataset. Events were selected that were deemed of high enough quality for physics analyses. This dataset equates to a total integrated luminosity of $\mathcal{L} = 140.1 \pm 1.2$ fb^{-1} [128][79].

MC simulated events are used to model most of the backgrounds from SM processes and the $V(H \to b\bar{b})$ signal processes. For the nominal signal processes, the MC generator POWHEG-BOX V2 [129] + MINLO [130] was used to model the hard scatter with the NNPDF3.0NLO PDF [131] and the AZNLO [132] set of tuned parameters. The cross-section was calculated at NNLO(QCD)+NLO(EW) with the mass of the Higgs boson fixed at 125 GeV. For the $gg \to ZH$ sample only, the cross-section was calculated at NLO+NLL. The parton showering was modelled using PYTHIA 8.212 [133].

The nominal single-top and pair-produced-top samples were modelled with POWHEG-BOX V2 with the NNPDF3.0NLO PDF and A14 [134] set of tuned parameters. The cross-sections were calculated at NNLO+NNLL for $t\bar{t}$, NLO for the s- and t-channel single-top and approximate NNLO for the Wt-channel, all with the mass of the top-quark fixed at 172.5 GeV. The parton showering was modelled using PYTHIA 8.230. Only the leptonic and semi-leptonic top-quark decays are included. The Wt-channel processes are produced using the Diagram Subtraction

TABLE 5.6: The nominal MC generators used to simulate the signal and background processes. All three lepton flavours are taking into consideration when the samples are generated. The order of the cross-section calculations apply to the expansion of the strong coupling constant α_s, unless otherwise specified. ME, PS and UE are acronyms for Matrix Element, Parton Shower and Underlying Event respectively. (^{a}) The events were generated using the first PDF in the NNPDF3.0NLO set and then reweighted to the PDF4LHC15NLO [140] set. (^{b}) The $pp \to ZH$ cross-section calculation includes both qq- and gg-induced productions, so the $qq \to ZH$ process is normalised using the $pp \to ZH$ cross-section after subtracting the $gg \to ZH$ contribution.

Process	**ME Generator**	**ME PDF**	**PS and Hadronisation**	**UE Model Tune**	**Cross-Section Order**
Signal. Mass set to 125 GeV and $b\bar{b}$ branching fraction set to 58%					
$qq \to WH \to l\nu b\bar{b}$ MiNLO	POWHEG-BOX V2 +	NNPDF3.0NLO^a	PYTHIA 8.212	AZNLO NLO(EW)	NNLO(QCD)+
$qq \to ZH \to (\nu\nu/ll)b\bar{b}$ MiNLO	POWHEG-BOX V2 +	NNPDF3.0NLO^a	PYTHIA 8.212	AZNLO NLO(EW)	NNLO(QCD)^b+
$gg \to ZH \to (\nu\nu/ll)b\bar{b}$	POWHEG-BOX V2	NNPDF3.0NLO^a	PYTHIA 8.212	AZNLO	NLO+NLL
Top quark. Mass set to 172.5 GeV					
$t\bar{t}$	POWHEG-BOX v2	NNPDF3.0NLO	PYTHIA 8.230	A14	NNLO+NNLL
s-channel single-top					NLO
t-channel single-top					NLO
Wt					Approximate NNLO
W/Z + jets					
$W \to l\nu$	SHERPA 2.2.1	NNPDF3.0NNLO	SHERPA 2.2.1	Default	NNLO
$Z/\gamma^* \to ll$					
$Z \to \nu\nu$					
Diboson					
$qq \to WW$	SHERPA 2.2.1	NNPDF3.0NNLO	SHERPA 2.2.1	Default	NLO
$qq \to WZ$					
$qq \to ZZ$					
$gg \to VV$					

(DS) method [135]. This method includes a gauge invariant subtraction term that locally cancels the $t\bar{t}$ contribution to the matrix element calculations, since there are some interference effects from $t\bar{t}$ processes in Wt calculations.

The nominal V+jets and diboson samples were modelled using SHERPA 2.2.1 [136] with the NNPDF3.0NNLO PDF and default set of tuned parameters. The cross-sections were calculated at NNLO for V+jets and NLO for diboson. SHERPA was also used to model the parton showering.

All simulated events were passed through a GEANT4 [87] simulation of the ATLAS detector [88], as described in Section 3.2.5. The effects of pileup were modelled by overlaying minimum bias events simulated with the soft QCD processes of PYTHIA 8.186 with the A3 [137] set of tuned parameters and the NNPDF2.3LO [138] PDF. For all the non-SHERPA generated samples, the EVTGENv1.6.0 program [139] was used for the decays of the bottom and charm hadrons. A summary of all the MC generators used for this analysis is given in Table 5.6.

5.3.1 Data-driven background modelling

The work in this section was performed by the author.

While most of the backgrounds are modelled using MC simulations, other backgrounds are modelled using data-driven techniques. These processes are usually poorly modelled by the MC generators and so require a data-driven estimation. Another case is if applying selections results in a region that is pure in a certain background, then the data from that region can be used instead of the MC since it will have less associated uncertainties.

5.3.1.1 Data-driven top background estimation

In the earlier rounds of the $VH \to b\bar{b}$ analysis, before the previous round, the top ($t\bar{t}$ and single-top Wt) modelling uncertainties were found to be a limiting factor in the STXS measurements. Due to this, a data-driven approach to the top backgrounds in the 2-lepton channel was implemented. Using the nominal selections but requiring opposite flavour leptons instead of same flavour leptons, we obtain a region that is over 99% pure in $t\bar{t}$ and single-top Wt events. This region is therefore called the $e\mu$-control region, or $e\mu$-CR. Since the purity of top events in the $e\mu$-CR is so high, the data in the $e\mu$-CR can be considered as representing the top processes. In the $t\bar{t}$ and Wt processes, the reconstructed vector boson usually represents a single W boson in the 1-lepton channel and an unknown origin due to E_T^{miss} in the 0-lepton channel. In the 2-lepton channel however, the leptons are almost always taken from two different W bosons. This provides a lepton-flavour symmetry in the 2-lepton channel between the analysis regions, containing events where the W bosons decay to ee or $\mu\mu$, and the $e\mu$-CR, where the W bosons decay to $e\mu$ or μe. This flavour symmetry, along with the purity of the top processes in the $e\mu$-CR allows for the data in the $e\mu$-CR to be directly used in the analysis regions, without the need of any uncertainties other than the dominant statistical contributions. The $e\mu$-CR data is therefore used to represent the 2-lepton top processes in the likelihood fit instead of the MC simulated top samples. The data-MC plots of the BDT distribution in the $e\mu$ control region are shown in Figure 5.13. As can be seen, the $t\bar{t}$ and single-top backgrounds account for almost all the data. Any biases between the analysis regions and $e\mu$-CRs due to the difference in acceptances, reconstruction or triggers are determined by taking the ratio of the MC top background yield in the analysis regions to the MC yield in the $e\mu$-CR, and applying this as a scale factor. This scale factor was found to agree with the value of 1 within uncertainty. So while the data-driven top estimate reduces the impact of the uncertainties from the modelling of the top processes in simulation, we are still reliant on the simulation in estimating this data-driven sample. Validation studies performed for the previous round of this analysis [24] showed that the shapes of the nominal selection top backgrounds agreed within statistical uncertainty of the

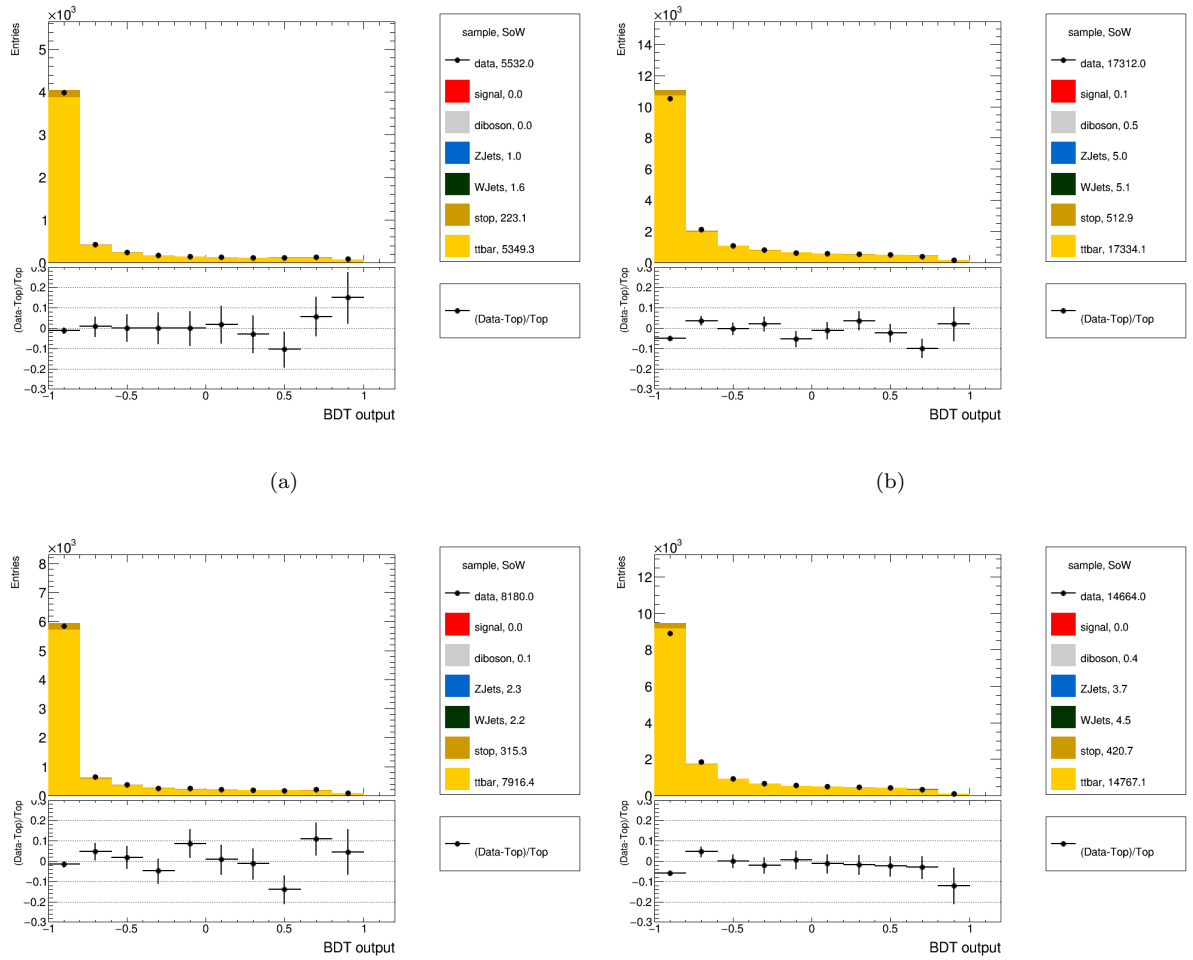

FIGURE 5.13: The data-MC plots of the BDT distribution in the $e\mu$ control region, inclusive of the three p_T^V regions. Figures (a) and (b) are the 2- and ≥3-jet regions for the jet p_T selections of 20 GeV, while (c) and (d) are the 2- and ≥3-jet regions for the jet p_T selections of 30 GeV. The bottom panels in each plot show the data minus top contribution, all divided by the top contribution. The upper legend shows the different samples with their corresponding yield, or some-of-weights (SoW).

shapes in the $e\mu$-CR. More information relating to the uncertainties of this region are defined in Section 6.2.7.1.

5.3.1.2 Nominal multijet estimation

The cross-section for the production of multijet (MJ) events due to QCD processes at the LHC is large, and thus can potentially contribute to the backgrounds in this analysis despite having no genuine E_T^{miss} or prompt leptons. These events can pass the analysis selections if a jet is misreconstructed as a lepton, or non-prompt leptons coming from weak decays are

misreconstrcted as prompt leptons. Due to the topology of the 2-lepton channel, and the anti-QCD cuts applied in the 0-lepton channel, MJ events are negligible in thse regions. However, in the 1-lepton channel, MJ events occur on the percent level. Due to the amount of events needed to simulate MJ events in this analysis and the fact that simulation doesn't reproduce fake lepton events accurately enough, a data-driven technique is used to estimate the MJ contribution via a template method. A MJ control region (MJ-CR) is created from data for each lepton flavour (e, μ), number of jets (two and three), and is inclusive of p_T^V ($150 < p_T^V < 400$ GeV) as well as SR and CRs. The MJ-CRs have the same selections as the signal region, except the lepton isolation cuts, as defined in Table 5.1, are inverted. Due to limited events in these CRs, the requirement on the number of b-tagged jets is relaxed from exactly two to exactly one. The distribution of the W-boson candidate transverse mass m_T^W is used for the template since it provides the best discrimination between MJ events and the other simulated backgrounds, as found in the previous round of the analysis [24]. Within the MJ-CRs, the simulated background samples are subtracted from the data to obtain a data-driven estimate of the shape of the MJ contribution, providing a MJ template. Fits of the backgrounds to the data using the m_T^W distribution in the 2-tag, isolated regions corresponding to each MJ-CR are then performed, using the MJ template to represent the MJ shape. In the m_T^W distribution, there is very little separation between the top and W+jets backgrounds. To improve the discrimination between these two simulated backgrounds in the MJ fit, a W+jets heavy flavour (W+hf) enriched region is defined, using the selection $m_{BB} < 75$ GeV and $m_{top} > 225$ GeV. The mass of the top-quark candidate m_{top} is defined in Section 5.2.3. The W+hf depleted region ($m_{BB} > 75$ GeV or $m_{top} < 225$ GeV) is used to create the m_T^W distribution, while the events from the W+hf enriched region are added as a single bin to the end of the m_T^W distribution. The MJ fit is then performed using this new distribution.

This MJ fit simultaneously extracts the normalisations of the W+jets, top ($t\bar{t}$ and s-top) and MJ backgrounds, while the other simulated backgrounds have their normalisations fixed to their predictions. The MJ normalisation is used to obtain a scale factor ($SF = \frac{\text{post-MJ-fit yield}}{\text{pre-MJ-fit yield}}$) that scales the MJ templates from the MJ-CRs to the normalisation expected in the analysis regions, for any variable under study. These scaled MJ templates are then used as the MJ estimate in the final likelihood fit. The normalisations of the W+jets and top backgrounds are used in the systematic uncertainty calculations, as described in Section 6.2.7.2.

The post-MJ-fit plots for both the 20 GeV and 30 GeV jet p_T selections are shown in Figure 5.14 for the electron contributions, and Figure 5.15 for the muon contributions. The corresponding yields and scale factors are shown in Table 5.7. The electron channel is by far the dominant contributor to the MJ background, with the 3-jet regions contributing the most. The muon channel has a very small MJ contribution, going to zero in the 3-jet region of the 30 GeV jet selection. This contrasts with the other regions where the 30 GeV jet selection regions have a larger absolute MJ contribution compared to the 20 GeV jet selection regions. Additionally, the 2-jet electron channel is the only region where the percentage of MJ in the background increases

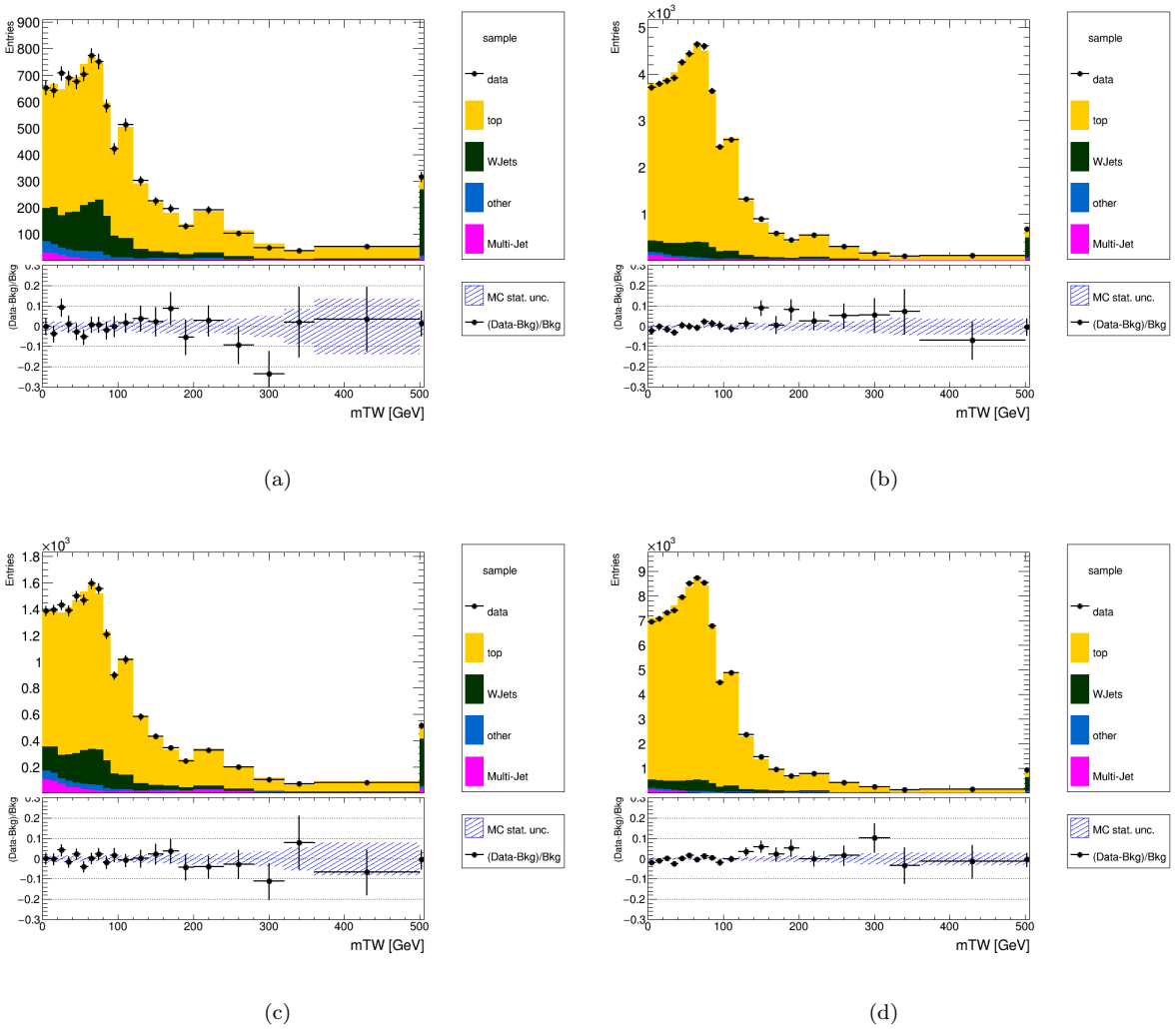

FIGURE 5.14: The post-fit plots of the MJ fit for the electron channel. Figures (a) and (b) are the 2- and 3-jet regions for the jet p_T selections of 20 GeV, while (c) and (d) are the 2- and 3-jet regions for the jet p_T selections of 30 GeV. The final bin in each plot is the W+hf enriched region. The ratio plots show the difference between the data and the backgrounds, normalised by the backgrounds. The top contribution combines the $t\bar{t}$ and single-top samples, while the "other" consists of the diboson, Z+jets and signal samples.

when tightening the jet p_T selection. This may be due to the electron channel having more fake low-p_T jets due to misreconstructed electrons.

As mentioned above, the MJ templates are obtained in a control region where n^b_{jets}=1. However, the final maximum likelihood fit uses an BDT distribution for the SRs which is trained on events that have n^b_{jets}=2. The tagged jets' pseudo-continuous b-tagging (PCBT) bin is used as an input to the BDT (see Section 4.3.3.1 for more on PCBT). To overcome the lack of a second tagged jet, the values of the PCBT bin scores for all the events in the MJ-CR are probabilistically assigned based on the PCBT bin distributions of the data in the 2-tagged, isolated regions. If a jet passes the b-tagging requirement, it will either fall into the 70%-60% b-tagging efficiency

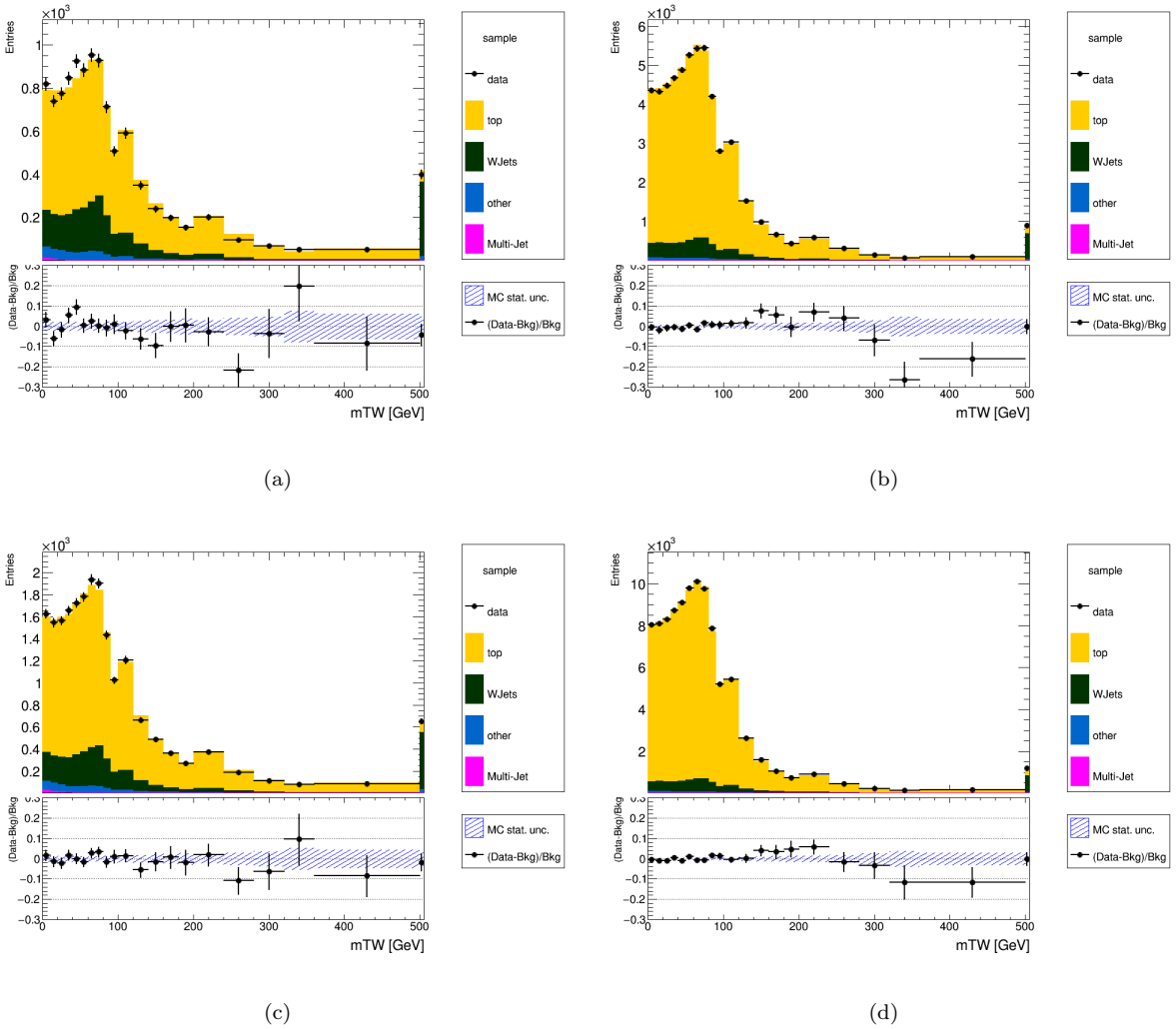

FIGURE 5.15: The post-fit plots of the MJ fit for the muon channel. Figures (a) and (b) are the 2- and 3-jet regions for the jet p_T selections of 20 GeV, while (c) and (d) are the 2- and 3-jet regions for the jet p_T selections of 30 GeV. The final bin in each plot is the W+hf enriched region. The ratio plots show the difference between the data and the backgrounds, normalised by the backgrounds. The top contribution combines the $t\bar{t}$ and single-top samples, while the "other" consists of the diboson, Z+jets and signal samples.

PCBT bin, or the 60%-0% bin. For the input variables to the BDT, these bins correspond to the value of 4 and 5 respectively. Since each of the two b-tagged jets can fall into one of these two PCBT bins, there is a total of four possible combinations of PCBT scores per event. The probability distribution of the PCBT bins in the 1-lepton, 2-tag regions of the data events are shown in Table 5.8. Here, $b1$ is the b-tagged jet with the highest p_T, while $b2$ is the other b-tagged jet. The subscripts indicate which PCBT bin they fall into. These probabilities are used to randomly assign the PCBT bin scores to the tagged jet and the highest p_T non-tagged jet in the events in the MJ-CR, so that a BDT score can be obtained for those events.

TABLE 5.7: The yields, percentage of the total background, and the scale factors (SF) obtained from the MJ fit. The values for the different jet p_T selections are shown as well, namely the 20 GeV and 30 GeV selections.

Region	Bkg	**Yield**		**% of Total**		**SF**	
		20 GeV	30 GeV	20 GeV	30 GeV	20 GeV	30 GeV
2-jet, e	Top	6242	13558	71.6	76.4	0.945	0.956
	W+jets	1983	3034	22.8	17.1	1.248	1.211
	MJ	174	638	2.0	3.6	0.030	0.060
2-jet, μ	Top	7463	16083	71.2	77.8	0.967	0.985
	W+jets	2509	3773	24.0	18.2	1.212	1.174
	MJ	39	91	0.4	0.4	0.003	0.004
3-jet, e	Top	41792	80019	88.9	92.2	0.931	0.953
	W+jets	3891	5227	8.3	6.0	1.145	1.168
	MJ	768	859	1.6	1.0	0.08	0.078
3-jet, μ	Top	48452	91747	88.7	92.3	0.924	0.944
	W+jets	5388	6691	9.9	6.7	1.228	1.179
	MJ	4	0	0.0	0.0	0.000	0.000

TABLE 5.8: The probabilities, in percent, of an event in the 1-lepton, 2-tag regions of data containing the highest p_T b-tagged jet ($b1$) and the other b-tagged jet ($b2$) falling in the PCBT bin of 4 or 5. The regions are split by the number of jets (two or three) and the flavour of the lepton (e or μ). The values for the different jet p_T selections of 20 and 30 GeV are shown as well.

		2-jet, e		**3-jet,** e		**2-jet,** μ		**3-jet,** μ	
		$b1_4$	$b1_5$	$b1_4$	$b1_5$	$b1_4$	$b1_5$	$b1_4$	$b1_5$
20 GeV	$b2_5$	11.79	67.01	18.09	64.04	16.55	62.79	14.64	61.90
	$b2_4$	4.01	17.20	3.39	14.48	4.99	15.68	4.26	19.21
30 GeV	$b2_5$	16.08	62.06	18.55	63.75	15.23	61.68	15.43	59.00
	$b2_4$	3.58	18.28	4.52	13.17	5.74	17.36	3.99	21.58

5.4 Maximum profile likelihood estimation

The signal strength is calculated using a binned maximum profile likelihood fit to data across all 14 signal and 28 control regions simultaneously. In particular, the fit to the signal regions is done using a transformed BDT output, while single-bin distributions are used in the control regions to constrain the background yields. The signal strength is defined as the ratio of the signal yield extracted from the likelihood fit, divided by the SM expectations of the production cross-section multiplied by the Higgs boson branching ratio to $b\bar{b}$:

$$\mu_{VH} = \frac{[\sigma_{VH} \times \mathrm{BR}(H \to b\bar{b})]_{\mathrm{measured}}}{[\sigma_{VH} \times \mathrm{BR}(H \to b\bar{b})]_{\mathrm{theory}}}. \tag{5.5}$$

The likelihood is constructed as the product over all the bins of the Poisson probability to observe n_i events in bin i when N_i^{exp} events are expected in bin i:

$$L_{poisson} = \prod_{i \in bins} \frac{(N_i^{exp})^{n_i}}{n_i!} e^{N_i^{exp}}. \tag{5.6}$$

The number of expected events can be expanded into the signal s_i and background b_i components as:

$$N_i^{exp} = \mu \cdot s_i + \sum_{j \in bkg} k_j \cdot b_{i,j}. \tag{5.7}$$

The k_j are the scale factors (or normalisations) for each background component, similar to what μ is for the signal. Since the signal strength is what we want to extract from the fit, the μ parameter is often called the Parameter of Interest (PoI). All the other parameters are known as Nuisance Parameters (NPs). Systematic uncertainties enter the likelihood as α_k, where each α_k is modelled as a Gaussian distribution and acts as a penalty term (constraint) to the likelihood, of the form:

$$\mathcal{L}_{syst} = \prod_{k \in NP} \frac{1}{\sqrt{2\pi}\sigma_k} \exp - \frac{(\alpha_k - \alpha_{0k})^2}{2\sigma_k} \tag{5.8}$$

Here, α_k is the parameter to be fitted, while α_{0k} and σ_k are the central value and uncertainty assigned to the parameter k before the fit is performed. Often for convenience, the central value is assumed to be zero $\alpha_{0k} = 0$ with an uncertainty of unity $\sigma_k = 1$, thus expressing the NPs in units of σ_k. This method of defining the NPs allows for easier interpretation of the NPs in the fit.

Due to the limited number of MC simulated events, the statistical uncertainties on the MC backgrounds are also considered in the likelihood [141]. These uncertainties enter as Poisson defined NPs with expected background events B_i and observed events b_i, and take the form:

$$\mathcal{L}_{stat} = \prod_{i \in bins} \frac{(B_i)^{b_i} e^{-B_i}}{\Gamma(b_i + 1)} \tag{5.9}$$

The Poisson is modified with a Gamma function instead of a factorial since in Monte Carlo the number of events may not be integer values. The expected background yield is defined as $B_i = \gamma_i b_i$, where the γ_i are the NPs. Since there is only one γ_i per bin, it represents the total background in that bin.
The resultant likelihood is the product of all three likelihoods, and looks like:

$$\mathcal{L}(\mu, \boldsymbol{\alpha}, \boldsymbol{\gamma}) = \mathcal{L}_{poisson}(\mu, \boldsymbol{\alpha}, \boldsymbol{\gamma}) \times \mathcal{L}_{syst}(\boldsymbol{\alpha}) \times \mathcal{L}_{stat}(\boldsymbol{\gamma}) \tag{5.10}$$

The values of μ and σ_μ are obtained by maximising the likelihood function $\mathcal{L}(\mu, \boldsymbol{\theta})$ with respect to all the parameters. Here θ represents all the NPs other than the signal strength. However, to test a certain hypothesis for μ, a likelihood ratio is created to be a test statistic[142]:

$$\lambda(\mu) = \frac{\mathcal{L}(\mu, \hat{\hat{\boldsymbol{\theta}}})}{\mathcal{L}(\hat{\mu}, \hat{\boldsymbol{\theta}})}, \tag{5.11}$$

where $\hat{\mu}$ and $\hat{\boldsymbol{\theta}}$ are the parameters that maximise the likelihood, while $\hat{\hat{\boldsymbol{\theta}}}$ maximises the likelihood for a given value of μ. Usually, a fit is first done to test the background-only hypothesis $\mu = 0$ (the null hypothesis) against the alternative hypothesis where $\mu > 0$. If the null hypothesis cannot be rejected, i.e., $\hat{\mu}$ is not significantly far away from 0, then the null hypothesis is changed to assume the alternative hypothesis is true ($\mu = 1$) and an exclusion fit is performed using the CL_s method[143]. A more convenient way to represent the test statistic is as a negative log:

$$t_\mu = -2 \log \lambda(\mu). \tag{5.12}$$

Instead of maximising the likelihood, we can minimise the log-likelihood t_μ. In this case, the data is more likely to represent the hypothesis the closer t_μ is to zero, with the minimum giving the best fit value for μ. The upper and lower uncertainties on μ, σ_μ^+ and σ_μ^-, can then be found by taking the difference between $\hat{\mu}$ and the μ values above and below $\hat{\mu}$ respectively that result in $t_\mu = 1$.
Assuming the null hypothesis to be true, t_μ will be asymptotically distributed as a chi-square with one degree of freedom, as according to Wilk's theorem [144]. Therefore, to measure an approximate p-value, we can compare the value of t_0 to the chi-square value, giving the formula:

$$p_0 = \int_{t_{0,obs}}^{\infty} f(t_0|\mu)\, dt_0. \tag{5.13}$$

The observed value $t_{0,obs}$ comes from the data and $f(t_0|\mu)$ is the probability density function of t_0 under the assumption of the chosen value of μ, in this case $\mu = 0$. The p-value is interpreted as the probability, assuming the null hypothesis is true, that the given data is incompatible with the null hypothesis. Thus, if the p-value is below some threshold, the null hypothesis can be rejected. Assuming normal distributions, the p-value can be converted to a significance Z

using:

$$Z = \Phi^{-1}(1 - p_0), \tag{5.14}$$

where Φ^{-1} is the inverse of the cumulative distribution of a standard Gaussian. In particle physics, a threshold of $Z = 3\sigma$ ($p_0 = 0.003$) is considered for evidence, and $Z = 5\sigma$ ($p_0 = 2.87 \times 10^{-7}$) for discovery of a hypothesis.

Before performing a likelihood fit on the actual data, tests need to be done to make sure the analysis setup and systematics correctly describe what is happening. To do this without using the actual data, a representative dataset is used, known as the Asimov dataset. The Asimov dataset is created from the likelihood by using the nominal values of the NPs and setting the yields to those expected from the simulations. Using Wilk's theorem and the central-limit theorem, for a large number of events, $\sqrt{t_0}$ is distributed as a Gaussian and the significance can be represented as $Z = \sqrt{t_0}$. For Gaussian counting, this reduces to $Z = \frac{\hat{S}}{\sqrt{B}}$, where $\hat{S}$ is the maximum likelihood estimator for the signal. However, assuming Poisson counting, the significance reduces to [142]:

$$Z = \sqrt{2\left((\hat{S} + B)\log\left(1 + \frac{\hat{S}}{B}\right) - \hat{S}\right)}. \tag{5.15}$$

5.5 STXS $VH \to b\bar{b}$ signal parametrisation

For the theoretical background and overview of the STXS framework, please see Section 2.5.1. Within the STXS framework, the bins are defined by truth level definitions of the final state objects. The Higgs boson is assumed to be produced on-shell and has a global cut on the rapidity of the Higgs of $|\mathcal{Y}_H| < 2.5$ applied across all the bins. This cut is applied since the current experiments have no sensitivity outside of this range. The vector bosons are defined by summing all the products of their leptonic decays, including the neutrinos. The electrons and muons have all the final state radiation photons added back to the lepton and no restrictions are applied on the transverse momentum or rapidity of the leptons. The p_T of the truth vector bosons is defined as $p_T^{V,truth}$. The truth jets are reconstructed as anti-k_T jets with a radius of $R = 0.4$ and using all stable particles originating from the hadron decay chains. This excludes all the decay products from the Higgs boson and leptonically decaying vector bosons, as these are already used to define the Higgs and vector bosons respectively. The truth jets have no restrictions on their rapidity but must have $p_T > 30$ GeV. This p_T cut is to help reduce the number of jets coming from pileup interactions when applied in the reconstruction level. With these jet definitions, as opposed to the reconstruction level, the number of jets per STXS region is defined as the number of jets additional to the two jets created by the two b-quarks originating from the Higgs boson decay, from here on referred to as n_{jets}^{add}. Hence, an event that passes all the analysis cuts and has n_{jets}^{b}=2 with no other jets would be considered a 2-jet event at

reconstruction level, but n_{jets}^{add}=0 at the STXS level.
The possible STXS bins for the $(V \to \text{leptons})H$ production are shown in Figure 5.16. Due to a limited fiducial volume, not all the $p_T^{V,truth}$ bins can be studied. And due to limited statistics, some of the smaller bins have to be combined into larger bins. The signal strengths calculated in each STXS bin being studied enter the likelihood fit as a nuisance parameter, and since they are the parameters we are interested in calculating, they are known as Parameters of Interest (PoI). The scheme used in the previous round of the $V(H \to b\bar{b})$ resolved analysis [24] was the 5 PoI scheme, where the bins are:

- $WH, 150 < p_T^{W,truth} < 250$ **GeV,** $n_{jets}^{add} \geq 0$**:** Combines the n_{jets}^{add} bins for the $q\bar{q} \to WH$ process for $150 < p_T^{W,truth} < 250$ GeV
- $WH, 250 < p_T^{W,truth} < 400$ **GeV,** $n_{jets}^{add} \geq 0$**:** Combines the n_{jets}^{add} bins for the $q\bar{q} \to WH$ process for $250 < p_T^{W,truth} < 400$ GeV
- $ZH, 75 < p_T^{Z,truth} < 150$ **GeV,** $n_{jets}^{add} \geq 0$**:** Combines the n_{jets}^{add} bins for the combined $q\bar{q} \to ZH$ and $gg \to ZH$ processes for $75 < p_T^{Z,truth} < 150$ GeV
- $ZH, 150 < p_T^{Z,truth} < 250$ **GeV,** $n_{jets}^{add} \geq 0$**:** Combines the n_{jets}^{add} bins for the combined $q\bar{q} \to ZH$ and $gg \to ZH$ processes for $150 < p_T^{Z,truth} < 250$ GeV
- $ZH, 250 < p_T^{Z,truth} < 400$ **GeV,** $n_{jets}^{add} \geq 0$**:** Combines the n_{jets}^{add} bins for the combined $q\bar{q} \to ZH$ and $gg \to ZH$ processes for $250 < p_T^{Z,truth} < 400$ GeV

All the bins with $p_T^{V,truth} > 400$ GeV are studied in the boosted analysis. All the bins in Figure 5.16 not mentioned in this list have their cross-sections set to the SM values and act as backgrounds in the fit. For this thesis, an extension to this 5 PoI scheme is studied whereby each of the 5 STXS bins are split by n_{jets}^{add} into the $n_{jets}^{add} = 0$ and $n_{jets}^{add} \geq 1$ bins, creating 10 bins (10 PoI scheme). This extension is to expand the measurement of the previous round, providing new regions to calculate the signal strengths and possibly further increase the sensitivity to certain BSM effects. However, the statistical limits will be pushed in some of the new STXS PoI scheme bins.
The implementation of the STXS framework within the likelihood fit is done through a combination of both the analysis regions defined in Section 5.2, and the STXS regions defined above. Since the STXS regions are defined using the truth record of the Higgs boson's decay, only the signal samples will have both analysis and STXS regions, while the background samples are only defined by the analysis regions. Each signal event is therefore categorised into an analysis region by using the reconstruction level observables, and categorised into the STXS regions by using the truth level observables as shown in Figure 5.16, i.e., the generated production mode, the $p_T^{V,truth}$ and n_{jets}^{add}. The signal events are then assigned to one of the POIs, as defined above, based on their STXS region. Therefore, each analysis-defined signal region does not have one

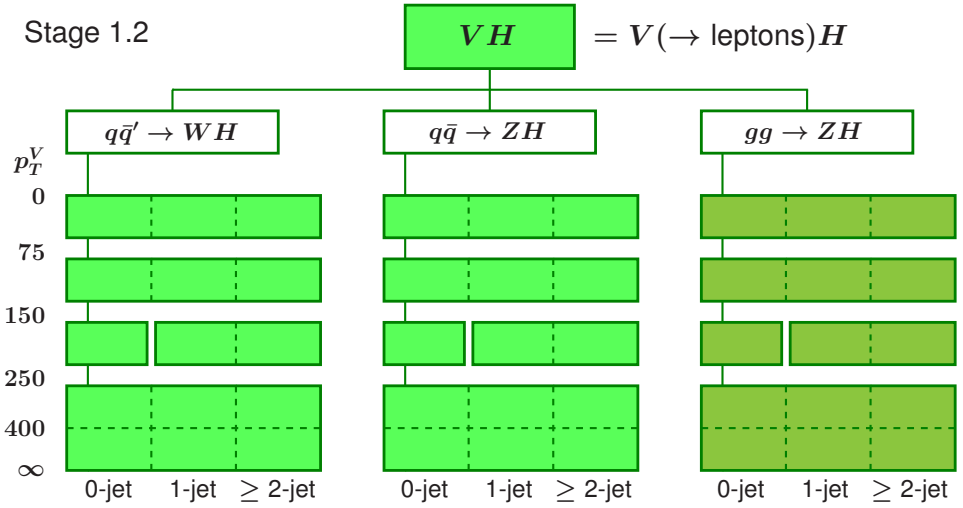

FIGURE 5.16: Diagram illustrating the bins STXS bins in the VH analysis as part of the stage 1.2 STXS framework [22].

POI representing the signal in that region but rather has multiple STXS based POIs representing the signal in that region. The analysis regions will however have a particular POI that it correlates to the strongest, where the p_T^V and number of jet definitions match closest between the analysis region and the STXS region. As an example, the signal in the 2-jet, 150 $< p_T^V <$ 250 GeV regions will be dominated by the signal that falls in the $n_{jets}^{add} = 0$, 150 $< p_T^{V,truth} <$ 250 GeV STXS region. Additionally, the lepton channels target the POIs based on the production mode. The WH POIs are targeted by the 1-lepton channel, the ZH POIs for $p_T^V > 150$ GeV are targeted by both the 0- and 2-lepton channels, while the ZH, 75 $< p_T^{V,truth} <$ 150 GeV POIs are targeted by only the 2-lepton channel. Due to the misreconstruction of some leptons and jets however, the 0-lepton channel also has a significant amount of the WH signal.

There are three different STXS schemes studied in this thesis. The 5 and 10 POI STXS schemes defined above, and the 2 POI STXS scheme where the two STXS bins are the $p_T^{V,truth}$ and n_{jets}^{add} inclusive WH and ZH regions. A summary of these regions is shown in Table 5.9.

TABLE 5.9: The three main STXS fit POI schemes shown in this thesis and what selections are used to define them. Each successive column shows the additional selections applied to the region in the column before it. The first column is a selection on the production, the second column is an additional selection on the transverse momentum of the vector boson (p_T^V), and the third column is an additional selection on n_{jets}^{add}. Since these are STXS regions, the selections are applied at truth level.

2 POI	**5 POI**	**10 POI**
WH	$150 \leq p_T^{W,truth} < 250$ GeV	$n_{jets}^{add} = 0$
		$n_{jets}^{add} \geq 1$
	$250 \leq p_T^{W,truth} < 400$ GeV	$n_{jets}^{add} = 0$
		$n_{jets}^{add} \geq 1$
ZH	$75 \leq p_T^{Z,truth} < 150$ GeV	$n_{jets}^{add} = 0$
		$n_{jets}^{add} \geq 1$
	$150 \leq p_T^{Z,truth} < 250$ GeV	$n_{jets}^{add} = 0$
		$n_{jets}^{add} \geq 1$
	$250 \leq p_T^{Z,truth} < 400$ GeV	$n_{jets}^{add} = 0$
		$n_{jets}^{add} \geq 1$

Chapter 6

Systematic uncertainties

Within the $VH(H \to b\bar{b})$ analysis, there are several sources of uncertainties that impact the result, and they can be grouped into two categories. The first are the experimental uncertainties that come from the experimental apparatus and reconstruction, i.e., the accelerator, detector and reconstruction of the objects. The other group is the systematic uncertainties that come from the modelling of the signal and background processes, which in this thesis is the dominant source of uncertainties. These pertain to the production of the simulated samples and the size of the effects that arise due to the choice of phase space studied.

6.1 Experimental uncertainties

The experimental uncertainties depend on how the different objects are reconstructed and corrected, as well as how the detector and accelerator performed. To correct the simulation to match better with data, due to either simplified detector responses or difficulty in theoretical modelling, Scale Factors (SF) are applied to the MC which are obtained via data-to-MC comparisons. The different Combined Performance (CP) groups in ATLAS provide the necessary SFs and their associated uncertainties of the different physics objects. Each analysis within ATLAS then uses these centrally provided SFs to correct the MC and estimate the total uncertainty that these sources have on their respective analysis. A summary of the experimental uncertainties is given in Table 6.1.

6.1.1 Luminosity and pileup

The luminosity uncertainty is calculated by comparing the LUCID-2 [79] measurements to several other detectors. The dominant source of this uncertainty comes from extrapolating from the Van der Meer scans [78] performed at low luminosity to the high luminosity of the

data-taking runs. For the data taking periods of 2015-2016, 2017 and 2018, the uncertainties were found to be 0.93%, 1.13% and 1.1% respectively, giving a total uncertainty of 0.83% on the total Run-2 integrated luminosity of 140 fb^{-1} [128]. More on the luminosity is given in Section 3.1.2.

The production of the simulated samples occurs before or during the data-taking periods. This means the amount of pileup present in the data that these simulated samples are produced for is unknown at the time of production and so estimates of the pileup have to be made. Once the data has been collected, the pileup estimations in the simulation can be weighted to match what was found in the data. Before calculating the pileup weights, the average number of collisions per bunch crossing (μ) in the data is scaled down by a factor of 1.03. The upper and lower bound for the uncertainty is then estimated using a factor of 0.99 and 1.07 respectively, applied to the unscaled value [145]. More information on the pileup is given in Section 3.1.3.

6.1.2 Lepton and E_T^{miss} triggers

The E_T^{miss} trigger uncertainties are related to the scale factors that account for the E_T^{miss} trigger efficiency turn-on, derived using W+jets events [121]. The uncertainties accounted for are the statistical error on the W+jets samples used, the dependence on the specific process used which is accounted for by comparing to $t\bar{t}$ and Z+jets events, as well as the kinematic dependence of the E_T^{miss} efficiency on the scalar sum of the jet p_T (S_T) which was only relevant for the 2017 data taking year.

Similarly to the E_T^{miss} trigger, the lepton trigger uncertainties are related to their efficiencies. For the electron trigger, there is one uncertainty that deals with the statistical and systematic uncertainties, while the muon trigger has separate statistical and systematic uncertainties.

6.1.3 Lepton reconstruction

Electrons

The uncertainties on the reconstruction and identification efficiencies are calculated using $Z \to ee$, $W \to e\nu$ and $J\psi \to ee$ in bins of p_T and η. The uncertainties are largest at low p_T and approach zero at higher p_T. The uncertainty on the energy scale and resolution of the electrons are calculated using $Z \to ee$ events by comparing the invariant mass distributions in different η-bins between data and MC [99].

Muons

The uncertainties on the muon reconstruction, isolation and track-to-vertex association are calculated using $Z \to \mu\mu$ and $J/\psi \to \mu\mu$ events. The J/ψ is used in the low p_T range ($p_T < 15$ GeV) while the Z events are used for the high p_T range ($p_T > 15$ GeV). The isolation scale

factors and uncertainties are only supported in the range $10 < p_T < 500$ GeV and so a scale factor of 1 ± 0.05 is used outside this range. The corrections and uncertainties for the muon momentum scale and resolution are calculated using the same samples as just mentioned, but with a p_T boundary of 20 GeV instead of 15 GeV [101].

τ-leptons

Since τ-leptons aren't directly used in this analysis, the impact of the hadronically decaying τ-lepton uncertainties are negligible on the analysis. The uncertainties used are related to the energy scale, and are only applied when calculating E_T^{miss}.

All uncertainties related to the leptons only have small effects on the analysis.

6.1.4 Jets

While there is a baseline set of parameters related to the jet uncertainties, this analysis uses a reduced set of 23 parameters based on the principal component analysis [146]. The uncertainties related to the JES and JER are the main sources of uncertainty for jets. These are described in Section 4.3.2. The JER uncertainties are obtained by comparing the simulation before and after the smearing has been applied, with the difference in the jet energey resolution per jet being the uncertainty [109]. JES uncertainties are a combination of several components, with the majority coming from data-driven techniques which account for assumptions made in the simulation, sample statistics and the propagated uncertainties on the energy scales of the other reconstructed objects [108]. The JES uncertainties are determined by either varying the parameters of the object selection or comparing the nominal simulated sample to an alternative sample that differs in one or more aspects. The other sources of jet uncertainties include the mismodelling of pileup in the simulation, jet response and the flavour composition of jets in simulation (light-quark, b-quark and gluon-initiated jets), high-p_T jets and the η-intercalibration procedure [107].

6.1.4.1 Flavour tagging

The SFs for the flavour tagging are applied per jet depending on the truth flavour and p_T of the jet, with the product of these SFs applied to the event weight. If a jet passes the tagging requirement, a tagging efficiency SF is applied, whereas if it doesn't pass, a mistagging SF is applied. These SFs are then adjusted by the uncertainties given by the CP groups to obtain new weights that are used as the uncertainties. There are approximately 40 systematic components per jet flavour (b, c, τ, light), but to have a more manageable amount, the flavour tagging CP group has combined several components to reduce the number of components to 3, 3, and 5 for the b, c and light components respectively at the 70% working point [116][147]. Two additional

uncertainties are related to the extrapolations. The first is the extrapolation from the lower p_T regions where the scale factors are determined, to the higher p_T regions that this thesis covers [148]. The second is the extrapolation from b-quark calibrations to the c-quark calibrations due to c-jet isolation being more difficult and c-jet events often having fewer events. The flavour tagging uncertainties tend to have the largest impact of the experimental uncertainties on the likelihood fit, and the main contribution to this is the modelling of the $t\bar{t}$ sample used to train the tagging algorithm.

6.1.5 E_T^{miss}

Since E_T^{miss} is calculated using the jets and the leptons, the uncertainties from these objects are also propagated into the uncertainty for the E_T^{miss}. This is the unceratinty due to the hard terms in the E_T^{miss} calculation. Additional to these are the uncertainties due to the soft terms of the E_T^{miss} calculation (defined in Section 4.4). There is the uncertainty on the scale of the track-based E_T^{miss} due to the tracks in the jets, as wel las the uncertainties on the track-based soft term for longitudinal resolution and scale, and transverse resolution [120].

A summary of all these experimental uncertainties is given in Table 6.1.

TABLE 6.1: A summary of the experimental uncertainties used in this analysis. Given is the source and a brief description of the uncertainty.

Source	**Description**
	Event
Luminosity	Uncertainty on the full run-2 luminosity
Pileup re-weighting	Uncertainty from re-weighting the average number of collisions per bunch crossing in simulation to data
	Triggers
Electron trigger efficiency	Uncertainty on the efficiency of the electron trigger
Muon trigger efficiency	Uncertainty on the efficiency of the muon trigger. Statistical and systematic
E_T^{miss} trigger efficiency	Uncertainty on the efficiency of the E_T^{miss} trigger. Statistical and kinematic & process dependencies
	Leptons
Electron efficiency	Uncertainty on the reconstruction, isolation and ID efficiencies for the electrons
Electron energy scale	Uncertainties on the electron energy scale and resolution
Muon efficiency	Uncertainties on the reconstruction, isolation and ID efficiencies for the muons. Separate contributions for statistical and systematic effects
Muon momentum resolution	Uncertainties on the muon momentum resolution in the ID and muon systems
Muon momentum scale	Uncertainties on the momentum scale and charge dependant momentum scale
Tau energy scale	Uncertainties on the energy scale for hadronically decaying τ-leptons
	Jets
Jet energy scale (JES)	Uncertainties on the jet energy scales from in-situ measurements from the detector, modelling, statistics and mixed terms
JES eta-intercalibration	Uncertainties on the jet energy scales from eta-intercalibrations from modelling, statistics and non-closure
JES flavour composition	Uncertainties on the jet energy scale due to the flavour composition of the VV and VH processes, as well as the different flavour responses
JES pileup	Uncertainties on the jet energy scale of the pileup
JES high energy	Uncertainties on the energy scale of punch-through jets and high-p_T jets
Jet energy resolution (JER)	Uncertainties on the jet energy resolution, with an additional component for the difference between MC and data
JVT efficiency	Uncertainty on the Jet Vertex Tagger efficiency
	Flavour Tagging
Flavour tagging efficiencies	Uncertainties on the efficiencies for b-tagging, c-tagging, light jet tagging and τ-tagging
Flavour tagging extrapolation	Uncertainty on the extrapolation to high-p_T jets
	Missing Transverse Energy
E_T^{miss} soft term	Uncertainties on the track-based soft term for longitudinal resolution and scale, and transverse resolution
E_T^{miss} jet tracks	Uncertainty on the scale of the track-based E_T^{miss} due to the tracks in the jets

6.2 Modelling uncertainties

These uncertainties can be split into normalisation or shape effects. The normalisation uncertainties only impact the total number of events in the region the uncertainty is applied to, and are calculated as ratios of yields. The normalisation uncertainties for the dominant backgrounds are left unconstrained in the final likelihood fit, while less dominant backgrounds have a constraint applied to their normalisation obtained from a comparison between the nominal and alternative samples. These uncertainties impact the cross-sections of the samples. Another form of normalisation uncertainty is the extrapolation uncertainties, which are used to account for any mismodelling that arises from categorising the events into different regions. The uncertainties are usually calculated as a double ratio of the yields between the two regions and the nominal and alternative samples, as such:

$$\frac{N_A^{nominal}}{N_B^{nominal}} / \frac{N_A^{alternative}}{N_B^{alternative}}. \tag{6.1}$$

Here, N is the yield for the nominal or alternative samples, when extrapolating from region A into region B. To decouple the extrapolation uncertainties from the pure normalisation uncertainties, both the nominal and alternative samples are normalised to the same cross-section so that they cancel in the ratio. Flavour ratio uncertainties are also calculated in the same manner as the extrapolation uncertainties. These take into account any possible mismodelling of the flavour composition of the samples. The flavour of an event depends on the true origin of the two tagged jets in the event. Each jet can be classified as originating from a bottom quark (b), a charm quark (c) or a light quark (l). The event flavour is the combination of these, giving six possible event flavours: bb, bc, bl, cc, cl and l. The four "heavy" flavours (bb, bc, bl, cc) are often grouped together to form the heavy flavour (hf) category. The flavour ratios are calculated using Equation 6.1, but where N_B is the number of events categorised as bb, while N_A is any of the other flavours within the heavy flavour category. The two light flavours (cl and l) have so few events that they aren't considered.

Shape effects take into account differences due to the shape of the distributions, and how events may migrate between different bins in a distribution or across region boundaries. The uncertainties that cover the shape effects are usually the ratio of a distribution of the alternative sample to the distribution of the nominal sample, depending on what the uncertainty needs to cover, for example the Matrix Element (ME) or Parton Shower (PS) and Underlying Event (UE) differences. A fit is done to the ratio and the nominal distribution is scaled by this fit to obtain the uncertainty histograms used in the likelihood fit. The distributions are normalised to the same area before finding the ratio so that only the shape effects are considered. The nominal distributions are weighted instead of using the alternative distribution directly since the alternative samples tend to have far fewer statistics. A simple sketch to illustrate this method is given in Figure 6.1.

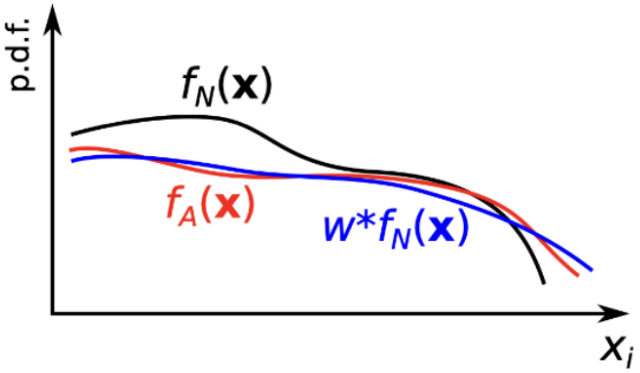

FIGURE 6.1: Sketch illustrating the reweighting of the nominal distribution ($f_N(\boldsymbol{x})$ in black) to the alternative distribution ($f_A(\boldsymbol{x})$ in red), resulting in the reweighted distribution ($w*f_N(\boldsymbol{x})$ in blue) [149]. The variable x_i is any one on the kinematic variables used to obtain the shape uncertainty.

A summary of the modelling uncertainties in this analysis are given in Tables 6.6 and 6.7

For the measurement presented in this thesis, the uncertainties most likely to be affected by the increase in the additional central jet p_T selection, and those deemed most impactful on the signal strengths in likelihood fit, were recalculated by the author. The other modelling uncertainties follow the same per-event uncertainties as derived in the previous round of the analysis [24]. Nevertheless, due to differences in the event selection, the total uncertainty used in the fit naturally adjusts to account for the specific event composition. The uncertainties calculated by the author are specifically referred to in the following sub-sections.

6.2.1 VH signal uncertainties

The VH signal samples can be split into the gluon-initiated and quark-initiated processes. For these processes, two systematic variations were used to obtain the uncertainties. These are:

- POWHEG+PYTHIA 8 Internal variations: There are six internal weight variations on the renormalisation μ_R and factorisation μ_F scales (each varied by a factor of 2 and/or 0.5, but not anti-correlated). The scales are varied since they are not fixed by theory, but are somewhat arbitrary, and have a direct role in the cross-section calculation. These μ_R and μ_F scale variations are used to calculate shape uncertainties in a similar way to how alternative MC generators are used. The multiple parton interaction cut-off parameter is varied between 1.91 GeV and 2.05 GeV with the nominal value set at 2.00 GeV. Variations on two sets of eigentunes for the AZNLO parton shower tune are also done to cover the primordial transverse momentum[1] and initial-state radiation cut-off.

[1]The primordial transverse momentum is the inherent transverse momentum that each parton within the proton possesses prior to any collisions.

- POWHEG+HERWIG 7: Uses the same POWHEG setup as with the nominal samples, however uses a different generator in HERWIG 7 [150] for the underlying event and parton shower so that these effects can be isolated.

Since the VH samples are the signal processes, the normalisations are set to their theoretical predictions. The uncertainties on the overall normalisation and $H \to b\bar{b}$ branching fraction follow the recommendations of the LHC Higgs working group [151]. They are 1.7%, 0.7% and 25% for the branching fraction, $barq \to VH$ cross-section and the $gg \to ZH$ cross-section respectively. QCD scale uncertainties on the overall VH cross-section are obtained by varying μ_R and μ_F in the NNLO(NLO) QCD + NLO EW fixed order $qq(gg)$ initiated calculations respectively. These are separate to the scale variations used for the shape uncertainties as described above, as these are varied by $\frac{1}{3}$ and 3.

As described in the STXS uncertainties references [152][153], migration uncertainties across the STXS p_T^V and n_{jet} bin boundaries are evaluated for the VH signal using the MC QCD scale variations of μ_R and μ_F. Uncertainties on the STXS bin cross-sections are evaluated using parton distribution function (PDF) variations of the PDF4LHC15_30 PDFs [154], and the PDF α_s variations. Acceptance uncertainties between the reconstruction level bins and STXS bins are calculated with parton shower and underlying event variations, using the four POWHEG+PYTHIA 8 AZNLO tune variations and POWHEG+HERWIG 7.

For the shape uncertainties of the signal samples, the distributions of m_{BB} and p_T^V are studied. For both of these there are the PS and UE variations, and the QCD scale variations. For the PS and UE variations, the nominal sample is compared to POWHEG+HERWIG 7. For m_{BB}, since the uncertainties were found to be roughly the same for the different n_{jets} and lepton channels, only the 1-lepton, 2-jet m_{BB} distribution is used for all the regions due to this region having the largest statistics. To account for the jet reconstruction effects, the m_{BB} calculated using the truth jets matched to the two tagged jets is used instead of the m_{BB} calculated from the reconstructed jets. For p_T^V, the shapes are calculated inclusively of p_T^V, but separated by the number of jets and whether the signal sample is $W \to l\nu$, $Z \to ll$ or $Z \to \nu\nu$. These six are combined as one nuisance parameter in the likelihood fit.

The shape uncertainties due to the scale variations are calculated in the same way for the m_{BB} and p_T^V variables. The uncertainties are taken as the largest deviation from the nominal distribution of the 6 different μ_R and μ_F combinations. They are calculated separately for n_{jets} and whether the signal sample is $W \to l\nu$, $Z \to ll$ or $Z \to \nu\nu$, and all of these are combined as one nuisance parameter. However, there is an additional split by production mechanism, i.e., qq or gg initiated production, which are kept as two separate nuisance parameters. So, the qq initiated uncertainty will have all three qq signal processes, while the gg will have the two $ggZH$ processes. An additional shape uncertainty on the p_T^V distribution due to NLO EW corrections is applied.

6.2.2 Z+jets uncertainties

The work in this section was performed by the author.

There are two systematic variations used for the Z+jets background uncertainties:

- Sherpa 2.2.1 Internal variations: Internal weight variations on the renormalisation μ_R and factorisation μ_F scales, as well as PDF variations, using MMHT2014nnlo68cl [155] and CT14nnlo [156].
- MadGraph 5_aMC@NLO+Pythia 8: Uses MadGraph 5 [157] with the NNPDF2.3LO PDF set and the ATLAS A14 tune for the ME, and Pythia 8 for the PS and UE. Used to assess in combination the matrix element and parton shower effects.

The Z+jets sample is one of the dominant background samples in this thesis, being the dominant in the 2-lepton and 0-lepton channel. The Z+jets samples are split by the true jet flavour of the two tagged jets, with the heavy flavour (Z+hf) sample being comprised of the bb, bc, bl and cc components, and the cl and l flavours are left individually separate. The Z+hf sample normalisation uncertainties are decorrelated by two and three jets and are unconstrained in the likelihood fit (allowed to freely float). Both Z+hf sample normalisations are also decorrelated in the 2-lepton, 75 $<p_T^V <$ 150 GeV region. This is because the yield in the low p_T^V region is close to three times the yield in the $p_T^V >$ 150 GeV regions combined, and the background composition is not as dominated by the Z+jets events. The Z+cl and Z+l sample normalisations have individually constrained uncertainties, calculated as the ratio of the nominal MC to the alternative MC (i.e. Sherpa to MadGraph), and are calculated inclusive of the number of jets.
There are three groups of extrapolation uncertainties for the Z+jets samples. The first is an extrapolation uncertainty from the 2-lepton channel to the 0-lepton channel, applied in the 0-lepton channel. Its is calculated inclusive of n_{jets} and p_T^V. This is done since the shape systematic uncertainties are derived in the 2-lepton channel and applied in the 0-lepton channel due to the higher purity of the Z+jets samples in the 2-lepton channel. The second group are the extrapolation uncertainties from the CRs to the SR, with separate uncertainties for the CRHigh and CRLow regions. Each one is calculated separately for two and three jets, as well as 0- and 2-lepton. However, in the fit, they are correlated by n_{jets} and lepton channel. Each CR to SR extrapolation uncertainty is then decorrelated in the fit by the 2-lepton 75 $<p_T^V <$ 150 GeV region. This gives a total of eight calculated CR to SR extrapolation uncertainties, acting as four nuisance parameters. The CR to SR extrapolation uncertainties are used to increase the degrees of freedom in the likelihood fit by affecting the yield migrations between the CRs and SR, which are decorrelated from the shape affect of the m_{BB} and p_T^V uncertainties. The

TABLE 6.2: A summary of the normalisation and acceptance uncertainties for the Z+jets background, showing the total contribution from the Sherpa 2.2.1 internal weight variations, and MADGRAPH 5_aMC@NLO+PYTHIA 8 (MG5Py8) separately. The values for the different jet p_T selections are shown as well, namely the 20 GeV and 30 GeV selections.

		20 GeV				**30 GeV**			
		0 Lep		**2 Lep**		**0 Lep**		**2 Lep**	
		2-jet	**3-jet**	**2-jet**	**$\geq$ 3-jet**	**2-jet**	**3-jet**	**2-jet**	**$\geq$ 3-jet**
Norm-Z+cl	Sherpa	24.16				23.32			
	MG5Py8	42.04				46.30			
	Total	48.49				51.84			
Norm-Z+l	Sherpa	28.67				23.63			
	MG5Py8	8.48				6.83			
	Total	29.90				24.60			
2/0 Lep	Sherpa	9.28		-		7.75		-	
	MG5Py8	0.15		-		1.40		-	
	Total	9.28		-		7.87		-	
CRLow/SR	Sherpa	2.82	1.82	7.33	5.00	2.65	1.76	5.80	5.28
	MG5Py8	15.73	5.79	3.81	2.59	12.43	12.10	2.90	2.07
	Total	15.98	6.07	8.26	5.63	12.71	12.23	6.49	5.67
CRHigh/SR	Sherpa	3.19	2.54	6.95	3.49	2.94	2.30	5.90	2.65
	MG5Py8	1.60	3.85	8.22	3.13	0.30	5.65	9.96	1.06
	Total	3.57	4.61	10.77	4.69	2.96	6.10	11.57	2.86
Z+bc/Z+bb	Sherpa	4.35		6.50	3.78	3.88		5.31	4.32
	MG5Py8	78.86		76.79	76.81	77.27		69.87	80.50
	Total	78.98		77.06	76.91	77.37		70.08	80.61
Z+bl/Z+bb	Sherpa	5.95		8.51	4.11	5.48		7.73	4.26
	MG5Py8	44.43		29.48	43.27	41.12		31.41	45.26
	Total	44.82		30.68	43.46	41.48		32.34	45.46
Z+cc/Z+bb	Sherpa	3.08		8.48	10.54	2.47		14.54	6.71
	MG5Py8	12.94		2.17	9.76	14.45		4.47	7.79
	Total	13.30		8.75	14.36	14.66		15.21	10.28

final group of extrapolation uncertainties are the flavour ratios within the Z+hf category. There is one uncertainty for each event flavour (bc, bl, cc) relative to the bb flavour, and calculated separately for the 0- and 2-lepton channels, with an additional separation by two and ≥ 3 jets in the 2-lepton case. These are correlated in the fit across lepton channel and n_{jets}, resulting in nine uncertainties, applied as three nuisance parameters.

A summary of the normalisation and extrapolation uncertainties is shown in Table 6.2. While the breakdown of the V+jets backgrounds by flavour were kept the same as in the previous round of the analysis, the use of the DL1r b-tagger, with its higher charm and light jet rejection, has reduced the number events that do not have two truth level b-jets. Due to the modelling in the MADGRAPH generator, this change in event flavour is more pronounced than in SHERPA, hence why the MADGRAPH contribution to the flavour extrapolation uncertainties is so large.

TABLE 6.3: The values of the parameters as defined in Equation 6.2 for both the p_T^V and m_{BB} shape uncertainties for the Z+jets background.

Shape uncertainty	Parameters a	b
p_T^V	-0.097	1.02
m_{BB}	0.000511	0.93

For the Z+jets shape uncertainties, instead of doing a two-point MC-MC comparison, a data driven technique is used. Due to the high purity of Z+jets events in the 2-lepton channel, the uncertainties are derived there and applied in both the 0- and 2-lepton channels. Using a data-driven approach in the 2-lepton channel produces a more accurate Z+jets background estimate, resulting in smaller uncertainties. In the 2-lepton channel, the W+jets and VV MC, as well as the top $e\mu$ data-driven estimate (described in Section 5.3.1.1), are subtracted from the data. This is done in a region inclusive of n_{jets}, p_T^V and SR+CRs to increase the statistics. This leaves a very pure Z+jets data-driven estimate. To ensure there is negligible signal, only the m_{BB} sidebands ($m_{BB} < 80$ GeV and $m_{BB} > 140$ GeV) are used in both the p_T^V and m_{BB} shape calculations. The extra-wide window is to ensure the VZ diboson processes are also removed from the data so as not to bias the VZ fits. The Z+jets nominal MC is scaled to the data-driven Z+jets sample, and a fit is done to the ratio of the two distributions. The p_T^V and m_{BB} functions obtained from this fit are used to re-weight the nominal distribution to create the shape variations that act as the upper and lower shape uncertainties. These functions are defined as following, with p_T^V and m_{BB} in GeV:

$$f(p_T^V) = a \times \log_{10}(p_T^V/50) + b$$
$$f(m_{BB}) = \begin{cases} a \times m_{BB} + b, & \text{if } m_{BB} \leq 300 \text{ GeV} \\ a \times 300 + b, & \text{if } m_{BB} > 300 \text{ GeV}. \end{cases} \quad (6.2)$$

The p_T^V and m_{BB} distributions, as well as the resultant functions, are shown in Figure 6.2. Only the results of the 30 GeV jet p_T selections are shown since there were negligible differences between the results of the fit for the 20 GeV and 30 GeV cases. The values of the parameters a and b for both the p_T^V and m_{BB} shape uncertainties are given in Table 6.3. These two shape uncertainties are decorrelated by the 75 $< p_T^V <$ 150 GeV and $p_T^V >$ 150 GeV regions in the likelihood fit.

Due to the difference in the tagged jet corrections applied between the 0- and 2-lepton channels (refer to Section 4.3.3.2), the values for the m_{BB} distribution are obtained using the GSC jets (see Section 4.3.2) instead of the b-jet-corrected jets.

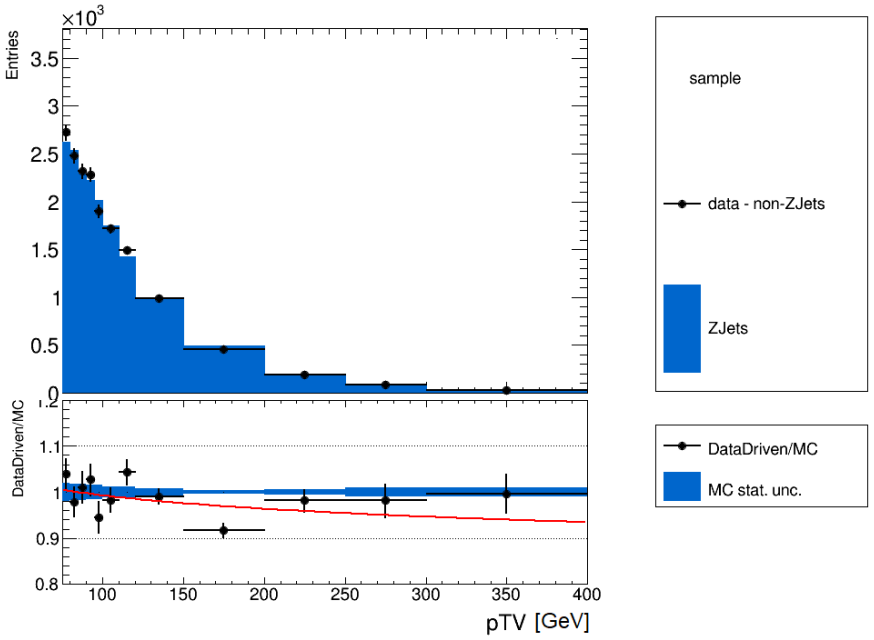

(a)

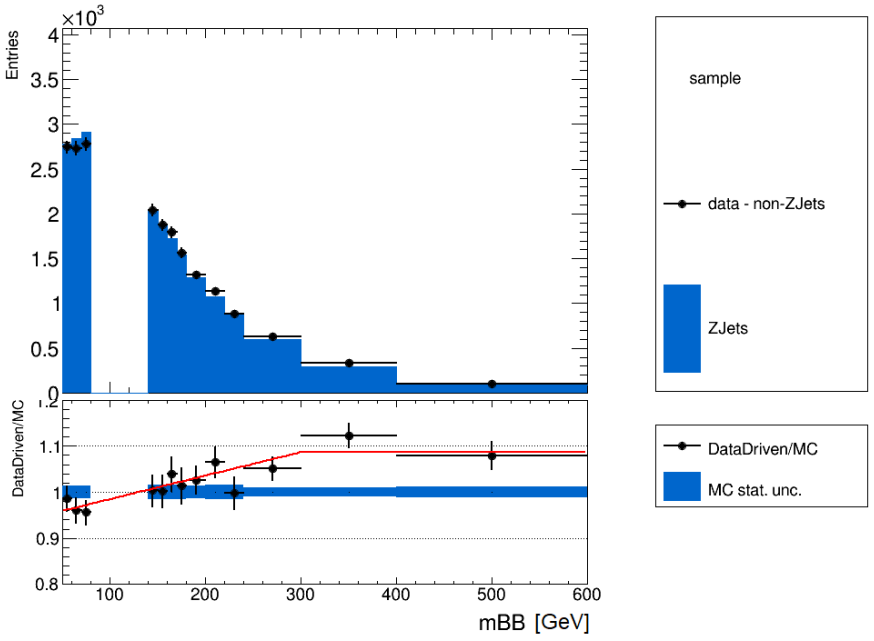

(b)

FIGURE 6.2: Histograms of the data-driven estimate of the Z+jets background (black points) and the Z+jets MC sample (blue) normalised to the data-driven estimate, in the 2-lepton channel and inclusive of the number of jets and p_T^V . The red line is the result of a fit to the ratio of the data-driven estimate to the Z+jets MC background. Figure (a) shows the p_T^V shape uncertainty and figure (b) shows the m_{BB} shape uncertainty, calculated using the invariant mass of the jets before any b-jet corrections are applied. The gap in figure (b) of 80 $< m_{BB} <$ 140 GeV is to remove the data that lies within the peak of the diboson and signal distributions.

6.2.3 W+jets uncertainties

There are two systematic variations used for the uncertainties of the W+jets process:

- Sherpa 2.2.1 Internal variations: Internal weight variations on the renormalisation μ_R and factorisation μ_F scales, as well as PDF variations, using MMHT2014nnlo68cl and CT14nnlo.
- MadGraph 5_aMC@NLO+Pythia 8: Uses MadGraph 5 with the NNPDF2.3LO PDF set and the ATLAS A14 tune for the ME, and Pythia 8 for the PS and UE. Used to assess in combination the matrix element and parton shower effects.

The W+jets sample is one of the dominant background samples, so there are some unconstrained normalisations in the likelihood fit. Similar to the Z+jets events, the W+jets events are split by jet flavour. The normalisations of the W+hf sample, separated by two and three jets, are left to freely float, while the W+cl and W+l normalisations have individually fixed uncertainties that are inclusive of the number of jets. There is an additional extrapolation uncertainty from the 1-lepton to the 0-lepton channel, since the 1-lepton channel provides the best constraint on the W+hf events.
The acceptance uncertainties cover a CR to SR extrapolation, calculated separately for the CRHigh and CRLow, two and three jets, as well as 0- and 1-lepton. Unlike the Z+jets sample however, these are all correlated in the fit, resulting in the eight CR to SR extrapolation uncertainties acting as one nuisance parameter. These are used to increase the degrees of freedom in the likelihood fit by affecting the yield migrations between the CRs and SR, which is decorrelated from the shape affect from CARL (see Section 6.2.3.1). The other acceptance uncertainties are the flavour ratios within the W+hf category. There is one uncertainty for each flavour (bc, bl, cc) relative to bb, and calculate separately for the 0- and 1-lepton channel. In the fit, they are correlated by channel, resulting in the 6 uncertainties being applied as three nuisance parameters.
In terms of the shapes, there are essentially two variables used. The first is the p_T^V shape, obtained separately for two and three jets events, as well as per flavour in the W+hf category. The W+cl and W+l flavours are negligible and therefore not considered. A fit to the ratio between the nominal sample and MadGraph is used. Due to low statistics in the 0-lepton channel, only the 1-lepton p_T^V shapes are used in the likelihood fit, being applied to both 0- and 1-lepton. It is correlated between the flavours and decorrelated between two and three jets, providing two nuisance parameters. The second shape uncertainty is the CARL uncertainty, described in Section 6.2.3.1. For the W+jets samples, CARL is trained separately for 0- and 1-lepton channels, and by event flavour, with the number of jets input as an auxiliary variable. Only the three dominant flavours in the W+hf category are used, namely the bb, bc and cc events. CARL

is trained to separate the nominal MC from MadGraph, with the weight used to create the uncertainty calculated directly from the output. The CARL uncertainty is correlated by across 0- and 1-lepton, as well as the event flavours, providing one nuisance parameter in the final fit. A p_T^V shape used in addition to the CARL shape is to improve the coverage of the migrations that may occur between the p_T^V regions.

6.2.3.1 Calibrated likelihood ratio estimator (CARL)

The typical way to model the impact of shape effects due to different ME calculations or PS modelling is to compare the distribution of the nominal sample to the distribution of an alternative sample that is different in either the ME or PS. Unfortunately, the alternative samples are often produced with far less events compared to the nominal samples, resulting in larger statistical uncertainties and fluctuations per bin. This lack of statistical power can cause issues when the final likelihood fit tries to interpolate between the nominal and alternative distributions. This can be overcome by reweighting the nominal distribution to look like the alternative distribution and using that as the shape variation in the fit. This greatly improves the statistical power of the shape variation, despite still having some artifacts from the fluctuations in the original alternative sample. The reweighting usually takes the form of a ratio of the distributions of one kinematic variable that has a large impact on the results of the study. This ratio is then used to reweight the nominal sample, on an event-by-event basis, so that the shape matches the alternative sample. A problem with this method however, is that the reweighting only really works for the variable (dimension) in which the ratio was calculated, and it does not necessarily pass the closure test when studying its effects on other variables (dimensions). This could be repeated for multiple variables, but then the problem of one reweighting undoing the effects of another becomes possible. This method thus does not consider the correlations between the different variables in this simple reduction from p-dimensions to one dimension.
A way around this problem is to use a multivariate technique to estimate the p-dimensional ratio as a 1-dimensional ratio in a less lossy way. This will take the p number of variables as input to the algorithm, which will be trained to separate the nominal sample from the alternative sample, and output a 1-dimensional distribution from which the rewighting value can be directly obtained. The name of this technique is the Calibrated Likelihood Ratio Estimator (CARL)[158] and uses a Deep Neural Network (DNN,) based on pyTorch[159]. The output of the DNN estimates the probability that the event is from the alternative sample, or mathematically:

$$\hat{s}(\boldsymbol{x}) \xrightarrow{N\to\infty} \mathcal{P}(A|\boldsymbol{x}), \tag{6.3}$$

where $\hat{s}$ is the output of the DNN, N is the number of events used for training and $\mathcal{P}(A|\boldsymbol{x})$ is the probability that the event is from the alternative sample given the set of input variables $\boldsymbol{x}$. The probabilities from which the MC events are sampled would then be $\mathcal{P}(\boldsymbol{x}|N)$ for the nominal

and $\mathcal{P}(\boldsymbol{x}|A)$ for the alternative. The ratio of these probabilities can be written as, and using Bayes theorem:

$$r(\boldsymbol{x}) = \frac{\mathcal{P}(\boldsymbol{x}|N)}{\mathcal{P}(\boldsymbol{x}|A)} = \frac{\mathcal{P}(N|\boldsymbol{x})\mathcal{P}(A)}{\mathcal{P}(A|\boldsymbol{x})\mathcal{P}(N)}. \tag{6.4}$$

Given that the nominal and alternative samples are normalised to the same value, and that $\mathcal{P}(N|\boldsymbol{x}) = 1 - \mathcal{P}(A|\boldsymbol{x})$, Equation 6.4 reduces to:

$$r(\boldsymbol{x}) = \frac{1 - \mathcal{P}(A|\boldsymbol{x})}{\mathcal{P}(A|\boldsymbol{x})}. \tag{6.5}$$

Now, subbing Equation 6.3 into Equation 6.5, the weight applied to the nominal sample per event can be obtained from the ratio estimate as:

$$w = \frac{1}{\hat{r}(\boldsymbol{x})} = \frac{\hat{s}(\boldsymbol{x})}{1 - \hat{s}(\boldsymbol{x})}. \tag{6.6}$$

As can be seen, the reweighting can be obtained directly from the output of the neural network. An example illustration of the this p-dimensional reduction process is shown in Figure 6.3.

The variables used as input for the training of CARL are shown in Table 6.4, with most of the variables defined in Section 5.2.3. The new variables introduced for CARL are the sum of the transverse momenta of the jets additional to the tagged jets ($\Sigma p_T^{j_{\text{add.}}}$), and the minimum distance between the additional jets and the tagged jets ($\min[\Delta R(j_{\text{add.}}, (b_1, b_2))]$). The auxiliary variables are those that aren't directly trained on, but are used to improve generalisation and feature learning. The variables Flavour b_1 and Flavour b_2 are the truth flavours of the two tagged jets, providing individual information of the jets.

The reweighting algorithm CARL replaces the previous algorithm known as BDTr (Boosted Decision Tree reweighting), described in [24]. CARL, being a DNN, can model more intricate patterns with less loss of information than the BDTr. Refer to Section 5.2.2 for more information on the differences between a BDT and a DNN. Additionally, the weight can be obtained directly from the output of CARL, whereas the BDTr required an additional fit to the ratio of the BDT output distributions for the nominal and alternative samples. This additional fit is represented by $r(x)$ in Figure 6.3. To improve the effects due to the different p_T^V bins, the BDTr also required the inputs for its training to be reweighted by the p_T^V distribution first. Going from the BDTr to CARL has thus dropped the number of steps required to obtain the reweighting value from three to one, while reducing the lossiness of the model dimensional reduction.

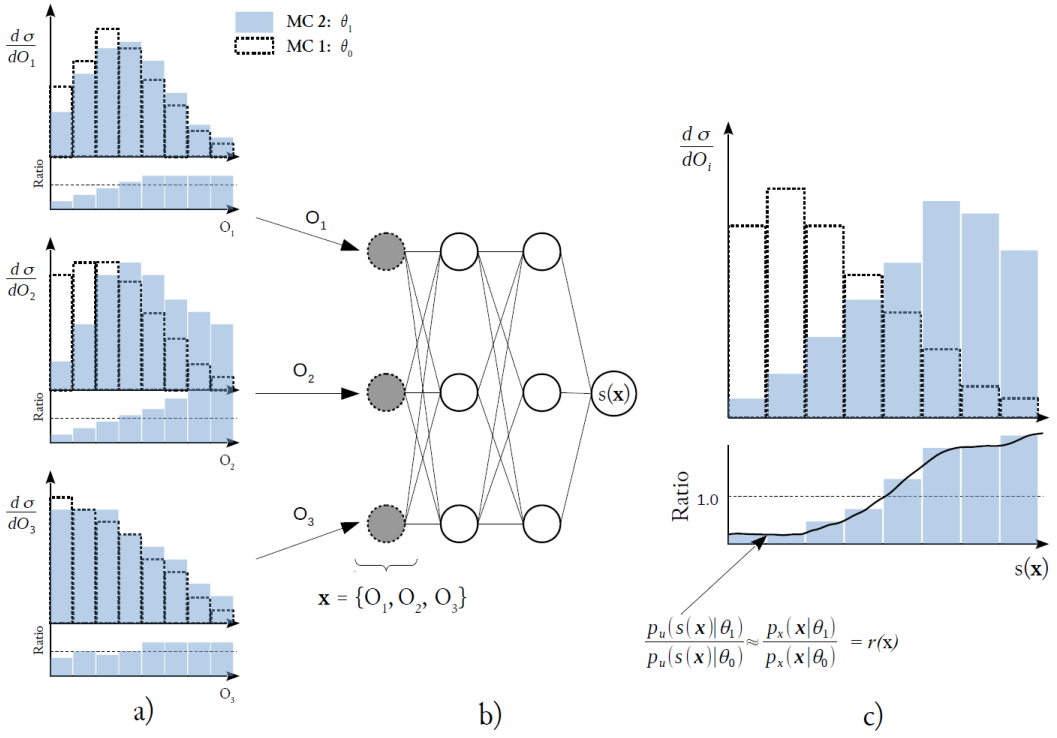

FIGURE 6.3: Illustration of the reduction of a 3-dimensional ratio to a 1-dimensional ratio using a DNN [149]. The O_i are different kinematic variables for the two MC samples, the alternative sample θ_1 and the nominal sample θ_0. The three distributions are shown in (a), with them being input to the DNN in (b) that is trained to classify ($s(x)$) the two samples. The $s(x)$ distribution for both samples is shown in (c) with the density ratio $r(x)$ given by the curved line in the ratio plot.

TABLE 6.4: Summary of the variables used to train the CARL DNN used to obtain shape uncertainties for the W+jets and $t\bar{t}$ samples in the 0- and 1-lepton channels. The variables are defined in Section 6.2.3.1.

Variable	**0-Lepton**	**1-Lepton**
m_{bb}	✓	✓
$\Delta R(b_1, b_2)$	✓	✓
$p_T^{b_1}$	✓	✓
$p_T^{b_2}$	✓	✓
p_T^V		✓
$\Delta\phi(V, H)$	✓	✓
$\lvert\Delta\eta(b_1, b_2)\rvert$	✓	
M_{eff}	✓	
E_T^{miss}	$\equiv p_T^V$	✓
$\min[\Delta\phi(\ell, b_i)]$		✓
m_T^W		✓
$\Delta Y(W, H)$		✓
m_{top}		✓
binned DL1r(b_1)	✓	✓
binned DL1r(b_2)	✓	✓
Only in 3-jet events		
m_{bbj}	✓	✓
$\min[\Delta R(j_{\text{add.}}, (b_1, b_2))]$	✓	✓
$\Sigma p_T^{j_{\text{add.}}}$	✓	✓
Auxiliary variables		
nJets	✓	✓
Flavour b_1	✓	✓
Flavour b_2	✓	✓

6.2.4 Top pair production uncertainties

Due to the topologies of the different lepton channels, the 0- and 1-lepton channels have a different prescription than the 2-lepton channel for $t\bar{t}$ processes. For the 2-lepton channel refer to Section 6.2.7.1.
There are three systematic variations used for the uncertainty estimations of the $t\bar{t}$ samples in the 0- and 1-lepton channels:

- Powheg+Pythia 8 - Low/High radiation: Maximum or minimum internal weight variations on the renormalisation and factorisation scales. These are for the non-all-hadronic and dilepton samples. The non-all-hadronic samples have a filter applied that require at least one leptonically decaying W boson.
- Powheg+Herwig 7: Same Powheg setup but using Herwig 7 for PS and UE with the CTEQ6L1 PDF set with H7UE tune [150]. Used to assess the parton shower effects.
- MadGraph 5_aMC@NLO+Pythia 8: Same Pythia 8 setup but using MadGraph 5 with the CT10f4 PDF set for the ME. Used to assess the matrix element effects.

The $t\bar{t}$ background is one of the dominant background processes, so the normalisations are left to freely float, and are separated between the 2- and 3-jet regions. Due to it being the dominant background in the 1-lepton channel, the uncertainties are derived there and applied in both the 0- and 1-lepton channels. Validation studies performed for the previous round of this analysis [24] show that this transfer is valid. The uncertainty on this extrapolation is treated as an acceptance uncertainty between the 0- and 1-lepton channels, and inclusive of the number of jets.
The flavour composition uncertainties for the $t\bar{t}$ sample are based on the dominant flavours. Due to the large branching fraction for a top quark decaying to a bottom quark (0.957 ± 0.034 [11]), only the bb and bc components are non-negligible, so the other components (bl, cc, cl, ll) are classified together as "other". Therefore, there are two flavour composition uncertainties for the bc/bb acceptance and the "other"$/bb$ acceptance. Each of the flavour acceptances also have one uncertainty for the ME variation and one for the PS variation, giving four uncertainties in total. They are calculated separately for 0- and 1-lepton channels but correlated in the fit.
For the shape uncertainties, there is a p_T^V shape derived separately for the 0- and 1-lepton channels, as well as the 2- and 3-jet regions. For the 0-lepton channel, the $E_T^{miss} > 150$ GeV distribution is used, while in 1-lepton, the $p_T^V > 75$ GeV distribution is used. A fit is done to the ratio of the nominal sample to MadGraph 5_aMC@NLO+Pythia 8, since this provides the largest variation. Unlike for the CARL shapes for the W+jets sample (Section 6.2.3), there are separate CARL shapes for the ME and PS contributions in the $t\bar{t}$ samples since neither dominate over the other. Also, the training is done separately for the bb and "other" flavour

categories, as well as 0- and 1-lepton. There is no split by number of jets since these are entered as auxiliary variables. The ME contribution is decorrelated by two and three jets, but correlated across lepton channels and flavours, while the PS contribution is correlated in the number of jets, but decorrelated in lepton channel. There is an additional decorrelation in the 1-lepton channel with a specific PS contribution for the 150 $< p_T^V <$ 250 GeV, 3-jet region. There are no CR to SR extrapolation uncertainties for the $t\bar{t}$ sample since the CARL shape uncertainty covers the CR to SR migrations.

6.2.5 Single-top production uncertainties

For the 2-lepton channel, see Section 6.2.7.1.
There are four systematic variations used for the uncertainty estimations of the single-top samples:

- Powheg+Pythia 8 - Low/High radiation: Maximum or minimum internal weight variations on the renormalisation and factorisation scale.
- Powheg+Pythia 8 - Wt channel DR: The Diagram Removal (DR) scheme is used for matrix element calculation as opposed to the Diagram Subtraction (DS) used in the nominal sample.
- Powheg+Herwig ++: Same Powheg setup but using Herwig++[160] for PS and UE with the CTEQ6L1 PDF set with UE-EE-5 tune. Used to assess the parton shower effects.
- MadGraph 5_aMC@NLO+Herwig++: Same Herwig++ setup but using MadGraph 5 with the CT10f4 PDF set for the ME. Used to assess the matrix element effects.

Since the single-top samples are a minor background in this analysis, the normalisation uncertainties are not left freely floating, but calculated by comparisons between nominal samples and alternative samples. There are three sub-samples, being s-channel, t-channel and Wt-channel. The s-channel sample has a negligible contribution and so it only has a normalisation uncertainty. The t- and Wt-channel samples have additional p_T^V and m_{BB} shape uncertainties correlated across all regions. Since normalisation uncertainties of the single-top processes are not split by the number of jets, acceptance uncertainties are used to add extra freedom within each jet region. There are acceptance uncertainties for the t-channel process, as well as acceptances decorrelated by jet flavour (bb or other) for the Wt-channel, since due to the topology of the Wt process, a significant difference was found between the $Wt \to b\bar{b}$ and $Wt \to b(c/l)$ events. Due to this, the Wt sample shape uncertainties are also calculated split by the these flavours, however correlated as just one nuisance parameter in the likelihood fit.

6.2.6 Diboson uncertainties

There are three systematic variations used for the uncertainty estimations of the diboson samples:

- Sherpa 2.2.1 μ_R/μ_F Scales: Internal weight variations on the renormalisation and factorisation scales.
- Powheg+Pythia 8: CT10 NLO PDF set used for the hard-scatter and the CTEQ6L1 PDF with AZNLO tune is used for the parton shower.
- Powheg+Herwig ++: Same Powheg setup but using Herwig++ for PS and UE with the CTEQ6L1 PDF set with UE-EE-5 tune.

Since the diboson samples are a minor background in this analysis, the normalisation uncertainties are constrained in the likelihood fit and are calculated by comparing the nominal sample to the Sherpa scale variations and Powheg. There are three sub-samples, being WW, WZ and ZZ. The WW sample contributes less than 0.1% and so it only has a normalisation uncertainty. The WZ and ZZ samples have p_T^V and m_{BB} shape uncertainties for ME and UE variations across all regions. Each shape uncertainty is calculated separately for 2- and 3-jet regions, as well as if the process is WZ or ZZ in 0-lepton, or ZZ in 2-lepton. However, they are correlated as one nuisance parameter in the likelihood fit. There are acceptance uncertainties for the 2- and 3-jet categories as well as between the 0- and 1-lepton, and 0- and 2-lepton channels.

6.2.7 Data-driven background uncertainties

The work in this section was performed by the author.

6.2.7.1 Two lepton data-driven top estimate

A description of the $e\mu$ control region is given in Section 5.3.1.1, but in summary, due to the topology of the 2-lepton channel, it is possible to use the data from a top $e\mu$ control region instead of using the top MC samples to represent the top backgrounds.
The flavour symmetry of the $t\bar{t}$ and Wt samples implies that the top-$e\mu$ control region and the signal regions should have very similar shapes in their distributions. To correct for any differences in normalisation, a scale factor α is derived as follows:

$$N_{data}^{SR} = \frac{N_{data}^{CR}}{N_{MC}^{CR}} \times N_{MC}^{SR} = \frac{N_{MC}^{SR}}{N_{MC}^{CR}} \times N_{data}^{CR} = \alpha \times N_{data}^{CR} \tag{6.7}$$

Here, N is the total number of $t\bar{t}$ and single-top events, SR and CR refer to the signal region and $e\mu$ control region respectively. The extrapolation factor α can be estimated using the top MC simulations since the same kinematic selections are applied in the SR and $e\mu$-CR, and due to the flavour symmetry of the $t\bar{t}$ and Wt processes. The ratio of the yield of the simulated top events in the $e\mu$-CR and the simulated top events in the signal selection was found to be one, with a statistical uncertainty of less than 0.01 coming from the simulated samples. This uncertainty is used as the extrapolation uncertainty since no other uncertainties were found to create a bias larger than this. This method eliminates most of the experimental and theoretical uncertainties leaving the data statistics in the $e\mu$-CR to be the dominant uncertainty for the data-driven top background estimate. Since there is no bias on the shapes or normalisations between the nominal regions and the $e\mu$-CR, the data in the $e\mu$-CR can be used directly in the nominal regions.

6.2.7.2 Multijet background estimate

Since the multijet (MJ) backgrounds are data-driven, as described in Section 5.3.1.2, there are no alternative samples used in the uncertainty calculations, rather slight variations on how the template is obtained. For the shape uncertainties, there are two uncertainties obtained. The first one applies the top and W+jets background normalisations obtained from the MJ fit to the top and W+jets samples in the MJ-CR before subtracting the MC from the data, providing a new MJ template. The second shape uncertainty applies additional isolation requirements on the leptons, which reduces the extrapolation uncertainty from the MJ-CRs to the analysis regions. For the electrons, the additional energy in the calorimeters in a cone of $R = 0.2$ around the electron must be less than 12 GeV, while for the muons, the additional momentum due to tracks in a cone of $R = 0.2$ around the muon must be less than 2.9 GeV. These extra isolation requirements are applied in the MJ control region before subtracting the MC from the data. The distributions used are the same as those that are input to the maximum likelihood fit, i.e., MVA for the signal regions and p_T^V for the low and high CRs. These shape variations are normalised to the nominal MJ estimate so that a shape-only systematic uncertainty is obtained. The differences between the shape variations and the nominal shape are used as the two shape uncertainties in the likelihood fit. A comparison of the nominal MVA MJ distribution to the two MJ shape uncertainties are shown in Figure 6.4 for the electron channel and Figure 6.5 for the muon channel. The variations due to scaling the W+jets and top backgrounds first (blue histogram) are very small, while the variations due to the tighter isolation requirements (red histogram) are quite erratic since a lot of events are removed.

For the normalisation uncertainties, there are multiple sources. Two of the sources require new MJ fits to be carried out, while the other three are the statistical uncertainties from the nominal and shape variation distributions. For the new fits, the first one uses the ϕ distance between

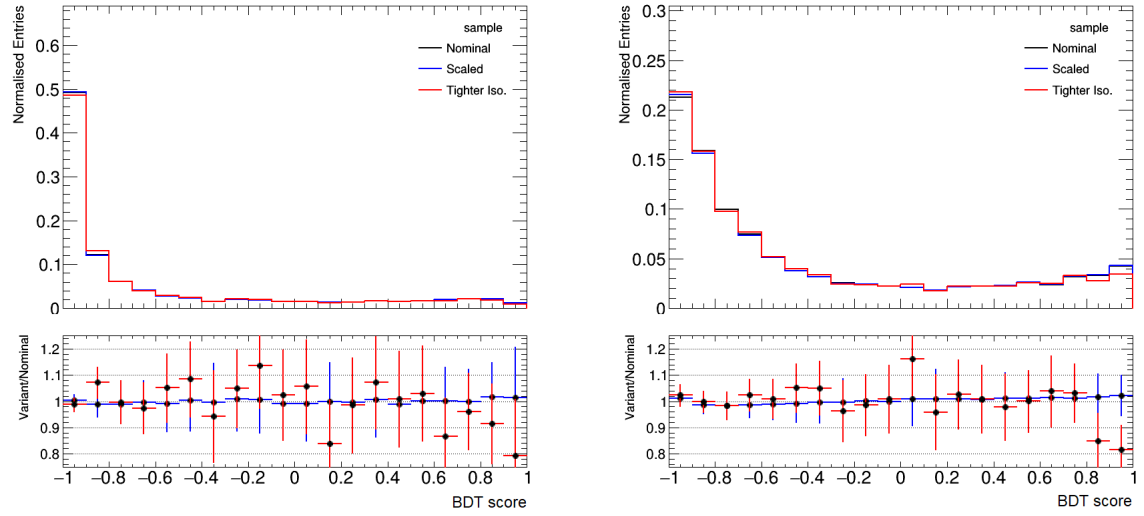

(a)

(b)

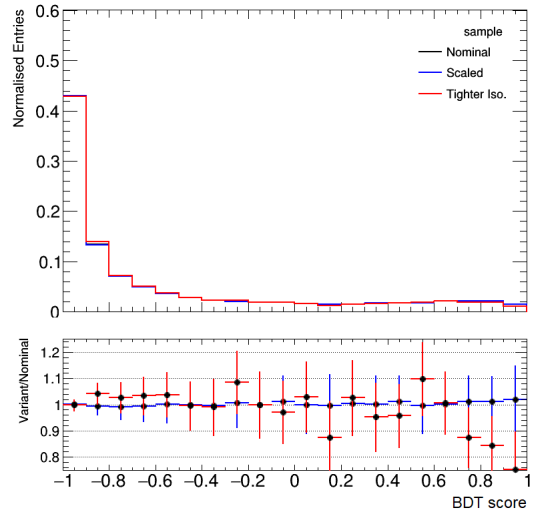

(c)

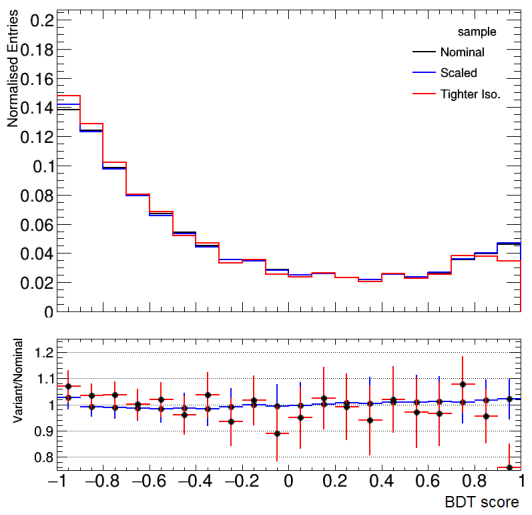

(d)

FIGURE 6.4: A comparison of the nominal MVA electron MJ distribution (black), the shape uncertainty obtained by applying the background normalisations first (blue), and the shape uncertainty obtained by applying tighter isolation requirements on the leptons (red). All histograms are normalised to the same area. Figures (a) and (b) are the 2- and 3-jet regions for the jet p_T selections of 20 GeV, while (c) and (d) are the 2- and 3-jet regions for the jet p_T selections of 30 GeV. The bottom panels show the ratio of the variations to the nominal.

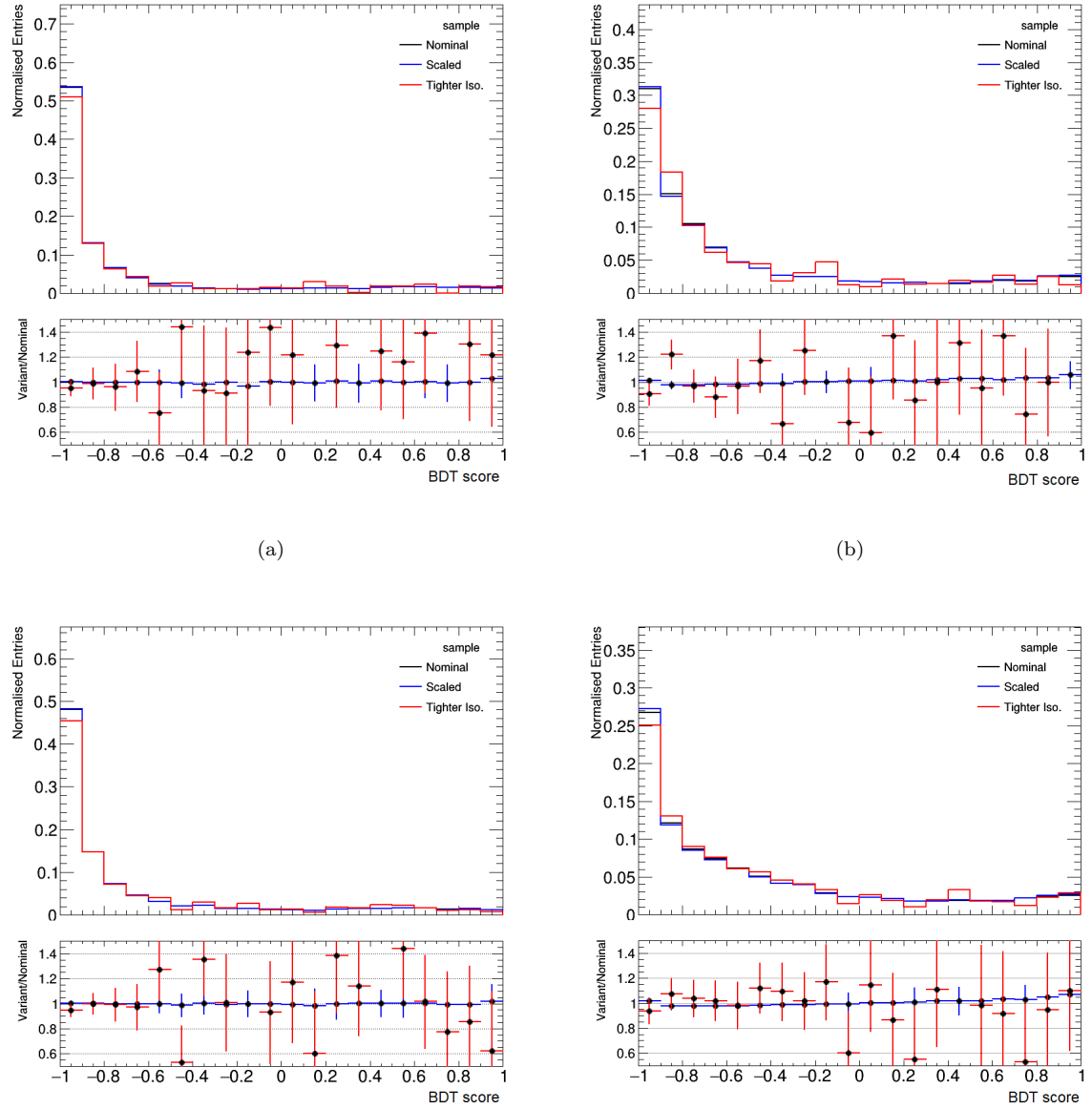

FIGURE 6.5: A comparison of the nominal MVA muon MJ distribution (black), the shape uncertainty obtained by applying the background normalisations first (blue), and the shape uncertainty obtained by applying tighter isolation requirements on the leptons (red). All histograms are normalised to the same area. Figures (a) and (b) are the 2- and 3-jet regions for the jet p_T selections of 20 GeV, while (c) and (d) are the 2- and 3-jet regions for the jet p_T selections of 30 GeV. The bottom panels show the ratio of the variations to the nominal.

TABLE 6.5: The final normalisation uncertainties for the multijet background, combining the statistical uncertainty from the nominal MJ and the two shape uncertainties, as well as the two yield differences obtained from the normalisation MJ fits. The values for the different jet p_T selections are shown as well, namely the 20 GeV and 30 GeV selections.

Region	20 GeV	30 GeV
2-jet, e	$^{+75\%}_{-63\%}$	$^{+49\%}_{-71\%}$
3-jet, e	$^{+43\%}_{-100\%}$	$^{+66\%}_{-95\%}$
2-jet, μ	$^{+3\%}_{-100\%}$	$^{+2\%}_{-97\%}$
3-jet, μ	$^{+1\%}_{-100\%}$	$^{+2\%}_{-100\%}$

the lepton and E_T^{miss} ($\Delta\phi(l,E_T^{miss})$) instead of the m_T^W distribution to perform the MJ fit. The $\Delta\phi(l,E_T^{miss})$ distribution has a decent separation between the MJ background and the other backgrounds, but not as good as the m_T^W distribution. The second normalisation calculation only applies to the electron channel as it removes the $E_T^{miss} > 30$ GeV requirement and performs the MJ fit on the m_T^W distribution including the $E_T^{miss} < 30$ GeV events. The difference between the yields of the MJ backgrounds obtained from these two additional MJ fits and the yields of the MJ backgrounds obtained from the nominal MJ fits are used as the normalisation uncertainties. These are then combined in quadrature with the statistical uncertainty of the nominal MJ background, as well as the statistical uncertainty of the MJ backgrounds obtained from the two shape uncertainties. The final normalisation uncertainties for the MJ backgrounds, combining all five components, are shown in Table 6.5. All the MJ regions have large lower bounds on the normalisation, while only the electron channels have large upper bounds.

TABLE 6.6: A summary of the modelling uncertainties for VH and V+jets samples used in this analysis. Given is the source and a brief description of the uncertainty.

Source	**Description**
	VH
Normalisations	Set to theoretical predictions, decorrelated by $qq \to VH$ and $gg \to ZH$. Additional uncertainty on the $H \to b\bar{b}$ branching ratio
Shapes	Shape uncertainties for the p_T^V and m_{BB} distributions, correlated by the number of jets and vector boson decay. Each has a QCD scale variation decorrelated by $qq \to VH$ and $gg \to ZH$, and an UE & PS variation. Additionally, p_T^V has a PDF variation decorrelated by $qq \to VH$ and $gg \to ZH$, and an NLO electro-weak variation.
	VH **STXS**
Normalisations	Uncertainties on the cross-sections in the STXS bins due to PDF and α_S variations
Acceptances	Migration uncertainties calculated between the STXS bins for each p_T^V and additional-jets bins, all decorrelated by $qq \to VH$ and $gg \to ZH$. Acceptances between the STXS bins and reconstruction level bins, using PYTHIA AZNLO tune variations and HERWIG
	Z**+jets**
Normalisations	Freely floating Z+hf normalisations decorrelated by 2- and 3-jet, and decorrelated in 2-lepton 75 GeV$<p_T^V<$150 GeV. Uncertainties on the normalisations for Z+cl and Z+l calculated via two-point MC-MC comparisons
Acceptances	Acceptance uncertainty for extrapolation from 2- to 0-lepton. CRHigh and CRLow to SR acceptances correlated by 2- and 3-jet and 0- and 2-lepton, but decorrelated in 2-lepton 75 GeV$<p_T^V<$150 GeV
Flavour composition	Flavour ratios for each bc, bl and cc comparison to bb, all correlated by 0- and 2-lepton with additional correlation between 2- and $\geq$ 3-jet in 2-lepton
Shapes	Data driven shape uncertainties for the p_T^V and m_{BB} distributions, decorrelated in 2-lepton 75 GeV$<p_T^V<$150 GeV
	W**+jets**
Normalisations	Freely floating W+hf normalisations decorrelated by 2- and 3-jet. Uncertainties on the normalisations for W+cl and W+l calculated via two-point MC-MC comparisons
Acceptances	Acceptance uncertainty for extrapolation from one to 0-lepton. CR to SR acceptances correlated by 2- and 3-jet and 0- and 1-lepton
Flavour composition	Flavour ratios for each bc, bl and cc comparison to bb, all correlated by 0- and 1-lepton
Shapes	Shape uncertainty on the p_T^V distribution, correlated between flavours and decorrelated by 2- and 3-jet. BDTr shape uncertainty correlated by 2- and 3-jet and 0- and 1-lepton

TABLE 6.7: A summary of the modelling uncertainties for top, diboson and data-driven samples used in this analysis. Given is the source and a brief description of the uncertainty.

Source	**Description**
	Top Pair (0+1 Lepton)
Normalisations	Freely floating and decorrelated by 2- and 3-jet
Acceptances	Acceptance uncertainty from 1-lepton to 0-lepton, correlated by 2- and 3-jet
Flavour Composition	Flavour acceptances for bc to bb processes, and "other" to bb processes, with separate uncertainties for ME and PS
Shapes	Shape uncertainties for p_T^V , decorrelated by 2- and 3-jet. BDTr shapes for the ME decorrelated by 2- and 3-jet, correlated by 0- and 1-lepton. BDTr shapes for the PS correlated by 2- and 3-jet, decorrelated by 0-lepton, 1-lepton with three jets and 150 GeV$<p_T^V<$250 Gev, and the rest of 1-lepton
	Single-Top (0+1 Lepton)
Normalisations	Uncertainties on the normalisations for each process calculated via two-point MC-MC comparisons
Shapes	Only for t- and Wt-processes. Each process has its own shape, as well as one each for p_T^V and m_{BB}
Acceptances	Flavour acceptances for the Wt-process split by bb and "other". Single acceptance for the t-process. All correlated by 2- and 3-jet
	Diboson
Normalisations	Uncertainties on the normalisations for each process (WW, WZ, ZZ) calculated via two-point MC-MC comparisons
Shapes	Only for WZ and ZZ processes. Two each for p_T^V and m_{BB} , split by by ME and UE. Correlated by 2- and 3-jet events, WZ and ZZ processes
Acceptances	Only for WZ and ZZ processes. Acceptance uncertainties between 2- and 3-jet, between 0- and 1-lepton, and between 0- and 2-lepton
	Data-Driven Backgrounds
Top $e\mu$ normalisations	Uncertainty on data statistics in $e\mu$-CR and extrapolation from $e\mu$-CR to SR
Multijet normalisations	Uncertainties on the normalisations obtained from using a different variable for the template fit, and including low E_T^{miss} events in e channel, These are added in quadrature with the nominal and shape statistical uncertainties. Decorrelated by lepton production and correlated by the number of jets
Multijet shapes	Shape uncertainties due to a reduced isolation region, applying scale factors before the template fit

Chapter 7

Measurement of the $VH, H \to b\bar{b}$ process within kinematic regions

This chapter presents a measurement of the $VH, H \to b\bar{b}$ process within the STXS framework. In particular, the measurement is an expansion on the number of STXS regions (see Section 5.5) measured in the 2021 paper by the ATLAS collaboration [24]. Additionally, a study into the effects of increasing the p_T selections of the central jets additional to the b-tagged jets is performed. The results of these studies are presented in terms of the STXS signal strength measurements.

The study in this thesis is part of the new ATLAS analysis which combines the $VH, H \to b\bar{b}$ resolved with the boosted $VH, H \to b\bar{b}$ analysis, as well as the resolved $VH, H \to c\bar{c}$ analysis. Since the boosted analysis targets the high momenta regions ($p_T^V > 400$ GeV), the resolved $VH, H \to b\bar{b}$ analysis has an upper limit on the p_T^V of 400 GeV. This is one of the major differences between the study in this thesis and the previous round of the analysis, as the previous round had no upper limit on the p_T^V.

For clarification, there are three different analyses that are often referred to in this section. There is the published 2021 paper referenced above [24] (referred to as "the previous round of the analysis"), the update to this analysis by the ATLAS collaboration [23] (referred to as "the new ATLAS analysis"), and the analysis presented in this thesis (referred to as "in this thesis").

7.1 Introduction

The study of Higgs boson production is important not only to test the SM, but also because it is sensitive to the effects of many BSM theories. Some of the BSM theories may not show up easily when doing a single fiducial cross-section measurement, as the BSM theories may be more dominant in smaller kinematic regions of the $VH, H \to b\bar{b}$ phase space. Studying the

production within the STXS framework provides these smaller regions to study the BSM effects (Described in Sections 2.5.1 and 5.5). Additionally, the STXS framework provides a method to easily combine measurements from different experiments as well as different production and decay modes of the Higgs boson. This is due to the similar definition of the kinematic regions across the different production modes and experiments.
In the previous round of the analysis, an STXS measurement was done using five kinematic regions, with the WH production split into two p_T^V regions, and the ZH production split into three p_T^V regions. The measurement presented in this thesis aims to study those same regions, but splitting each one into two smaller regions defined by the number of jets, resulting in 10 STXS regions. This will increase the granularity of the STXS measurement, potentially improving the sensitivity to BSM effects. It is believed however, that the limited amount of data may result in large statistical uncertainties, reducing the sensitivity in some of the new STXS regions. To improve the results, an increase in the p_T threshold applied to the non-tagged central jets is performed, going from $p_T > 20$ GeV to $p_T > 30$ GeV. The idea is that the increased threshold will improve the correlation between the STXS regions and their corresponding reconstruction level regions (reco regions), since at the STXS level, a threshold of $p_T > 30$ GeV is already applied to the truth jets not assigned to the Higgs boson. An improved correlation between the STXS and reco regions will result in an increased amount of signal in the reco regions coming from their corresponding STXS regions, thus reducing the correlations between the STXS signal strengths in the likelihood fit. A reduced correlation between the signal strengths should decrease the uncertainties on their values.

7.2 Impact of tighter jet p_T selections

This section will look at some of the impacts of the tighter additional jet p_T selections and how they cause events to migrate between the number of jet categories. How the correlations between the reco regions and the STXS regions change, and how the composition of the largest background, $t\bar{t}$, is altered due to this tighter selection is studied.
The main motivation behind tightening the additional-jet p_T selection is to improve the correlation between the STXS regions and their corresponding reco regions. For example, the STXS region of WH, $150 < p_T^V < 250$ GeV, zero additional jets will correspond strongest with the 1-lepton, $150 < p_T^V < 250$ GeV, 2-jet reco region. The better the correlation, the better the measurement of the signal strength and cross-section should be for the STXS regions. This improved correlation between the analysis and STXS regions will also reduce the correlations between each POI in the likelihood fit. Since the analysis events require at least two jets, of which exactly two need to be b-tagged, increasing the threshold on the p_T of the non-tagged central jets will not lead to a vetoing of any events. Instead, events with jets that do not pass this new threshold will migrate from higher n_{jets} regions to lower n_{jets} regions. As an example,

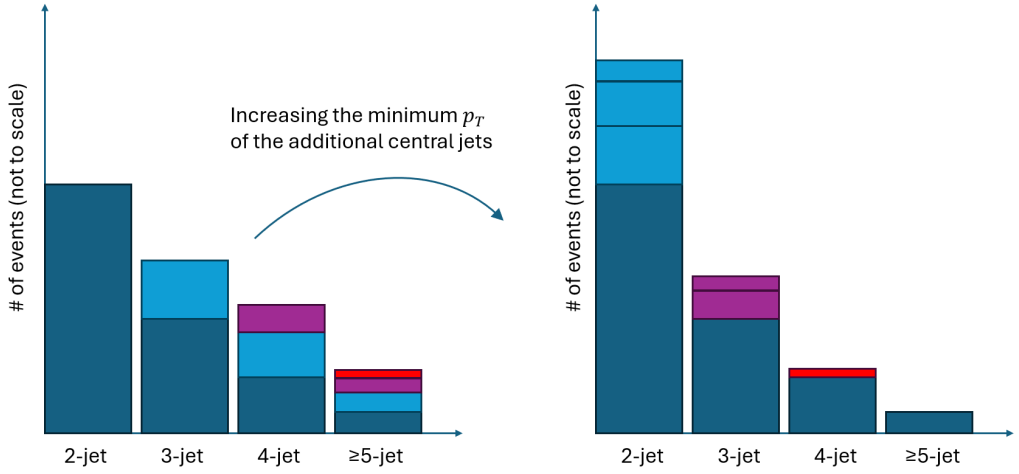

(a)

FIGURE 7.1: A simple illustration of how the events migrate between the n_{jets} categories after increasing the minimum p_T selection on the jets additional to the b-tagged jets. The number of events per n_{jets} category are in arbitrary units. The darker blue represents events that do not migrate, the light blue represents events that become 2-jet events, purple become 3-jet events and red become 4-jet events. Since 2-btag jets are always required, no events can migrate out of the 2-jet region.

if the third jet (which failed the tagging by definition) in a 3-jet event is a central jet with $p_T = 25$ GeV, when the jet selection is increased from 20 GeV to 30 GeV, this third jet will no longer be counted as a jet, and the event becomes a 2-jet event. The amount of migration differs between different processes, as well as what region is being studied. A simple diagram illustrating this migration is shown in Figure 7.1.

A comparison of pre-fit yields before and after tightening the additional-central-jet p_T selection to 30 GeV is provided in Table 7.1 for the 0-lepton, 2-jet, 150 $< p_T^V <$ 250 GeV signal region, and Table 7.2 for the 0-lepton, 3-jet, 150 $< p_T^V <$ 250 GeV signal region. The pre-fit yields for all the signal regions are given in Appendix A.1. For the 2-jet region, since events can't move out of this category, there is only an increase in events. In the 3-jet region, some events will move out into the 2-jet region, while others will move in from the $\geq$ 4-jet regions. The largest migration occurs for the $t\bar{t}$ background, since its n_{jets} distribution peaks around five jets, with the two b-quarks coming from the top decays, and the W bosons more likely to decay to quarks than leptons. A more in depth discussion on the $t\bar{t}$ background is given in Section 7.2.1.
Comparing the amount of migration happening between the 2- and 3-jet regions, unfortunately the 3-jet region gets a larger increase in the background compared to the signal, reducing the S/B in the 3-jet regions.

The impact on these correlations due to the increased jet p_T selection can be seen in Figure 7.2. The plot shows the percentage of each STXS region in each reco region, with the 20 GeV scenario on the left of the vertical lines, and the 30 GeV scenario on the right. For the regions

TABLE 7.1: The pre-fit yields for the 0-lepton, 2-jet, 150 $< p_T^V <$ 250 GeV signal region. The values for the different jet p_T selections are shown as well, namely the 20 GeV and 30 GeV selections, and the ratios are the yields in the 30 GeV case relative to the 20 GeV case. The percentages in the brackets next to some of the background (signal) yields are the percentage of that sample relative to the total background (signal) yield. The ZH, $p_T^V \leq 75$ GeV and WH, $p_T^V \leq 150$ GeV signal samples are the signal events that passed the reco level selections, but do not belong to any of the STXS regions under study. The V+hf samples are the subset of heavy flavour samples of the corresponding V+jets samples.

	20 GeV	**30 GeV**	**Ratio**
Z+hf	2050.0 ± 280.0	3420.0 ± 400.0	1.67
Z+jets	2050.0 ± 280.0 (48.7%)	3440.0 ± 400.0 (42.5%)	1.68
W+hf	546.0 ± 65.0	917.0 ± 95.0	1.68
W+jets	565.0 ± 70.0 (13.4%)	950.0 ± 100.0 (11.7%)	1.68
single-top	231.0 ± 43.0 (5.5%)	462.0 ± 84.0 (5.7%)	2
$t\bar{t}$	1010.0 ± 210.0 (24.0%)	2760.0 ± 490.0 (34.1%)	2.73
diboson	345.0 ± 97.0 (8.2%)	490.0 ± 130.0 (6.0%)	1.42
ZH, $p_T^V \leq 75$ GeV	0 ± 0	0.0047 ± 0.0074 (0.0%)	0
ZH, 75 $< p_T^V <$ 150 GeV, n_{jets}^{add}=0	9.6 ± 2.3 (6.9%)	14.8 ± 3.6 (7.3%)	1.54
ZH, 75 $< p_T^V <$ 150 GeV, $n_{jets}^{add} \geq 1$	0.52 ± 0.38 (0.4%)	1.16 ± 0.79 (0.6%)	2.2
ZH, 150 $< p_T^V <$ 250 GeV, n_{jets}^{add}=0	85.0 ± 14.0 (60.7%)	119.0 ± 19.0 (58.5%)	1.4
ZH, 150 $< p_T^V <$ 250 GeV, $n_{jets}^{add} \geq 1$	2.9 ± 1.1 (2.1%)	7.7 ± 2.8 (3.8%)	2.7
ZH, 250 $< p_T^V <$ 400 GeV, n_{jets}^{add}=0	9.2 ± 1.9 (6.6%)	12.2 ± 2.5 (6.0%)	1.33
ZH, 250 $< p_T^V <$ 400 GeV, $n_{jets}^{add} \geq 1$	0.43 ± 0.21 (0.3%)	0.99 ± 0.48 (0.5%)	2.3
WH, $p_T^V \leq 150$ GeV	2.21 ± 0.98 (1.6%)	3.8 ± 1.7 (1.9%)	1.7
WH, 150 $< p_T^V <$ 250 GeV, n_{jets}^{add}=0	22.9 ± 2.8 (16.4%)	33.3 ± 3.1 (16.4%)	1.45
WH, 150 $< p_T^V <$ 250 GeV, $n_{jets}^{add} \geq 1$	0.6 ± 0.21 (0.4%)	1.69 ± 0.57 (0.8%)	2.8
WH, 250 $< p_T^V <$ 400 GeV, n_{jets}^{add}=0	6.34 ± 0.8 (4.5%)	8.21 ± 0.9 (4.0%)	1.29
WH, 250 $< p_T^V <$ 400 GeV, $n_{jets}^{add} \geq 1$	0.228 ± 0.083 (0.2%)	0.54 ± 0.19 (0.3%)	2.4
Signal	138.0 ± 19.0	200.0 ± 26.0	1.45
Background	4210.0 ± 510.0	8100.0 ± 840.0	1.92
Data	5177.0	9526.0	1.84

with additional jets, the correlation improves by up to 50% in some regions. While the regions with no additional jets get slightly worse correlations, they start off high enough that the impact is small.

A smaller impact of tightening the jet selection is the effect it has on the number of pileup jets. Since pileup jets tend to have low p_T, tightening the selection will reduce the amount of pileup in the events. A proxy for this is shown in Figure 7.3. Plotted here is the average difference between the total number of central jets and the number of central jets with a matching truth jet in the $t\bar{t}$ sample, as a function of the average number of collisions per bunch crossing, μ. The truth record is not kept for pileup jets, and so an unmatched reco jet is likely to be a pileup jet. As can be seen, the increase in the jet p_T selection results in a drop of the average number of unmatched jets by about 50%. The peak of the μ distribution is around 30, as shown in Figure 3.3.

TABLE 7.2: The pre-fit yields for the 0-lepton, 3-jet, 150 $< p_T^V <$ 250 GeV signal region. The values for the different jet p_T selections are shown as well, namely the 20 GeV and 30 GeV selections, and the ratios are the yields in the 30 GeV case relative to the 20 GeV case. The percentages in the brackets next to some of the background (signal) yields are the percentage of that sample relative to the total background (signal) yield. The ZH, $p_T^V \leq 75$ GeV and WH, $p_T^V \leq 150$ GeV signal samples are the signal events that passed the reco level selections, but do not belong to any of the STXS regions under study. The V+hf samples are the subset of heavy flavour samples of the corresponding V+jets samples.

	20 GeV	**30 GeV**	**Ratio**
Z+hf	2920.0 ± 320.0	3880.0 ± 420.0	1.33
Z+jets	2930.0 ± 320.0 (27.9%)	3900.0 ± 420.0 (19.2%)	1.33
W+hf	1170.0 ± 110.0	1740.0 ± 150.0	1.49
W+jets	1190.0 ± 110.0 (11.3%)	1780.0 ± 150.0 (8.8%)	1.5
single-top	750.0 ± 140.0 (7.1%)	1380.0 ± 280.0 (6.8%)	1.84
$t\bar{t}$	5200.0 ± 1200.0 (49.5%)	12800.0 ± 2200.0 (63.1%)	2.46
diboson	370.0 ± 110.0 (3.5%)	410.0 ± 130.0 (2.0%)	1.11
ZH, $p_T^V \leq 75$ GeV	0.006 ± 0.013 (0.0%)	0.007 ± 0.012 (0.0%)	1.14
ZH, 75 $< p_T^V <$ 150 GeV, n_{jets}^{add}=0	6.5 ± 2.6 (5.0%)	4.7 ± 2.1 (3.4%)	0.72
ZH, 75 $< p_T^V <$ 150 GeV, $n_{jets}^{add} \geq 1$	4.0 ± 1.2 (3.1%)	6.9 ± 2.1 (5.0%)	1.73
ZH, 150 $< p_T^V <$ 250 GeV, n_{jets}^{add}=0	45.6 ± 8.7 (34.8%)	29.1 ± 6.6 (21.1%)	0.64
ZH, 150 $< p_T^V <$ 250 GeV, $n_{jets}^{add} \geq 1$	35.7 ± 8.0 (27.3%)	56.0 ± 12.0 (40.5%)	1.57
ZH, 250 $< p_T^V <$ 400 GeV, n_{jets}^{add}=0	4.03 ± 0.79 (3.1%)	2.32 ± 0.55 (1.7%)	0.58
ZH, 250 $< p_T^V <$ 400 GeV, $n_{jets}^{add} \geq 1$	4.3 ± 1.1 (3.3%)	6.4 ± 1.6 (4.6%)	1.49
WH, $p_T^V \leq 150$ GeV	2.49 ± 0.71 (1.9%)	2.7 ± 0.87 (2.0%)	1.08
WH, 150 $< p_T^V <$ 250 GeV, n_{jets}^{add}=0	14.7 ± 1.7 (11.2%)	10.8 ± 1.6 (7.8%)	0.73
WH, 150 $< p_T^V <$ 250 GeV, $n_{jets}^{add} \geq 1$	7.6 ± 1.1 (5.8%)	12.8 ± 1.6 (9.3%)	1.68
WH, 250 $< p_T^V <$ 400 GeV, n_{jets}^{add}=0	3.43 ± 0.42 (2.6%)	2.51 ± 0.36 (1.8%)	0.73
WH, 250 $< p_T^V <$ 400 GeV, $n_{jets}^{add} \geq 1$	2.57 ± 0.39 (2.0%)	3.85 ± 0.5 (2.8%)	1.5
Signal	128.0 ± 15.0	136.0 ± 16.0	1.06
Background	10500.0 ± 1300.0	20300.0 ± 2300.0	1.93
Data	11114.0	21347.0	1.92

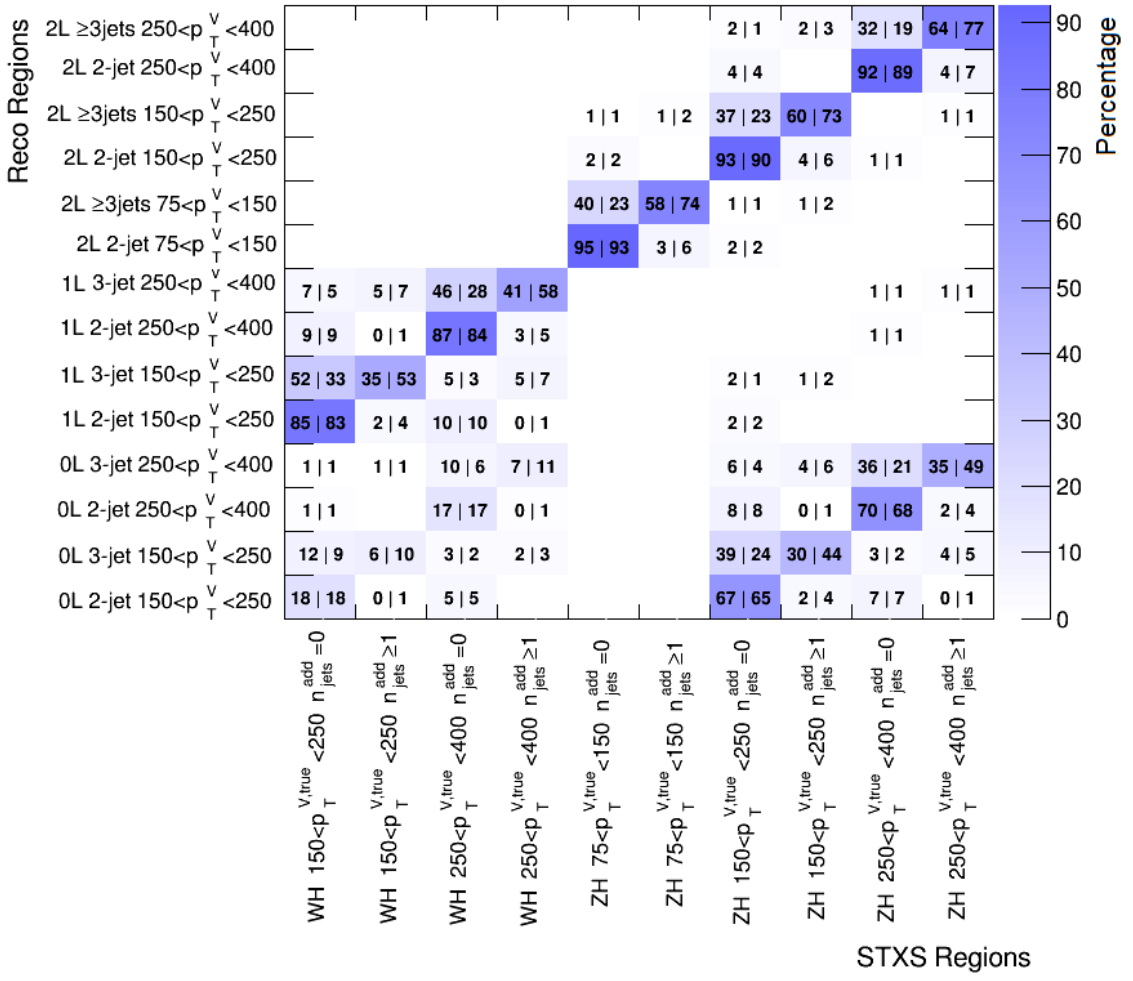

(a)

FIGURE 7.2: A correlation plot between the reconstruction level signal regions (y-axis) and the STXS regions (x-axis) used in the ten parameter-of-interest studies. Shown is the percentage of each STXS region per each reconstruction level region, with the 20 GeV jet p_T selections on the left of the vertical bars, and the 30 GeV jet p_T selections on the right. Each row sums up to 100 per left or right side of the vertical line, within rounding. The number of jets for the reco regions are the total number of jets, while for the STXS regions it's the number of jets additional to the two b-quark jets. The units of the p_T^V are all in GeV.

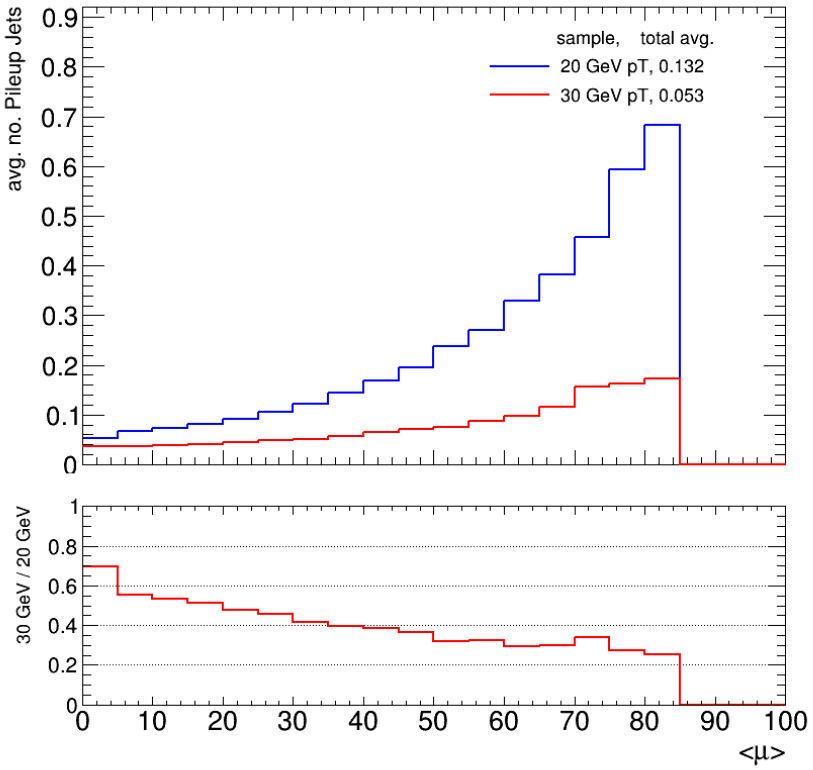

(a)

FIGURE 7.3: A plot of the event averaged difference between the total number of central jets and the number of central jets with a matching truth jet, as a function of the number of collisions per bunch crossing, μ. This acts as a proxy for the number of pileup jets as a function of the number of collisions, since jets with no matched truth jet are likely to be pileup jets. Shown is the $t\bar{t}$ sample in the 0-lepton channel, with ≥ 2 jets and $E_T^{miss} \geq 150$ GeV. The blue histogram represents the pileup jets for the 20 GeV jet p_T selection, while the red histogram is for the 30 GeV selection. Most of the events lie in the range $10 < \mu < 50$, with a peak at 30. In the legend is also shown the average number of pileup jets averaged over the range of collisions per bunch crossing.

7.2.1 Impact on $t\bar{t}$ flavour composition

As shown in Tables 7.1 and 7.2, there is almost a 150% increase in the $t\bar{t}$ background after tightening the jet p_T selection to 30 GeV. This makes the $t\bar{t}$ background far more dominant, especially in the 3-jet regions. To better understand what is happening, the flavour composition and decay of the $t\bar{t}$ processes is studied.

The first study is decomposing the $t\bar{t}$ sample into its dominant flavours, i.e., into bb and bc flavours, in the higher p_T^V regions of the 3-jet regions. Shown in Figure 7.4 are the $\Delta R(b_1, b_2)$-p_T^V distributions for the bb and bc components of the $t\bar{t}$ background in the 0-lepton, 3-jet, $250 < E_T^{miss} < 400$ GeV region. The bc component of the $t\bar{t}$ background is more signal-like, and while the bb component is the dominant flavour of the $t\bar{t}$ sample, the bc component becomes more dominant in the SR due to the signal region selections at high E_T^{miss}. From studies performed by the author, the minimum $\Delta\phi$ between the E_T^{miss} and the jets in the event was found to be $> 135°$ for the bc component, yet $< 90°$ for the bb component. This, along with the smaller ΔR between the two b-tagged jets in the bc component implies that the two b-tagged jets come from the same top-quark decay. The other top-quark decay in the bc component likely falls outside of the detector acceptance, providing the large E_T^{miss} that is almost opposite in direction to the direction of the b-tagged dijet system. This results in the high E_T^{miss} regions having a different flavour composition compared to the lower E_T^{miss} regions.

Additionally, in the BDT distribution of the $t\bar{t}$ events split by flavour in the 3-jet region in Figure 7.5, the bc component peaks at the right of the distribution, where the signal events also peak, especially in the high p_T^V region. There is also a slight shift in the distribution towards the right when tightening the jet p_T selections, so not only is there an increase in the $t\bar{t}$ background with the tighter selections, but that background is also more signal-like. Finally, the decay of the W-bosons from the top-quark decays in $t\bar{t}$ events are shown in Figure 7.6 for the 2-jet, 0- and 1-lepton channels, after tightening the jet p_T selections. The histograms are split by the n_{jets} region that the events migrated from. In the 0-lepton channel, the dominant decay of the W-bosons include at least one decaying to a τ-lepton, with most of the migrated events having one W-boson decaying hadronically and the other decays to a τ-lepton. The dominance of the τ-lepton decays makes sense since the requirement on the number of jets (exactly two or exactly three) reduces the contribution from both W-bosons decaying hadronically. The lepton (e, μ) veto then reduces the contribution from both W-bosons decaying leptonically. This leaves the events that have at least one W-boson decaying to a τ-lepton, which then decays hadronically, passing the event selections due to no distinction between quark-induced jets and τ-induced jets. While the 1-lepton channel is dominated by the semi-leptonic $t\bar{t}$ decays, especially in the migrated events, there is a large contribution from dileptonic decays with the one W-boson decaying to a τ-lepton.

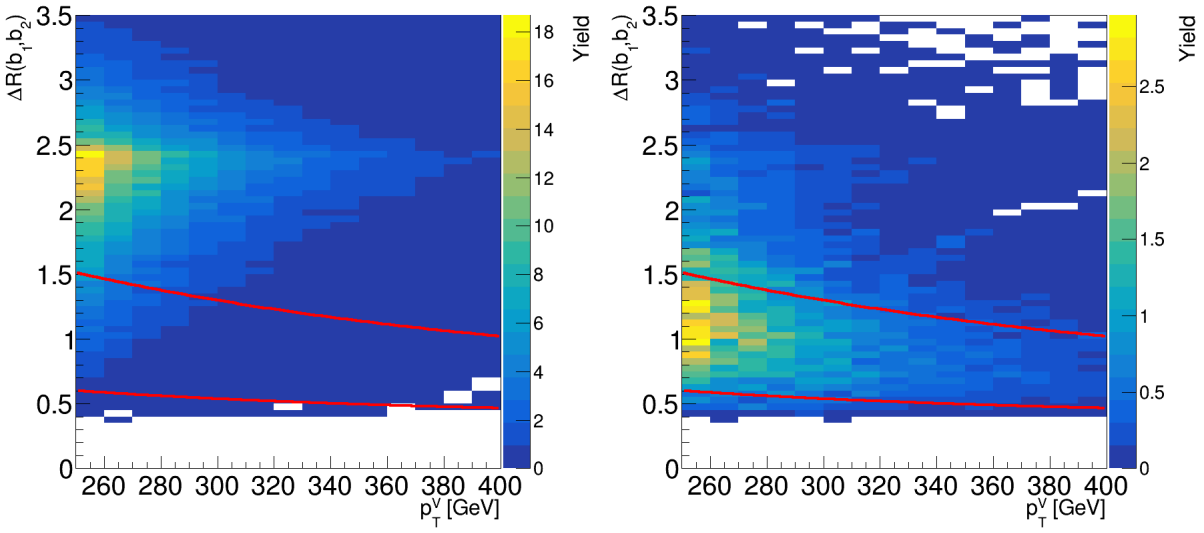

(a) (b)

FIGURE 7.4: The two-dimensional $\Delta R(b_1, b_2)$-p_T^V distribution for the 0-lepton, 3-jet, 250 $< p_T^V <$ 400 GeV $t\bar{t}$ background for the 30 GeV jet p_T selection. In figure (a) is the truth bb flavoured component, while (b) shows the truth bc flavoured component. The red lines are the boundaries of the signal region to the control regions. As a reminder, p_T^V in the 0-lepton channel is defined as E_T^{miss} .

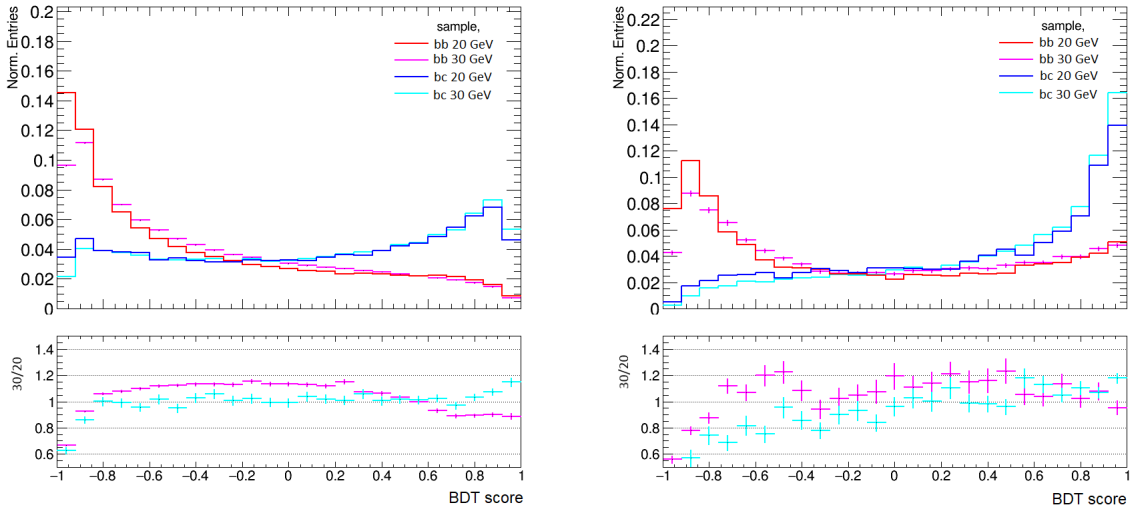

(a) (b)

FIGURE 7.5: The BDT distributions of the $t\bar{t}$ background in the 1-lepton, 3-jet signal regions split by the truth flavour of the tagged jets. Figure (a) is the 150 $< p_T^V <$ 250 GeV region, and figure (b) is the 250 $< p_T^V <$ 400 GeV region. In red (magenta) are the bb flavoured events for the 20 GeV and 30 GeV jet p_T selections respectively, while in blue (cyan) are the bc flavoured events for the 20 GeV and 30 GeV jet p_T selections respectively. All histograms are normalised to the same area.

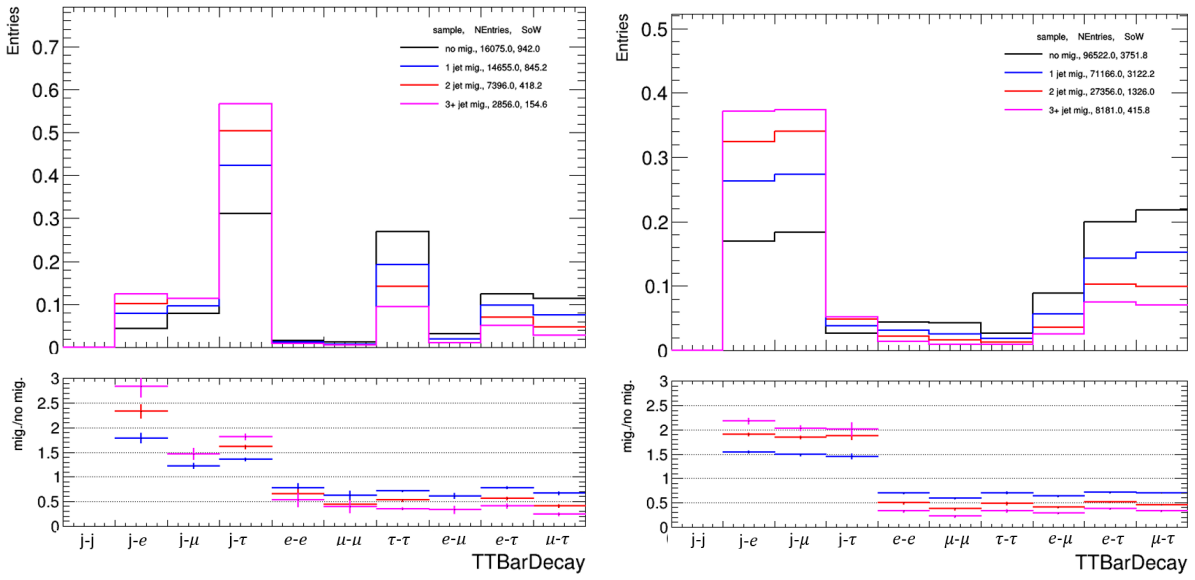

(a) (b)

FIGURE 7.6: Histograms showing the decays of the two W-bosons from the top quark decays in $t\bar{t}$ events in the 2-jet, 150 $< p_T^V <$ 250 GeV signal regions with the 30 GeV jet p_T selections, for the 0-lepton (a) and 1-lepton (b) channels. The possible decays shown for the W-bosons are to two quarks (j), or an electron/muon/tau lepton (e, μ, τ) plus neutrino. The black histogram represents the events that do not migrate, corresponding to the distribution for the 20 GeV selections. The other histograms show how many jets were lost in the events that migrated to the 2-jet region after tightening the additional-jet p_T selection to 30 GeV. The blue histogram represents the old 3-jet events, red was the 4-jet events and the magenta was $\geq$ 5-jet events. All histograms are normalised to the same area. The bottom panel shows the ratio of the migrated events to those that did not migrate. In the legend, NEntries is the number of simulated events, while SoW is the sum-of-weights for those events.

7.3 STXS measurements

This section presents the results of the STXS measurements performed using a maximum likelihood fit. The focus is on the 10 POI STXS measurement, and comparing the two different additional central jet p_T selections of 20 GeV and 30 GeV. There will also be a brief look at the other STXS POI schemes, namely those shown in Table 5.9, as well as some fits measuring the signal strengths defined by the reco regions instead of the STXS regions.

7.3.1 Results

For the results of the 10 POI STXS fits as well as the impact of the tighter jet p_T selections, the significances and signal strength measurements will be shown. Unless otherwise stated, all the observed results are from unconditional fits to data, i.e., all the parameters in the fit are allowed to vary. The expected significances are obtained from a fit to an Asimov dataset built using the post-fit parameters from a conditional fit to data, i.e., the parameters-of-interest are the only parameters not allowed to vary in the fit.
Starting with the significances, the results of the five POI STXS fits are shown in Table 7.3, along with the one and two POI STXS results. While the values of the expected significances somewhat agree between the two different jet p_T selections, there are noticeable differences with the observed significances, especially in the WH regions. Both selections observe the ZH process above 5 sigma, and the WH process above 4 sigma. However, all the WH significances get worse with the increased p_T selection, and most of the ZH significances are worse as well. More interesting results are in the 10 POI STXS fits, the significances of which are shown in Table 7.4. Comparing the expected significances between the 20 and 30 GeV additional jet p_T selections, they all increase when tightening the selection, except for the WH, n_{jets}^{add}=1 POIs. Almost all the n_{jets}^{add}=0 POIs have an observed significance higher than expected. Only two of the POIs with $n_{jets}^{add} \geq$ 1 in the 20 GeV case have a decrease in significance between expected and observed, whereas four of those POIs in the 30 GeV case drop, with three having decreases large enough to make the significances negative. These three happen to have the lowest expected significances as well however. Comparing the observed significances, all of the $n_{jets}^{add} geq 1$ POIs have decreased significances when tightening the additional jet p_T selections, while all the n_{jets}^{add}=0 POIs increase, except for the WH, $150 < p_T^{V,truth} < 250$. This suggests some bias towards the number of jets in the events. The increase in the expected significances, especially of the $n_{jets}^{add} geq 1$ POIs, is what was used to justify the increased p_T selections on the additional central jets. But it seems the data favours a large decrease in the normalisation of some of these signal samples, as can be seen in the yield tables in Appendix A.1. However, despite these large decreases in normalisation, the uncertainties on their yields are very large,

TABLE 7.3: Significances for the fits to the 5 POI STXS scheme, for the jet p_T selection of 20 GeV and 30 GeV. The expected values come from an Asimov fit built from a conditional fit to data, while the observed is from the unconditional fit to data. Also shown are the results from the 2 (1) POI STXS fits, split only by WH and ZH (fully inclusive).

STXS regions	**20 GeV**		**30 GeV**	
	Exp.	**Obs.**	**Exp.**	**Obs.**
WH, $150 < p_T^{W,truth} < 250$ GeV	2.566	3.339	2.397	2.558
WH, $250 < p_T^{W,truth} < 400$ GeV	2.850	3.133	2.583	2.947
WH	4.069	4.901	3.658	4.069
ZH, $75 < p_T^{Z,truth} < 150$ GeV	1.417	1.397	1.298	1.539
ZH, $150 < p_T^{Z,truth} < 250$ GeV	3.234	4.826	3.224	4.449
ZH, $250 < p_T^{Z,truth} < 400$ GeV	2.988	2.311	2.969	2.232
ZH	4.605	5.402	4.529	5.033
VH	6.366	7.561	6.220	6.948

TABLE 7.4: Significances for the fits to the 10 POI STXS scheme, for the jet p_T selection of 20 GeV and 30 GeV. The expected values come from an Asimov fit built from a conditional fit to data, while the observed is from the unconditional fit to data.

STXS regions	**20 GeV**		**30 GeV**	
	Exp.	**Obs.**	**Exp.**	**Obs.**
WH, $150 < p_T^{W,truth} < 250$ GeV, $n_{jets}^{add} = 0$	2.130	2.735	2.075	2.621
WH, $150 < p_T^{W,truth} < 250$ GeV, $n_{jets}^{add} \geq 1$	0.341	0.563	0.459	-0.056
WH, $250 < p_T^{W,truth} < 400$ GeV, $n_{jets}^{add} = 0$	2.397	2.929	2.173	3.129
WH, $250 < p_T^{W,truth} < 400$ GeV, $n_{jets}^{add} \geq 1$	0.482	0.087	0.710	-0.131
ZH, $75 < p_T^{Z,truth} < 150$ GeV, $n_{jets}^{add} = 0$	1.062	1.184	1.128	1.796
ZH, $75 < p_T^{Z,truth} < 150$ GeV, $n_{jets}^{add} \geq 1$	0.565	0.400	0.720	-0.145
ZH, $150 < p_T^{Z,truth} < 250$ GeV, $n_{jets}^{add} = 0$	2.407	3.126	2.736	3.749
ZH, $150 < p_T^{Z,truth} < 250$ GeV, $n_{jets}^{add} \geq 1$	1.048	2.170	1.260	1.258
ZH, $250 < p_T^{Z,truth} < 400$, $n_{jets}^{add} = 0$	2.236	1.120	2.431	1.940
ZH, $250 < p_T^{Z,truth} < 400$, $n_{jets}^{add} \geq 1$	0.961	1.607	1.176	0.512

and in both the 20 GeV and the 30 GeV additional jet p_T selection cases. This suggests a statistical limitation for these POIs.

Looking at the reco fits with the 14 POIs being the 14 signal regions at the reco level with no STXS definitions, for which the significances are shown in Table 7.5, a similar story is shown there. All the 3-jet regions do worse in the 30 GeV case, for both expected and observed

TABLE 7.5: Significances for the fits to the 14 signal reconstruction regions, for the jet p_T selection of 20 GeV and 30 GeV. The expected values come from an Asimov fit built from a conditional fit to data, while the observed is from the unconditional fit to data. Also shown are the results from the three POI fit to the reconstruction regions, split only by lepton.

Reco. regions	**20 GeV**		**30 GeV**	
	Exp.	**Obs.**	**Exp.**	**Obs.**
0 Lep, 150 GeV $< p_T^V <$ 250 GeV, n_{jets}= 2	2.600	3.425	2.628	4.008
0 Lep, 250 GeV $< p_T^V <$ 400 GeV, n_{jets}= 2	2.464	2.054	2.552	2.947
0 Lep, 150 GeV $< p_T^V <$ 250 GeV, n_{jets}= 3	1.709	1.760	1.293	1.573
0 Lep, 250 GeV $< p_T^V <$ 400 GeV, n_{jets}= 3	1.760	1.888	1.408	0.879
0 Lep combined	3.920	4.180	3.789	4.562
1 Lep, 150 GeV $< p_T^V <$ 250 GeV, n_{jets}= 2	2.720	3.503	2.702	3.389
1 Lep, 250 GeV $< p_T^V <$ 400 GeV, n_{jets}= 2	2.912	3.435	2.681	3.233
1 Lep, 150 GeV $< p_T^V <$ 250 GeV, n_{jets}= 3	1.736	2.086	1.131	0.126
1 Lep, 250 GeV $< p_T^V <$ 400 GeV, n_{jets}= 3	1.676	1.477	1.411	0.392
1 Lep combined	4.304	5.087	3.955	4.032
2 Lep, 75 GeV $< p_T^V <$ 150 GeV, n_{jets}= 2	1.117	1.376	1.132	1.979
2 Lep, 150 GeV $< p_T^V <$ 250 GeV, n_{jets}= 2	2.095	2.455	2.265	2.991
2 Lep, 250 GeV $< p_T^V <$ 400 GeV, n_{jets}= 2	1.760	0.961	1.905	1.065
2 Lep, 75 GeV $< p_T^V <$ 150 GeV, $n_{jets}\geq$ 3	1.109	1.086	0.964	0.126
2 Lep, 150 GeV $< p_T^V <$ 250 GeV, $n_{jets}\geq$ 3	2.197	4.131	1.801	1.806
2 Lep, 250 GeV $< p_T^V <$ 400 GeV, $n_{jets}\geq$ 3	1.742	1.784	1.494	0.759
2 Lep combined	3.957	4.807	3.767	3.822

significances, along with the 2-jet 1-lepton regions, while the 0- and 2-lepton 2-jet regions do the opposite. The combined 0-lepton observed is better in the 30 GeV case, while the other lepton channels are worse. The combined 1-lepton result in the 20 GeV case is the only one to pass the 5 sigma value. With most of the 3-jet regions having a lower observed significance than the expected in the 30 GeV case points to potential mismodelling of the backgrounds. Another possible cause of this, or maybe even in conjunction with mismodelling, is the migrations occurring from increasing the jet p_T selections. In the 3-jet regions there is an increase in the number of backgrounds similar to the increase in the 2-jet regions, however the increase in the amount of signal is a lot smaller, so the signal to background ratio decreases more in the 3-jet regions compared to the 2-jet regions. This can be seen when comparing the 2-jet Table 7.1 to the 3-jet Table 7.2 of the 0-lepton, $150 < p_T^V < 250$ GeV, signal region pre-fit yields.

Moving on to the signal strength results, and as a reminder, the signal strengths are essentially the ratio of the amount of signal measured vs the amount of expected signal:

$$\mu_{VH} = \frac{[\sigma_{VH} \times \mathrm{BR}(H \to b\bar{b})]_{\mathrm{measured}}}{[\sigma_{VH} \times \mathrm{BR}(H \to b\bar{b})]_{\mathrm{theory}}}. \tag{7.1}$$

The inclusive VH signal strengths and the WH and ZH results are shown in Figure 7.7. The VH signal strength for the 30 GeV case is the only value that lies just outside 1 sigma from a central value of 1. The results from the ATLAS paper [23] were $VH = 1.02 \pm 0.18$, $WH = 0.95 \pm 0.26$ and $ZH = 1.08 \pm 0.24$, and from the CMS paper [161] they were $VH = 1.15 \pm 0.21$, $WH = 1.31 \pm 0.35$ and $ZH = 1.07 \pm 0.24$. To be noted, in the CMS paper, the 0- and 1-lepton channels have a p_T cut of 25 GeV applied to all jets, while in 2-lepton it is 20 GeV. Their 0-lepton channel also has tighter cuts applied to the tagged jets of 60 GeV and 35 GeV for the leading and sub-leading jets respectively. The central values of the signal strengths for this thesis are larger than the previous round of this analysis (The ATLAS results just mentioned), particularly for the 20 GeV case, and the uncertainties are slightly larger as well. This is interesting, since the 30 GeV case seems to have results closer to the previous round, despite the previous round using 20 GeV.

The results for the 5 POI fits are given in Figure 7.8. The two $p_T^V > 250$ regions agree well between the 20 and 30 GeV jet selections, while the 150 GeV $< p_T^V <$ 250 GeV regions are slightly closer to 1 in the 30 GeV. The ZH, $75 < p_T^Z < 150$ GeV signal strength has flipped sides of 1 between the two different selections. All signal strengths agree with 1 within 1 sigma, except for ZH, $150 < p_T^Z < 250$ GeV which for both selections agree comfortably within 2 sigma. The uncertainties on the two WH and the low p_T^V ZH get worse in the 30 GeV case, which happens to be the same regions that the three negative significances fall into.

The results for the 10 POI fits are shown in Figure 7.9. The uncertainties on the signal strengths in the $n_{jets}^{add} \geq 1$ regions are very large, showing that the 5 POI results are dominated by the $n_{jets}^{add} = 0$ STXS regions. The 30 GeV jet p_T selections reduce these uncertainties by around 25%. However, in agreement with the significances, the 30 GeV signal strengths for the $n_{jets}^{add} \geq 1$ events in the WH regions and the low p_T^V ZH region have negative central values. This implies that the background predictions in the regions dominated by these POIs are larger than the data, and thus a negative signal is required to match the data and MC better. While some of the POIs have shifted quite a bit after increasing the jet p_T selections, the 20 GeV and 30 GeV signal strengths still agree within uncertainty. Most of the signal strengths also agree with $\mu = 1$ within 1 sigma, while the rest comfortably agree within 2 sigma.

The only comparisons to be made with the published results are the two ZH, $150 < p_T^Z < 250$ GeV values in the CMS paper, since this is the only STXS region that they split by the number of jets. They get $\mu = 0.42 \pm 0.48$ for the $n_{jets}^{add} = 0$ POI, and $\mu = -0.56 \pm 1.06$ for the $n_{jets}^{add} \geq 1$ POI. While both are below $\mu = 1$ within 1 sigma, the results in this thesis for those same POIs all have central values above $\mu = 1$, with some above $\mu = 1$ within 1 sigma. So, CMS gets

the opposite results for these regions. In the ATLAS combined paper [23], they unfortunately do not split the WH POIs by n_{jets}^{add}, so only a comparison of the ZH results can be made. In addition, the ATLAS paper only has cross section measurement results, whereas this thesis only has signal strength results. Within uncertainties, the results in this thesis agree with those in the ATLAS paper. In particular, for the ZH, $75 < p_T^Z < 150$ GeV signal strengths, a similar trend is observed. The central value of the n_{jets}^{add}=0 signal strength is above 1, with the $n_{jets}^{add} geq 1$ central value well below 1 and with a large uncertainty bad. However, their ZH, $75 < p_T^Z < 150$ GeV, $n_{jets}^{add} geq 1$ signal strengths is above 0.

The signal strengths for the 14 reco POIs are shown in Figure 7.10. The 20 GeV results agree comfortably with $\mu = 1$ within 1 sigma, except for 2-lepton, $150 < p_T^Z < 250$ GeV, $n_{jets} \geq 3$ jets. This is the reco region within which the ZH, $150 < p_T^Z < 250$ GeV, $n_{jets}^{add} \geq 1$ STXS region is most dominant, which also lay just outside of 1 sigma away from $\mu = 1$. In the 30 GeV case, there are a few that only just agree $\mu = 1$ within 1 sigma, and the regions most correlated with the STXS regions in the 10 STXS POI fit that have a negative signal strength are all quite close to zero, though not negative. The anti-correlations between the STXS POIs that differ only by n_{jets}^{add} may be the cause for the negative signal strengths observed in the STXS fit (see Figure 7.11). The correlations are obtained from the covariance matrix of the fit, defined as:

$$\rho_{ij} = \frac{1}{\sigma_i \sigma j} \text{cov}_{ij}, \tag{7.2}$$

where ρ_{ij} is the correlation between parameter i and j, cov_{ij} is the covariance between the two parameters i and j, and σ_i and σj are the uncertainties on the parameters i and j. The correlations show us how much one parameter changes with respect to a change in another parameter. While the correlations are reduced in the 30 GeV case as compared to the 20 GeV case, and predicted by Figure 7.2, the n_{jets}^{add}=0 POIs could be overpowering the $n_{jets}^{add} \geq 1$ POIs because of how much lower the S/B is in the 3-jet reco regions, where the $n_{jets}^{add} \geq 1$ POIs are most prominent. The signal strengths of the n_{jets}^{add}=0 POIs are mostly being determined in the 2-jet reco regions where they are quite dominant, and their sub-dominant, but large presence in the 3-jet regions cause the fit to reduce the $n_{jets}^{add} \geq 1$ POI signal strengths.

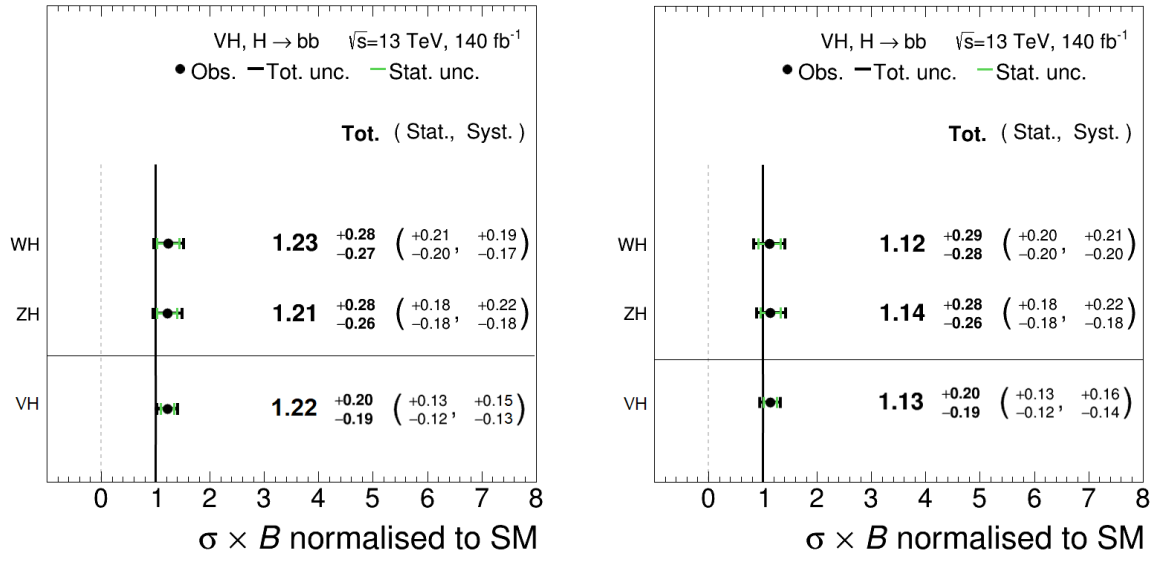

(a) (b)

FIGURE 7.7: Signal strength measurements for both the 2 and 1 POI STXS schemes, for the 20 GeV jet p_T selections (a) and 30 GeV (b). Shown are the central values, with the statistical uncertainty given by the green bands, and the total uncertainty given by the black bands.

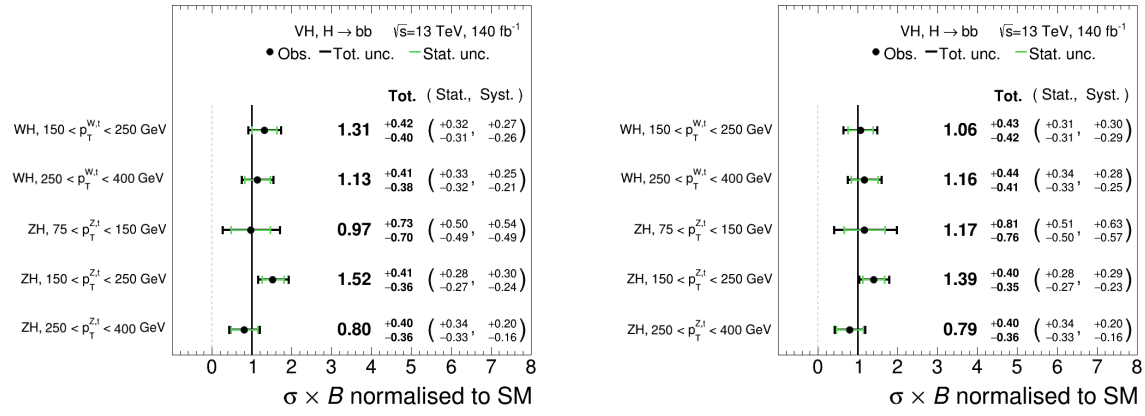

(a) (b)

FIGURE 7.8: Signal strength measurements for the 5 POI STXS scheme, for the 20 GeV jet p_T selections (a) and 30 GeV (b). Shown are the central values, with the statistical uncertainty given by the green bands, and the total uncertainty given by the black bands.

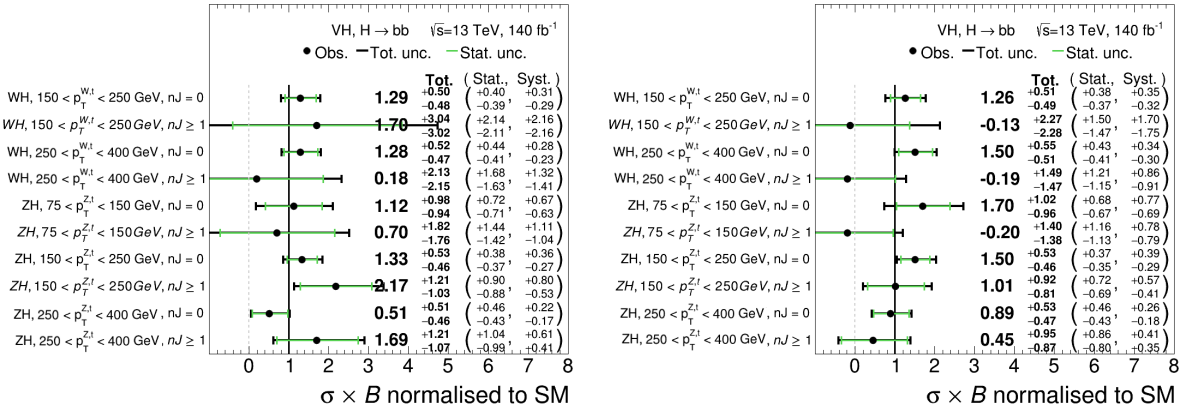

(a) (b)

FIGURE 7.9: Signal strength measurements for the 10 POI STXS scheme, for the 20 GeV jet p_T selections (a) and 30 GeV (b). Shown are the central values, with the statistical uncertainty given by the green bands, and the total uncertainty given by the black bands. In these plots, nJ is the equivalent of n_{jets}^{add}.

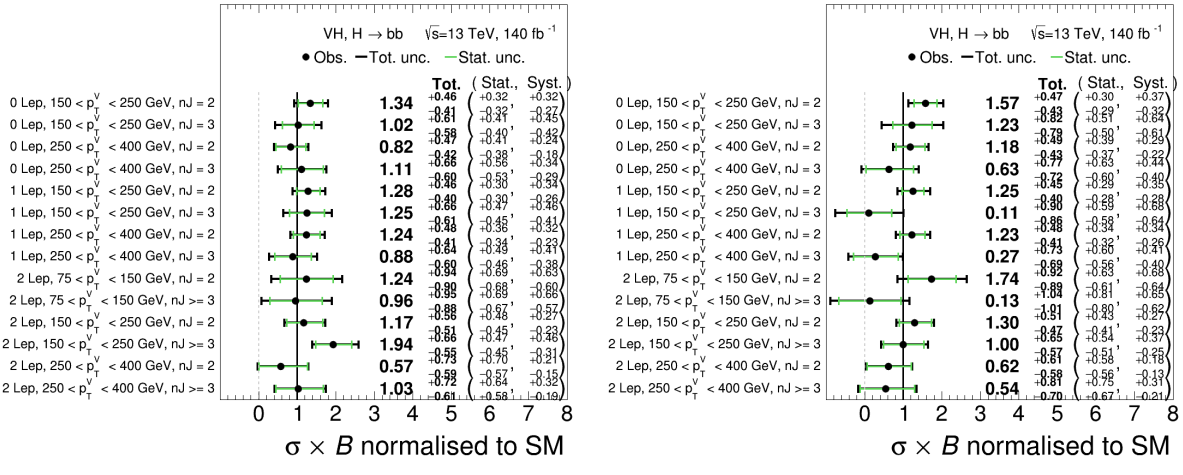

(a) (b)

FIGURE 7.10: Signal strength measurements for each of the 14 signal reconstruction regions, for the 20 GeV jet p_T selections (a) and 30 GeV (b). Shown are the central values, with the statistical uncertainty given by the green bands, and the total uncertainty given by the black bands. In these plots, nJ is the equivalent of n_{jets}.

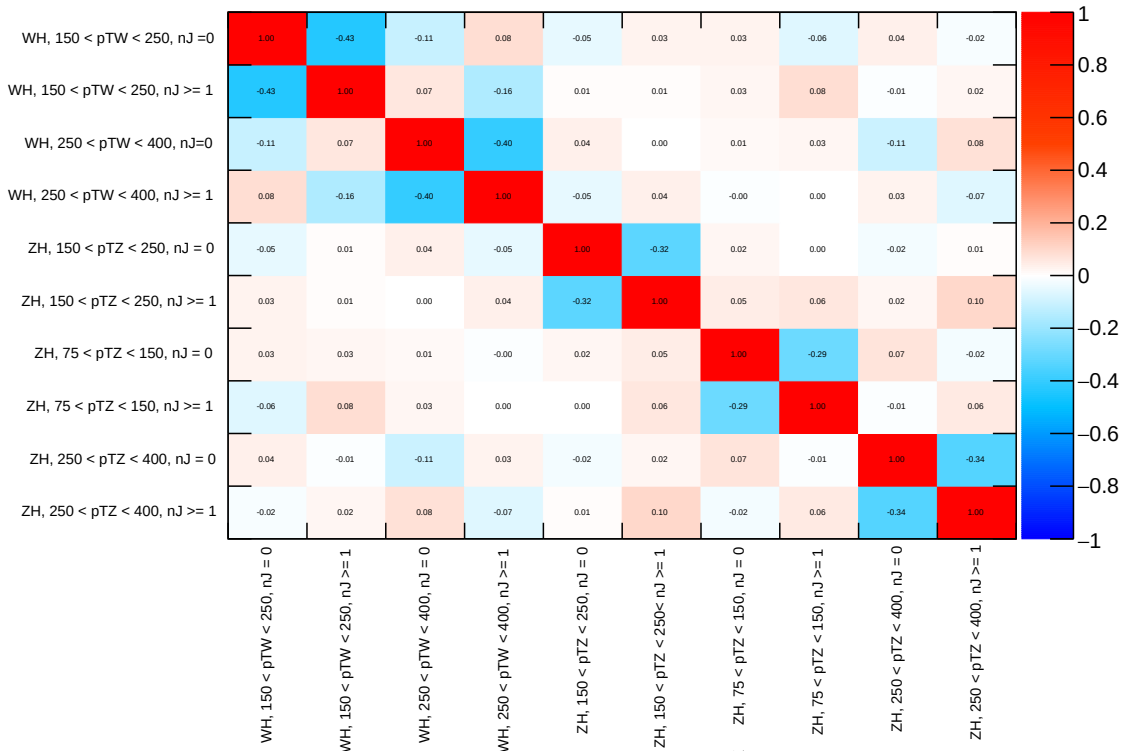

(a)

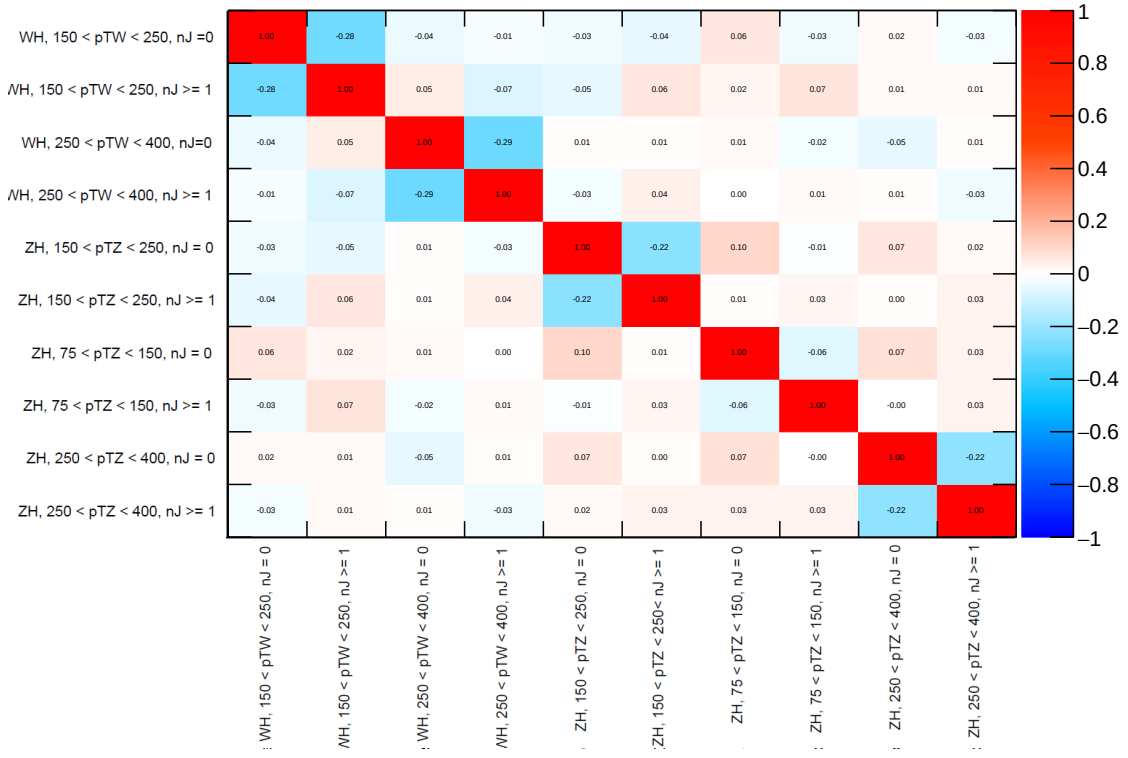

(b)

FIGURE 7.11: Correlations between each of the parameters of interest in the 10 POI STXS fit, for the 20 GeV jet p_T selections (a) and 30 GeV (b). In these plots, nJ is the equivalent of n_{jets}^{add}.

7.3.2 Uncertainty rankings and breakdowns

Looking closer at the uncertainties of the different POIs, there are the nuisance parameter rankings, pulls and POI uncertainty breakdowns. The nuisance parameter rankings rate the impact of the different nuisance parameters on the signal strength being measured. Once the unconditional fit has been performed, each nuisance parameter α is varied to its $\pm 1\sigma$ value and fixed to that value. The fit is then redone and the change in the signal strength of the POI is observed. This shows which nuisance parameters the signal strength is most sensitive to.
How much the nuisance parameters change in the fit can be seen by looking at the normalised pulls. The normalised pulls are defined as the difference in the best fit value ($\hat{\alpha}$) of a nuisance and its pre-fit value (α_0), and normalised by its pre-fit error (σ_{α_0}). Or mathematically:

$$\text{pull} = \frac{\hat{\alpha} - \alpha_0}{\sigma_{\alpha_0}}. \tag{7.3}$$

The post-fit uncertainty of a nuisance parameter is obtained from the covariance matrix, such that:

$$\sigma^2_{\alpha_i} = \text{cov}_{\alpha_i,\alpha_i} = \left(-\frac{\partial^2 \ln(\mathcal{L})}{\partial\alpha_i \partial\alpha_i} \right)^{-1} \tag{7.4}$$

If the fit is particularly sensitive to the nuisance parameter, the uncertainty is considered to be "constrained" and the post-fit uncertainty will be smaller than the pre-fit value. Otherwise, the post-fit uncertainty should stay the same as the pre-fit value. So, when looking at the normalised pulls, the central value indicates how many sigmas the fit wants to move the parameter from its pre-fit value. And the smaller the error band is, the more information there is from the data in understanding this parameter and thus the more constrained the parameter is.
To understand the impact of a group of nuisance parameters on a certain POI, e.g. the parameters related to $t\bar{t}$, an uncertainty breakdown is done. After the unconditional fit to the data is performed, an additional fit is performed where all the nuisance parameters from a group are fixed to their central values. The impact on the uncertainty of the signal strength is then defined as the quadrature difference between the uncertainty obtained from the unconditional fit ($\sigma_{\hat{\mu}}$) and the new uncertainty obtained after fixing the nuisance parameters ($\sigma^{\text{fix}}_{\hat{\mu}}$), such as impact$= \sqrt{(\sigma_{\hat{\mu}})^2 - (\sigma^{\text{fix}}_{\hat{\mu}})^2}$. The total statistical impact is obtained by fitting all the non-floating normalisations to their nominal value, and letting only the free-floating normalisations vary. The total systematic impact is the difference in quadrature between the nominal uncertainty and the statistical uncertainty. The "data statistics only" impact is the uncertainty obtained when all the nuisance parameters are fixed to their nominal values. The floating normalisation uncertainty is the quadrature difference between the nominal error and the error from a fit where only the normalisation factors are fixed to their best fit value.
The ranking plots for two of the negative signal strength POIs of the 30 GeV jet p_T selection are given in Figure 7.12 for the WH, $250 < p_T^W < 400$ GeV, $n^{add}_{jets} \geq 1$ POI and Figure 7.13 for

the ZH, $75 < p_T^Z < 150$ GeV, $n_{jets}^{add} \geq 1$ POI. A comparison between the 20 GeV and 30 GeV selections is also made in these figures. For the WH POI, the nuisance parameter with the largest impact is the correlated POI WH, $250 < p_T^W < 400$ GeV, $n_{jets}^{add}=0$, with the $t\bar{t}$ and W+jets normalisation and shape uncertainties following that. While for the 20 GeV case one of the shape uncertainties for the multijet background ranks very high, this same parameter drops in the 30 GeV case, but the normalisation for the multijet background (alpha_SysMJNorm_El_J3) now becomes very dominant. The WH, $250 < p_T^W < 400$ GeV, $n_{jets}^{add} \geq 1$ POI is most dominant in the 1-lepton, 3-jet, $250 < p_T^W < 400$ GeV reco region, and this reco region has the most dominant multijet contribution. The ZH POI has the correlated POI ZH, $75 < p_T^Z < 150$ GeV, $n_{jets}^{add}=0$ as the largest impact in 20 GeV while in 30 GeV the largest impact is the statistical uncertainty on the data-driven top estimate (MVA DDStat) in the right most bin in the BDT distribution in the 2-lepton, $75 < p_T^Z < 150$ GeV, $n_{jets} \geq 3$ region. The reduction in the correlations of the POIs is most likely why the correlated POI is no longer ranking in the 30 GeV case. The ranking plots for all 10 of the POIs is provided in Appendix B.1.

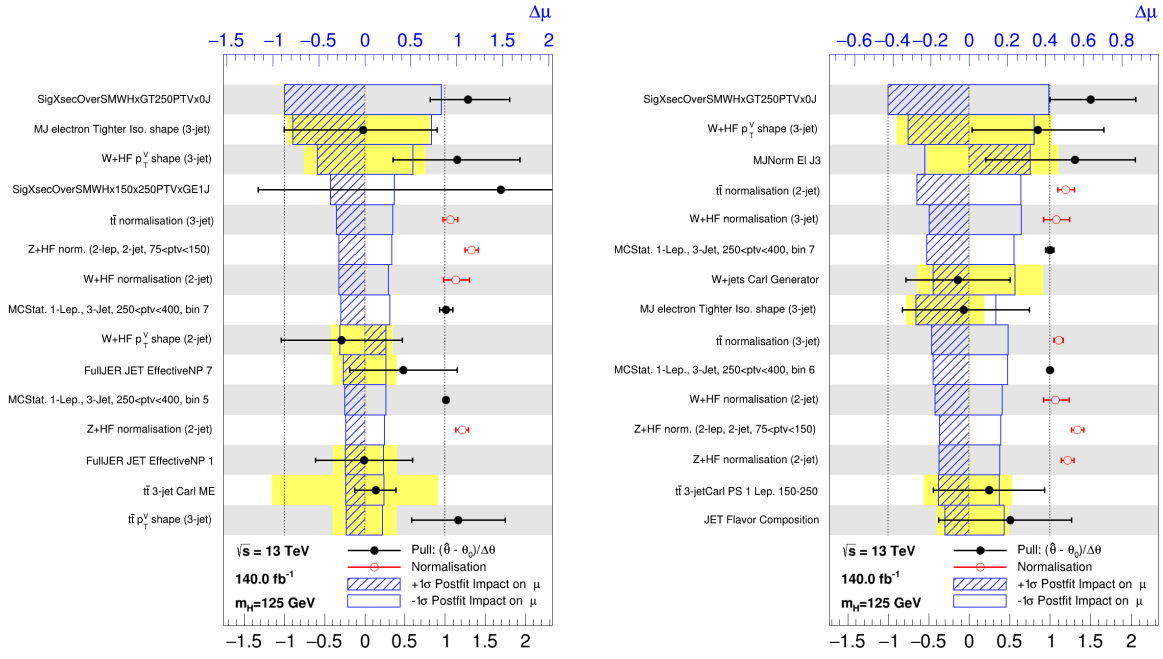

(a) (b)

FIGURE 7.12: The ranking of the nuisance parameters, in descending order, in terms of their impact on the WH, $250 < p_T^W < 400$ GeV, $n_{jets}^{add} \geq 1$ signal strength $\hat{\mu}$ for the 20 GeV jet p_T selections (a) and 30 GeV (b). The blue boxes, relating to the top x-axis, show the post-fit impact on $\hat{\mu}$ after fixing the nuisance parameter to the $\pm 1\sigma$ post-fit uncertainty, and re-running the fit. The solid yellow box shows the pre-fit impact. The black points, relating to the bottom x-axis, are the pulls, illustrating how much the parameter deviates from its pre-fit value, with the error bands showing post-fit error, and both normalised by the pre-fit error. The red points are the free floating normalisations, with the pre-fit values set to unity. MCStat is the total statistical uncertainty, per bin, of all the non-data samples.

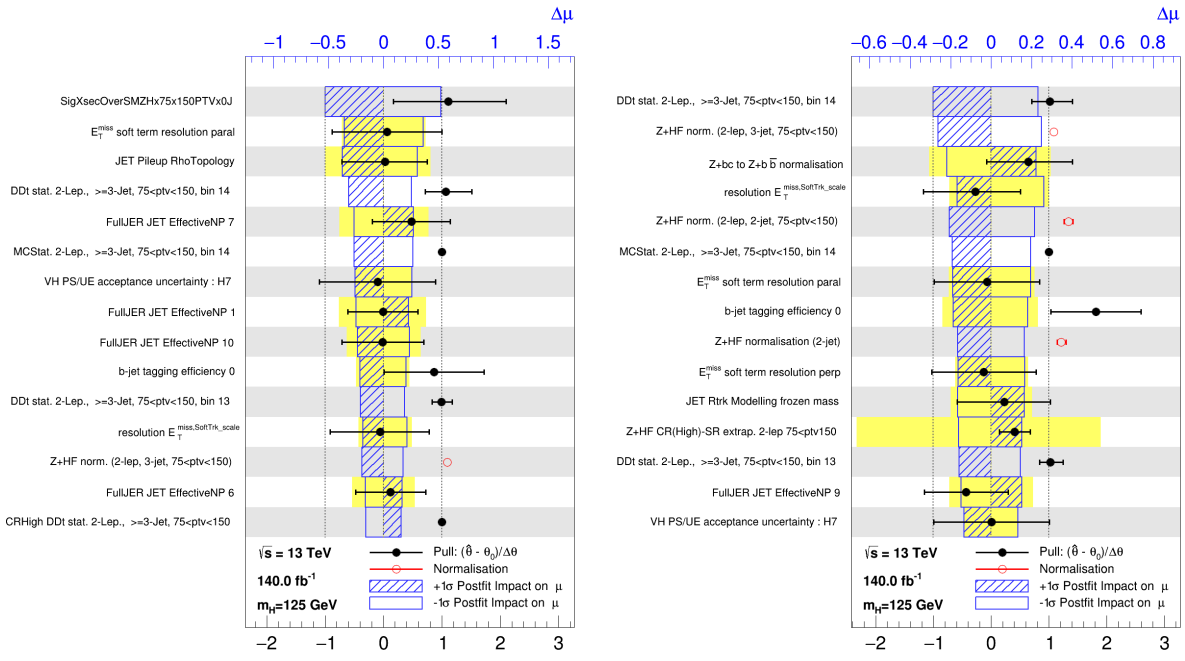

(a) (b)

FIGURE 7.13: The ranking of the nuisance parameters, in descending order, in terms of their impact on the ZH, $75 < p_T^Z < 150$ GeV, $n_{jets}^{add} \geq 1$ signal strength $\hat{\mu}$ for the 20 GeV jet p_T selections (a) and 30 GeV (b). The blue boxes, relating to the top x-axis, show the post-fit impact on $\hat{\mu}$ after fixing the nuisance parameter to the $\pm 1\sigma$ post-fit uncertainty, and re-running the fit. The solid yellow box shows the pre-fit impact. The black points, relating to the bottom x-axis, are the pulls, illustrating how much the parameter deviates from its pre-fit value, with the error bands showing post-fit error, and both normalised by the pre-fit error. The red points are the free floating normalisations, with the pre-fit values set to unity. MCStat is the total statistical uncertainty, per bin, of all the non-data samples, while "DDt stat" is the statistical uncertainty, per bin, for just the data-driven top estimate.

TABLE 7.6: Breakdown of the contributions to the total uncertainty on the signal strength of each parameter of interest in the 10 POI unconditional STXS fit to data, for the jet p_T selection of 30 GeV. Shown in this table are all the WH signal strengths.

Uncertainty source	**WH, n_{jets}^{add}= 0, 150 < p_T^W < 250 GeV**	**WH, $n_{jets}^{add}\geq$ 1, 150 < p_T^W < 250 GeV**	**WH, n_{jets}^{add}= 0, 250 < p_T^W < 400 GeV**	**WH, $n_{jets}^{add}\geq$ 1, 250 < p_T^W < 400 GeV**
μ value	1.26	-0.13	1.5	-0.19
Total uncertainty	0.503	2.275	0.530	1.477
DataStat	0.376	1.486	0.424	1.182
FullSyst	0.334	1.723	0.318	0.884
Data stat only	0.324	1.250	0.374	1.035
MC stat	0.115	0.543	0.108	0.364
Top-emu CR stat	0.024	0.167	0.020	0.044
Floating normalisations	0.193	0.910	0.167	0.568
Modelling: VH	0.091	0.224	0.152	0.195
Modelling: Background	0.200	0.849	0.204	0.666
Multijet	0.052	0.399	0.066	0.384
Modelling: single-top	0.061	0.281	0.023	0.163
Modelling: ttbar	0.152	0.709	0.053	0.275
Modelling: W+jets	0.093	0.241	0.187	0.445
Modelling: Z+jets	0.077	0.161	0.042	0.135
Modelling: Diboson	0.068	0.168	0.074	0.102
Experimental Syst	0.164	1.021	0.112	0.359
Detector: lepton	0.005	0.031	0.004	0.007
Detector: MET	0.042	0.244	0.058	0.089
Detector: JET	0.132	0.755	0.076	0.288
Detector: FTAG (b-jet)	0.039	0.289	0.031	0.057
Detector: FTAG (c-jet)	0.057	0.425	0.038	0.141
Detector: FTAG (l-jet)	0.005	0.100	0.015	0.007
Detector: PU	0.047	0.134	0.026	0.113
Lumi	0.008	0.018	0.011	0.012

The breakdowns of the uncertainties for all the WH POIs are given in Table 7.6 and the ZH POIs are given in Table 7.7, both for the 30 GeV jet p_T selection. For a comparison of these to the 20 GeV selections, see Appendix B.2. For the WH POIs, the dominant modelling uncertainties are for the $t\bar{t}$ background in the medium p_T^V region and the W+jets background in the high p_T^V region. For the ZH POIs, the dominant modelling uncertainties are from the Z+jets background, and in the low p_T^V region the data-driven top estimate.

TABLE 7.7: Breakdown of the contributions to the total uncertainty on the signal strength of each parameter of interest in the 10 POI unconditional STXS fit to data, for the jet p_T selection of 30 GeV. Shown in this table are all the ZH signal strengths.

Uncertainty source	**ZH, n_{jets}^{add}= 0, 75 < p_T^Z < 150 GeV**	**ZH, $n_{jets}^{add}\geq$ 1, 75 < p_T^Z < 150 GeV**	**ZH, n_{jets}^{add}= 0, 150 < p_T^Z < 250 GeV**	**ZH, $n_{jets}^{add}\geq$ 1, 150 < p_T^Z < 250 GeV**	**ZH, n_{jets}^{add}= 0, 250 < p_T^Z < 400 GeV**	**ZH, $n_{jets}^{add}\geq$ 1, 250 < p_T^Z < 400 GeV**
μ value	1.7	-0.2	1.5	1.01	0.89	0.45
Total uncertainty	0.990	1.391	0.495	0.863	0.499	0.909
DataStat	0.671	1.146	0.360	0.707	0.447	0.827
FullSyst	0.728	0.787	0.338	0.492	0.219	0.377
Data stat only	0.560	0.901	0.320	0.610	0.419	0.771
MC stat	0.275	0.308	0.095	0.151	0.103	0.174
Top-emu CR stat	0.243	0.401	0.035	0.109	0.019	0.048
Floating normalisations	0.424	0.414	0.199	0.357	0.139	0.249
Modelling: VH	0.202	0.302	0.235	0.258	0.132	0.168
Modelling: Background	0.487	0.499	0.175	0.227	0.143	0.261
Multijet	0.016	0.059	0.024	0.017	0.030	0.040
Modelling: single-top	0.037	0.036	0.015	0.032	0.005	0.027
Modelling: ttbar	0.118	0.196	0.120	0.156	0.073	0.073
Modelling: W+jets	0.094	0.068	0.032	0.034	0.019	0.062
Modelling: Z+jets	0.370	0.335	0.115	0.151	0.071	0.163
Modelling: Diboson	0.094	0.097	0.073	0.053	0.047	0.024
Experimental Syst	0.506	0.501	0.149	0.248	0.068	0.147
Detector: lepton	0.148	0.051	0.029	0.056	0.013	0.034
Detector: MET	0.324	0.371	0.048	0.037	0.035	0.067
Detector: JET	0.321	0.317	0.128	0.223	0.044	0.109
Detector: FTAG (b-jet)	0.199	0.188	0.021	0.101	0.020	0.040
Detector: FTAG (c-jet)	0.018	0.011	0.033	0.018	0.009	0.020
Detector: FTAG (l-jet)	0.014	0.036	0.009	0.013	0.005	0.020
Detector: PU	0.000	0.015	0.022	0.024	0.026	0.007
Lumi	0.014	0.011	0.011	0.009	0.007	0.007

7.3.3 Data-MC comparisons

The final thing to have a look at is how well the MC distributions match the data distributions after the likelihood fit. The 14 signal region post-fit MVA distributions in log-scale, of both the 20 and the 30 GeV jet p_T selections, are shown in Figures 7.14 for the 0-lepton 2-jet regions, Figure 7.15 for the 0-lepton 3-jet regions, Figure 7.16 for the 1-lepton 2-jet regions, Figure 7.17 for the 1-lepton 3-jet regions, Figure 7.18 for the 2-lepton 2-jet regions, and Figure 7.19 for the 2-lepton $\geq$ 3-jet regions. The log scale emphasizes how small the signal is in the reco regions best corresponding to the STXS regions that had negative signal strengths. Or in other words, the two 3-jet 1-lepton regions, and the $\geq$ 3-jet, 75$<p_T^V<$150 GeV 2-lepton region. All the MVA distributions have the transformation D applied to the binning, as described in Section 5.2.4. The pre-fit and post-fit Data-MC distributions of the 14 signal regions (with no log-scale) and 28 control regions, as defined in the likelihood fit, are provided in Appendix A.3. A comparison of the pre-fit to post-fit yields for all the signal regions are provided in Appendix A.1. For a comparison of the control region yields, looking at the Data-MC plots should be fine since they are single-binned distributions.

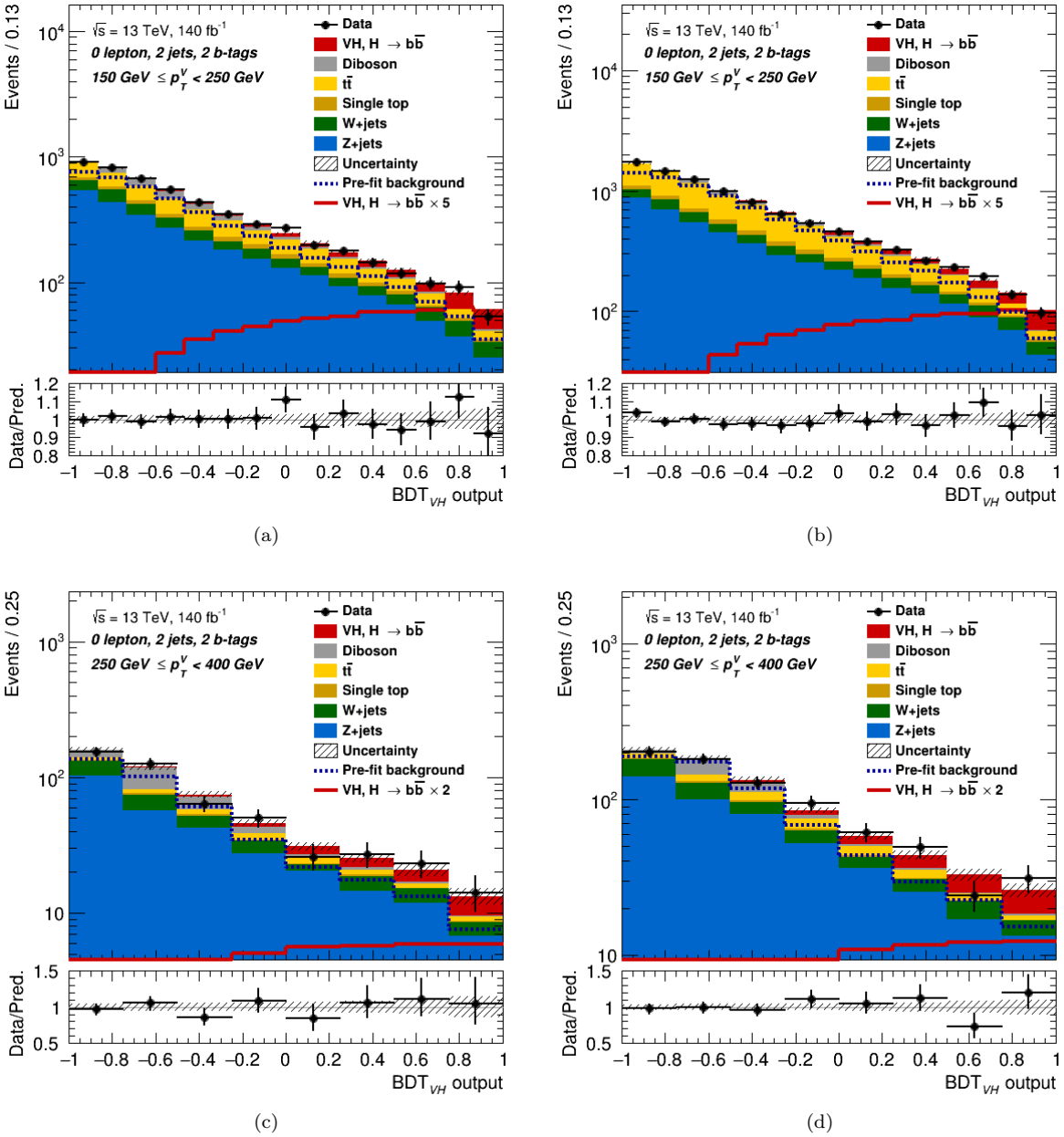

FIGURE 7.14: The data-MC plots of the post-fit BDT distribution, in the log scale, for the 0-lepton, 2-jet, signal regions. The top row shows the 150 $< p_T^V <$ 250 GeV region, while the bottom row shows the 250 $< p_T^V <$ 400 GeV region. The left column has the jet p_T selections of 20 GeV, while the right column has jet p_T selections of 30 GeV. The red line is the signal (filled red histogram) scaled by the factor given in the legend so that the shape of the signal is easier to see, and the dashed blue line is the total pre-fit background. The bottom sub-plot shows the ratio of the data to the theory prediction, along with the relative post-fit error given by the shaded band.

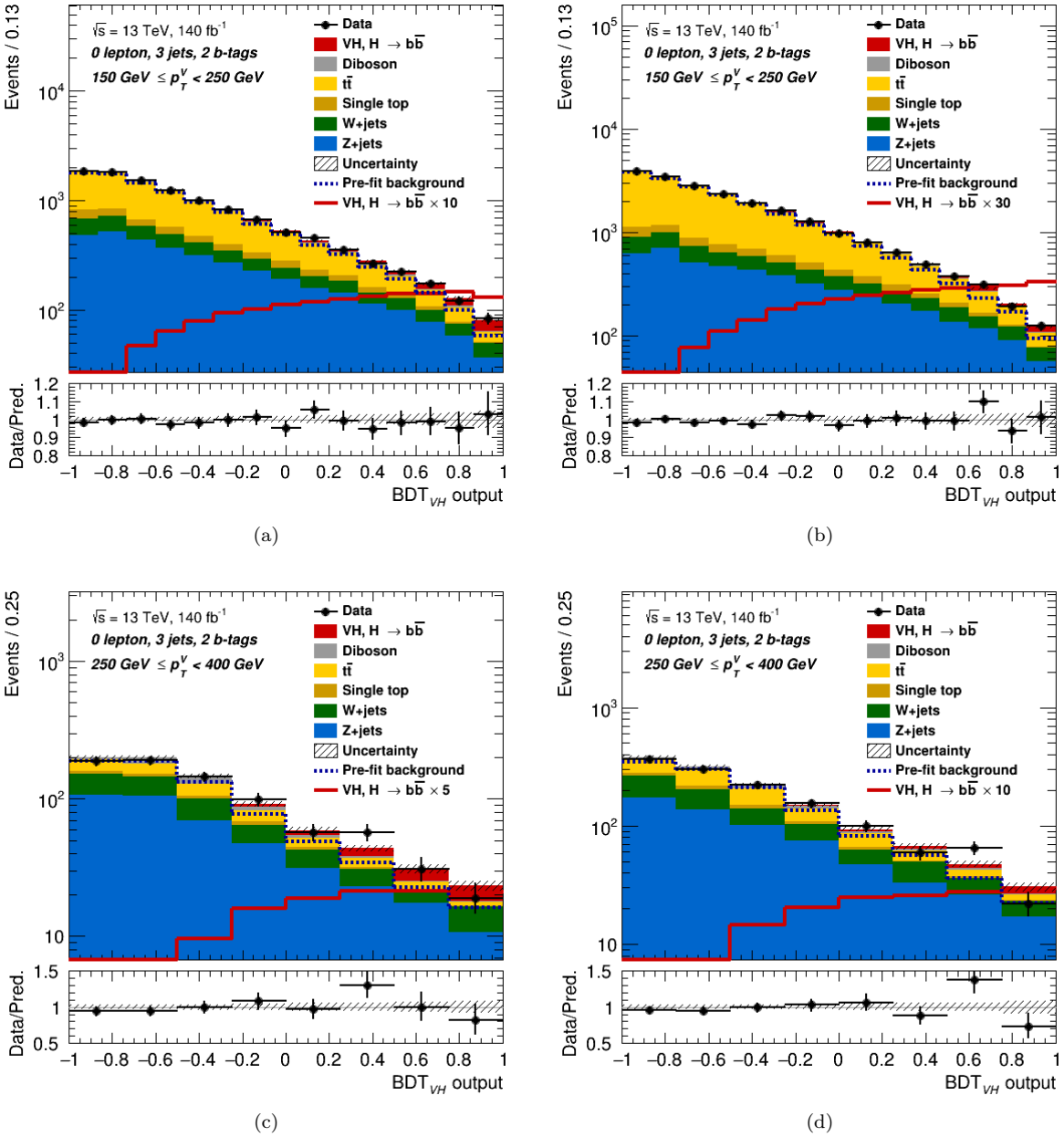

FIGURE 7.15: The data-MC plots of the post-fit BDT distribution, in the log scale, for the 0-lepton, 3-jet, signal regions. The top row shows the 150 $< p_T^V <$ 250 GeV region, while the bottom row shows the 250 $< p_T^V <$ 400 GeV region. The left column has the jet p_T selections of 20 GeV, while the right column has jet p_T selections of 30 GeV. The red line is the signal (filled red histogram) scaled by the factor given in the legend so that the shape of the signal is easier to see, and the dashed blue line is the total pre-fit background. The bottom sub-plot shows the ratio of the data to the theory prediction, along with the relative post-fit error given by the shaded band.

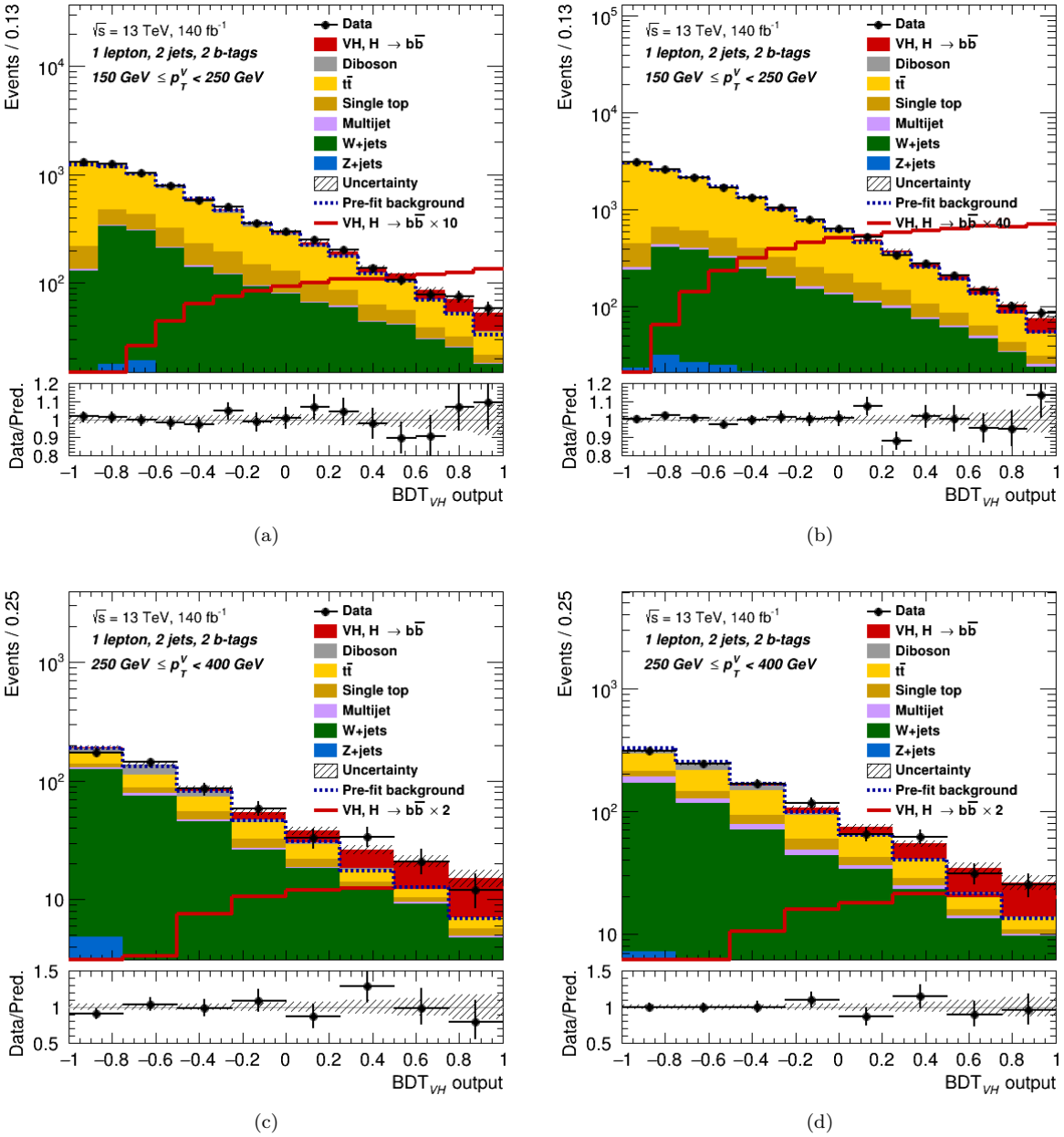

FIGURE 7.16: The data-MC plots of the post-fit BDT distribution, in the log scale, for the 1-lepton, 2-jet, signal regions. The top row shows the 150 $< p_T^V <$ 250 GeV region, while the bottom row shows the 250 $< p_T^V <$ 400 GeV region. The left column has the jet p_T selections of 20 GeV, while the right column has jet p_T selections of 30 GeV. The red line is the signal (filled red histogram) scaled by the factor given in the legend so that the shape of the signal is easier to see, and the dashed blue line is the total pre-fit background. The bottom sub-plot shows the ratio of the data to the theory prediction, along with the relative post-fit error given by the shaded band.

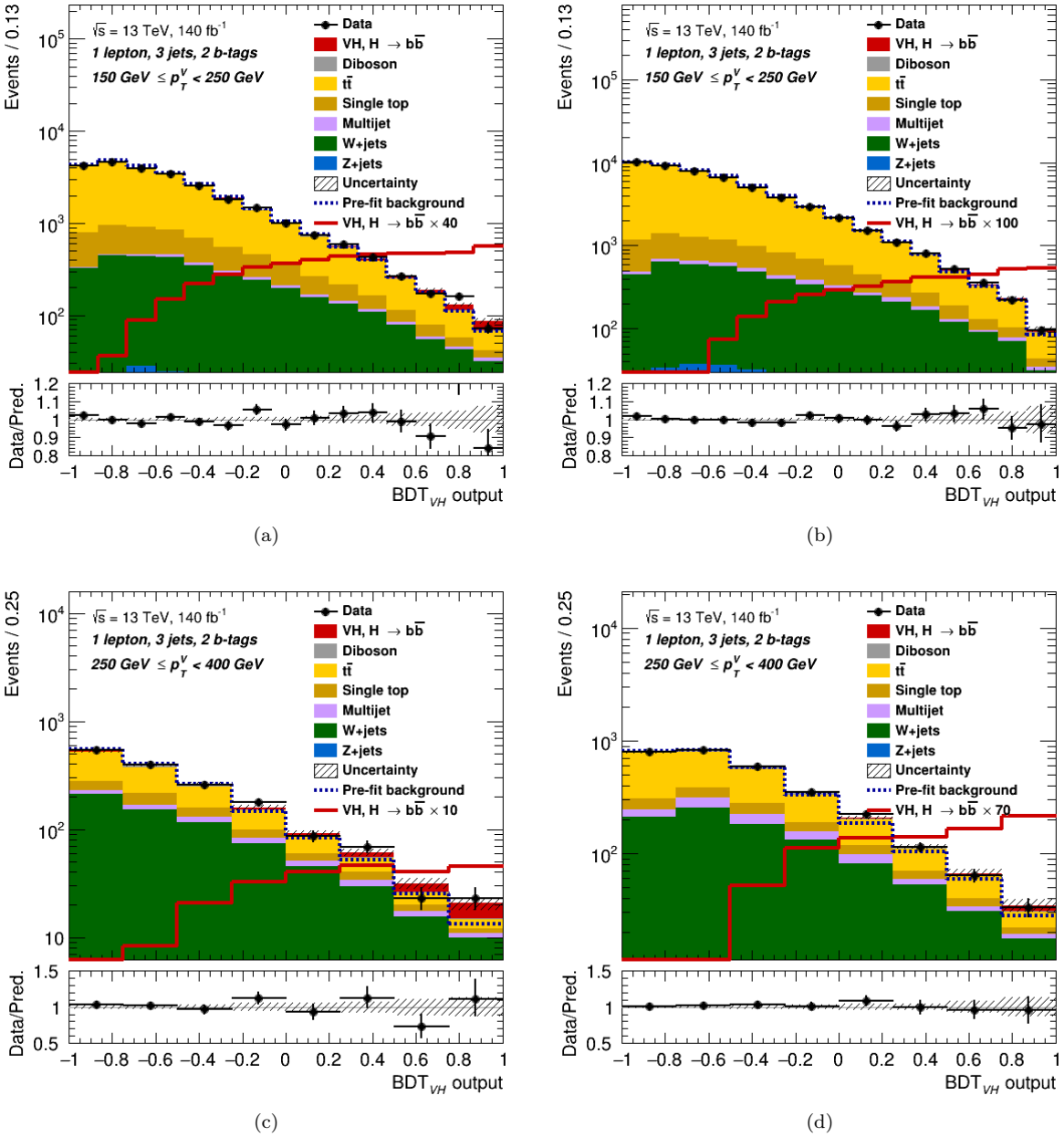

FIGURE 7.17: The data-MC plots of the post-fit BDT distribution, in the log scale, for the 1-lepton, 3-jet, signal regions. The top row shows the 150 $< p_T^V <$ 250 GeV region, while the bottom row shows the 250 $< p_T^V <$ 400 GeV region. The left column has the jet p_T selections of 20 GeV, while the right column has jet p_T selections of 30 GeV. The red line is the signal (filled red histogram) scaled by the factor given in the legend so that the shape of the signal is easier to see, and the dashed blue line is the total pre-fit background. The bottom sub-plot shows the ratio of the data to the theory prediction, along with the relative post-fit error given by the shaded band.

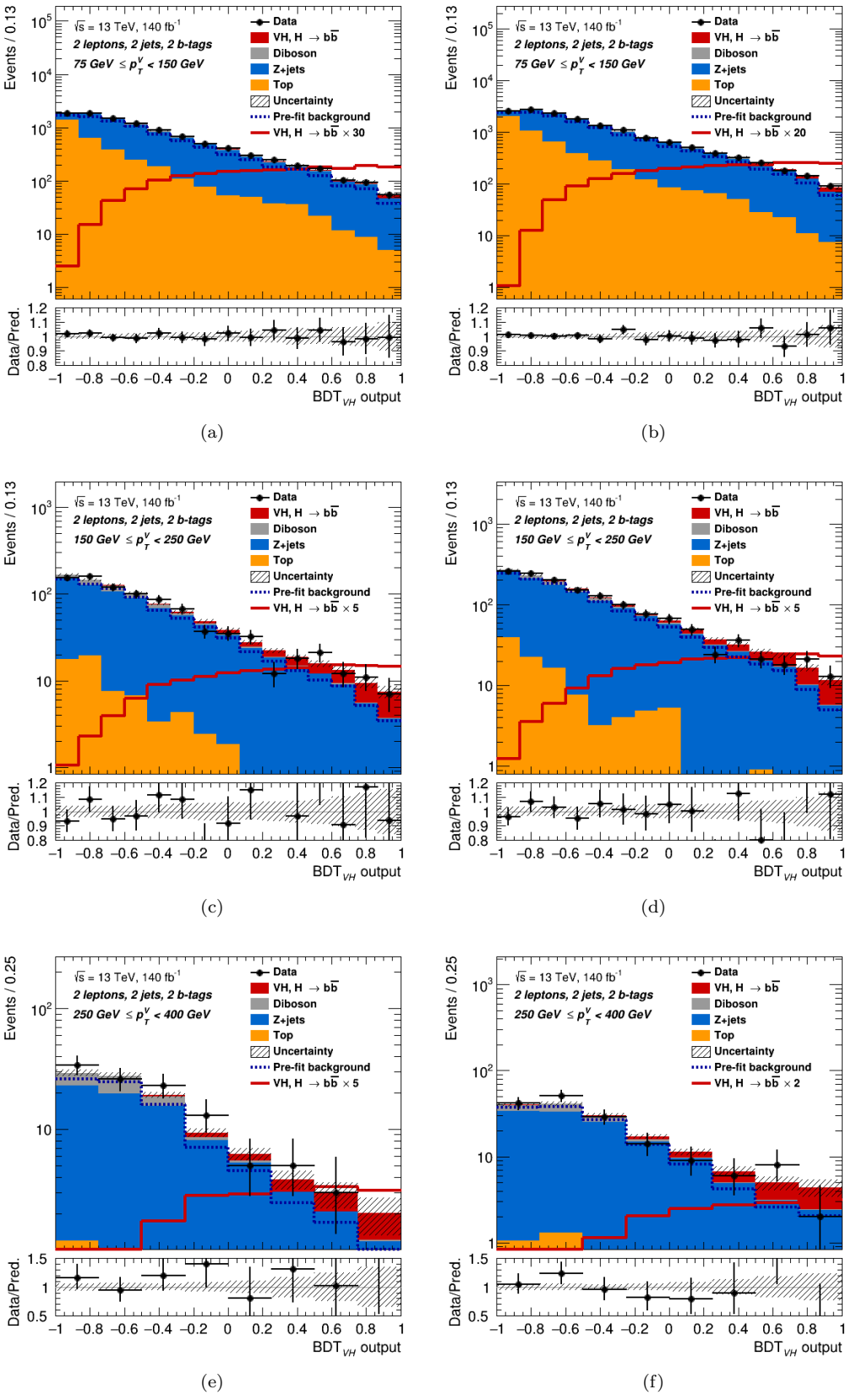

FIGURE 7.18: The data-MC plots of the post-fit BDT distribution, in the log scale, for the 2-lepton, 2-jet, signal regions. The top row shows the 75 $< p_T^V <$ 150 GeV region, the middle row the 150 $< p_T^V <$ 250 GeV region, and the bottom row shows the 250 $< p_T^V <$ 400 GeV region. The left column has the jet p_T selections of 20 GeV, while the right column has jet p_T selections of 30 GeV. The red line is the signal (filled red histogram) scaled by the factor given in the legend so that the shape of the signal is easier to see, and the dashed blue line is the total pre-fit background. The bottom sub-plot shows the ratio of the data to the theory prediction, along with the relative post-fit error given by the shaded band.

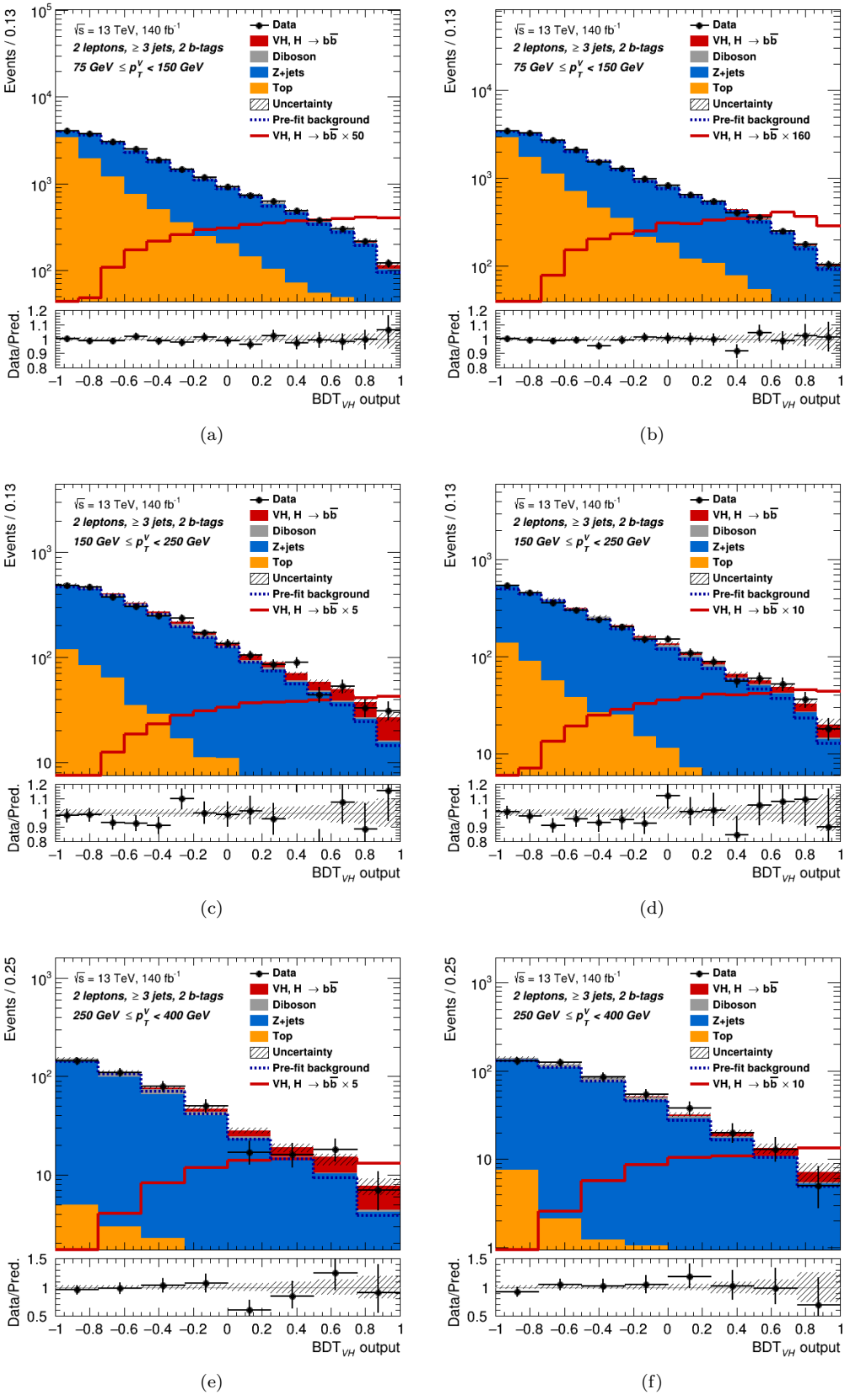

FIGURE 7.19: The data-MC plots of the post-fit BDT distribution, in the log scale, for the 2-lepton, $\geq$ 3-jet, signal regions. The top row shows the 75 $< p_T^V <$ 150 GeV region, the middle row the 150 $< p_T^V <$ 250 GeV region, and the bottom row shows the 250 $< p_T^V <$ 400 GeV region. The left column has the jet p_T selections of 20 GeV, while the right column has jet p_T selections of 30 GeV. The red line is the signal (filled red histogram) scaled by the factor given in the legend so that the shape of the signal is easier to see, and the dashed blue line is the total pre-fit background. The bottom sub-plot shows the ratio of the data to the theory prediction, along with the relative post-fit error given by the shaded band.

One thing of particular interest that is noticeable in the plots, is the larger multijet contribution in the 30 GeV jet p_T selection plots, particularly the 3-jet regions (Figure 7.17). While the increase looks to be more in the background bins of the MVA distribution, the post-fit distributions of some extra variables were looked at to see if there was any possible mismodelling of the multijet background. In particular, the m_T^W and E_T^{miss} distributions. These post-fit plots were obtained from a likelihood built using the results of the fit to the MVA distributions. The m_T^W distribution was used to calculate the pre-fit yields of the multijet estimates, and the E_T^{miss} distribution discriminates the multijet background the best. Firstly looking at the m_T^W distributions in Figure 7.20 for the four different 1-lepton signal regions. There is no obvious mismodelling apparent, though with the regions split by p_T^V , it can be seen how in the high p_T^V regions the multijet background has a significant contribution at the high m_T^W values. Looking at the E_T^{miss} distributions, in Figure 7.21, for the same four regions, some mismodelling is present. Just as a note, the sharp jump at $E_T^{miss} = 30$ GeV is due to the extra selection in the electron channel of $E_T^{miss} > 30$ GeV to reduce the multijet background. There seems to be a general trend of the MC over-shooting the data in the low E_T^{miss} regions, while the opposite happens in the higher E_T^{miss} regions. This is particularly evident in the 3-jet regions, where some bins disagree by up to 25%, although there is a large uncertainty in those bins as well, making this large discrepancy not statistically significant. The bins where the multijet background is largest tend to over-shoot the data, while where the it is smallest, the data is larger than the prediction. Looking at the rankings in Figure 7.12, the normalisation of the 3-jet electron multijet sample for the 30 GeV jet p_T selection has a large upward pull of about 1.3 (third NP). Since the μ-channel multijet contribution is negligible in the 3-jet regions, this e-channel pull is affecting the entire multijet estimate in these regions. This is a bit counter-intuitive since one would expect the increased jet p_T selections to reduce the softer multijet contribution. The error bars on the pull of the normalisation of the 3-jet electron multijet sample are larger than 1, indicating that the data is providing less information on this multijet sample than was expected. As a reminder, the 3-jet, 1-lepton regions are the regions where two of the three negative signal strength STXS signal samples are most dominant. This could be one of the reasons for the low signal strengths.

Other kinematic distributions were examined to try find a reason for why the comparison of the observed to expected significances for the 30 GeV jet p_T selection was was so different compared to the 20 GeV jet p_T selection. However, there were no significant differences found between the data and MC, nor any consistent differences that may account for difference in the behaviour of the significances. As examples, the post-fit distribution of the p_T of the third jet was studied, since these jets are the ones that have the additional p_T selection applied to. Also the η distribution of the third jet was studied to see if there were any differences between events where the third jet was a central jet and the events where it's a forward jet. There was general agreement between the MC and the data, and no bins that had large uncertainties like in the E_T^{miss} distribution in Figure 7.21. Given that events were migrating down from higher

n_{jets} categories, it was thought the difference in the modelling between the lower n_{jets} regions and the higher n_{jets} regions may have contributed to the difference in the behaviour of the significances. However, since the free-floating normalisation NPs are separate for the 2-jet and 3-jet regions, the effect of any mismodelling would be covered by these NPs.
So despite all these checks into the possible cause of the differences between the 20 GeV and 30 GeV additional jet p_T selection results, no clear cause of mismodelling could be found. And considering how large the uncertainties are on the results, and that they agree with the SM expectations, the variation between the 20 and 30 GeV results is likely due to statistical fluctuations. This is particularly relevant to the $n_{jets}^{add} \geq 1$ POIs.

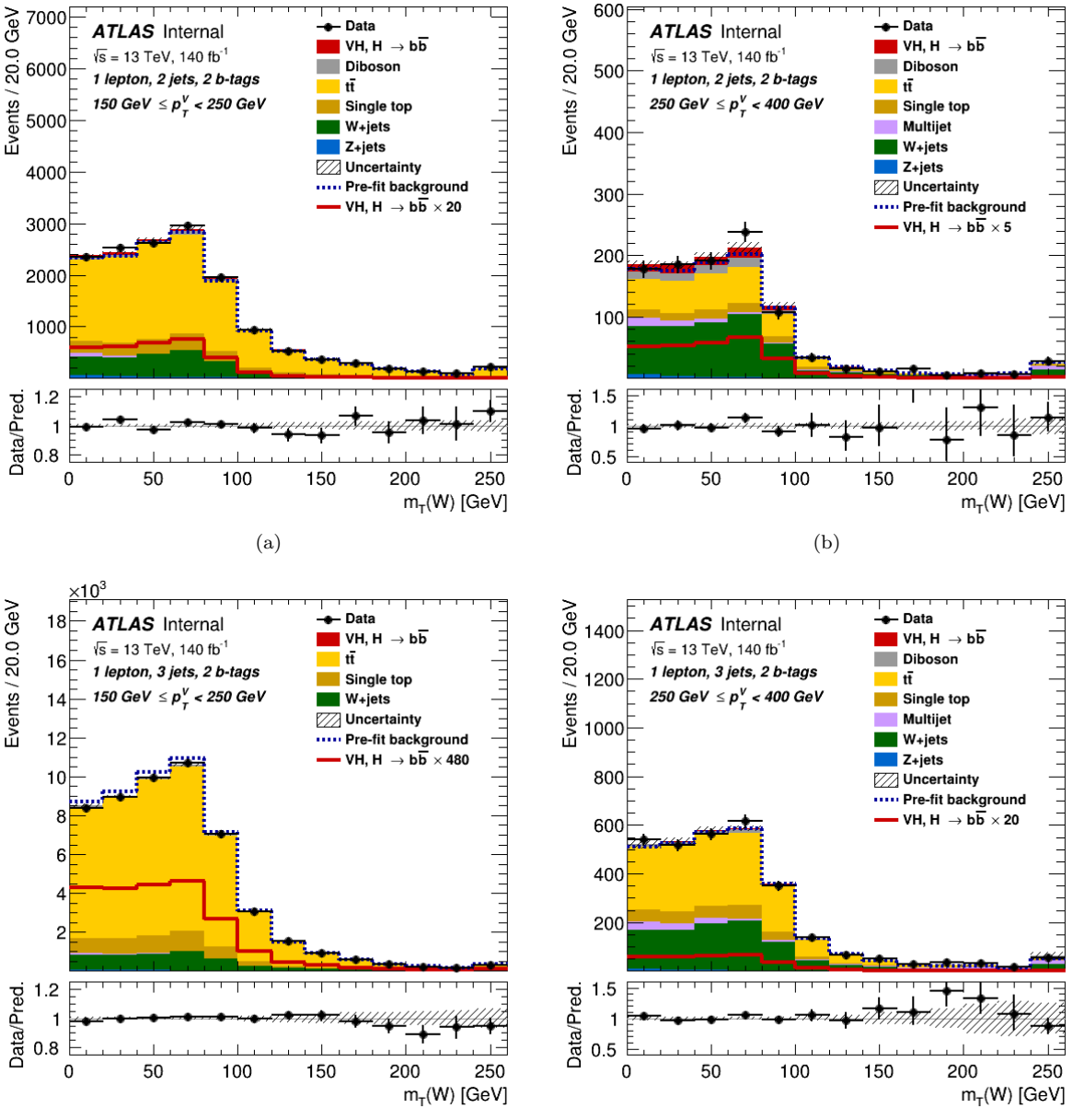

FIGURE 7.20: The data-MC plots of the 30 GeV jet p_T selection post-fit m_T^W distributions for the 1-lepton signal regions. The top row has the 2-jet regions, with the 3-jet regions in the bottom row, and the left column has the $150 < p_T^V < 250$ GeV regions, while the right contains the $250 < p_T^V < 400$ GeV regions. The red line is the signal (filled red histogram) scaled by the factor given in the legend so that the shape of the signal is easier to see, and the dashed blue line is the total pre-fit background. The bottom sub-plot shows the ratio of the data to the theory prediction, along with the relative post-fit error given by the shaded band.

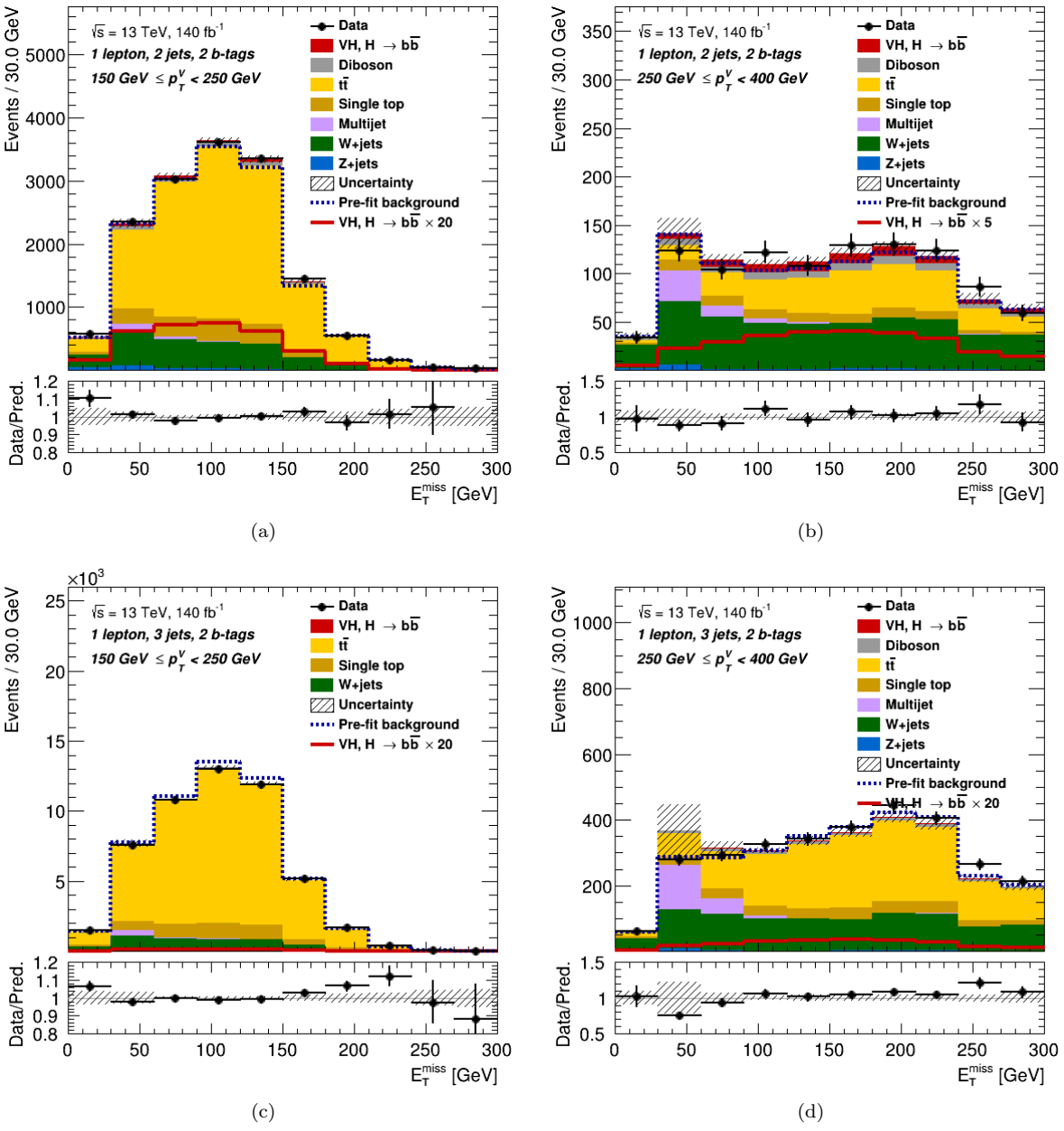

FIGURE 7.21: The data-MC plots of the 30 GeV jet p_T selection post-fit E_T^{miss} distributions for the 1-lepton signal regions. The top row has the 2-jet regions, with the 3-jet regions in the bottom row, and the left column has the 150 $< p_T^V <$ 250 GeV regions, while the right contains the 250 $< p_T^V <$ 400 GeV regions. The sharp jump at $E_T^{miss} = 30$ GeV is due to the extra selection in the electron channel of $E_T^{miss} > 30$ GeV to reduce the multijet background. The red line is the signal (filled red histogram) scaled by the factor given in the legend so that the shape of the signal is easier to see, and the dashed blue line is the total pre-fit background. The bottom sub-plot shows the ratio of the data to the theory prediction, along with the relative post-fit error given by the shaded band.

Chapter 8

Conclusion

After the discovery of several SM particles at CERN during its lifetime, we are now at a point where we are not confident in the direction from which the next discovery is going to come. As such, there is now a bigger focus on performing precision measurements of SM processes. In particular, given how central the Higgs mechanism and Higgs boson are to the SM, performing precision measurements of Higgs processes is our opportunity of finding any deviations from the SM and any hints of possible beyond the SM theories.

This thesis presents an updated study of the production of the SM Higgs boson in association with a W or a Z boson, where the Higgs boson decays to a $b\bar{b}$ pair and the W/Z bosons decay leptonically. The data used was the full Run-2 ATLAS dataset, corresponding to 140 fb^{-1} of integrated luminosity, which was collected in proton-proton collisions at a centre of mass energy of $\sqrt{s} = 13$ TeV. The study was performed within the STXS framework, which provides smaller kinematic regions within which to measure the signal strengths and cross-sections of Higgs boson production. These smaller regions provide phase spaces where BSM effects may become more prominent, and that could otherwise be washed out in fully fiducial measurements.

The work in this thesis expanded on the previous ATLAS STXS measurement of the $VH \to b\bar{b}$ process [24] by splitting each of the STXS regions by the number of truth jets additional to the truth jets produced by the Higgs decay. Additionally, since this new split would separate events by the number of jets they contain, an increase in the jet p_T selection from 20 to 30 GeV was applied to the additional jets which improved the correlation between the STXS regions and the reconstruction level regions, reducing the uncertainties on the measurements.

The inclusive VH signal strengths were measured with observed (expected) significances of 7.6 (6.4) and 6.9 (6.2) for the 20 and 30 GeV p_T selections, respectively. Additionally, the ZH process was observed with an observed (expected) significance of 5.4 (4.6) and 5.0 (4.5) for the 20 and 30 GeV selection respectively. The WH process was measured with an observed (expected) significance of 4.9 (4.1) and 4.1 (3.7) for the 20 and 30 GeV selection respectively. The corresponding signal strengths were measured to be $\mu = 1.22 \pm 0.19$ for the 20 GeV jet

p_T selection and $\mu = 1.13 \pm 0.19$ for 30 GeV jet p_T selection for the VH processes. The ZH processes obtained $\mu = 1.21 \pm 0.27$ and $\mu = 1.14 \pm 0.27$ for the 20 and 30 GeV selections respectively, and the WH processes obtained $\mu = 1.23 \pm 0.28$ and $\mu = 1.12 \pm 0.29$ for the 20 and 30 GeV selections respectively. The measurements of the expanded STXS regions showed that the uncertainties on the $n_{jets}^{add} \geq 1$ signal strengths are still too large to make any statistically significant conclusions. However, tightening the selection on the additional-jet p_T did reduce these uncertainties by about 25% on average. The ZH, $150 < p_T^V < 250$ GeV, $n_{jets}^{add} = 0$ signal strength was the only one to not agree within 1 sigma of the SM expectation, instead agreeing comfortably within 2 sigma. Unfortunately, three of the $n_{jets}^{add} \geq 1$ signal strengths had negative values in the 30 GeV selection. It is promising to see that despite this, the uncertainties on the signal strengths in these regions were still reduced, and the central values were within 1 sigma of the SM expectations. Despite various studies, there were no clear causes for this negative shift. It is likely due to statistical fluctuations, given the larger migration of background relative to signal into the 3-jet regions compared to the 2-jet regions, and the fit thus favouring the background. Although the uncertainties on the $n_{jets}^{add} \geq 1$ signal strengths were large, the uncertainties of the $n_{jets}^{add} = 0$ WH and $n_{jets}^{add} = 0$ ZH signal strengths were only 18% to 24% and 26% to 32% respectively larger compared to their corresponding signal strengths with no jet splitting (The 5 POI signal strengths). This shows how the non-jet-split signal strengths are dominated by the $n_{jets}^{add} = 0$ signal, and that splitting by n_{jets}^{add} still provides statistically significant results for the $n_{jets}^{add} = 0$ signal strengths. Additionally, the increased p_T selection on the additional central jets reduced the uncertainties on the signal strengths that had very large uncertainties (the $n_{jets}^{add} \geq 1$ signal strengths), while only slightly increasing the uncertainties on the signal strengths that had the smaller uncertainties (the $n_{jets}^{add} = 0$ signal strengths). The reduction of up to 30% in the large uncertainties outweighs the small increase of up to 5% in the smaller uncertainties. The results also show the intended reduction of the correlations between the signal strengths in the maximum likelihood fit. The results of the expected significances shown in this thesis led to the new ATLAS analysis using the increased jet p_T selection.

There are several changes that could be implemented in this thesis that would help reduce uncertainties in the results and which are implemented by the new ATLAS analysis [23]. Due to time constraints, these changes weren't implemented in this thesis, although despite this, the results are still reasonable, agreeing well with the standard model. The implemented changes include deriving the $\Delta R(b_1, b_2) - p_T^V$ cuts that define the signal region split by the number of leptons. The definitions obtained in the 1-lepton channel didn't describe the 2-lepton channel as well as in the 0-lepton channel, as illustrated in Figure 5.9. Therefore, deriving them separately in the 2-lepton channel ensures the desired amount of signal events in the signal regions.

In relation to the truth flavours of the jets that pass the b-tagging, with the updated tagger that is used in this thesis, the rejection of non-b-jets is higher. This reduces the number of events in the lighter jet categories, making it difficult to model them in the fit. Combining some of these regions in the V+jets samples helps improve the modelling of those backgrounds. For example,

reducing the current three separate event flavours based on the truth flavour of the two tagged jets of heavy flavour (bb, bc, bl, cc), cl and ll, to just two flavours, heavy (bb and cc) and other (bc, bl, cl, ll). In the new ATLAS analysis, ll flavoured events are left separate due to their larger contribution in the regions targeting $VH \to c\bar{c}$. With the large migrations that occur for the $t\bar{t}$ background after tightening the jet p_T selection, more focus on this background is needed. The difference is large enough in the distributions between the bb flavoured and bc flavoured $t\bar{t}$ events, as shown in Figure 7.5, to warrant splitting the $t\bar{t}$ events by flavour in a similar way that is done for the V+jets backgrounds, but with the reduced categories as mentioned above. This removes the dominant effect of the bb $t\bar{t}$ component on the bc component in the 3-jet and high p_T^V regions.

Given how many of the $t\bar{t}$ events have W-bosons from the top quark decay decaying into τ-leptons , shown in Figure 7.6, using a τ-tagger to identify the τ-jets helps to classify the events into the correct n_{jets} category, improving correlations between the STXS and analysis regions.

The control region distributions in the likelihood fit currently only use a one binned distribution. A final potential change would be to instead use a multi-binned distribution in these regions, providing better constraints on the backgrounds. In the new ATLAS analysis, this is implemented in the 1- and 2-lepton channels, using a BDT distribution trained to separate W+jets and $t\bar{t}$ in the 1-lepton CRLow, and a p_T^V distribution in CRHigh for both 1- and 2-lepton channels. My suggested implementation for the analysis in this thesis would be to use 3- and 5-binned E_T^{miss} distribution for the CRLow and CRHigh respectively. The E_T^{miss} distribution has a better discrimination between $t\bar{t}$ and V+jets in the 1- and 2-lepton channels compared to p_T^V , with $p_T^V \equiv E_T^{miss}$ in the 0-lepton channel. The E_T^{miss} distribution will also help discriminate against the MJ background in the 1-lepton channel, which seems to be under-constrained in this thesis (refer to the large pull on the MJ normalisation in Figure 7.12 and the E_T^{miss} distribution in Figure 7.21).

The larger data sets anticipated from Run-3 of the Large Hadron Collider, along with reduced statistical uncertainties and improved analysis techniques, should enhance the statistical significance of measurements in the expanded STXS regions in the near future.

Appendix A

Data-MC plots and yields

This appendix contains extra information on the 10 POI STXS fit described in Chapter 7. In particular, the pre-fit and post-fit yields A.1 and Data-MC plots A.3 with comparisons between the jet p_T selection of 20 GeV and 30 GeV. There is also a particular look at the yield differences of the MC samples used to define the signal and control regions A.2 using the $\Delta R(b_1, b_2) - p_T^V$ selections.

A.1 Pre-fit and post-fit yield tables

This section shows a comparison of the 14 post-fit to pre-fit signal region yields of the 10 POI STXS fits, for both the 20 GeV and 30 GeV jet p_T selections. The control region yields are not shown in these tables, however the control region Data-MC plots are shown in Section A.3. Since the control regions use single binned distributions, the plots are essentially showing the yields of those regions. The yields tables are as follows:

- 0-lepton, 2-jet, 150 $< p_T^V <$ 250 GeV signal region: Table A.1
- 0-lepton, 3-jet, 150 $< p_T^V <$ 250 GeV signal region: Table A.2
- 0-lepton, 2-jet, 250 $< p_T^V <$ 400 GeV signal region: Table A.3
- 0-lepton, 3-jet, 250 $< p_T^V <$ 400 GeV signal region: Table A.4
- 1-lepton, 2-jet, 150 $< p_T^V <$ 250 GeV signal region: Table A.5
- 1-lepton, 3-jet, 150 $< p_T^V <$ 250 GeV signal region: Table A.6
- 1-lepton, 2-jet, 250 $< p_T^V <$ 400 GeV signal region: Table A.7
- 1-lepton, 3-jet, 250 $< p_T^V <$ 400 GeV signal region: Table A.8
- 2-lepton, 2-jet, 75 $< p_T^V <$ 150 GeV signal region: Table A.9
- 2-lepton, $\geq$ 3-jet, 75 $< p_T^V <$ 150 GeV signal region: Table A.10
- 2-lepton, 2-jet, 150 $< p_T^V <$ 250 GeV signal region: Table A.11
- 2-lepton, $\geq$ 3-jet, 150 $< p_T^V <$ 250 GeV signal region: Table A.12
- 2-lepton, 2-jet, 250 $< p_T^V <$ 400 GeV signal region: Table A.13
- 2-lepton, $\geq$ 3-jet, 250 $< p_T^V <$ 400 GeV signal region: Table A.14

TABLE A.1: The post-fit vs pre-fit yields for the 0-lepton, 2-jet, 150 $< p_T^V <$ 250 GeV signal region. The upper table is for the 20 GeV jet p_T selection, while the lower table is for 30 GeV. The percentages in the brackets next to the background (signal) yields are the percentage of that sample relative to the total background (signal). For the STXS regions, the number of jets is the number of jets additional to the Higgs decay. The other ZH and WH yields are the signal events that fall outside of the STXS regions under study. The Z+hf sample is the heavy flavour component of the Z+jets sample, likewise for W+jets. Tops is the sum of the $t\bar{t}$ and Single-top samples.

	Pre-fit	**Post-fit**	**Post/Pre**
Z+hf	2050.0 ± 280.0	2720.0 ± 110.0	1.33 ± 0.19
Z+jets	2050.0 ± 280.0 (48.8%)	2730.0 ± 110.0 (54.9%)	1.33 ± 0.19
W+hf	546.0 ± 65.0	565.0 ± 65.0	1.03 ± 0.17
W+jets	565.0 ± 70.0 (13.4%)	585.0 ± 66.0 (11.8%)	1.04 ± 0.17
Single-top	231.0 ± 43.0 (5.5%)	210.0 ± 32.0 (4.2%)	0.91 ± 0.22
$t\bar{t}$	1010.0 ± 210.0 (24.0%)	1090.0 ± 110.0 (21.9%)	1.08 ± 0.25
Tops	1240.0 ± 230.0	1300.0 ± 110.0	1.05 ± 0.21
diboson	345.0 ± 97.0 (8.2%)	358.0 ± 54.0 (7.2%)	1.04 ± 0.33
Other ZH	0.00 ± 0.00 (0.0%)	0.00 ± 0.00 (0.0%)	0.91 ± 0.92
ZH, 75 $< p_T^Z <$150 GeV, n_{jets}^{add}=0	9.6 ± 2.3 (6.9%)	10.5 ± 9.2 (6.3%)	1.09 ± 0.99
ZH, 75 $< p_T^Z <$150 GeV, $n_{jets}^{add}\geq$1	0.52 ± 0.38 (0.4%)	0.31 ± 0.78 (0.2%)	0.6 ± 1.6
ZH, 150 $< p_T^Z <$250 GeV, n_{jets}^{add}=0	85.0 ± 14.0 (60.7%)	106.0 ± 36.0 (63.8%)	1.25 ± 0.47
ZH, 150 $< p_T^Z <$250 GeV, $n_{jets}^{add}\geq$1	2.9 ± 1.1 (2.1%)	5.7 ± 3.4 (3.4%)	2 ± 1.4
ZH, 250 $< p_T^Z <$400 GeV, n_{jets}^{add}=0	9.2 ± 1.9 (6.6%)	4.3 ± 4.1 (2.6%)	0.47 ± 0.46
ZH, 250 $< p_T^Z <$400 GeV, $n_{jets}^{add}\geq$1	0.43 ± 0.21 (0.3%)	0.67 ± 0.52 (0.4%)	1.6 ± 1.4
Other WH	2.21 ± 0.98 (1.6%)	2.10 ± 0.92 (1.3%)	0.95 ± 0.59
WH, 150 $< p_T^W <$250 GeV, n_{jets}^{add}=0	22.9 ± 2.8 (16.4%)	28.0 ± 10.0 (16.9%)	1.22 ± 0.46
WH, 150 $< p_T^W <$250 GeV, $n_{jets}^{add}\geq$1	0.6 ± 0.21 (0.4%)	0.9 ± 1.7 (0.5%)	1.5 ± 2.9
WH, 250 $< p_T^W <$400 GeV, n_{jets}^{add}=0	6.34 ± 0.8 (4.5%)	7.5 ± 2.8 (4.5%)	1.18 ± 0.47
WH, 250 $< p_T^W <$400 GeV, $n_{jets}^{add}\geq$1	0.228 ± 0.083 (0.2%)	0.04 ± 0.42 (0.0%)	0.2 ± 1.8
Signal	138.0 ± 19.0	164.0 ± 36.0	1.19 ± 0.31
Background	4210.0 ± 510.0	4981.0 ± 65.0	1.18 ± 0.14
Data	5177.0	5177.0	1.00e+00

	Pre-fit	**Post-fit**	**Post/Pre**
Z+hf	3420.0 ± 400.0	4480.0 ± 180.0	1.31 ± 0.16
Z+jets	3440.0 ± 400.0 (42.5%)	4500.0 ± 180.0 (48.6%)	1.31 ± 0.16
W+hf	917.0 ± 95.0	870.0 ± 110.0	0.95 ± 0.16
W+jets	950.0 ± 100.0 (11.7%)	880.0 ± 110.0 (9.5%)	0.93 ± 0.15
Single-top	462.0 ± 83.0 (5.7%)	396.0 ± 64.0 (4.3%)	0.86 ± 0.21
$t\bar{t}$	2760.0 ± 490.0 (34.1%)	3110.0 ± 210.0 (33.6%)	1.13 ± 0.21
Tops	3220.0 ± 520.0	3510.0 ± 200.0	1.09 ± 0.19
diboson	490.0 ± 130.0 (6.0%)	375.0 ± 67.0 (4.0%)	0.77 ± 0.24
Other ZH	0.02 ± 0.02 (0.0%)	0.02 ± 0.01 (0.0%)	0.9 ± 1.1
ZH, 75 $< p_T^Z <$150 GeV, n_{jets}^{add}=0	14.8 ± 3.5 (7.3%)	24.0 ± 15.0 (9.3%)	1.6 ± 1.1
ZH, 75 $< p_T^Z <$150 GeV, $n_{jets}^{add}\geq$1	1.16 ± 0.79 (0.6%)	-0.2 ± 1.6 (-0.1%)	-0.2 ± -1.4
ZH, 150 $< p_T^Z <$250 GeV, n_{jets}^{add}=0	119.0 ± 19.0 (58.5%)	164.0 ± 47.0 (63.4%)	1.38 ± 0.45
ZH, 150 $< p_T^Z <$250 GeV, $n_{jets}^{add}\geq$1	7.7 ± 2.8 (3.8%)	6.9 ± 6.3 (2.7%)	0.9 ± 0.88
ZH, 250 $< p_T^Z <$400 GeV, n_{jets}^{add}=0	12.2 ± 2.5 (6.0%)	9.7 ± 5.3 (3.7%)	0.8 ± 0.46
ZH, 250 $< p_T^Z <$400 GeV, $n_{jets}^{add}\geq$1	0.99 ± 0.48 (0.5%)	0.39 ± 0.8 (0.2%)	0.39 ± 0.83
Other WH	3.80 ± 1.70 (1.9%)	3.80 ± 1.60 (1.5%)	1 ± 0.61
WH, 150 $< p_T^W <$250 GeV, n_{jets}^{add}=0	33.3 ± 3.1 (16.4%)	39.0 ± 15.0 (15.1%)	1.17 ± 0.46
WH, 150 $< p_T^W <$250 GeV, $n_{jets}^{add}\geq$1	1.69 ± 0.57 (0.8%)	-0.2 ± 3.5 (-0.1%)	-0.1 ± -2.1
WH, 250 $< p_T^W <$400 GeV, n_{jets}^{add}=0	8.21 ± 0.89 (4.0%)	11.4 ± 3.9 (4.4%)	1.39 ± 0.5
WH, 250 $< p_T^W <$400 GeV, $n_{jets}^{add}\geq$1	0.54 ± 0.19 (0.3%)	-0.09 ± 0.7 (-0.0%)	-0.2 ± -1.3
Signal	200.0 ± 26.0	256.0 ± 48.0	1.28 ± 0.29
Background	8100.0 ± 840.0	9269.0 ± 92.0	1.14 ± 0.12
Data	9526.0	9526.0	1.00e+00

TABLE A.2: The post-fit vs pre-fit yields for the 0-lepton, 3-jet, 150 $<p_T^V <$ 250 GeV signal region. The upper table is for the 20 GeV jet p_T selection, while the lower table is for 30 GeV. The percentages in the brackets next to the background (signal) yields are the percentage of that sample relative to the total background (signal). For the STXS regions, the number of jets is the number of jets additional to the Higgs decay. The other ZH and WH yields are the signal events that fall outside of the STXS regions under study. The Z+hf sample is the heavy flavour component of the Z+jets sample, likewise for W+jets. Tops is the sum of the $t\bar{t}$ and Single-top samples.

	Pre-fit	**Post-fit**	**Post/Pre**
Z+hf	2920.0 ± 320.0	3490.0 ± 170.0	1.2 ± 0.14
Z+jets	2930.0 ± 320.0 (28.1%)	3500.0 ± 170.0 (31.8%)	1.19 ± 0.14
W+hf	1170.0 ± 110.0	1140.0 ± 120.0	0.97 ± 0.14
W+jets	1190.0 ± 110.0 (11.4%)	1150.0 ± 120.0 (10.4%)	0.97 ± 0.13
Single-top	750.0 ± 140.0 (7.2%)	710.0 ± 130.0 (6.4%)	0.95 ± 0.25
$t\bar{t}$	5200.0 ± 1200.0 (49.8%)	5410.0 ± 240.0 (49.1%)	1.04 ± 0.24
Tops	6000.0 ± 1200.0	6120.0 ± 200.0	1.02 ± 0.21
diboson	370.0 ± 110.0 (3.5%)	253.0 ± 64.0 (2.3%)	0.68 ± 0.27
Other ZH	0.04 ± 0.12 (0.0%)	0.03 ± 0.08 (0.0%)	0.7 ± 3.1
ZH, 75 $< p_T^Z <$150 GeV, n_{jets}^{add}=0	6.5 ± 2.6 (5.0%)	7.6 ± 7.1 (4.0%)	1.2 ± 1.2
ZH, 75 $< p_T^Z <$150 GeV, $n_{jets}^{add}\geq$1	4.0 ± 1.2 (3.1%)	2.7 ± 6.8 (1.4%)	0.7 ± 1.7
ZH, 150 $< p_T^Z <$250 GeV, n_{jets}^{add}=0	45.6 ± 8.7 (34.8%)	61.0 ± 22.0 (31.9%)	1.34 ± 0.55
ZH, 150 $< p_T^Z <$250 GeV, $n_{jets}^{add}\geq$1	35.7 ± 8.0 (27.3%)	73.0 ± 36.0 (38.2%)	2 ± 1.1
ZH, 250 $< p_T^Z <$400 GeV, n_{jets}^{add}=0	4.03 ± 0.79 (3.1%)	2.0 ± 1.9 (1.0%)	0.5 ± 0.48
ZH, 250 $< p_T^Z <$400 GeV, $n_{jets}^{add}\geq$1	4.3 ± 1.1 (3.3%)	6.7 ± 4.5 (3.5%)	1.6 ± 1.1
Other WH	2.49 ± 0.71 (1.9%)	2.53 ± 0.65 (1.3%)	1.02 ± 0.39
WH, 150 $< p_T^W <$250 GeV, n_{jets}^{add}=0	14.7 ± 1.7 (11.2%)	18.9 ± 7.4 (9.9%)	1.29 ± 0.52
WH, 150 $< p_T^W <$250 GeV, $n_{jets}^{add}\geq$1	7.6 ± 1.1 (5.8%)	12.0 ± 22.0 (6.3%)	1.6 ± 2.9
WH, 250 $< p_T^W <$400 GeV, n_{jets}^{add}=0	3.43 ± 0.42 (2.6%)	4.3 ± 1.6 (2.2%)	1.25 ± 0.49
WH, 250 $< p_T^W <$400 GeV, $n_{jets}^{add}\geq$1	2.57 ± 0.39 (2.0%)	0.4 ± 5.1 (0.2%)	0.2 ± 2
Signal	128.0 ± 15.0	189.0 ± 40.0	1.48 ± 0.36
Background	10500.0 ± 1300.0	11029.0 ± 98.0	1.05 ± 0.13
Data	11114.0	11114.0	1.00e+00

	Pre-fit	**Post-fit**	**Post/Pre**
Z+hf	3880.0 ± 420.0	4730.0 ± 230.0	1.22 ± 0.14
Z+jets	3900.0 ± 420.0 (19.2%)	4760.0 ± 230.0 (22.3%)	1.22 ± 0.14
W+hf	1740.0 ± 150.0	1770.0 ± 230.0	1.02 ± 0.16
W+jets	1780.0 ± 150.0 (8.8%)	1810.0 ± 230.0 (8.5%)	1.02 ± 0.16
Single-top	1380.0 ± 280.0 (6.8%)	1180.0 ± 230.0 (5.5%)	0.86 ± 0.24
$t\bar{t}$	12800.0 ± 2200.0 (63.1%)	13300.0 ± 360.0 (62.3%)	1.04 ± 0.18
Tops	14200.0 ± 2200.0	14490.0 ± 290.0	1.02 ± 0.16
diboson	410.0 ± 130.0 (2.0%)	299.0 ± 82.0 (1.4%)	0.73 ± 0.31
Other ZH	0.05 ± 0.04 (0.0%)	0.04 ± 0.03 (0.0%)	0.89 ± 0.88
ZH, 75 $< p_T^Z <$150 GeV, n_{jets}^{add}=0	4.7 ± 2.1 (3.4%)	9.4 ± 6.7 (7.2%)	2 ± 1.7
ZH, 75 $< p_T^Z <$150 GeV, $n_{jets}^{add}\geq$1	6.9 ± 2.1 (5.0%)	-1.4 ± 9.4 (-1.1%)	-0.2 ± -1.4
ZH, 150 $< p_T^Z <$250 GeV, n_{jets}^{add}=0	29.1 ± 6.6 (21.1%)	46.0 ± 16.0 (35.3%)	1.58 ± 0.66
ZH, 150 $< p_T^Z <$250 GeV, $n_{jets}^{add}\geq$1	56.0 ± 12.0 (40.5%)	53.0 ± 44.0 (40.7%)	0.95 ± 0.81
ZH, 250 $< p_T^Z <$400 GeV, n_{jets}^{add}=0	2.32 ± 0.55 (1.7%)	2.2 ± 1.2 (1.7%)	0.95 ± 0.56
ZH, 250 $< p_T^Z <$400 GeV, $n_{jets}^{add}\geq$1	6.4 ± 1.6 (4.6%)	2.6 ± 5.2 (2.0%)	0.41 ± 0.82
Other WH	2.71 ± 0.86 (2.0%)	2.89 ± 0.83 (2.2%)	1.07 ± 0.46
WH, 150 $< p_T^W <$250 GeV, n_{jets}^{add}=0	10.8 ± 1.6 (7.8%)	14.2 ± 5.9 (10.9%)	1.31 ± 0.58
WH, 150 $< p_T^W <$250 GeV, $n_{jets}^{add}\geq$1	12.8 ± 1.5 (9.3%)	-2.0 ± 27.0 (-1.5%)	-0.2 ± -2.1
WH, 250 $< p_T^W <$400 GeV, n_{jets}^{add}=0	2.51 ± 0.36 (1.8%)	3.9 ± 1.4 (3.0%)	1.55 ± 0.6
WH, 250 $< p_T^W <$400 GeV, $n_{jets}^{add}\geq$1	3.85 ± 0.49 (2.8%)	-0.7 ± 5.3 (-0.5%)	-0.2 ± -1.4
Signal	136.0 ± 16.0	127.0 ± 51.0	0.93 ± 0.39
Background	20300.0 ± 2300.0	21360.0 ± 140.0	1.05 ± 0.12
Data	21347.0	21347.0	1.00e+00

TABLE A.3: The post-fit vs pre-fit yields for the 0-lepton, 2-jet, 250 $<p_T^V <$ 400 GeV signal region. The upper table is for the 20 GeV jet p_T selection, while the lower table is for 30 GeV. The percentages in the brackets next to the background (signal) yields are the percentage of that sample relative to the total background (signal). For the STXS regions, the number of jets is the number of jets additional to the Higgs decay. The other ZH and WH yields are the signal events that fall outside of the STXS regions under study. The Z+hf sample is the heavy flavour component of the Z+jets sample, likewise for W+jets. Tops is the sum of the $t\bar{t}$ and Single-top samples.

	Pre-fit	**Post-fit**	**Post/Pre**
Z+hf	211.0 ± 30.0	282.0 ± 12.0	1.34 ± 0.2
Z+jets	212.0 ± 30.0 (53.8%)	283.0 ± 12.0 (60.3%)	1.33 ± 0.2
W+hf	75.0 ± 15.0	74.4 ± 8.8	0.99 ± 0.23
W+jets	76.0 ± 15.0 (19.3%)	75.9 ± 8.9 (16.2%)	1 ± 0.23
Single-top	7.2 ± 1.8 (1.8%)	6.7 ± 1.4 (1.4%)	0.93 ± 0.3
$t\bar{t}$	24.6 ± 7.6 (6.2%)	24.7 ± 4.0 (5.3%)	1 ± 0.35
Tops	31.8 ± 8.1	31.3 ± 4.2	0.98 ± 0.28
diboson	74.0 ± 23.0 (18.8%)	79.0 ± 13.0 (16.8%)	1.07 ± 0.38
Other ZH	0.00 ± 0.00 (0.0%)	0.00 ± 0.00 (0.0%)	1.3 ± 2.8
ZH, 150 $< p_T^Z <$250 GeV, n_{jets}^{add}=0	2.41 ± 0.66 (7.9%)	3.2 ± 1.3 (14.5%)	1.33 ± 0.65
ZH, 150 $< p_T^Z <$250 GeV, $n_{jets}^{add}\geq$1	0.141 ± 0.071 (0.5%)	0.28 ± 0.18 (1.3%)	2 ± 1.6
ZH, 250 $< p_T^Z <$400 GeV, n_{jets}^{add}=0	21.4 ± 3.1 (70.3%)	10.5 ± 9.8 (47.5%)	0.49 ± 0.46
ZH, 250 $< p_T^Z <$400 GeV, $n_{jets}^{add}\geq$1	0.75 ± 0.3 (2.5%)	1.19 ± 0.88 (5.4%)	1.6 ± 1.3
WH, 150 $< p_T^W <$250 GeV, n_{jets}^{add}=0	0.39 ± 0.46 (1.3%)	0.46 ± 0.57 (2.1%)	1.2 ± 2
WH, 150 $< p_T^W <$250 GeV, $n_{jets}^{add}\geq$1	0.017 ± 0.024 (0.1%)	0.03 ± 0.069 (0.1%)	1.8 ± 4.8
WH, 250 $< p_T^W <$400 GeV, n_{jets}^{add}=0	5.2 ± 0.68 (17.1%)	6.4 ± 2.4 (29.0%)	1.23 ± 0.49
WH, 250 $< p_T^W <$400 GeV, $n_{jets}^{add}\geq$1	0.144 ± 0.058 (0.5%)	0.03 ± 0.29 (0.1%)	0.2 ± 2
Signal	30.5 ± 4.1	22.1 ± 9.5	0.72 ± 0.33
Background	394.0 ± 51.0	469.0 ± 14.0	1.19 ± 0.16
Data	484.0	484.0	1.00e+00

	Pre-fit	**Post-fit**	**Post/Pre**
Z+hf	349.0 ± 43.0	461.0 ± 19.0	1.32 ± 0.17
Z+jets	352.0 ± 43.0 (53.6%)	464.0 ± 19.0 (63.6%)	1.32 ± 0.17
W+hf	126.0 ± 24.0	114.0 ± 15.0	0.9 ± 0.21
W+jets	127.0 ± 24.0 (19.3%)	116.0 ± 15.0 (15.9%)	0.91 ± 0.21
Single-top	14.4 ± 3.6 (2.2%)	12.1 ± 2.7 (1.7%)	0.84 ± 0.28
$t\bar{t}$	62.0 ± 17.0 (9.4%)	62.0 ± 7.4 (8.5%)	1 ± 0.3
Tops	76.0 ± 18.0	74.2 ± 7.4	0.98 ± 0.25
diboson	101.0 ± 31.0 (15.4%)	75.0 ± 14.0 (10.3%)	0.74 ± 0.27
Other ZH	0.00 ± 0.00 (0.0%)	0.00 ± 0.00 (0.0%)	0.9 ± 2
ZH, 75 $< p_T^Z <$150 GeV, $n_{jets}^{add}\geq$1	0.0012 ± 0.0019 (0.0%)	-0.0002 ± 0.0014 (-0.0%)	-0.2 ± -1.2
ZH, 150 $< p_T^Z <$250 GeV, n_{jets}^{add}=0	3.7 ± 1.0 (8.6%)	5.6 ± 2.1 (13.6%)	1.51 ± 0.7
ZH, 150 $< p_T^Z <$250 GeV, $n_{jets}^{add}\geq$1	0.31 ± 0.14 (0.7%)	0.3 ± 0.28 (0.7%)	1 ± 1
ZH, 250 $< p_T^Z <$400 GeV, n_{jets}^{add}=0	28.8 ± 4.1 (67.2%)	24.0 ± 13.0 (58.1%)	0.83 ± 0.47
ZH, 250 $< p_T^Z <$400 GeV, $n_{jets}^{add}\geq$1	1.87 ± 0.73 (4.4%)	0.8 ± 1.6 (1.9%)	0.43 ± 0.87
WH, 150 $< p_T^W <$250 GeV, n_{jets}^{add}=0	0.62 ± 0.72 (1.4%)	0.8 ± 0.95 (1.9%)	1.3 ± 2.1
WH, 150 $< p_T^W <$250 GeV, $n_{jets}^{add}\geq$1	0.047 ± 0.066 (0.1%)	-0.01 ± 0.11 (-0.0%)	-0.2 ± -2.4
WH, 250 $< p_T^W <$400 GeV, n_{jets}^{add}=0	7.1 ± 0.8 (16.6%)	9.9 ± 3.4 (24.0%)	1.39 ± 0.5
WH, 250 $< p_T^W <$400 GeV, $n_{jets}^{add}\geq$1	0.4 ± 0.15 (0.9%)	-0.07 ± 0.55 (-0.2%)	-0.2 ± -1.4
Signal	42.9 ± 5.3	41.0 ± 13.0	0.96 ± 0.33
Background	657.0 ± 71.0	729.0 ± 20.0	1.11 ± 0.12
Data	772.0	772.0	1.00e+00

TABLE A.4: The post-fit vs pre-fit yields for the 0-lepton, 3-jet, 250 $<p_T^V <$ 400 GeV signal region. The upper table is for the 20 GeV jet p_T selection, while the lower table is for 30 GeV. The percentages in the brackets next to the background (signal) yields are the percentage of that sample relative to the total background (signal). For the STXS regions, the number of jets is the number of jets additional to the Higgs decay. The other ZH and WH yields are the signal events that fall outside of the STXS regions under study. The Z+hf sample is the heavy flavour component of the Z+jets sample, likewise for W+jets. Tops is the sum of the $t\bar{t}$ and Single-top samples.

	Pre-fit	**Post-fit**	**Post/Pre**
Z+hf	335.0 ± 40.0	408.0 ± 20.0	1.22 ± 0.16
Z+jets	338.0 ± 40.0 (47.5%)	412.0 ± 20.0 (53.8%)	1.22 ± 0.16
W+hf	146.0 ± 27.0	161.0 ± 17.0	1.1 ± 0.23
W+jets	147.0 ± 27.0 (20.7%)	162.0 ± 17.0 (21.1%)	1.1 ± 0.23
Single-top	26.2 ± 6.1 (3.7%)	25.0 ± 5.3 (3.3%)	0.95 ± 0.3
$t\bar{t}$	131.0 ± 30.0 (18.4%)	119.0 ± 13.0 (15.5%)	0.91 ± 0.23
Tops	158.0 ± 32.0	144.0 ± 14.0	0.91 ± 0.2
diboson	69.0 ± 22.0 (9.7%)	48.0 ± 12.0 (6.3%)	0.7 ± 0.28
Other ZH	0.00 ± 0.00 (0.0%)	0.00 ± 0.00 (0.0%)	1.2 ± 1.7
ZH, 75 $< p_T^Z <$150 GeV, $n_{jets}^{add}\geq$1	0.0022 ± 0.0036 (0.0%)	0.0018 ± 0.0056 (0.0%)	0.8 ± 2.9
ZH, 150 $< p_T^Z <$250 GeV, n_{jets}^{add}=0	1.72 ± 0.75 (6.4%)	2.5 ± 1.3 (8.6%)	1.45 ± 0.99
ZH, 150 $< p_T^Z <$250 GeV, $n_{jets}^{add}\geq$1	1.03 ± 0.3 (3.8%)	2.2 ± 1.1 (7.5%)	2.1 ± 1.2
ZH, 250 $< p_T^Z <$400 GeV, n_{jets}^{add}=0	9.8 ± 1.9 (36.3%)	5.1 ± 4.8 (17.5%)	0.52 ± 0.5
ZH, 250 $< p_T^Z <$400 GeV, $n_{jets}^{add}\geq$1	9.4 ± 1.8 (34.8%)	15.0 ± 10.0 (51.4%)	1.6 ± 1.1
WH, 150 $< p_T^W <$250 GeV, n_{jets}^{add}=0	0.31 ± 0.18 (1.1%)	0.42 ± 0.28 (1.4%)	1.4 ± 1.2
WH, 150 $< p_T^W <$250 GeV, $n_{jets}^{add}\geq$1	0.15 ± 0.17 (0.6%)	0.24 ± 0.49 (0.8%)	1.6 ± 3.7
WH, 250 $< p_T^W <$400 GeV, n_{jets}^{add}=0	2.59 ± 0.34 (9.6%)	3.3 ± 1.3 (11.3%)	1.27 ± 0.53
WH, 250 $< p_T^W <$400 GeV, $n_{jets}^{add}\geq$1	1.99 ± 0.31 (7.4%)	0.4 ± 4.0 (1.4%)	0.2 ± 2
Signal	27.1 ± 3.2	29.5 ± 9.8	1.09 ± 0.38
Background	712.0 ± 70.0	766.0 ± 19.0	1.08 ± 0.11
Data	787.0	787.0	1.00e+00

	Pre-fit	**Post-fit**	**Post/Pre**
Z+hf	495.0 ± 56.0	607.0 ± 30.0	1.23 ± 0.15
Z+jets	499.0 ± 56.0 (41.8%)	610.0 ± 30.0 (47.2%)	1.22 ± 0.15
W+hf	230.0 ± 40.0	270.0 ± 37.0	1.17 ± 0.26
W+jets	232.0 ± 40.0 (19.4%)	273.0 ± 37.0 (21.1%)	1.18 ± 0.26
Single-top	51.0 ± 13.0 (4.3%)	46.0 ± 10.0 (3.6%)	0.9 ± 0.3
$t\bar{t}$	328.0 ± 59.0 (27.5%)	303.0 ± 23.0 (23.4%)	0.92 ± 0.18
Tops	379.0 ± 62.0	349.0 ± 23.0	0.92 ± 0.16
diboson	84.0 ± 26.0 (7.0%)	61.0 ± 17.0 (4.7%)	0.73 ± 0.3
Other ZH	0.00 ± 0.00 (0.0%)	0.00 ± 0.00 (0.0%)	0.72 ± 0.69
ZH, 75 $< p_T^Z <$150 GeV, n_{jets}^{add}=0	0.0009 ± 0.0014 (0.0%)	0.0016 ± 0.0026 (0.0%)	1.8 ± 4
ZH, 75 $< p_T^Z <$150 GeV, $n_{jets}^{add}\geq$1	0.0011 ± 0.0017 (0.0%)	-0.0002 ± 0.0014 (-0.0%)	-0.2 ± -1.3
ZH, 150 $< p_T^Z <$250 GeV, n_{jets}^{add}=0	1.34 ± 0.64 (4.6%)	2.4 ± 1.2 (12.7%)	1.8 ± 1.2
ZH, 150 $< p_T^Z <$250 GeV, $n_{jets}^{add}\geq$1	1.87 ± 0.57 (6.4%)	1.9 ± 1.6 (10.1%)	1.02 ± 0.91
ZH, 250 $< p_T^Z <$400 GeV, n_{jets}^{add}=0	6.0 ± 1.4 (20.4%)	5.9 ± 3.3 (31.3%)	0.98 ± 0.6
ZH, 250 $< p_T^Z <$400 GeV, $n_{jets}^{add}\geq$1	14.6 ± 2.6 (49.7%)	6.0 ± 12.0 (31.8%)	0.41 ± 0.83
WH, 150 $< p_T^W <$250 GeV, n_{jets}^{add}=0	0.26 ± 0.16 (0.9%)	0.39 ± 0.28 (2.1%)	1.5 ± 1.4
WH, 150 $< p_T^W <$250 GeV, $n_{jets}^{add}\geq$1	0.28 ± 0.3 (1.0%)	-0.04 ± 0.67 (-0.2%)	-0.1 ± -2.4
WH, 250 $< p_T^W <$400 GeV, n_{jets}^{add}=0	1.78 ± 0.32 (6.1%)	2.9 ± 1.0 (15.4%)	1.63 ± 0.63
WH, 250 $< p_T^W <$400 GeV, $n_{jets}^{add}\geq$1	3.24 ± 0.42 (11.0%)	-0.6 ± 4.4 (-3.2%)	-0.2 ± -1.4
Signal	29.4 ± 3.5	19.0 ± 13.0	0.65 ± 0.45
Background	1190.0 ± 110.0	1293.0 ± 28.0	1.09 ± 0.1
Data	1289.0	1289.0	1.00e+00

TABLE A.5: The post-fit vs pre-fit yields for the 1-lepton, 2-jet, 150 $<p_T^V <$ 250 GeV signal region. The upper table is for the 20 GeV jet p_T selection, while the lower table is for 30 GeV. The percentages in the brackets next to the background (signal) yields are the percentage of that sample relative to the total background (signal). For the STXS regions, the number of jets is the number of jets additional to the Higgs decay. The other ZH and WH yields are the signal events that fall outside of the STXS regions under study. The Z+hf sample is the heavy flavour component of the Z+jets sample, likewise for W+jets. Tops is the sum of the $t\bar{t}$ and Single-top samples. Multijet is the total multijet contribution, while Multijet e-channel is just the multijet contribution from the electron channel.

	Pre-fit	**Post-fit**	**Post/Pre**
Z+hf	95.0 ± 12.0	108.8 ± 6.7	1.15 ± 0.16
Z+jets	96.0 ± 12.0 (1.4%)	110.1 ± 6.8 (1.6%)	1.15 ± 0.16
W+hf	1470.0 ± 150.0	1560.0 ± 160.0	1.06 ± 0.15
W+jets	1490.0 ± 150.0 (22.4%)	1580.0 ± 170.0 (23.3%)	1.06 ± 0.16
Single-top	880.0 ± 160.0 (13.2%)	820.0 ± 130.0 (12.1%)	0.93 ± 0.22
$t\bar{t}$	3970.0 ± 610.0 (59.6%)	4020.0 ± 220.0 (59.2%)	1.01 ± 0.17
Tops	4850.0 ± 690.0	4830.0 ± 180.0	1 ± 0.15
diboson	228.0 ± 79.0 (3.4%)	255.0 ± 62.0 (3.8%)	1.12 ± 0.47
Multijet	49.0 ± 28.0	43.0 ± 26.0	0.88 ± 0.73
Multijet e-channel	40.0 ± 28.0	34.0 ± 25.0	0.85 ± 0.86
Other ZH	0.01 ± 0.00 (0.0%)	0.01 ± 0.00 (0.0%)	1.02 ± 0.41
ZH, 75 $< p_T^Z <$150 GeV, n_{jets}^{add}=0	0.329 ± 0.073 (0.2%)	0.37 ± 0.32 (0.2%)	1.1 ± 1
ZH, 75 $< p_T^Z <$150 GeV, $n_{jets}^{add}\geq$1	0.028 ± 0.025 (0.0%)	0.017 ± 0.045 (0.0%)	0.6 ± 1.7
ZH, 150 $< p_T^Z <$250 GeV, n_{jets}^{add}=0	2.39 ± 0.38 (1.7%)	3.0 ± 1.0 (1.8%)	1.26 ± 0.46
ZH, 150 $< p_T^Z <$250 GeV, $n_{jets}^{add}\geq$1	0.087 ± 0.037 (0.1%)	0.16 ± 0.1 (0.1%)	1.8 ± 1.4
ZH, 250 $< p_T^Z <$400 GeV, n_{jets}^{add}=0	0.471 ± 0.085 (0.3%)	0.22 ± 0.21 (0.1%)	0.47 ± 0.45
ZH, 250 $< p_T^Z <$400 GeV, $n_{jets}^{add}\geq$1	0.021 ± 0.01 (0.0%)	0.034 ± 0.026 (0.0%)	1.6 ± 1.5
Other WH	11.10 ± 2.30 (7.9%)	11.00 ± 2.00 (6.6%)	0.99 ± 0.27
WH, 150 $< p_T^W <$250 GeV, n_{jets}^{add}=0	109.0 ± 11.0 (78.0%)	133.0 ± 50.0 (79.3%)	1.22 ± 0.47
WH, 150 $< p_T^W <$250 GeV, $n_{jets}^{add}\geq$1	2.83 ± 0.99 (2.0%)	4.5 ± 8.1 (2.7%)	1.6 ± 2.9
WH, 250 $< p_T^W <$400 GeV, n_{jets}^{add}=0	13.0 ± 2.1 (9.3%)	15.4 ± 6.0 (9.2%)	1.18 ± 0.5
WH, 250 $< p_T^W <$400 GeV, $n_{jets}^{add}\geq$1	0.49 ± 0.2 (0.4%)	0.08 ± 0.93 (0.0%)	0.2 ± 1.9
Signal	128.0 ± 14.0	157.0 ± 46.0	1.23 ± 0.38
Background	6730.0 ± 810.0	6836.0 ± 82.0	1.02 ± 0.12
Data	7019.0	7019.0	1.00e+00

	Pre-fit	**Post-fit**	**Post/Pre**
Z+hf	181.0 ± 18.0	204.0 ± 12.0	1.13 ± 0.13
Z+jets	182.0 ± 18.0 (1.2%)	206.0 ± 12.0 (1.4%)	1.13 ± 0.13
W+hf	2340.0 ± 200.0	2290.0 ± 280.0	0.98 ± 0.15
W+jets	2380.0 ± 200.0 (16.3%)	2320.0 ± 280.0 (15.8%)	0.97 ± 0.14
Single-top	1670.0 ± 310.0 (11.5%)	1440.0 ± 250.0 (9.8%)	0.86 ± 0.22
$t\bar{t}$	10000.0 ± 1700.0 (68.7%)	10480.0 ± 370.0 (71.2%)	1.05 ± 0.18
Tops	11600.0 ± 1800.0	11920.0 ± 290.0	1.03 ± 0.16
diboson	330.0 ± 110.0 (2.3%)	280.0 ± 76.0 (1.9%)	0.85 ± 0.36
Multijet	179.0 ± 95.0	159.0 ± 84.0	0.89 ± 0.67
Multijet e-channel	157.0 ± 94.0	136.0 ± 84.0	0.87 ± 0.75
Other ZH	0.01 ± 0.00 (0.0%)	0.01 ± 0.00 (0.0%)	0.7 ± 0.34
ZH, 75 $< p_T^Z <$150 GeV, n_{jets}^{add}=0	0.56 ± 0.12 (0.3%)	0.95 ± 0.57 (0.4%)	1.7 ± 1.1
ZH, 75 $< p_T^Z <$150 GeV, $n_{jets}^{add}\geq$1	0.064 ± 0.057 (0.0%)	-0.012 ± 0.083 (-0.0%)	-0.2 ± -1.3
ZH, 150 $< p_T^Z <$250 GeV, n_{jets}^{add}=0	3.7 ± 0.54 (1.8%)	5.1 ± 1.5 (2.3%)	1.38 ± 0.45
ZH, 150 $< p_T^Z <$250 GeV, $n_{jets}^{add}\geq$1	0.257 ± 0.096 (0.1%)	0.23 ± 0.21 (0.1%)	0.89 ± 0.88
ZH, 250 $< p_T^Z <$400 GeV, n_{jets}^{add}=0	0.66 ± 0.11 (0.3%)	0.53 ± 0.29 (0.2%)	0.8 ± 0.46
ZH, 250 $< p_T^Z <$400 GeV, $n_{jets}^{add}\geq$1	0.052 ± 0.022 (0.0%)	0.021 ± 0.043 (0.0%)	0.4 ± 0.84
Other WH	17.80 ± 3.70 (8.8%)	17.80 ± 3.10 (7.9%)	1 ± 0.27
WH, 150 $< p_T^W <$250 GeV, n_{jets}^{add}=0	152.0 ± 13.0 (75.3%)	178.0 ± 69.0 (79.0%)	1.17 ± 0.46
WH, 150 $< p_T^W <$250 GeV, $n_{jets}^{add}\geq$1	8.1 ± 2.8 (4.0%)	-1.0 ± 16.0 (-0.4%)	-0.1 ± -2
WH, 250 $< p_T^W <$400 GeV, n_{jets}^{add}=0	17.4 ± 2.5 (8.6%)	23.9 ± 8.5 (10.6%)	1.37 ± 0.53
WH, 250 $< p_T^W <$400 GeV, $n_{jets}^{add}\geq$1	1.22 ± 0.5 (0.6%)	-0.2 ± 1.6 (-0.1%)	-0.2 ± -1.3
Signal	184.0 ± 16.0	208.0 ± 66.0	1.13 ± 0.37
Background	14700.0 ± 1900.0	14910.0 ± 130.0	1.01 ± 0.13
Data	15147.0	15147.0	1.00e+00

TABLE A.6: The post-fit vs pre-fit yields for the 1-lepton, 3-jet, 150 $<p_T^V <$ 250 GeV signal region. The upper table is for the 20 GeV jet p_T selection, while the lower table is for 30 GeV. The percentages in the brackets next to the background (signal) yields are the percentage of that sample relative to the total background (signal). For the STXS regions, the number of jets is the number of jets additional to the Higgs decay. The other ZH and WH yields are the signal events that fall outside of the STXS regions under study. The Z+hf sample is the heavy flavour component of the Z+jets sample, likewise for W+jets. Tops is the sum of the $t\bar{t}$ and Single-top samples. Multijet is the total multijet contribution, while Multijet e-channel is just the multijet contribution from the electron channel.

	Pre-fit	**Post-fit**	**Post/Pre**
Z+hf	190.0 ± 14.0	209.0 ± 12.0	1.1 ± 0.1
Z+jets	191.0 ± 14.0 (0.7%)	210.0 ± 12.0 (0.8%)	1.1 ± 0.1
W+hf	2980.0 ± 210.0	3090.0 ± 310.0	1.04 ± 0.13
W+jets	3010.0 ± 210.0 (11.5%)	3120.0 ± 310.0 (12.4%)	1.04 ± 0.13
Single-top	3140.0 ± 580.0 (12.0%)	2970.0 ± 510.0 (11.8%)	0.95 ± 0.24
$t\bar{t}$	19600.0 ± 2600.0 (74.7%)	18610.0 ± 560.0 (74.1%)	0.95 ± 0.13
Tops	22700.0 ± 2800.0	21570.0 ± 320.0	0.95 ± 0.12
diboson	310.0 ± 120.0 (1.2%)	221.0 ± 76.0 (0.9%)	0.71 ± 0.37
Multijet	160.0 ± 110.0	191.0 ± 66.0	1.19 ± 0.92
Multijet e-channel	150.0 ± 110.0	190.0 ± 66.0	1.3 ± 1
Other ZH	0.03 ± 0.04 (0.0%)	0.03 ± 0.03 (0.0%)	0.9 ± 1.6
ZH, 75 $< p_T^Z <$150 GeV, n_{jets}^{add}=0	0.3 ± 0.19 (0.2%)	0.34 ± 0.36 (0.2%)	1.1 ± 1.4
ZH, 75 $< p_T^Z <$150 GeV, $n_{jets}^{add}\geq$1	0.207 ± 0.06 (0.2%)	0.13 ± 0.33 (0.1%)	0.6 ± 1.6
ZH, 150 $< p_T^Z <$250 GeV, n_{jets}^{add}=0	1.96 ± 0.37 (1.6%)	2.55 ± 0.95 (1.6%)	1.3 ± 0.54
ZH, 150 $< p_T^Z <$250 GeV, $n_{jets}^{add}\geq$1	1.24 ± 0.25 (1.0%)	2.5 ± 1.2 (1.5%)	2 ± 1
ZH, 250 $< p_T^Z <$400 GeV, n_{jets}^{add}=0	0.535 ± 0.093 (0.4%)	0.26 ± 0.25 (0.2%)	0.49 ± 0.47
ZH, 250 $< p_T^Z <$400 GeV, $n_{jets}^{add}\geq$1	0.27 ± 0.061 (0.2%)	0.43 ± 0.28 (0.3%)	1.6 ± 1.1
Other WH	12.43 ± 2.98 (9.9%)	12.83 ± 2.57 (7.8%)	1.03 ± 0.32
WH, 150 $< p_T^W <$250 GeV, n_{jets}^{add}=0	58.2 ± 6.7 (46.2%)	76.0 ± 29.0 (46.4%)	1.31 ± 0.52
WH, 150 $< p_T^W <$250 GeV, $n_{jets}^{add}\geq$1	39.2 ± 4.9 (31.1%)	60.0 ± 110.0 (36.6%)	1.5 ± 2.8
WH, 250 $< p_T^W <$400 GeV, n_{jets}^{add}=0	6.17 ± 0.66 (4.9%)	7.9 ± 3.0 (4.8%)	1.28 ± 0.51
WH, 250 $< p_T^W <$400 GeV, $n_{jets}^{add}\geq$1	5.4 ± 1.0 (4.3%)	1.0 ± 10.0 (0.6%)	0.2 ± 1.9
Signal	113.5 ± 7.2	150.0 ± 100.0	1.32 ± 0.89
Background	26400.0 ± 2900.0	25330.0 ± 180.0	0.96 ± 0.11
Data	25505.0	25505.0	1.00e+00

	Pre-fit	**Post-fit**	**Post/Pre**
Z+hf	286.0 ± 18.0	308.0 ± 19.0	1.077 ± 0.095
Z+jets	286.0 ± 18.0 (0.5%)	308.0 ± 19.0 (0.6%)	1.077 ± 0.095
W+hf	4080.0 ± 290.0	4370.0 ± 570.0	1.07 ± 0.16
W+jets	4130.0 ± 300.0 (7.8%)	4430.0 ± 570.0 (8.6%)	1.07 ± 0.16
Single-top	5200.0 ± 1000.0 (9.8%)	4540.0 ± 820.0 (8.8%)	0.87 ± 0.23
$t\bar{t}$	43200.0 ± 3300.0 (81.2%)	42010.0 ± 910.0 (81.4%)	0.972 ± 0.077
Tops	48500.0 ± 3600.0	46540.0 ± 490.0	0.96 ± 0.072
diboson	380.0 ± 140.0 (0.7%)	300.0 ± 110.0 (0.6%)	0.79 ± 0.41
Multijet	180.0 ± 140.0	450.0 ± 320.0	2.5 ± 2.6
Multijet e-channel	180.0 ± 140.0	450.0 ± 320.0	2.5 ± 2.6
Other ZH	0.04 ± 0.03 (0.0%)	0.04 ± 0.03 (0.1%)	0.9 ± 0.84
ZH, 75 $< p_T^Z <$150 GeV, n_{jets}^{add}=0	0.27 ± 0.17 (0.2%)	0.52 ± 0.44 (0.8%)	1.9 ± 2
ZH, 75 $< p_T^Z <$150 GeV, $n_{jets}^{add}\geq$1	0.4 ± 0.11 (0.3%)	-0.08 ± 0.55 (-0.1%)	-0.2 ± -1.4
ZH, 150 $< p_T^Z <$250 GeV, n_{jets}^{add}=0	1.51 ± 0.32 (1.2%)	2.31 ± 0.8 (3.7%)	1.53 ± 0.62
ZH, 150 $< p_T^Z <$250 GeV, $n_{jets}^{add}\geq$1	2.09 ± 0.4 (1.7%)	2.0 ± 1.6 (3.2%)	0.96 ± 0.79
ZH, 250 $< p_T^Z <$400 GeV, n_{jets}^{add}=0	0.514 ± 0.088 (0.4%)	0.44 ± 0.24 (0.7%)	0.86 ± 0.49
ZH, 250 $< p_T^Z <$400 GeV, $n_{jets}^{add}\geq$1	0.432 ± 0.097 (0.3%)	0.19 ± 0.37 (0.3%)	0.44 ± 0.86
Other WH	14.00 ± 3.00 (11.1%)	14.80 ± 2.60 (23.6%)	1.06 ± 0.29
WH, 150 $< p_T^W <$250 GeV, n_{jets}^{add}=0	35.8 ± 6.2 (28.4%)	48.0 ± 21.0 (76.4%)	1.34 ± 0.63
WH, 150 $< p_T^W <$250 GeV, $n_{jets}^{add}\geq$1	59.8 ± 6.3 (47.5%)	-10.0 ± 130.0 (-15.9%)	-0.2 ± -2.2
WH, 250 $< p_T^W <$400 GeV, n_{jets}^{add}=0	3.49 ± 0.56 (2.8%)	5.6 ± 2.0 (8.9%)	1.6 ± 0.63
WH, 250 $< p_T^W <$400 GeV, $n_{jets}^{add}\geq$1	7.6 ± 1.3 (6.0%)	-1.0 ± 10.0 (-1.6%)	-0.1 ± -1.3
Signal	111.9 ± 7.7	50.0 ± 120.0	0.4 ± 1.1
Background	53500.0 ± 3800.0	52050.0 ± 250.0	0.973 ± 0.069
Data	52170.0	52170.0	1.00e+00

TABLE A.7: The post-fit vs pre-fit yields for the 1-lepton, 2-jet, 250 $<p_T^V <$ 400 GeV signal region. The upper table is for the 20 GeV jet p_T selection, while the lower table is for 30 GeV. The percentages in the brackets next to the background (signal) yields are the percentage of that sample relative to the total background (signal). For the STXS regions, the number of jets is the number of jets additional to the Higgs decay. The other ZH and WH yields are the signal events that fall outside of the STXS regions under study. The Z+hf sample is the heavy flavour component of the Z+jets sample, likewise for W+jets. Tops is the sum of the $t\bar{t}$ and Single-top samples. Multijet is the total multijet contribution, while Multijet e-channel is just the multijet contribution from the electron channel.

	Pre-fit	**Post-fit**	**Post/Pre**
Z+hf	9.3 ± 1.4	11.11 ± 0.96	1.19 ± 0.21
Z+jets	9.3 ± 1.4 (1.8%)	11.11 ± 0.96 (2.2%)	1.19 ± 0.21
W+hf	294.0 ± 51.0	302.0 ± 30.0	1.03 ± 0.21
W+jets	298.0 ± 52.0 (59.1%)	305.0 ± 30.0 (59.6%)	1.02 ± 0.21
Single-top	40.9 ± 10.0 (8.1%)	38.6 ± 8.2 (7.5%)	0.94 ± 0.31
$t\bar{t}$	106.0 ± 32.0 (21.0%)	100.0 ± 16.0 (19.5%)	0.94 ± 0.32
Tops	147.0 ± 35.0	139.0 ± 16.0	0.95 ± 0.25
diboson	50.0 ± 19.0 (9.9%)	57.0 ± 15.0 (11.1%)	1.14 ± 0.53
Multijet	16.0 ± 10.0	13.6 ± 9.2	0.85 ± 0.78
Multijet e-channel	15.0 ± 10.0	12.6 ± 9.2	0.84 ± 0.83
Other ZH	0.00 ± 0.00 (0.0%)	0.00 ± 0.00 (0.0%)	0.8 ± 2
ZH, $150 < p_T^Z <$250 GeV, n_{jets}^{add}=0	0.052 ± 0.028 (0.1%)	0.071 ± 0.043 (0.2%)	1.4 ± 1.1
ZH, $150 < p_T^Z <$250 GeV, $n_{jets}^{add}\geq$1	0.0024 ± 0.0033 (0.0%)	0.0045 ± 0.0061 (0.0%)	1.9 ± 3.6
ZH, $250 < p_T^Z <$400 GeV, n_{jets}^{add}=0	0.465 ± 0.074 (1.2%)	0.23 ± 0.21 (0.5%)	0.49 ± 0.46
ZH, $250 < p_T^Z <$400 GeV, $n_{jets}^{add}\geq$1	0.0138 ± 0.0069 (0.0%)	0.019 ± 0.015 (0.0%)	1.4 ± 1.3
WH, $150 < p_T^W <$250 GeV, n_{jets}^{add}=0	3.35 ± 0.89 (8.7%)	4.3 ± 1.9 (9.1%)	1.28 ± 0.66
WH, $150 < p_T^W <$250 GeV, $n_{jets}^{add}\geq$1	0.145 ± 0.072 (0.4%)	0.23 ± 0.42 (0.5%)	1.6 ± 3
WH, $250 < p_T^W <$400 GeV, n_{jets}^{add}=0	33.6 ± 4.0 (86.9%)	42.0 ± 15.0 (89.3%)	1.25 ± 0.47
WH, $250 < p_T^W <$400 GeV, $n_{jets}^{add}\geq$1	1.03 ± 0.36 (2.7%)	0.2 ± 2.0 (0.4%)	0.2 ± 1.9
Signal	38.6 ± 4.4	47.0 ± 14.0	1.22 ± 0.39
Background	519.0 ± 74.0	526.0 ± 21.0	1.01 ± 0.15
Data	563.0	563.0	1.00e+00

	Pre-fit	**Post-fit**	**Post/Pre**
Z+hf	16.3 ± 1.8	19.9 ± 1.3	1.22 ± 0.16
Z+jets	16.3 ± 1.8 (1.8%)	19.9 ± 1.3 (2.2%)	1.22 ± 0.16
W+hf	468.0 ± 78.0	453.0 ± 55.0	0.97 ± 0.2
W+jets	474.0 ± 78.0 (51.5%)	460.0 ± 55.0 (51.2%)	0.97 ± 0.2
Single-top	84.0 ± 20.0 (9.1%)	77.0 ± 16.0 (8.6%)	0.92 ± 0.29
$t\bar{t}$	275.0 ± 83.0 (29.9%)	279.0 ± 32.0 (31.1%)	1.01 ± 0.33
Tops	359.0 ± 87.0	356.0 ± 33.0	0.99 ± 0.26
diboson	71.0 ± 26.0 (7.7%)	62.0 ± 18.0 (6.9%)	0.87 ± 0.41
Multijet	57.0 ± 33.0	50.0 ± 29.0	0.88 ± 0.72
Multijet e-channel	54.0 ± 32.0	47.0 ± 29.0	0.87 ± 0.74
Other ZH	0.00 ± 0.00 (0.0%)	0.00 ± 0.00 (0.0%)	0.45 ± 0.98
ZH, $150 < p_T^Z <$250 GeV, n_{jets}^{add}=0	0.084 ± 0.046 (0.2%)	0.132 ± 0.079 (0.2%)	1.6 ± 1.3
ZH, $150 < p_T^Z <$250 GeV, $n_{jets}^{add}\geq$1	0.0046 ± 0.0061 (0.0%)	0.0052 ± 0.008 (0.0%)	1.1 ± 2.3
ZH, $250 < p_T^Z <$400 GeV, n_{jets}^{add}=0	0.68 ± 0.11 (1.2%)	0.57 ± 0.3 (0.8%)	0.84 ± 0.46
ZH, $250 < p_T^Z <$400 GeV, $n_{jets}^{add}\geq$1	0.046 ± 0.021 (0.1%)	0.018 ± 0.037 (0.0%)	0.39 ± 0.82
WH, $150 < p_T^W <$250 GeV, n_{jets}^{add}=0	5.1 ± 1.4 (9.4%)	6.5 ± 3.0 (9.2%)	1.27 ± 0.68
WH, $150 < p_T^W <$250 GeV, $n_{jets}^{add}\geq$1	0.37 ± 0.17 (0.7%)	-0.05 ± 0.81 (-0.1%)	-0.1 ± -2.2
WH, $250 < p_T^W <$400 GeV, n_{jets}^{add}=0	45.4 ± 4.8 (83.3%)	64.0 ± 21.0 (90.6%)	1.41 ± 0.49
WH, $250 < p_T^W <$400 GeV, $n_{jets}^{add}\geq$1	2.8 ± 0.95 (5.1%)	-0.5 ± 3.7 (-0.7%)	-0.2 ± -1.3
Signal	54.5 ± 5.5	70.0 ± 21.0	1.28 ± 0.41
Background	980.0 ± 130.0	948.0 ± 30.0	0.97 ± 0.13
Data	1020.0	1020.0	1.00e+00

TABLE A.8: The post-fit vs pre-fit yields for the 1-lepton, 3-jet, 250 $<p_T^V <$ 400 GeV signal region. The upper table is for the 20 GeV jet p_T selection, while the lower table is for 30 GeV. The percentages in the brackets next to the background (signal) yields are the percentage of that sample relative to the total background (signal). For the STXS regions, the number of jets is the number of jets additional to the Higgs decay. The other ZH and WH yields are the signal events that fall outside of the STXS regions under study. The Z+hf sample is the heavy flavour component of the Z+jets sample, likewise for W+jets. Tops is the sum of the $t\bar{t}$ and Single-top samples. Multijet is the total multijet contribution, while Multijet e-channel is just the multijet contribution from the electron channel.

	Pre-fit	**Post-fit**	**Post/Pre**
Z+hf	19.5 ± 2.0	20.3 ± 1.5	1.04 ± 0.13
Z+jets	20.2 ± 2.0 (1.4%)	21.1 ± 1.5 (1.5%)	1.04 ± 0.13
W+hf	526.0 ± 88.0	627.0 ± 58.0	1.19 ± 0.23
W+jets	531.0 ± 88.0 (35.9%)	632.0 ± 58.0 (43.7%)	1.19 ± 0.23
Single-top	169.0 ± 36.0 (11.4%)	163.0 ± 32.0 (11.3%)	0.96 ± 0.28
$t\bar{t}$	690.0 ± 240.0 (46.7%)	582.0 ± 45.0 (40.2%)	0.84 ± 0.3
Tops	860.0 ± 240.0	745.0 ± 43.0	0.87 ± 0.25
diboson	67.0 ± 26.0 (4.5%)	48.0 ± 17.0 (3.3%)	0.72 ± 0.38
Multijet	56.0 ± 40.0	69.0 ± 24.0	1.23 ± 0.98
Multijet e-channel	56.0 ± 40.0	69.0 ± 24.0	1.23 ± 0.98
Other ZH	0.00 ± 0.00 (0.0%)	0.00 ± 0.00 (0.0%)	0.71 ± 0.78
ZH, 75 $< p_T^Z <$150 GeV, $n_{jets}^{add}\geq$1	0.0013 ± 0.002 (0.0%)	0.0008 ± 0.0025 (0.0%)	0.6 ± 2.1
ZH, 150 $< p_T^Z <$250 GeV, n_{jets}^{add}=0	0.041 ± 0.032 (0.1%)	0.064 ± 0.051 (0.2%)	1.6 ± 1.7
ZH, 150 $< p_T^Z <$250 GeV, $n_{jets}^{add}\geq$1	0.024 ± 0.019 (0.1%)	0.048 ± 0.045 (0.2%)	2 ± 2.5
ZH, 250 $< p_T^Z <$400 GeV, n_{jets}^{add}=0	0.346 ± 0.088 (1.0%)	0.18 ± 0.17 (0.6%)	0.52 ± 0.51
ZH, 250 $< p_T^Z <$400 GeV, $n_{jets}^{add}\geq$1	0.246 ± 0.047 (0.7%)	0.4 ± 0.26 (1.3%)	1.6 ± 1.1
Other WH	0.02 ± 0.02 (0.0%)	0.01 ± 0.02 (0.0%)	0.9 ± 1.8
WH, 150 $< p_T^W <$250 GeV, n_{jets}^{add}=0	2.42 ± 0.82 (7.0%)	3.4 ± 1.6 (11.4%)	1.4 ± 0.81
WH, 150 $< p_T^W <$250 GeV, $n_{jets}^{add}\geq$1	1.6 ± 0.33 (4.6%)	2.6 ± 4.7 (8.7%)	1.6 ± 3
WH, 250 $< p_T^W <$400 GeV, n_{jets}^{add}=0	15.9 ± 2.2 (45.8%)	21.1 ± 8.0 (70.8%)	1.33 ± 0.54
WH, 250 $< p_T^W <$400 GeV, $n_{jets}^{add}\geq$1	14.1 ± 2.0 (40.6%)	2.0 ± 29.0 (6.7%)	0.1 ± 2.1
Signal	34.7 ± 3.3	30.0 ± 26.0	0.86 ± 0.75
Background	1530.0 ± 270.0	1515.0 ± 40.0	0.99 ± 0.18
Data	1573.0	1573.0	1.00e+00

	Pre-fit	**Post-fit**	**Post/Pre**
Z+hf	30.1 ± 3.1	31.5 ± 2.0	1.05 ± 0.13
Z+jets	31.1 ± 3.1 (1.1%)	32.7 ± 2.1 (1.2%)	1.05 ± 0.12
W+hf	780.0 ± 130.0	920.0 ± 130.0	1.18 ± 0.26
W+jets	790.0 ± 130.0 (27.6%)	930.0 ± 130.0 (33.7%)	1.18 ± 0.25
Single-top	307.0 ± 67.0 (10.7%)	271.0 ± 55.0 (9.8%)	0.88 ± 0.26
$t\bar{t}$	1640.0 ± 470.0 (57.4%)	1455.0 ± 91.0 (52.7%)	0.89 ± 0.26
Tops	1940.0 ± 480.0	1726.0 ± 83.0	0.89 ± 0.22
diboson	90.0 ± 35.0 (3.1%)	70.0 ± 27.0 (2.5%)	0.78 ± 0.43
Multijet	73.0 ± 54.0	180.0 ± 130.0	2.5 ± 2.5
Multijet e-channel	73.0 ± 54.0	180.0 ± 130.0	2.5 ± 2.5
Other ZH	0.00 ± 0.00 (0.0%)	0.00 ± 0.00 (0.0%)	0.78 ± 0.77
ZH, 75 $< p_T^Z <$150 GeV, $n_{jets}^{add}\geq$1	0.001 ± 0.0015 (0.0%)	-0.0002 ± 0.0014 (-0.0%)	-0.2 ± -1.4
ZH, 150 $< p_T^Z <$250 GeV, n_{jets}^{add}=0	0.036 ± 0.028 (0.1%)	0.068 ± 0.055 (0.5%)	1.9 ± 2.1
ZH, 150 $< p_T^Z <$250 GeV, $n_{jets}^{add}\geq$1	0.05 ± 0.036 (0.1%)	0.051 ± 0.055 (0.3%)	1 ± 1.3
ZH, 250 $< p_T^Z <$400 GeV, n_{jets}^{add}=0	0.265 ± 0.071 (0.7%)	0.25 ± 0.15 (1.7%)	0.94 ± 0.62
ZH, 250 $< p_T^Z <$400 GeV, $n_{jets}^{add}\geq$1	0.413 ± 0.076 (1.2%)	0.18 ± 0.36 (1.2%)	0.44 ± 0.88
Other WH	0.02 ± 0.03 (0.1%)	0.02 ± 0.02 (0.1%)	0.9 ± 1.5
WH, 150 $< p_T^W <$250 GeV, n_{jets}^{add}=0	1.88 ± 0.71 (5.2%)	2.8 ± 1.4 (18.7%)	1.49 ± 0.93
WH, 150 $< p_T^W <$250 GeV, $n_{jets}^{add}\geq$1	2.58 ± 0.54 (7.2%)	-0.3 ± 6.0 (-2.0%)	-0.1 ± -2.3
WH, 250 $< p_T^W <$400 GeV, n_{jets}^{add}=0	9.6 ± 1.9 (26.8%)	15.9 ± 5.6 (106.2%)	1.66 ± 0.67
WH, 250 $< p_T^W <$400 GeV, $n_{jets}^{add}\geq$1	21.0 ± 2.5 (58.6%)	-4.0 ± 29.0 (-26.7%)	-0.2 ± -1.4
Signal	35.8 ± 3.4	15.0 ± 28.0	0.42 ± 0.78
Background	2930.0 ± 510.0	2941.0 ± 54.0	1 ± 0.18
Data	3009.0	3009.0	1.00e+00

TABLE A.9: The post-fit vs pre-fit yields for the 2-lepton, 2-jet, 75 $<p_T^V<$ 150 GeV signal region. The upper table is for the 20 GeV jet p_T selection, while the lower table is for 30 GeV. The percentages in the brackets next to the background (signal) yields are the percentage of that sample relative to the total background (signal). For the STXS regions, the number of jets is the number of jets additional to the Higgs decay. The other ZH and WH yields are the signal events that fall outside of the STXS regions under study. The Z+hf sample is the heavy flavour component of the Z+jets sample, likewise for W+jets. Tops is the $t\bar{t}$ +single-top data-driven estimate derived from the $e\mu$-CR.

	Pre-fit	**Post-fit**	**Post/Pre**
Z+hf	5060.0 ± 450.0	6290.0 ± 140.0	1.24 ± 0.11
Z+jets	5060.0 ± 450.0 (94.5%)	6300.0 ± 140.0 (95.7%)	1.25 ± 0.11
W+hf	0.237626 ± 2.7e-05	0.27 ± 0.039	1.14 ± 0.16
W+jets	0.237626 ± 2.7e-05 (0.0%)	0.27 ± 0.039 (0.0%)	1.14 ± 0.16
Tops	3238.0 ± 26.0	3284.0 ± 58.0	1.014 ± 0.02
diboson	293.0 ± 84.0 (5.5%)	284.0 ± 50.0 (4.3%)	0.97 ± 0.33
Other ZH	0.93 ± 3.08 (1.2%)	0.87 ± 2.79 (1.1%)	0.9 ± 4.3
ZH, 75 $< p_T^Z <$150 GeV, n_{jets}^{add}=0	72.8 ± 9.7 (94.0%)	76.0 ± 65.0 (95.0%)	1.04 ± 0.9
ZH, 75 $< p_T^Z <$150 GeV, $n_{jets}^{add}\geq$1	2.4 ± 0.72 (3.1%)	1.5 ± 3.8 (1.9%)	0.6 ± 1.6
ZH, 150 $< p_T^Z <$250 GeV, n_{jets}^{add}=0	1.28 ± 0.3 (1.7%)	1.57 ± 0.57 (2.0%)	1.23 ± 0.53
ZH, 150 $< p_T^Z <$250 GeV, $n_{jets}^{add}\geq$1	0.05 ± 0.037 (0.1%)	0.097 ± 0.079 (0.1%)	1.9 ± 2.1
Other WH	0.00 ± 0.01 (0.0%)	0.00 ± 0.00 (0.0%)	0.7 ± 1.4
WH, 150 $< p_T^W <$250 GeV, n_{jets}^{add}=0	0.0016 ± 0.0018 (0.0%)	0.0017 ± 0.0021 (0.0%)	1.1 ± 1.8
WH, 150 $< p_T^W <$250 GeV, $n_{jets}^{add}\geq$1	0.00031 ± 0.00033 (0.0%)	0.0005 ± 0.001 (0.0%)	1.6 ± 3.7
WH, 250 $< p_T^W <$400 GeV, n_{jets}^{add}=0	0.00033 ± 0.00048 (0.0%)	0.00039 ± 0.00057 (0.0%)	1.2 ± 2.4
Signal	77.0 ± 10.0	79.0 ± 64.0	1.03 ± 0.84
Background	8590.0 ± 480.0	9860.0 ± 110.0	1.148 ± 0.065
Data	10018.0	10018.0	1.00e+00

	Pre-fit	**Post-fit**	**Post/Pre**
Z+hf	7780.0 ± 580.0	9570.0 ± 180.0	1.23 ± 0.095
Z+jets	7810.0 ± 580.0 (95.1%)	9610.0 ± 180.0 (96.9%)	1.23 ± 0.094
W+hf	0.384283 ± 4.2e-05	0.407 ± 0.061	1.06 ± 0.16
W+jets	0.384283 ± 4.2e-05 (0.0%)	0.407 ± 0.061 (0.0%)	1.06 ± 0.16
Tops	5041.0 ± 40.0	5094.0 ± 75.0	1.011 ± 0.017
diboson	400.0 ± 110.0 (4.9%)	309.0 ± 64.0 (3.1%)	0.77 ± 0.27
Other ZH	1.29 ± 0.63 (1.2%)	1.15 ± 0.57 (0.7%)	0.89 ± 0.62
ZH, 75 $< p_T^Z <$150 GeV, n_{jets}^{add}=0	101.0 ± 12.0 (91.4%)	155.0 ± 88.0 (98.3%)	1.53 ± 0.89
ZH, 75 $< p_T^Z <$150 GeV, $n_{jets}^{add}\geq$1	6.3 ± 1.9 (5.7%)	-1.1 ± 7.6 (-0.7%)	-0.2 ± -1.2
ZH, 150 $< p_T^Z <$250 GeV, n_{jets}^{add}=0	1.82 ± 0.42 (1.6%)	2.47 ± 0.77 (1.6%)	1.36 ± 0.53
ZH, 150 $< p_T^Z <$250 GeV, $n_{jets}^{add}\geq$1	0.13 ± 0.096 (0.1%)	0.12 ± 0.13 (0.1%)	0.9 ± 1.2
Other WH	0.01 ± 0.01 (0.0%)	0.00 ± 0.01 (0.0%)	0.6 ± 1.2
WH, 150 $< p_T^W <$250 GeV, n_{jets}^{add}=0	0.003 ± 0.0055 (0.0%)	0.001 ± 0.0014 (0.0%)	0.33 ± 0.77
WH, 150 $< p_T^W <$250 GeV, $n_{jets}^{add}\geq$1	0.00036 ± 0.00044 (0.0%)	-4e-05 ± 0.00068 (-0.0%)	-0.1 ± -1.9
Signal	109.0 ± 14.0	157.0 ± 88.0	1.44 ± 0.83
Background	13250.0 ± 610.0	15010.0 ± 150.0	1.133 ± 0.053
Data	15253.0	15253.0	1.00e+00

TABLE A.10: The post-fit vs pre-fit yields for the 2-lepton, $\geq$ 3-jet, 75 $<p_T^V <$ 150 GeV signal region. The upper table is for the 20 GeV jet p_T selection, while the lower table is for 30 GeV. The percentages in the brackets next to the background (signal) yields are the percentage of that sample relative to the total background (signal). For the STXS regions, the number of jets is the number of jets additional to the Higgs decay. The other ZH and WH yields are the signal events that fall outside of the STXS regions under study. The Z+hf sample is the heavy flavour component of the Z+jets sample, likewise for W+jets. Tops is the $t\bar{t}$ +single-top data-driven estimate derived from the $e\mu$-CR.

	Pre-fit	**Post-fit**	**Post/Pre**
Z+hf	10800.0 ± 910.0	12140.0 ± 180.0	1.124 ± 0.096
Z+jets	10860.0 ± 920.0 (95.5%)	12200.0 ± 180.0 (96.7%)	1.123 ± 0.097
W+hf	3.537 ± 0.083	3.6 ± 0.48	1.02 ± 0.14
W+jets	3.537 ± 0.083 (0.0%)	3.6 ± 0.48 (0.0%)	1.02 ± 0.14
Tops	9130.34 ± 0.43	9097.0 ± 86.0	0.9963 ± 0.0094
diboson	510.0 ± 120.0 (4.5%)	414.0 ± 72.0 (3.3%)	0.81 ± 0.24
Other ZH	1.25 ± 11.17 (1.1%)	1.26 ± 11.37 (1.2%)	1 ± 13
ZH, 75 $< p_T^Z <$150 GeV, n_{jets}^{add}=0	46.0 ± 11.0 (39.4%)	53.0 ± 46.0 (48.7%)	1.2 ± 1
ZH, 75 $< p_T^Z <$150 GeV, $n_{jets}^{add}\geq$1	67.0 ± 11.0 (57.4%)	50.0 ± 120.0 (46.0%)	0.7 ± 1.8
ZH, 150 $< p_T^Z <$250 GeV, n_{jets}^{add}=0	0.96 ± 0.27 (0.8%)	1.31 ± 0.52 (1.2%)	1.36 ± 0.66
ZH, 150 $< p_T^Z <$250 GeV, $n_{jets}^{add}\geq$1	1.53 ± 0.35 (1.3%)	3.2 ± 1.5 (2.9%)	2.1 ± 1.1
Other WH	0.02 ± 0.02 (0.0%)	0.01 ± 0.01 (0.0%)	0.8 ± 1
WH, 150 $< p_T^W <$250 GeV, n_{jets}^{add}=0	0.0024 ± 0.0024 (0.0%)	0.0037 ± 0.0032 (0.0%)	1.5 ± 2
WH, 150 $< p_T^W <$250 GeV, $n_{jets}^{add}\geq$1	0.0058 ± 0.0056 (0.0%)	0.007 ± 0.013 (0.0%)	1.2 ± 2.5
WH, 250 $< p_T^W <$400 GeV, $n_{jets}^{add}\geq$1	0.00076 ± 0.00094 (0.0%)	0.0002 ± 0.0024 (0.0%)	0.3 ± 3.2
Signal	116.0 ± 18.0	100.0 ± 110.0	0.86 ± 0.96
Background	20510.0 ± 960.0	21720.0 ± 160.0	1.059 ± 0.05
Data	21710.0	21710.0	1.00e+00

	Pre-fit	**Post-fit**	**Post/Pre**
Z+hf	9250.0 ± 890.0	10300.0 ± 160.0	1.11 ± 0.11
Z+jets	9300.0 ± 900.0 (95.8%)	10360.0 ± 160.0 (97.0%)	1.11 ± 0.11
W+hf	3.491 ± 0.083	3.8 ± 0.59	1.09 ± 0.17
W+jets	3.491 ± 0.083 (0.0%)	3.8 ± 0.59 (0.0%)	1.09 ± 0.17
Tops	8203.25 ± 0.37	8157.0 ± 81.0	0.9944 ± 0.0099
diboson	405.0 ± 94.0 (4.2%)	316.0 ± 59.0 (3.0%)	0.78 ± 0.23
Other ZH	0.97 ± 0.42 (1.1%)	0.96 ± 0.40 (3.2%)	0.98 ± 0.59
ZH, 75 $< p_T^Z <$150 GeV, n_{jets}^{add}=0	20.8 ± 6.3 (22.9%)	40.0 ± 25.0 (132.3%)	1.9 ± 1.3
ZH, 75 $< p_T^Z <$150 GeV, $n_{jets}^{add}\geq$1	67.0 ± 10.0 (73.8%)	-13.0 ± 89.0 (-43.0%)	-0.2 ± -1.3
ZH, 150 $< p_T^Z <$250 GeV, n_{jets}^{add}=0	0.46 ± 0.15 (0.5%)	0.76 ± 0.29 (2.5%)	1.65 ± 0.83
ZH, 150 $< p_T^Z <$250 GeV, $n_{jets}^{add}\geq$1	1.56 ± 0.36 (1.7%)	1.5 ± 1.3 (5.0%)	0.96 ± 0.86
Other WH	0.01 ± 0.02 (0.0%)	0.01 ± 0.01 (0.0%)	0.7 ± 1
WH, 150 $< p_T^W <$250 GeV, n_{jets}^{add}=0	0.0019 ± 0.0012 (0.0%)	0.0019 ± 0.0012 (0.0%)	1 ± 0.89
WH, 150 $< p_T^W <$250 GeV, $n_{jets}^{add}\geq$1	0.0058 ± 0.0055 (0.0%)	-0.0006 ± 0.0098 (-0.0%)	-0.1 ± -1.7
WH, 250 $< p_T^W <$400 GeV, $n_{jets}^{add}\geq$1	0.00076 ± 0.0009 (0.0%)	-0.0002 ± 0.0013 (-0.0%)	-0.3 ± -1.7
Signal	90.0 ± 14.0	29.0 ± 90.0	0.3 ± 1
Background	17910.0 ± 930.0	18830.0 ± 140.0	1.051 ± 0.055
Data	18726.0	18726.0	1.00e+00

TABLE A.11: The post-fit vs pre-fit yields for the 2-lepton, 2-jet, 150 $<p_T^V <$ 250 GeV signal region. The upper table is for the 20 GeV jet p_T selection, while the lower table is for 30 GeV. The percentages in the brackets next to the background (signal) yields are the percentage of that sample relative to the total background (signal). For the STXS regions, the number of jets is the number of jets additional to the Higgs decay. The other ZH and WH yields are the signal events that fall outside of the STXS regions under study. The Z+hf sample is the heavy flavour component of the Z+jets sample, likewise for W+jets. Tops is the $t\bar{t}$ +single-top data-driven estimate derived from the $e\mu$-CR.

	Pre-fit	**Post-fit**	**Post/Pre**
Z+hf	608.0 ± 63.0	700.0 ± 26.0	1.15 ± 0.13
Z+jets	609.0 ± 63.0 (88.6%)	701.0 ± 26.0 (90.2%)	1.15 ± 0.13
W+hf	0.191557 ± 2.2e-05	0.216 ± 0.031	1.13 ± 0.16
W+jets	0.191557 ± 2.2e-05 (0.0%)	0.216 ± 0.031 (0.0%)	1.13 ± 0.16
Tops	63.69 ± 0.51	63.7 ± 7.8	1 ± 0.12
diboson	78.0 ± 22.0 (11.4%)	76.0 ± 13.0 (9.8%)	0.97 ± 0.32
Other ZH	0.00 ± 0.00 (0.0%)	0.00 ± 0.00 (0.0%)	0.91 ± 0.94
ZH, 75 $< p_T^Z <$150 GeV, n_{jets}^{add}=0	0.74 ± 0.87 (2.3%)	0.7 ± 1.0 (1.7%)	0.9 ± 1.8
ZH, 75 $< p_T^Z <$150 GeV, $n_{jets}^{add}\geq$1	0.024 ± 0.034 (0.1%)	0.016 ± 0.049 (0.0%)	0.7 ± 2.2
ZH, 150 $< p_T^Z <$250 GeV, n_{jets}^{add}=0	29.6 ± 5.3 (92.5%)	37.0 ± 12.0 (91.9%)	1.25 ± 0.46
ZH, 150 $< p_T^Z <$250 GeV, $n_{jets}^{add}\geq$1	1.18 ± 0.44 (3.7%)	2.3 ± 1.4 (5.7%)	1.9 ± 1.4
ZH, 250 $< p_T^Z <$400 GeV, n_{jets}^{add}=0	0.43 ± 0.14 (1.3%)	0.21 ± 0.2 (0.5%)	0.49 ± 0.49
ZH, 250 $< p_T^Z <$400 GeV, $n_{jets}^{add}\geq$1	0.018 ± 0.015 (0.1%)	0.026 ± 0.026 (0.1%)	1.4 ± 1.9
WH, 150 $< p_T^W <$250 GeV, $n_{jets}^{add}\geq$1	0.00039 ± 0.00048 (0.0%)	0.0006 ± 0.0014 (0.0%)	1.5 ± 4.1
Signal	32.0 ± 5.7	40.0 ± 12.0	1.25 ± 0.44
Background	751.0 ± 72.0	842.0 ± 23.0	1.12 ± 0.11
Data	872.0	872.0	1.00e+00

	Pre-fit	**Post-fit**	**Post/Pre**
Z+hf	1006.0 ± 83.0	1155.0 ± 37.0	1.15 ± 0.1
Z+jets	1008.0 ± 83.0 (90.2%)	1159.0 ± 37.0 (93.1%)	1.15 ± 0.1
W+hf	0.418955 ± 4.9e-05	0.445 ± 0.067	1.06 ± 0.16
W+jets	0.418955 ± 4.9e-05 (0.0%)	0.445 ± 0.067 (0.0%)	1.06 ± 0.16
Tops	104.48 ± 0.84	105.0 ± 10.0	1.005 ± 0.096
diboson	109.0 ± 31.0 (9.8%)	85.0 ± 18.0 (6.8%)	0.78 ± 0.28
Other ZH	0.00 ± 0.00 (0.0%)	0.00 ± 0.00 (0.0%)	0.69 ± 0.73
ZH, 75 $< p_T^Z <$150 GeV, n_{jets}^{add}=0	1.1 ± 1.2 (2.3%)	1.5 ± 1.9 (2.4%)	1.4 ± 2.3
ZH, 75 $< p_T^Z <$150 GeV, $n_{jets}^{add}\geq$1	0.063 ± 0.09 (0.1%)	-0.011 ± 0.075 (-0.0%)	-0.2 ± -1.2
ZH, 150 $< p_T^Z <$250 GeV, n_{jets}^{add}=0	41.9 ± 7.3 (89.5%)	57.0 ± 16.0 (92.2%)	1.36 ± 0.45
ZH, 150 $< p_T^Z <$250 GeV, $n_{jets}^{add}\geq$1	3.1 ± 1.1 (6.6%)	2.8 ± 2.6 (4.5%)	0.9 ± 0.9
ZH, 250 $< p_T^Z <$400 GeV, n_{jets}^{add}=0	0.61 ± 0.2 (1.3%)	0.5 ± 0.29 (0.8%)	0.82 ± 0.55
ZH, 250 $< p_T^Z <$400 GeV, $n_{jets}^{add}\geq$1	0.047 ± 0.035 (0.1%)	0.018 ± 0.038 (0.0%)	0.38 ± 0.86
Other WH	0.00 ± 0.00 (0.0%)	0.00 ± 0.00 (0.0%)	1 ± 2.2
WH, 150 $< p_T^W <$250 GeV, n_{jets}^{add}=0	0.0009 ± 0.0011 (0.0%)	0.00029 ± 0.00034 (0.0%)	0.32 ± 0.55
WH, 150 $< p_T^W <$250 GeV, $n_{jets}^{add}\geq$1	0.00039 ± 0.00048 (0.0%)	-5e-05 ± 0.00086 (-0.0%)	-0.1 ± -2.2
WH, 250 $< p_T^W <$400 GeV, $n_{jets}^{add}\geq$1	0.0004 ± 0.00059 (0.0%)	-7e-05 ± 0.00052 (-0.0%)	-0.2 ± -1.3
Signal	46.8 ± 8.1	62.0 ± 16.0	1.32 ± 0.41
Background	1223.0 ± 93.0	1349.0 ± 32.0	1.103 ± 0.088
Data	1412.0	1412.0	1.00e+00

TABLE A.12: The post-fit vs pre-fit yields for the 2-lepton, $\geq$ 3-jet, 150 $<p_T^V <$ 250 GeV signal region. The upper table is for the 20 GeV jet p_T selection, while the lower table is for 30 GeV. The percentages in the brackets next to the background (signal) yields are the percentage of that sample relative to the total background (signal). For the STXS regions, the number of jets is the number of jets additional to the Higgs decay. The other ZH and WH yields are the signal events that fall outside of the STXS regions under study. The Z+hf sample is the heavy flavour component of the Z+jets sample, likewise for W+jets. Tops is the $t\bar{t}$ +single-top data-driven estimate derived from the $e\mu$-CR.

	Pre-fit	**Post-fit**	**Post/Pre**
Z+hf	2110.0 ± 150.0	2291.0 ± 52.0	1.086 ± 0.081
Z+jets	2120.0 ± 150.0 (92.4%)	2299.0 ± 51.0 (94.2%)	1.084 ± 0.08
W+hf	1.186 ± 0.035	1.21 ± 0.16	1.02 ± 0.14
W+jets	1.186 ± 0.035 (0.1%)	1.21 ± 0.16 (0.0%)	1.02 ± 0.14
Tops	388.228 ± 0.017	377.0 ± 18.0	0.971 ± 0.046
diboson	174.0 ± 40.0 (7.6%)	141.0 ± 25.0 (5.8%)	0.81 ± 0.24
Other ZH	0.01 ± 0.00 (0.0%)	0.01 ± 0.00 (0.0%)	0.87 ± 0.33
ZH, 75 $< p_T^Z <$150 GeV, n_{jets}^{add}=0	0.55 ± 0.54 (0.9%)	0.69 ± 0.88 (0.6%)	1.3 ± 2
ZH, 75 $< p_T^Z <$150 GeV, $n_{jets}^{add}\geq$1	0.77 ± 0.67 (1.3%)	0.6 ± 1.6 (0.5%)	0.8 ± 2.2
ZH, 150 $< p_T^Z <$250 GeV, n_{jets}^{add}=0	22.3 ± 5.4 (36.5%)	31.0 ± 12.0 (27.8%)	1.39 ± 0.63
ZH, 150 $< p_T^Z <$250 GeV, $n_{jets}^{add}\geq$1	36.5 ± 7.6 (59.8%)	78.0 ± 36.0 (70.0%)	2.1 ± 1.1
ZH, 250 $< p_T^Z <$400 GeV, n_{jets}^{add}=0	0.32 ± 0.12 (0.5%)	0.16 ± 0.16 (0.1%)	0.5 ± 0.53
ZH, 250 $< p_T^Z <$400 GeV, $n_{jets}^{add}\geq$1	0.61 ± 0.17 (1.0%)	1.02 ± 0.68 (0.9%)	1.7 ± 1.2
Other WH	0.00 ± 0.00 (0.0%)	0.00 ± 0.00 (0.0%)	0.4 ± 1.3
WH, 150 $< p_T^W <$250 GeV, n_{jets}^{add}=0	0.0014 ± 0.0025 (0.0%)	0.0012 ± 0.0017 (0.0%)	0.9 ± 2
WH, 150 $< p_T^W <$250 GeV, $n_{jets}^{add}\geq$1	0.0018 ± 0.0018 (0.0%)	0.0014 ± 0.0026 (0.0%)	0.8 ± 1.6
WH, 250 $< p_T^W <$400 GeV, $n_{jets}^{add}\geq$1	0.0016 ± 0.0014 (0.0%)	0.0002 ± 0.0028 (0.0%)	0.1 ± 1.8
Signal	61.0 ± 10.0	111.0 ± 33.0	1.82 ± 0.62
Background	2680.0 ± 160.0	2818.0 ± 46.0	1.051 ± 0.065
Data	2868.0	2868.0	1.00e+00

	Pre-fit	**Post-fit**	**Post/Pre**
Z+hf	2070.0 ± 170.0	2299.0 ± 49.0	1.111 ± 0.094
Z+jets	2080.0 ± 170.0 (93.3%)	2312.0 ± 48.0 (95.1%)	1.112 ± 0.094
W+hf	0.995 ± 0.05	1.1 ± 0.18	1.11 ± 0.19
W+jets	0.995 ± 0.05 (0.0%)	1.1 ± 0.18 (0.0%)	1.11 ± 0.19
Tops	424.622 ± 0.019	414.0 ± 19.0	0.975 ± 0.045
diboson	149.0 ± 34.0 (6.7%)	117.0 ± 22.0 (4.8%)	0.79 ± 0.23
Other ZH	0.01 ± 0.00 (0.0%)	0.01 ± 0.00 (0.0%)	0.99 ± 0.33
ZH, 75 $< p_T^Z <$150 GeV, n_{jets}^{add}=0	0.28 ± 0.27 (0.5%)	0.53 ± 0.58 (0.9%)	1.9 ± 2.8
ZH, 75 $< p_T^Z <$150 GeV, $n_{jets}^{add}\geq$1	0.8 ± 0.7 (1.5%)	-0.2 ± 1.1 (-0.3%)	-0.3 ± -1.4
ZH, 150 $< p_T^Z <$250 GeV, n_{jets}^{add}=0	11.4 ± 3.2 (22.0%)	18.8 ± 6.9 (32.6%)	1.65 ± 0.76
ZH, 150 $< p_T^Z <$250 GeV, $n_{jets}^{add}\geq$1	38.6 ± 8.1 (74.4%)	38.0 ± 31.0 (66.0%)	0.98 ± 0.83
ZH, 250 $< p_T^Z <$400 GeV, n_{jets}^{add}=0	0.161 ± 0.063 (0.3%)	0.16 ± 0.1 (0.3%)	0.99 ± 0.73
ZH, 250 $< p_T^Z <$400 GeV, $n_{jets}^{add}\geq$1	0.65 ± 0.18 (1.3%)	0.29 ± 0.57 (0.5%)	0.45 ± 0.89
WH, 150 $< p_T^W <$250 GeV, $n_{jets}^{add}\geq$1	0.0018 ± 0.0014 (0.0%)	-0.0003 ± 0.005 (-0.0%)	-0.2 ± -2.8
WH, 250 $< p_T^W <$400 GeV, $n_{jets}^{add}\geq$1	0.0012 ± 0.0012 (0.0%)	-0.0002 ± 0.0019 (-0.0%)	-0.2 ± -1.6
Signal	52.0 ± 9.3	58.0 ± 30.0	1.12 ± 0.61
Background	2660.0 ± 180.0	2844.0 ± 44.0	1.069 ± 0.074
Data	2825.0	2825.0	1.00e+00

TABLE A.13: The post-fit vs pre-fit yields for the 2-lepton, 2-jet, 250 $<p_T^V <$ 400 GeV signal region. The upper table is for the 20 GeV jet p_T selection, while the lower table is for 30 GeV. The percentages in the brackets next to the background (signal) yields are the percentage of that sample relative to the total background (signal). For the STXS regions, the number of jets is the number of jets additional to the Higgs decay. The other ZH and WH yields are the signal events that fall outside of the STXS regions under study. The Z+hf sample is the heavy flavour component of the Z+jets sample, likewise for W+jets. Tops is the $t\bar{t}$ +single-top data-driven estimate derived from the $e\mu$-CR.

	Pre-fit	**Post-fit**	**Post/Pre**
Z+hf	63.9 ± 7.2	75.7 ± 3.5	1.18 ± 0.14
Z+jets	63.9 ± 7.2 (78.4%)	75.7 ± 3.5 (81.0%)	1.18 ± 0.14
Tops	1.996 ± 0.016	2.1 ± 1.5	1.05 ± 0.75
diboson	17.6 ± 5.3 (21.6%)	17.8 ± 3.2 (19.0%)	1.01 ± 0.35
ZH, 150 $< p_T^Z <$250 GeV, n_{jets}^{add}=0	0.3 ± 0.48 (3.7%)	0.43 ± 0.68 (9.5%)	1.4 ± 3.2
ZH, 150 $< p_T^Z <$250 GeV, $n_{jets}^{add}\geq$1	0.013 ± 0.021 (0.2%)	0.028 ± 0.046 (0.6%)	2.2 ± 5
ZH, 250 $< p_T^Z <$400 GeV, n_{jets}^{add}=0	7.5 ± 1.2 (92.3%)	3.6 ± 3.4 (79.3%)	0.48 ± 0.46
ZH, 250 $< p_T^Z <$400 GeV, $n_{jets}^{add}\geq$1	0.31 ± 0.12 (3.8%)	0.48 ± 0.36 (10.6%)	1.5 ± 1.3
Signal	8.2 ± 1.4	4.6 ± 3.3	0.56 ± 0.41
Background	83.5 ± 9.9	95.7 ± 3.9	1.15 ± 0.14
Data	110.0	110.0	1.00e+00

	Pre-fit	**Post-fit**	**Post/Pre**
Z+hf	107.0 ± 10.0	125.2 ± 4.9	1.17 ± 0.12
Z+jets	107.0 ± 10.0 (81.4%)	125.3 ± 4.9 (86.8%)	1.17 ± 0.12
Tops	1.996 ± 0.016	2.4 ± 1.6	1.2 ± 0.8
diboson	24.5 ± 7.1 (18.6%)	19.0 ± 4.0 (13.2%)	0.78 ± 0.28
ZH, 150 $< p_T^Z <$250 GeV, n_{jets}^{add}=0	0.43 ± 0.68 (3.7%)	0.6 ± 0.92 (6.3%)	1.4 ± 3.1
ZH, 150 $< p_T^Z <$250 GeV, $n_{jets}^{add}\geq$1	0.033 ± 0.053 (0.3%)	0.031 ± 0.056 (0.3%)	0.9 ± 2.3
ZH, 250 $< p_T^Z <$400 GeV, n_{jets}^{add}=0	10.3 ± 1.6 (89.2%)	8.5 ± 4.6 (89.9%)	0.83 ± 0.46
ZH, 250 $< p_T^Z <$400 GeV, $n_{jets}^{add}\geq$1	0.78 ± 0.29 (6.8%)	0.32 ± 0.64 (3.4%)	0.41 ± 0.83
WH, 250 $< p_T^W <$400 GeV, n_{jets}^{add}=0	0.00031 ± 0.00041 (0.0%)	0.00043 ± 0.00058 (0.0%)	1.4 ± 2.6
WH, 250 $< p_T^W <$400 GeV, $n_{jets}^{add}\geq$1	0.00033 ± 0.00038 (0.0%)	-5e-05 ± 0.00039 (-0.0%)	-0.2 ± -1.2
Signal	11.6 ± 2.0	9.4 ± 4.5	0.81 ± 0.41
Background	133.0 ± 13.0	146.7 ± 5.1	1.1 ± 0.11
Data	161.0	161.0	1.00e+00

TABLE A.14: The post-fit vs pre-fit yields for the 2-lepton, $\geq$ 3-jet, 250 $<p_T^V <$ 400 GeV signal region. The upper table is for the 20 GeV jet p_T selection, while the lower table is for 30 GeV. The percentages in the brackets next to the background (signal) yields are the percentage of that sample relative to the total background (signal). For the STXS regions, the number of jets is the number of jets additional to the Higgs decay. The other ZH and WH yields are the signal events that fall outside of the STXS regions under study. The Z+hf sample is the heavy flavour component of the Z+jets sample, likewise for W+jets. Tops is the $t\bar{t}$ +single-top data-driven estimate derived from the $e\mu$-CR.

	Pre-fit	**Post-fit**	**Post/Pre**
Z+hf	352.0 ± 25.0	386.0 ± 11.0	1.097 ± 0.084
Z+jets	354.0 ± 25.0 (88.9%)	388.0 ± 11.0 (91.5%)	1.096 ± 0.083
W+hf	0.275 ± 0.018	0.285 ± 0.041	1.04 ± 0.16
W+jets	0.275 ± 0.018 (0.1%)	0.285 ± 0.041 (0.1%)	1.04 ± 0.16
Tops	10.115 ± 0.00062	9.9 ± 3.1	0.98 ± 0.31
diboson	44.0 ± 10.0 (11.0%)	35.9 ± 6.7 (8.5%)	0.82 ± 0.24
Other ZH	0.00 ± 0.00 (0.0%)	0.00 ± 0.00 (0.0%)	0.9 ± 0.59
ZH, 150 $< p_T^Z <$250 GeV, n_{jets}^{add}=0	0.24 ± 0.38 (1.5%)	0.38 ± 0.61 (1.8%)	1.6 ± 3.6
ZH, 150 $< p_T^Z <$250 GeV, $n_{jets}^{add}\geq$1	0.39 ± 0.48 (2.5%)	0.9 ± 1.1 (4.3%)	2.3 ± 4
ZH, 250 $< p_T^Z <$400 GeV, n_{jets}^{add}=0	5.0 ± 1.2 (31.6%)	2.7 ± 2.5 (12.9%)	0.54 ± 0.52
ZH, 250 $< p_T^Z <$400 GeV, $n_{jets}^{add}\geq$1	10.2 ± 1.8 (64.4%)	17.0 ± 11.0 (81.0%)	1.7 ± 1.1
WH, 250 $< p_T^W <$400 GeV, n_{jets}^{add}=0	0.00031 ± 0.00049 (0.0%)	0.00046 ± 0.00073 (0.0%)	1.5 ± 3.3
WH, 250 $< p_T^W <$400 GeV, $n_{jets}^{add}\geq$1	0.0014 ± 0.0016 (0.0%)	0.0002 ± 0.0026 (0.0%)	0.1 ± 1.9
Signal	15.8 ± 2.3	21.0 ± 10.0	1.33 ± 0.66
Background	408.0 ± 28.0	434.0 ± 11.0	1.064 ± 0.078
Data	441.0	441.0	1.00e+00

	Pre-fit	**Post-fit**	**Post/Pre**
Z+hf	368.0 ± 30.0	414.0 ± 12.0	1.125 ± 0.097
Z+jets	369.0 ± 30.0 (90.1%)	416.0 ± 12.0 (92.8%)	1.127 ± 0.097
W+hf	0.275 ± 0.018	0.308 ± 0.05	1.12 ± 0.2
W+jets	0.275 ± 0.018 (0.1%)	0.308 ± 0.05 (0.1%)	1.12 ± 0.2
Tops	12.136 ± 0.00085	11.7 ± 3.3	0.96 ± 0.27
diboson	40.4 ± 9.4 (9.9%)	32.0 ± 6.3 (7.1%)	0.79 ± 0.24
Other ZH	0.00 ± 0.00 (0.0%)	0.00 ± 0.00 (0.0%)	0.95 ± 0.64
ZH, 150 $< p_T^Z <$250 GeV, n_{jets}^{add}=0	0.13 ± 0.21 (0.9%)	0.21 ± 0.33 (2.6%)	1.6 ± 3.6
ZH, 150 $< p_T^Z <$250 GeV, $n_{jets}^{add}\geq$1	0.43 ± 0.53 (3.1%)	0.42 ± 0.62 (5.2%)	1 ± 1.9
ZH, 250 $< p_T^Z <$400 GeV, n_{jets}^{add}=0	2.55 ± 0.7 (18.2%)	2.6 ± 1.4 (32.4%)	1.02 ± 0.62
ZH, 250 $< p_T^Z <$400 GeV, $n_{jets}^{add}\geq$1	10.9 ± 1.9 (77.8%)	4.8 ± 9.6 (59.8%)	0.44 ± 0.88
WH, 250 $< p_T^W <$400 GeV, $n_{jets}^{add}\geq$1	0.0017 ± 0.0016 (0.0%)	-0.0004 ± 0.0029 (-0.0%)	-0.2 ± -1.7
Signal	14.0 ± 2.2	8.0 ± 9.4	0.57 ± 0.68
Background	422.0 ± 32.0	460.0 ± 11.0	1.09 ± 0.087
Data	471.0	471.0	1.00e+00

A.2 $\Delta R(b_1, b_2) - p_T^V$ region yields

This section compares the yields of the MC samples used to define the p_T^V dependent $\Delta R(b_1, b_2)$ selection that is used to create the signal region (SR), as well as the two low and high control regions (CRLow and CRHigh). These selections were defined in the 1-lepton channel, and applied to the 0- and 2-lepton channels. The selections were chosen such that 10% of the diboson sample fell within CRLow, and that 5% (15%) of the signal sample fell in CRHigh for the 2 (3/3+) jets regions. Refer to Section 5.2.1.4 for more information.
The 2 jet events are in Table A.15, and the 3 jet events are in Table A.16. Only the 30 GeV jet p_T selection yields are shown as they show a similar story to the 20 GeV jet p_T selection.

TABLE A.15: The yields of the diboson and and signal samples in the CRLow, SR and CRHigh of the 0-, 1- and 2-lepton channels, for the 2 jet events. The yields are shown per p_T^V region.

Lepton Channel	**Sample**	**CRLow**	**SR**	**CRHigh**
		75-150ptv		
Two	Signal	0.95 (0.8%)	110.29 (93.5%)	6.74 (5.7%)
	Diboson	22.23 (5.1%)	402.83 (92.3%)	11.35 (2.6%)
		150-250ptv		
Zero	Signal	4.07 (1.9%)	203.45 (93.8%)	9.42 (4.3%)
	Diboson	59.83 (10.7%)	488.13 (87.3%)	11.11 (2.0%)
One	Signal	2.64 (1.2%)	201.67 (93.9%)	10.39 (4.8%)
	Diboson	38.63 (10.2%)	325.11 (86.1%)	13.87 (3.7%)
Two	Signal	0.30 (0.6%)	46.77 (93.8%)	2.81 (5.6%)
	Diboson	4.72 (4.0%)	109.30 (93.0%)	3.48 (3.0%)
		250-400ptv		
Zero	Signal	0.57 (1.1%)	46.63 (93.8%)	2.53 (5.1%)
	Diboson	10.04 (8.8%)	101.24 (88.3%)	3.32 (2.9%)
One	Signal	0.45 (0.7%)	58.50 (94.2%)	3.14 (5.1%)
	Diboson	8.07 (9.7%)	71.44 (85.6%)	3.93 (4.7%)
Two	Signal	0.04 (0.4%)	11.68 (94.0%)	0.70 (5.6%)
	Diboson	1.71 (6.3%)	24.50 (90.4%)	0.89 (3.3%)

TABLE A.16: The yields of the diboson and and signal samples in the CRLow, SR and CRHigh of the 0-, 1- and 2-lepton channels, for the 3 jet events. The yields are shown per p_T^V region.

Lepton channel	**Sample**	**CRLow**	**SR**	**CRHigh**
		75-150ptv		
Two	Signal	4.21 (3.7%)	90.81 (80.9%)	17.30 (15.4%)
	Diboson	52.72 (9.5%)	405.28 (73.4%)	94.46 (17.1%)
		150-250ptv		
Zero	Signal	3.33 (2.1%)	138.53 (86.4%)	18.46 (11.5%)
	Diboson	46.57 (9.0%)	413.81 (79.7%)	58.81 (11.3%)
One	Signal	3.14 (2.1%)	125.87 (82.8%)	23.01 (15.1%)
	Diboson	57.04 (10.3%)	381.74 (69.1%)	113.98 (20.6%)
Two	Signal	1.47 (2.2%)	51.92 (75.9%)	15.03 (22.0%)
	Diboson	19.99 (8.7%)	149.40 (65.1%)	60.27 (26.2%)
		250-400ptv		
Zero	Signal	1.03 (2.7%)	31.73 (81.9%)	5.96 (15.4%)
	Diboson	12.94 (11.0%)	83.69 (71.0%)	21.30 (18.1%)
One	Signal	1.23 (2.7%)	38.18 (82.3%)	6.95 (15.0%)
	Diboson	15.22 (10.1%)	89.91 (60.0%)	44.80 (29.9%)
Two	Signal	0.37 (1.8%)	14.18 (68.3%)	6.21 (29.9%)
	Diboson	6.17 (8.1%)	40.41 (53.3%)	29.27 (38.6%)

A.3 Data-MC Plots

This section contains all the Data-MC plots of the 14 signal regions and 28 control regions, for both the pre-fit and post-fit distributions of the 20 GeV and 30 GeV jet p_T selections. For the log-scale plots of the signal regions, please refer to Section 7.3.2. All these plots are shown in the same manner that the likelihood fit would see them. So the control regions are single-binned p_T^V distributions, while the signal regions are MVA distributions that have had the transformation D applied to the binning, as described in Section 5.2.4.
The plots are laid out as follows:

- 0-lepton, 2-jet, 150 $<p_T^V <$ 250 GeV, signal regions: Figure A.1
- 0-lepton, 2-jet, 150 $<p_T^V <$ 250 GeV, control regions: Figure A.2
- 0-lepton, 3-jet, 150 $<p_T^V <$ 250 GeV, signal regions: Figure A.3
- 0-lepton, 3-jet, 150 $<p_T^V <$ 250 GeV, control regions: Figure A.4
- 0-lepton, 2-jet, 250 $<p_T^V <$ 400 GeV, signal regions: Figure A.5
- 0-lepton, 2-jet, 250 $<p_T^V <$ 400 GeV, control regions: Figure A.6
- 0-lepton, 3-jet, 250 $<p_T^V <$ 400 GeV, signal regions: Figure A.7
- 0-lepton, 3-jet, 250 $<p_T^V <$ 400 GeV, control regions: Figure A.8
- 1-lepton, 2-jet, 150 $<p_T^V <$ 250 GeV, signal regions: Figure A.9
- 1-lepton, 2-jet, 150 $<p_T^V <$ 250 GeV, control regions: Figure A.10
- 1-lepton, 3-jet, 150 $<p_T^V <$ 250 GeV, signal regions: Figure A.11
- 1-lepton, 3-jet, 150 $<p_T^V <$ 250 GeV, control regions: Figure A.12
- 1-lepton, 2-jet, 250 $<p_T^V <$ 400 GeV, signal regions: Figure A.13
- 1-lepton, 2-jet, 250 $<p_T^V <$ 400 GeV, control regions: Figure A.14
- 1-lepton, 3-jet, 250 $<p_T^V <$ 400 GeV, signal regions: Figure A.15
- 1-lepton, 3-jet, 250 $<p_T^V <$ 400 GeV, control regions: Figure A.16
- 2-lepton, 2-jet, 75 $<p_T^V <$ 150 GeV, signal regions: Figure A.17
- 2-lepton, 2-jet, 75 $<p_T^V <$ 150 GeV, control regions: Figure A.18
- 2-lepton, $\geq$ 3-jet, 75 $<p_T^V <$ 150 GeV, signal regions: Figure A.19

- 2-lepton, $\geq$ 3-jet, 75 $<p_T^V <$ 150 GeV, control regions: Figure A.20
- 2-lepton, 2-jet, 150 $<p_T^V <$ 250 GeV, signal regions: Figure A.21
- 2-lepton, 2-jet, 150 $<p_T^V <$ 250 GeV, control regions: Figure A.22
- 2-lepton, $\geq$ 3-jet, 150 $<p_T^V <$ 250 GeV, signal regions: Figure A.23
- 2-lepton, $\geq$ 3-jet, 150 $<p_T^V <$ 250 GeV, control regions: Figure A.24
- 2-lepton, 2-jet, 250 $<p_T^V <$ 400 GeV, signal regions: Figure A.25
- 2-lepton, 2-jet, 250 $<p_T^V <$ 400 GeV, control regions: Figure A.26
- 2-lepton, $\geq$ 3-jet, 250 $<p_T^V <$ 400 GeV, signal regions: Figure A.27
- 2-lepton, $\geq$ 3-jet, 250 $<p_T^V <$ 400 GeV, control regions: Figure A.28

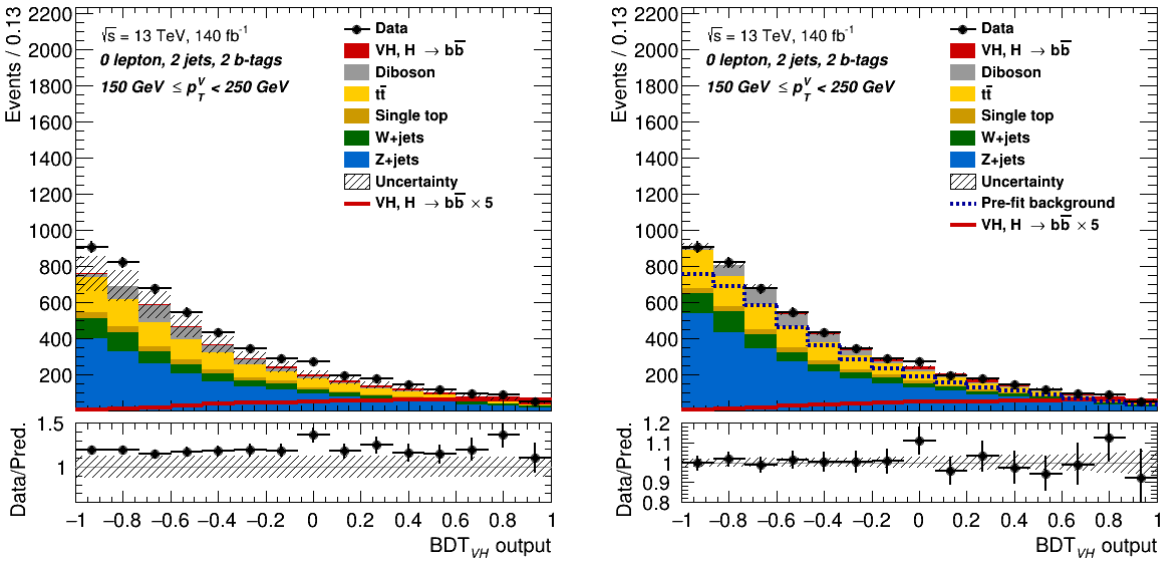

(a) (b)

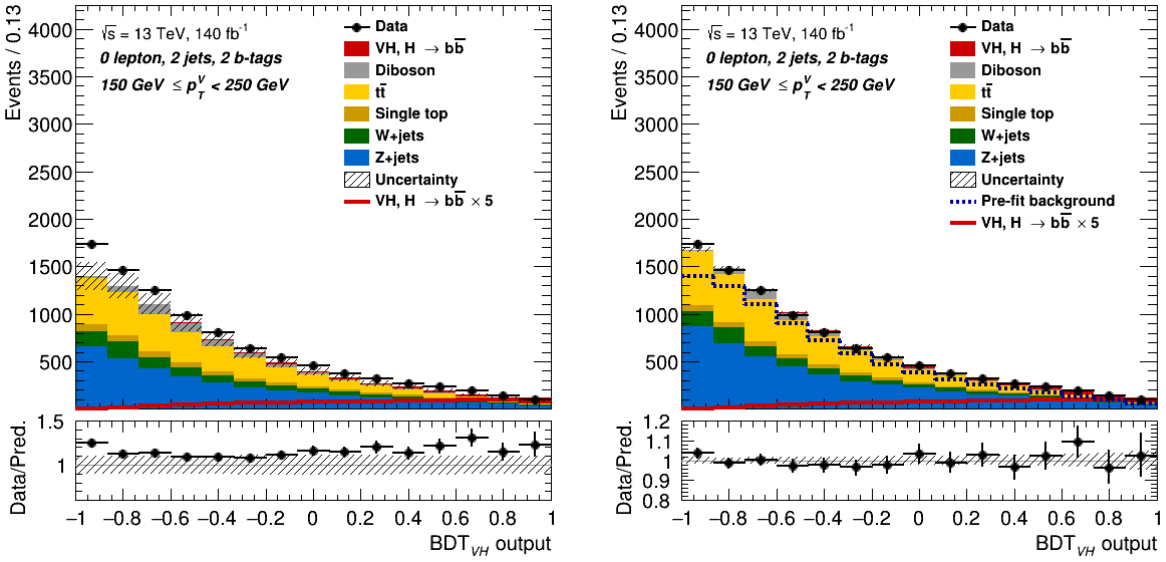

(c) (d)

FIGURE A.1: The data-MC plots of the BDT distribution for the 0-lepton, 2-jet, 150 $< p_T^V <$ 250 GeV, signal regions. The top row shows the jet p_T selection of 20 GeV, while the bottom row shows 30 GeV. The left column has the pre-fit plots, while the right column has the post-fit plots. The red line is the signal (filled red histogram) scaled by the factor given in the legend so that the shape of the signal is easier to see, and the dashed blue line is the total pre-fit background. The bottom sub-plot shows the ratio of the data to the theory prediction, along with the relative post-fit error given by the shaded band.

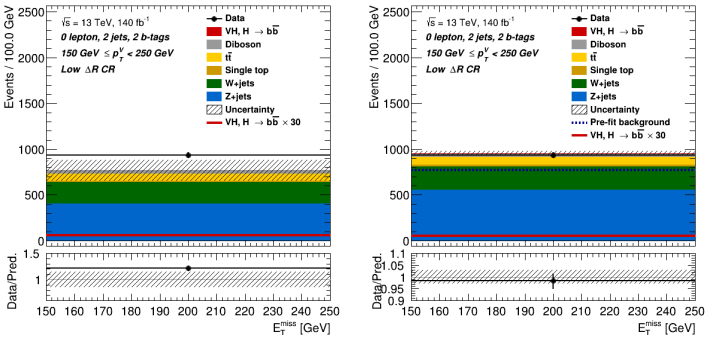

(a)

(b)

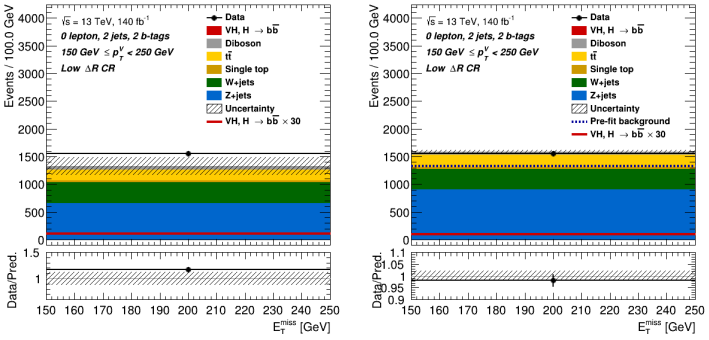

(c)

(d)

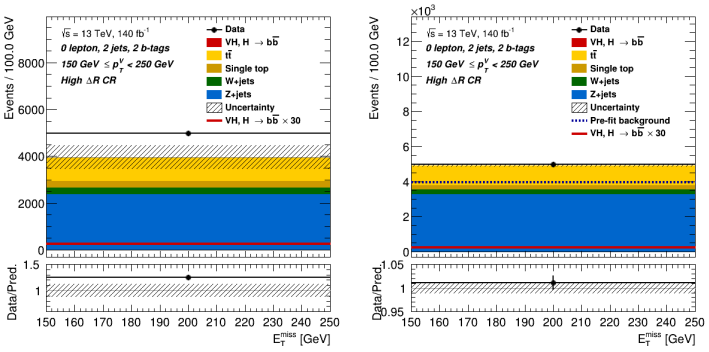

(e)

(f)

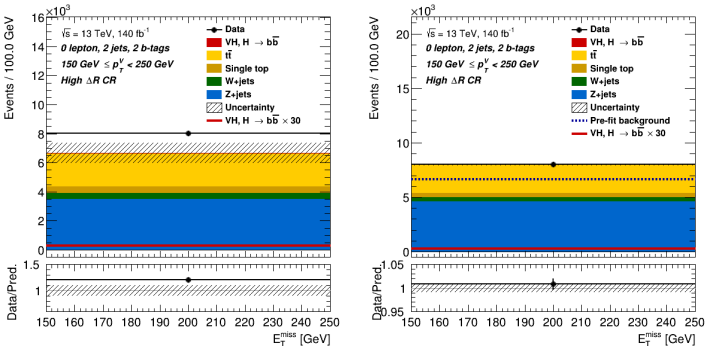

(g)

(h)

FIGURE A.2: The data-MC plots of the BDT distribution for the 0-lepton, 2-jet, 150 $< p_T^V <$ 250 GeV control regions. The left column has the pre-fit plots, while the right column has the post-fit plots. The top row shows the CRLow jet p_T selection of 20 GeV, the second row shows 30 GeV CRLow, the third row shows the 20 GeV CRHigh and the fourth row shows the 30 GeV CRHigh. The red line is the signal (filled red histogram) scaled by the factor given in the legend so that the shape of the signal is easier to see, and the dashed blue line is the total pre-fit background. The bottom sub-plot shows the ratio of the data to the theory prediction, along with the relative post-fit error given by the shaded band.

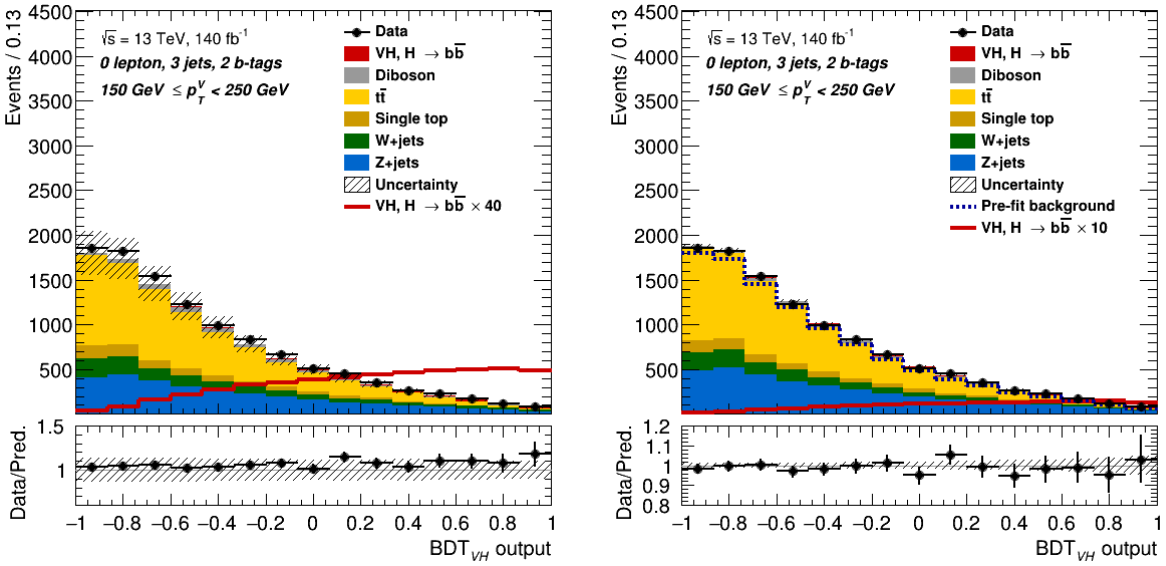

(a) (b)

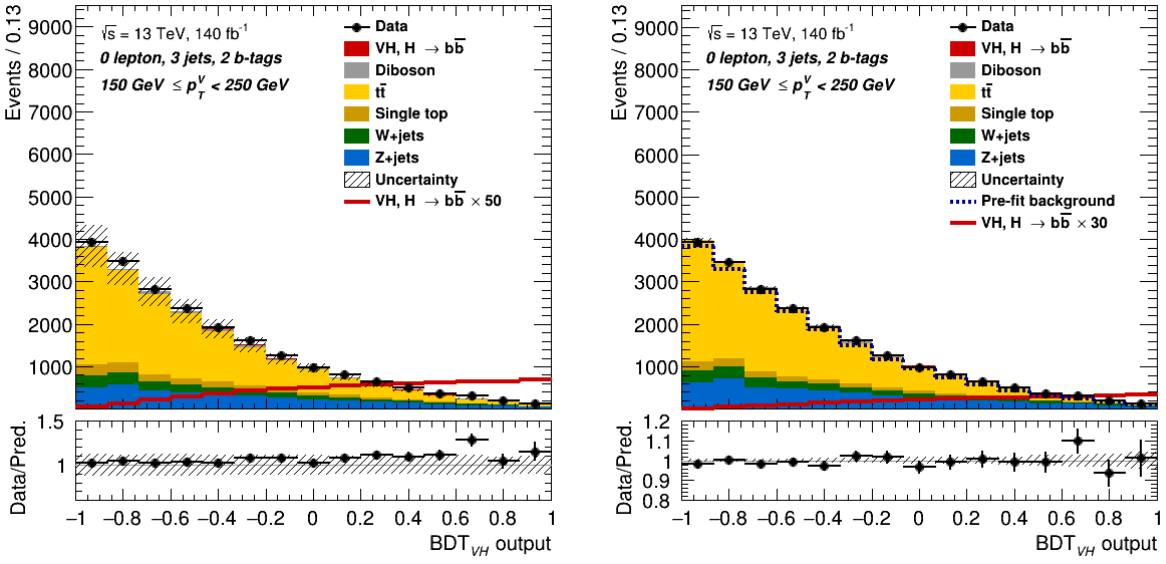

(c) (d)

FIGURE A.3: The data-MC plots of the BDT distribution for the 0-lepton, 3-jet, 150 $< p_T^V <$ 250 GeV, signal regions. The top row shows the jet p_T selection of 20 GeV, while the bottom row shows 30 GeV. The left column has the pre-fit plots, while the right column has the post-fit plots. The red line is the signal (filled red histogram) scaled by the factor given in the legend so that the shape of the signal is easier to see, and the dashed blue line is the total pre-fit background. The bottom sub-plot shows the ratio of the data to the theory prediction, along with the relative post-fit error given by the shaded band.

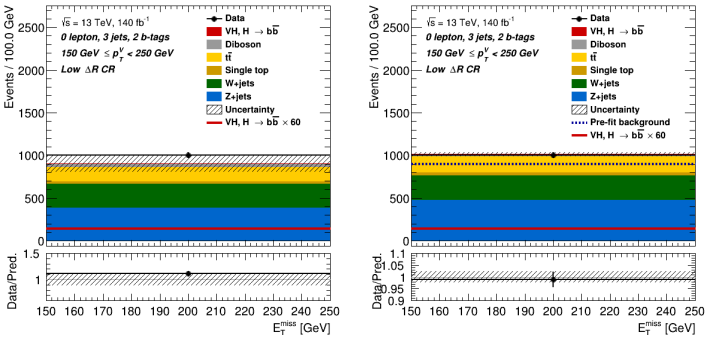

(a)

(b)

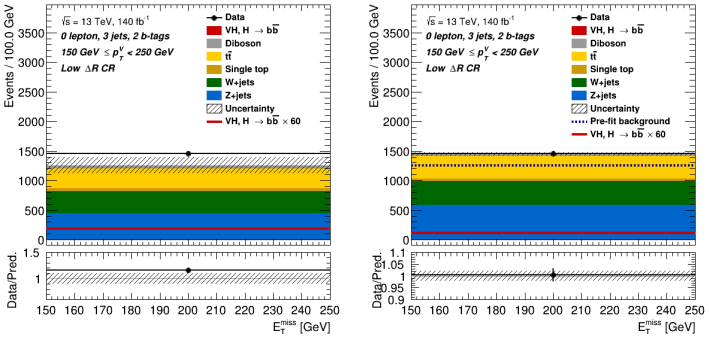

(c)

(d)

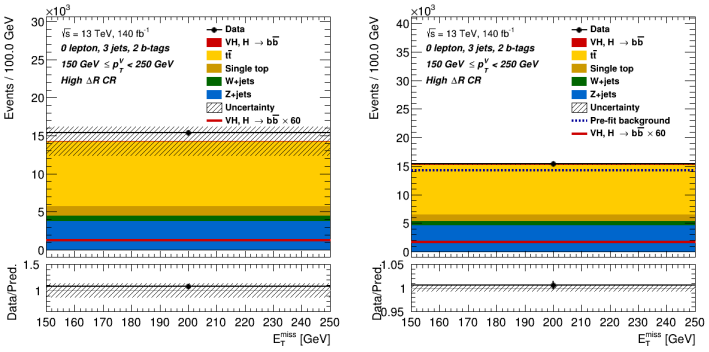

(e)

(f)

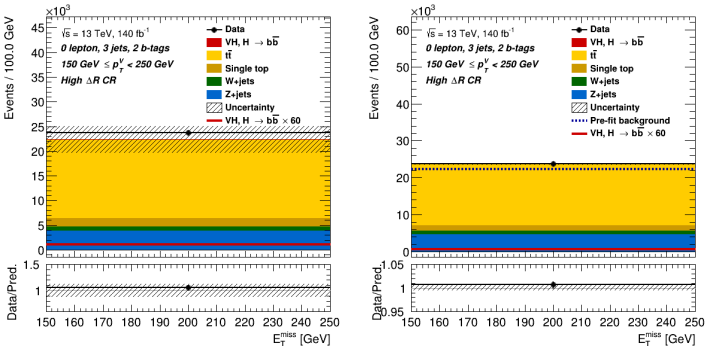

(g)

(h)

FIGURE A.4: The data-MC plots of the BDT distribution for the 0-lepton, 3-jet, 150 $< p_T^V <$ 250 GeV control regions. The left column has the pre-fit plots, while the right column has the post-fit plots. The top row shows the CRLow jet p_T selection of 20 GeV, the second row shows 30 GeV CRLow, the third row shows the 20 GeV CRHigh and the fourth row shows the 30 GeV CRHigh. The red line is the signal (filled red histogram) scaled by the factor given in the legend so that the shape of the signal is easier to see, and the dashed blue line is the total pre-fit background. The bottom sub-plot shows the ratio of the data to the theory prediction, along with the relative post-fit error given by the shaded band.

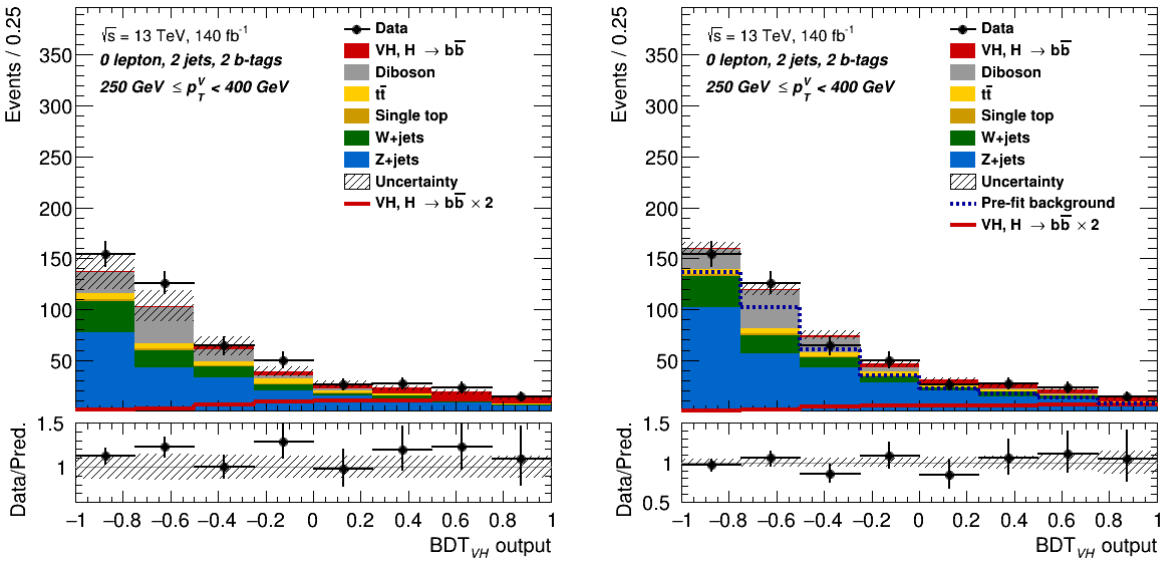

(a)

(b)

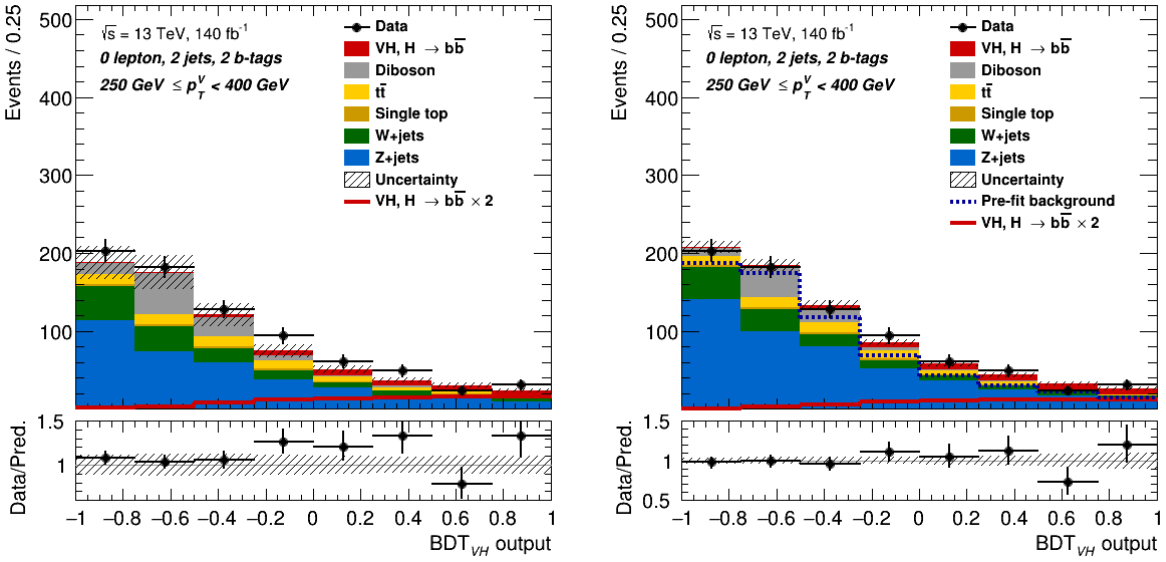

(c)

(d)

FIGURE A.5: The data-MC plots of the BDT distribution for the 0-lepton, 2-jet, 250 $< p_T^V <$ 400 GeV, signal regions. The top row shows the jet p_T selection of 20 GeV, while the bottom row shows 30 GeV. The left column has the pre-fit plots, while the right column has the post-fit plots. The red line is the signal (filled red histogram) scaled by the factor given in the legend so that the shape of the signal is easier to see, and the dashed blue line is the total pre-fit background. The bottom sub-plot shows the ratio of the data to the theory prediction, along with the relative post-fit error given by the shaded band.

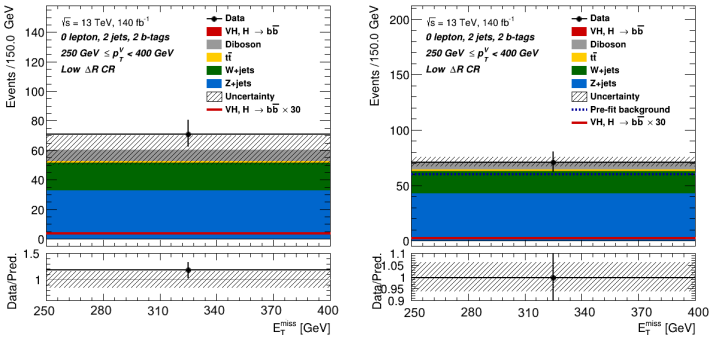

(a)

(b)

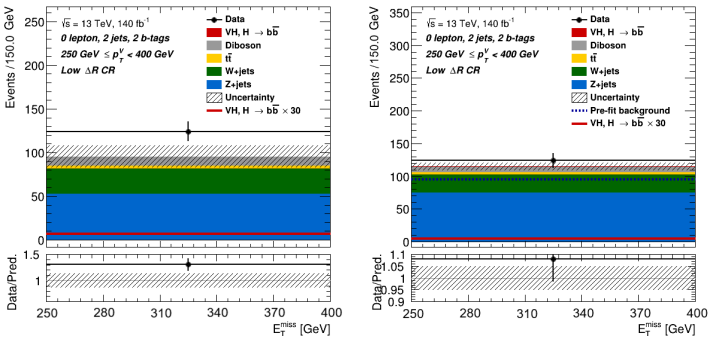

(c)

(d)

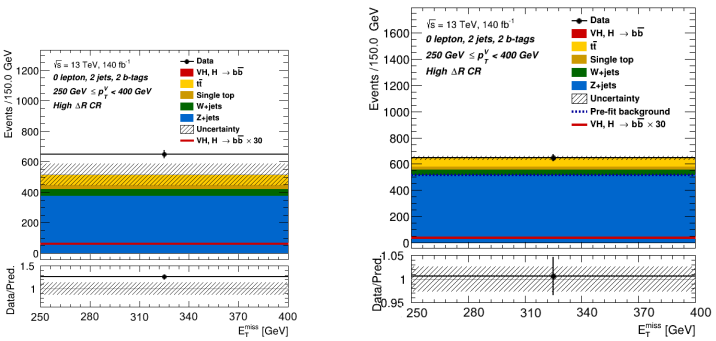

(e)

(f)

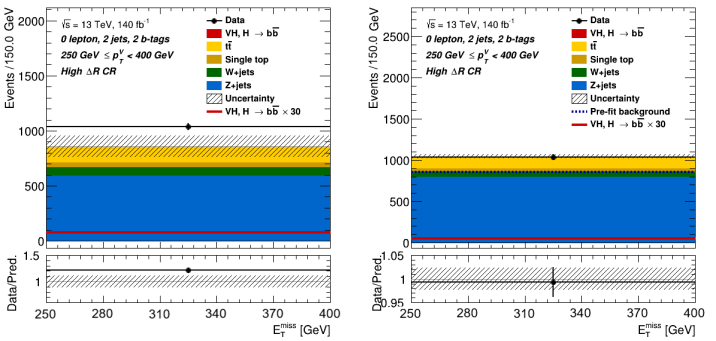

(g)

(h)

FIGURE A.6: The data-MC plots of the BDT distribution for the 0-lepton, 2-jet, 250 $< p_T^V <$ 400 GeV control regions. The left column has the pre-fit plots, while the right column has the post-fit plots. The top row shows the CRLow jet p_T selection of 20 GeV, the second row shows 30 GeV CRLow, the third row shows the 20 GeV CRHigh and the fourth row shows the 30 GeV CRHigh. The red line is the signal (filled red histogram) scaled by the factor given in the legend so that the shape of the signal is easier to see, and the dashed blue line is the total pre-fit background. The bottom sub-plot shows the ratio of the data to the theory prediction, along with the relative post-fit error given by the shaded band.

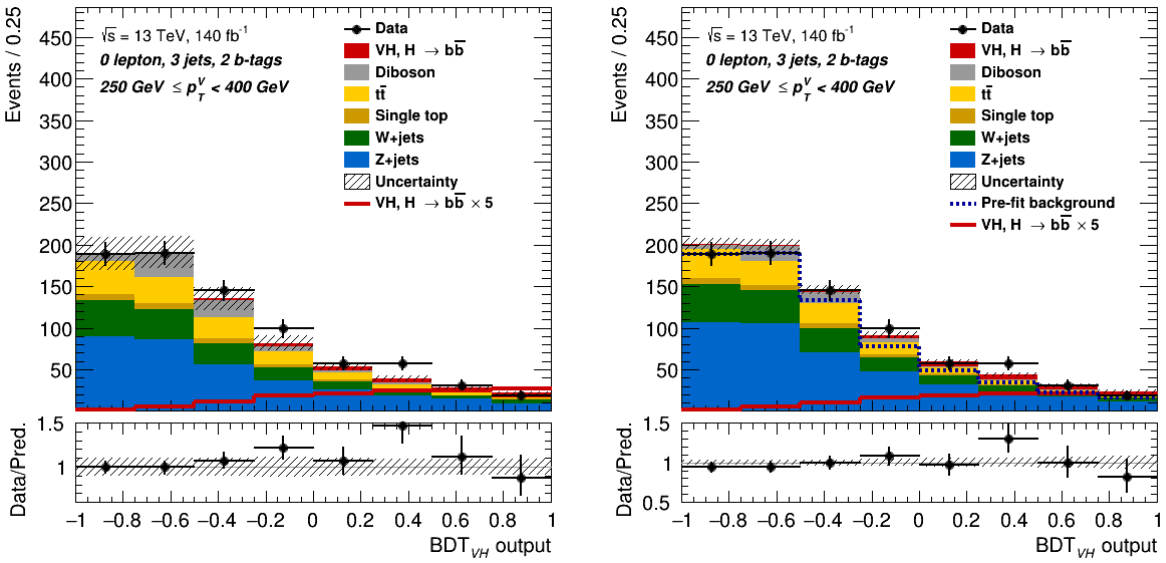

(a)

(b)

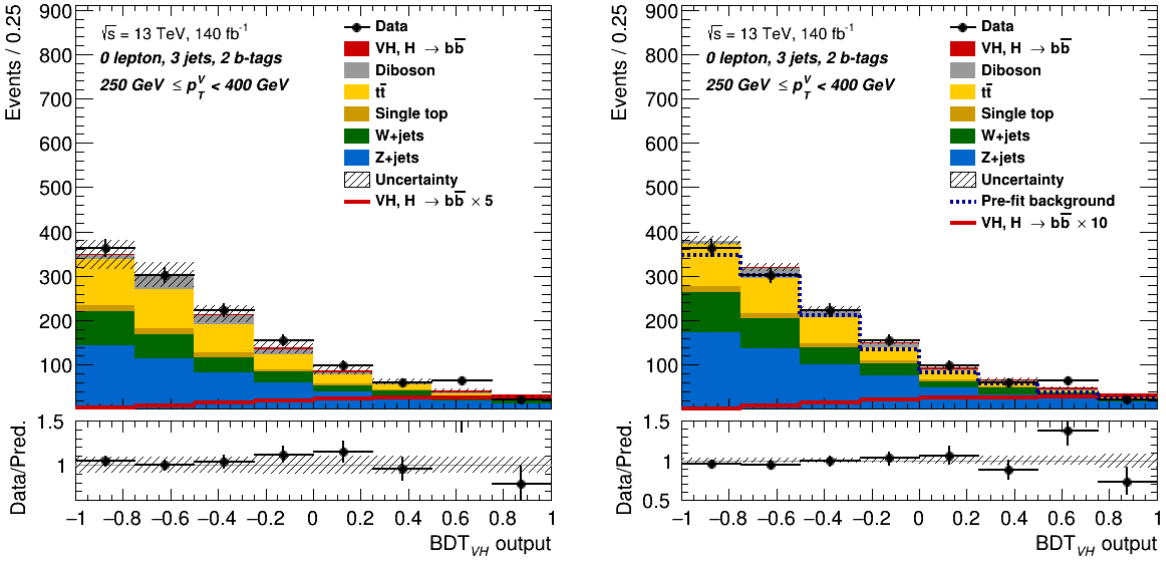

(c)

(d)

FIGURE A.7: The data-MC plots of the BDT distribution for the 0-lepton, 3-jet, 250 $< p_T^V <$ 400 GeV, signal regions. The top row shows the jet p_T selection of 20 GeV, while the bottom row shows 30 GeV. The left column has the pre-fit plots, while the right column has the post-fit plots. The red line is the signal (filled red histogram) scaled by the factor given in the legend so that the shape of the signal is easier to see, and the dashed blue line is the total pre-fit background. The bottom sub-plot shows the ratio of the data to the theory prediction, along with the relative post-fit error given by the shaded band.

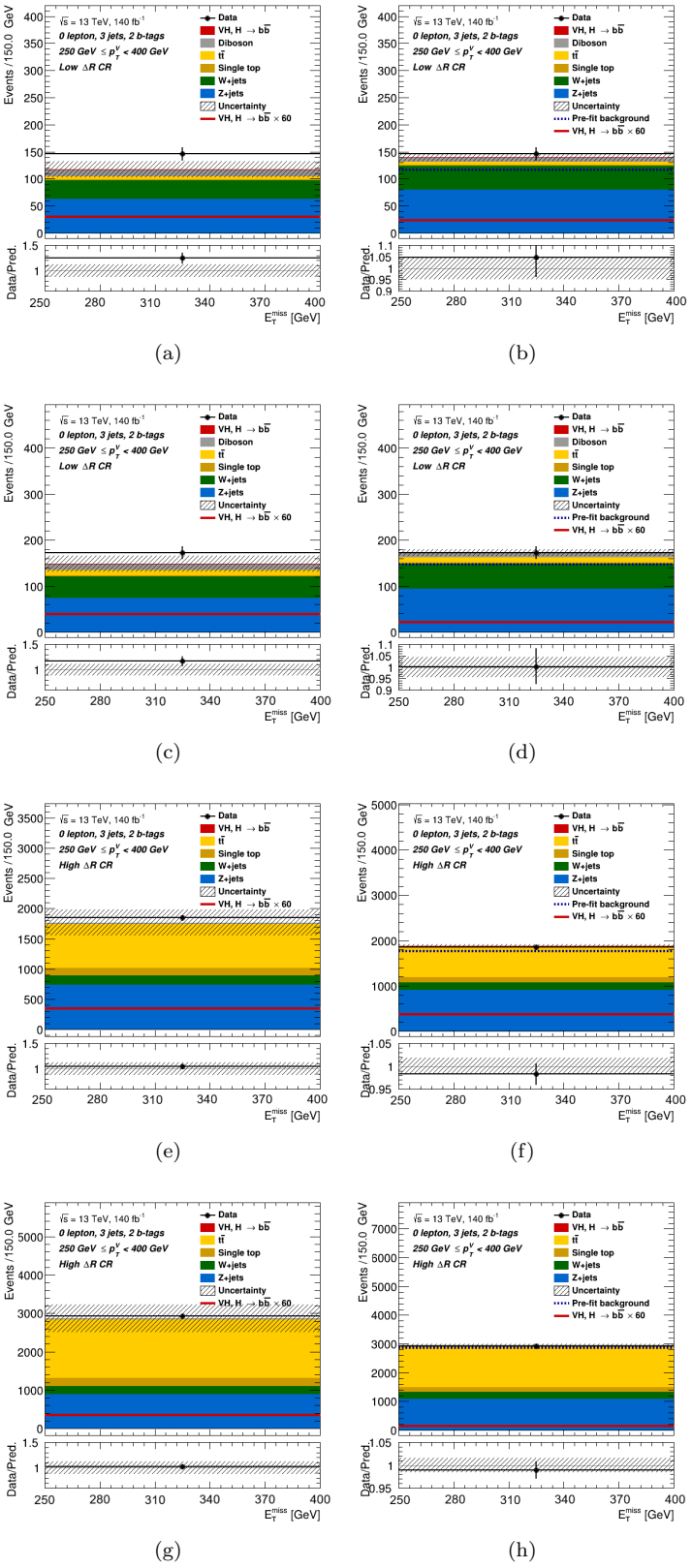

FIGURE A.8: The data-MC plots of the BDT distribution for the 0-lepton, 3-jet, 250 $< p_T^V <$ 400 GeV control regions. The left column has the pre-fit plots, while the right column has the post-fit plots. The top row shows the CRLow jet p_T selection of 20 GeV, the second row shows 30 GeV CRLow, the third row shows the 20 GeV CRHigh and the fourth row shows the 30 GeV CRHigh. The red line is the signal (filled red histogram) scaled by the factor given in the legend so that the shape of the signal is easier to see, and the dashed blue line is the total pre-fit background. The bottom sub-plot shows the ratio of the data to the theory prediction, along with the relative post-fit error given by the shaded band.

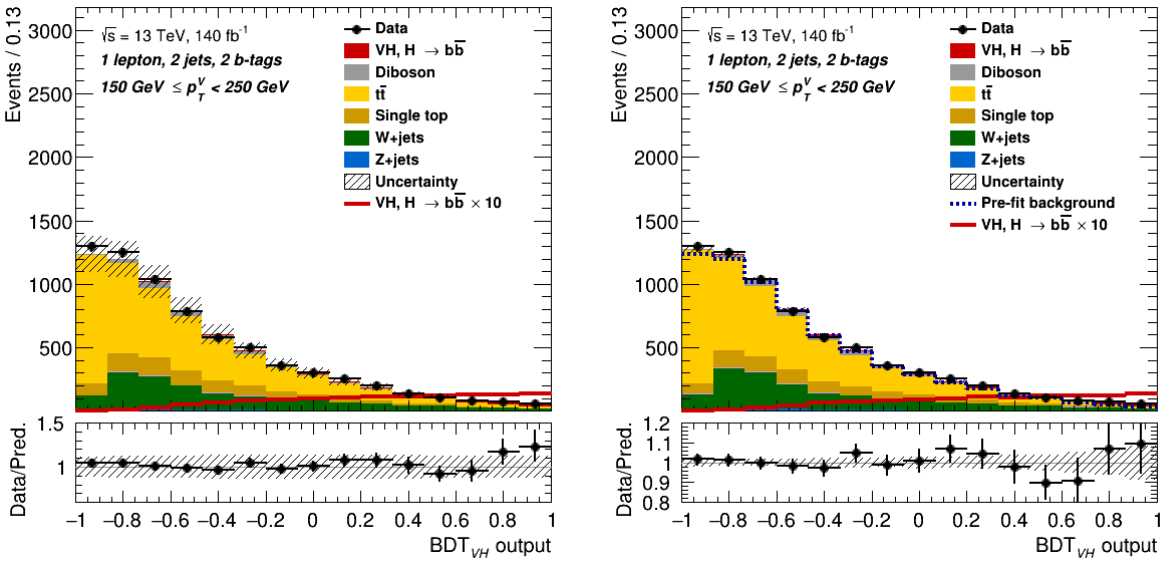

(a)

(b)

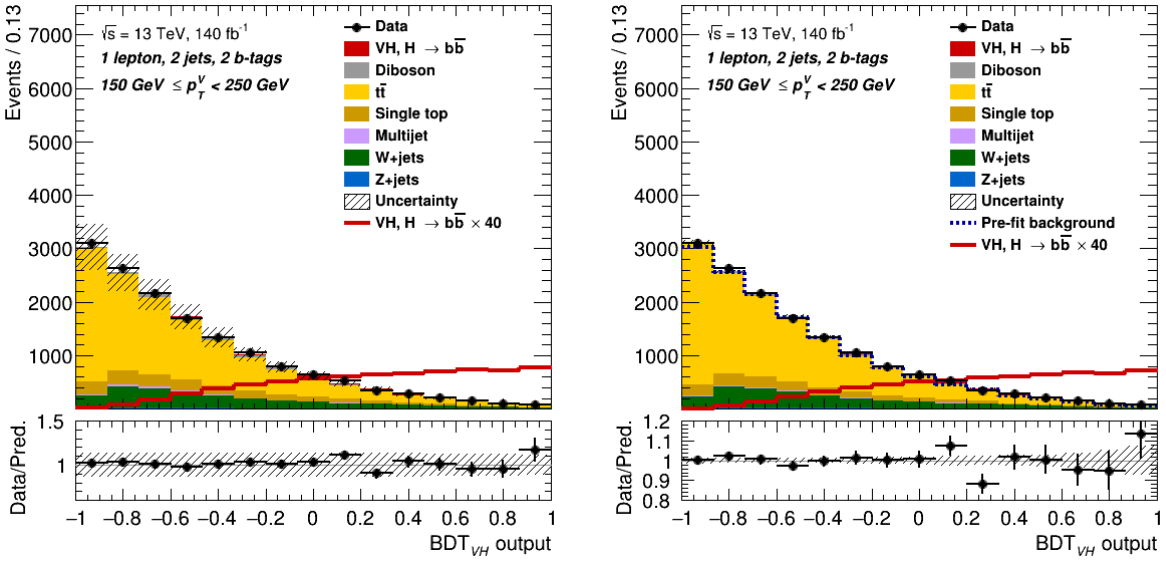

(c)

(d)

FIGURE A.9: The data-MC plots of the BDT distribution for the 1-lepton, 2-jet, 150 $< p_T^V <$ 250 GeV, signal regions. The top row shows the jet p_T selection of 20 GeV, while the bottom row shows 30 GeV. The left column has the pre-fit plots, while the right column has the post-fit plots. The red line is the signal (filled red histogram) scaled by the factor given in the legend so that the shape of the signal is easier to see, and the dashed blue line is the total pre-fit background. The bottom sub-plot shows the ratio of the data to the theory prediction, along with the relative post-fit error given by the shaded band.

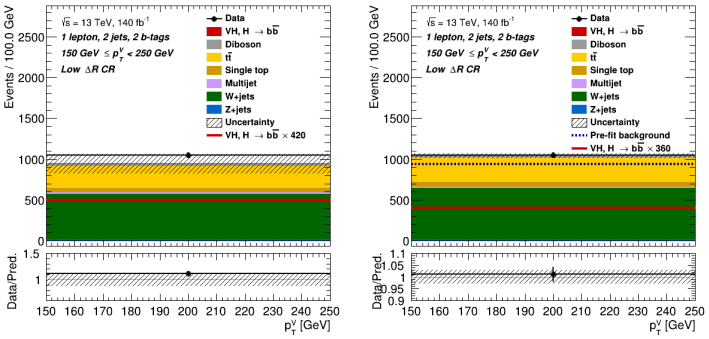

(a) (b)

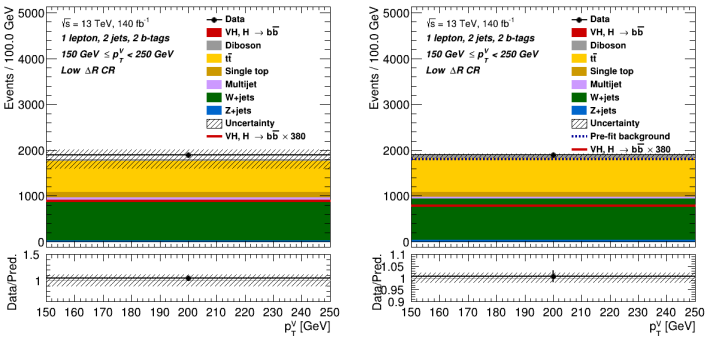

(c) (d)

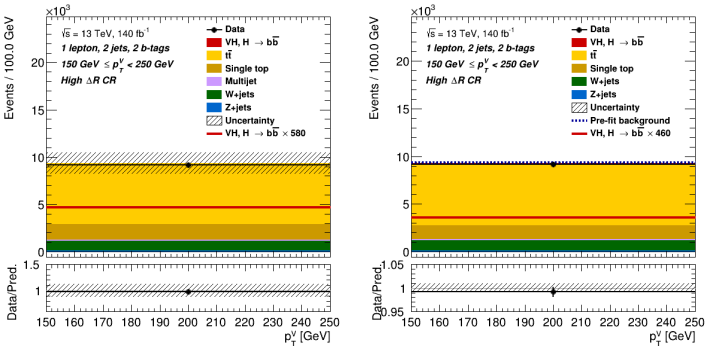

(e) (f)

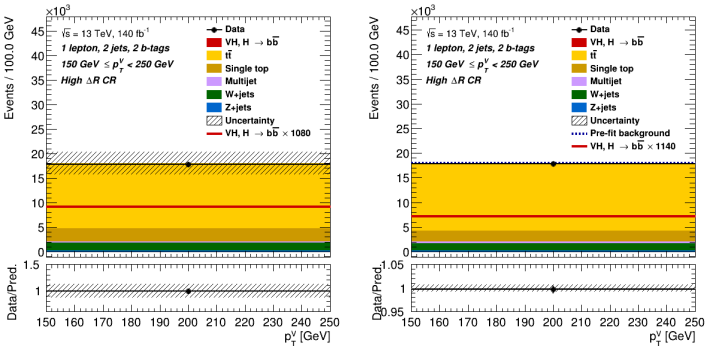

(g) (h)

FIGURE A.10: The data-MC plots of the BDT distribution for the 1-lepton, 2-jet, 150 $< p_T^V <$ 250 GeV control regions. The left column has the pre-fit plots, while the right column has the post-fit plots. The top row shows the CRLow jet p_T selection of 20 GeV, the second row shows 30 GeV CRLow, the third row shows the 20 GeV CRHigh and the fourth row shows the 30 GeV CRHigh. The red line is the signal (filled red histogram) scaled by the factor given in the legend so that the shape of the signal is easier to see, and the dashed blue line is the total pre-fit background. The bottom sub-plot shows the ratio of the data to the theory prediction, along with the relative post-fit error given by the shaded band.

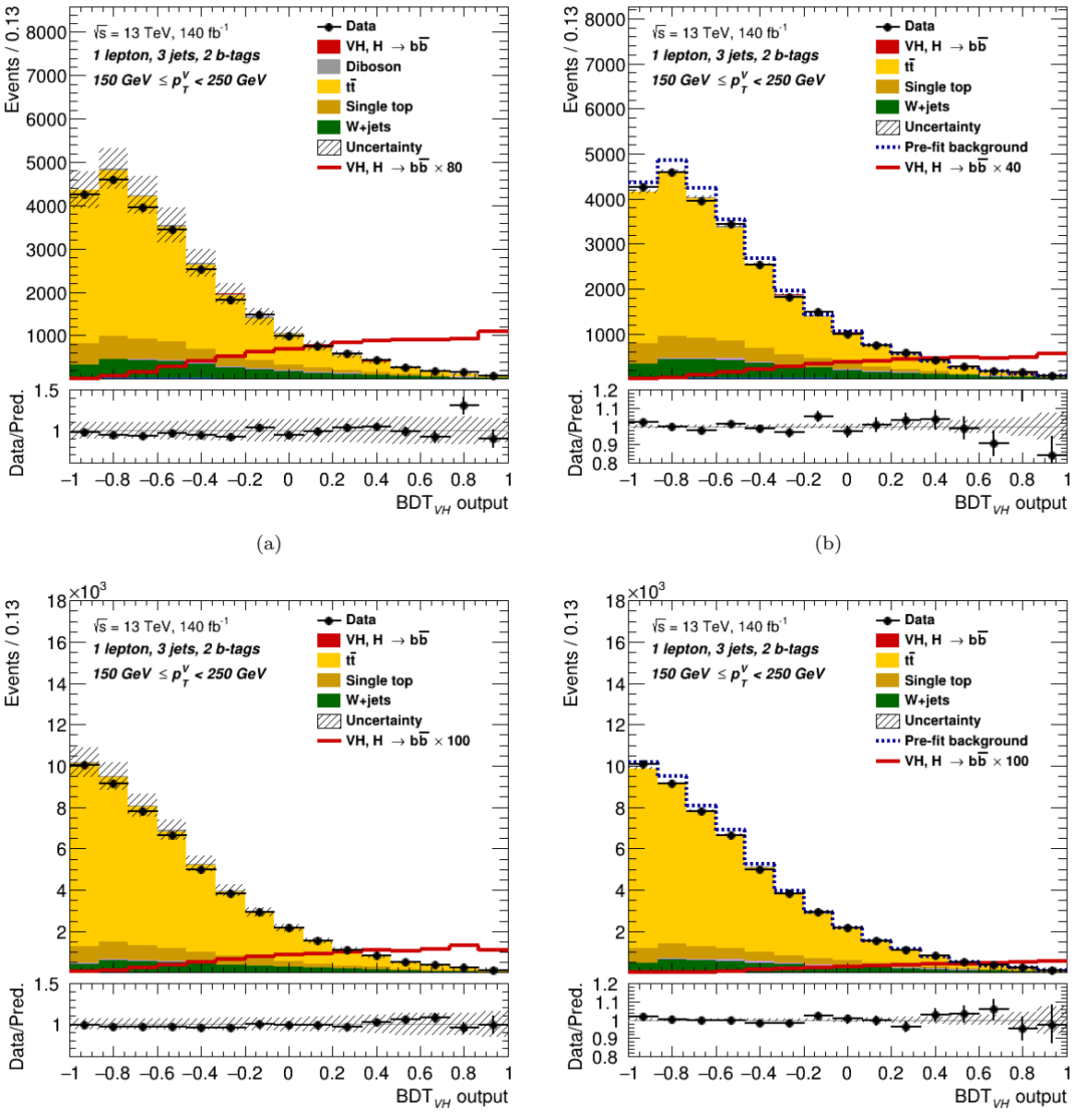

FIGURE A.11: The data-MC plots of the BDT distribution for the 1-lepton, 3-jet, 150 $< p_T^V <$ 250 GeV, signal regions. The top row shows the jet p_T selection of 20 GeV, while the bottom row shows 30 GeV. The left column has the pre-fit plots, while the right column has the post-fit plots. The red line is the signal (filled red histogram) scaled by the factor given in the legend so that the shape of the signal is easier to see, and the dashed blue line is the total pre-fit background. The bottom sub-plot shows the ratio of the data to the theory prediction, along with the relative post-fit error given by the shaded band.

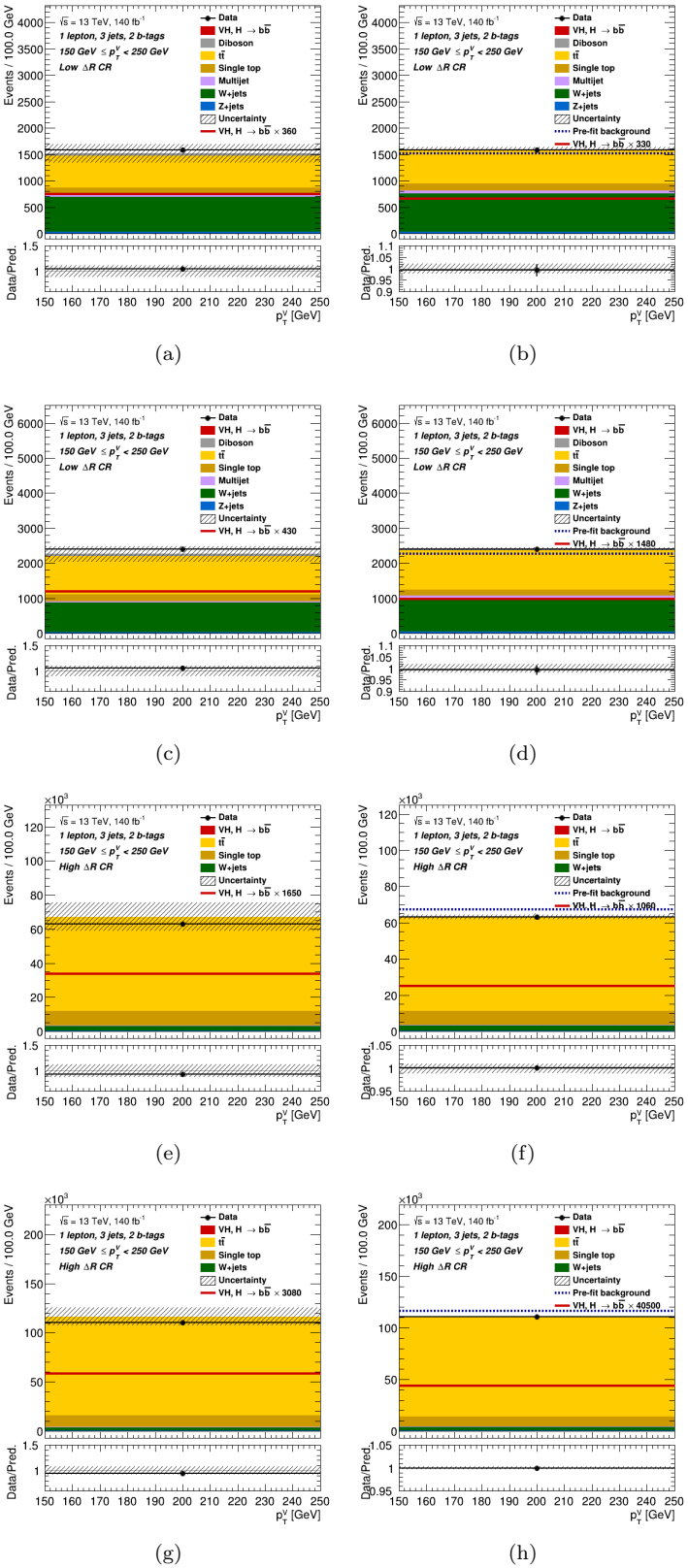

FIGURE A.12: The data-MC plots of the BDT distribution for the 1-lepton, 3-jet, 150 $< p_T^V <$ 250 GeV control regions. The left column has the pre-fit plots, while the right column has the post-fit plots. The top row shows the CRLow jet p_T selection of 20 GeV, the second row shows 30 GeV CRLow, the third row shows the 20 GeV CRHigh and the fourth row shows the 30 GeV CRHigh. The red line is the signal (filled red histogram) scaled by the factor given in the legend so that the shape of the signal is easier to see, and the dashed blue line is the total pre-fit background. The bottom sub-plot shows the ratio of the data to the theory prediction, along with the relative post-fit error given by the shaded band.

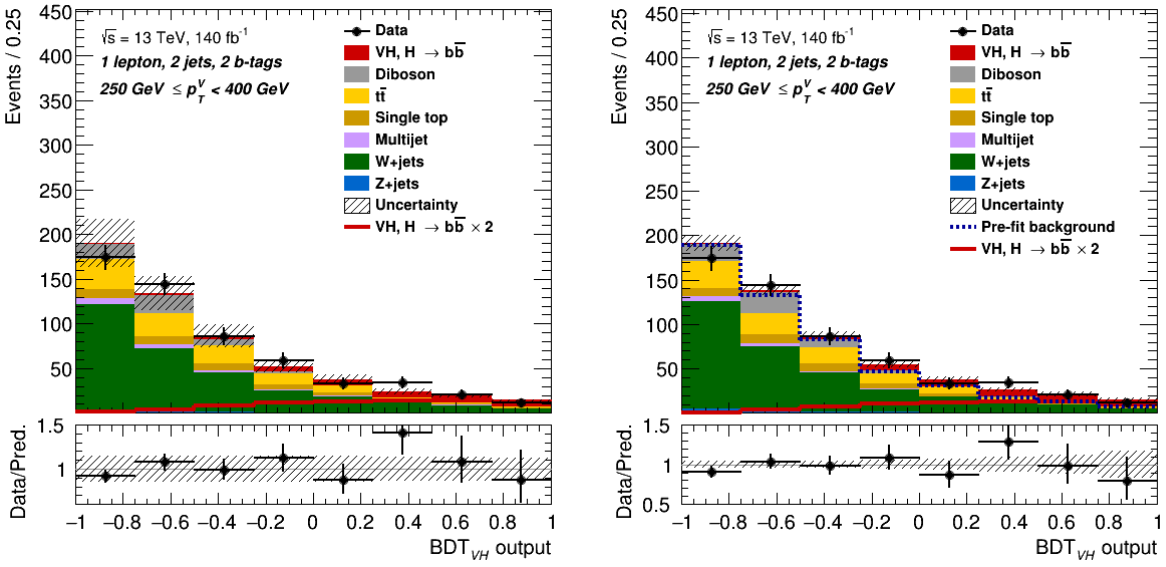

(a) (b)

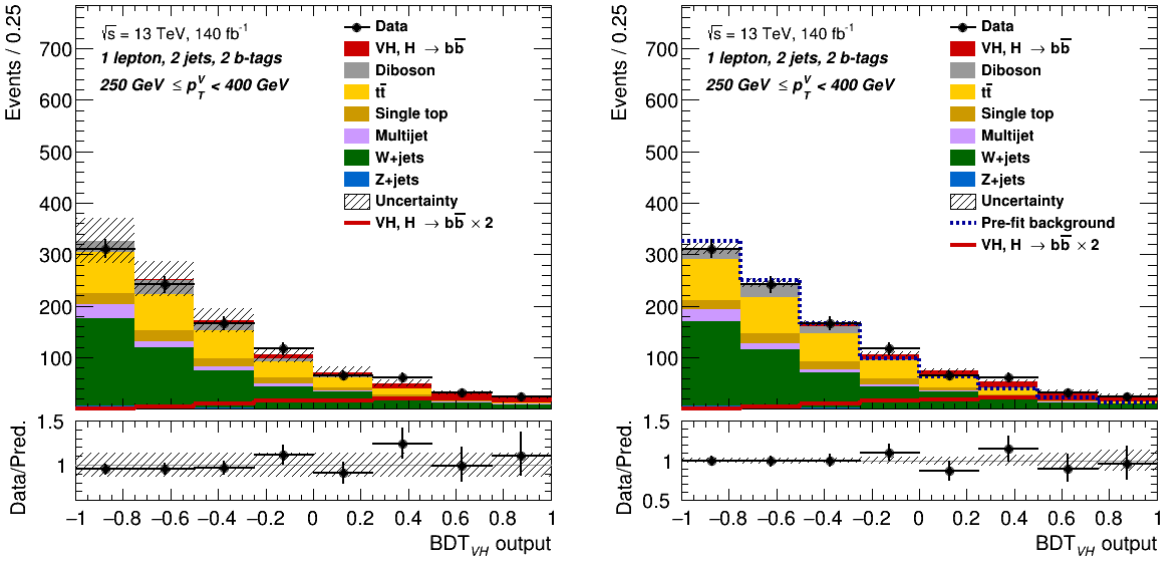

(c) (d)

FIGURE A.13: The data-MC plots of the BDT distribution for the 1-lepton, 2-jet, 250 $< p_T^V <$ 400 GeV, signal regions. The top row shows the jet p_T selection of 20 GeV, while the bottom row shows 30 GeV. The left column has the pre-fit plots, while the right column has the post-fit plots. The red line is the signal (filled red histogram) scaled by the factor given in the legend so that the shape of the signal is easier to see, and the dashed blue line is the total pre-fit background. The bottom sub-plot shows the ratio of the data to the theory prediction, along with the relative post-fit error given by the shaded band.

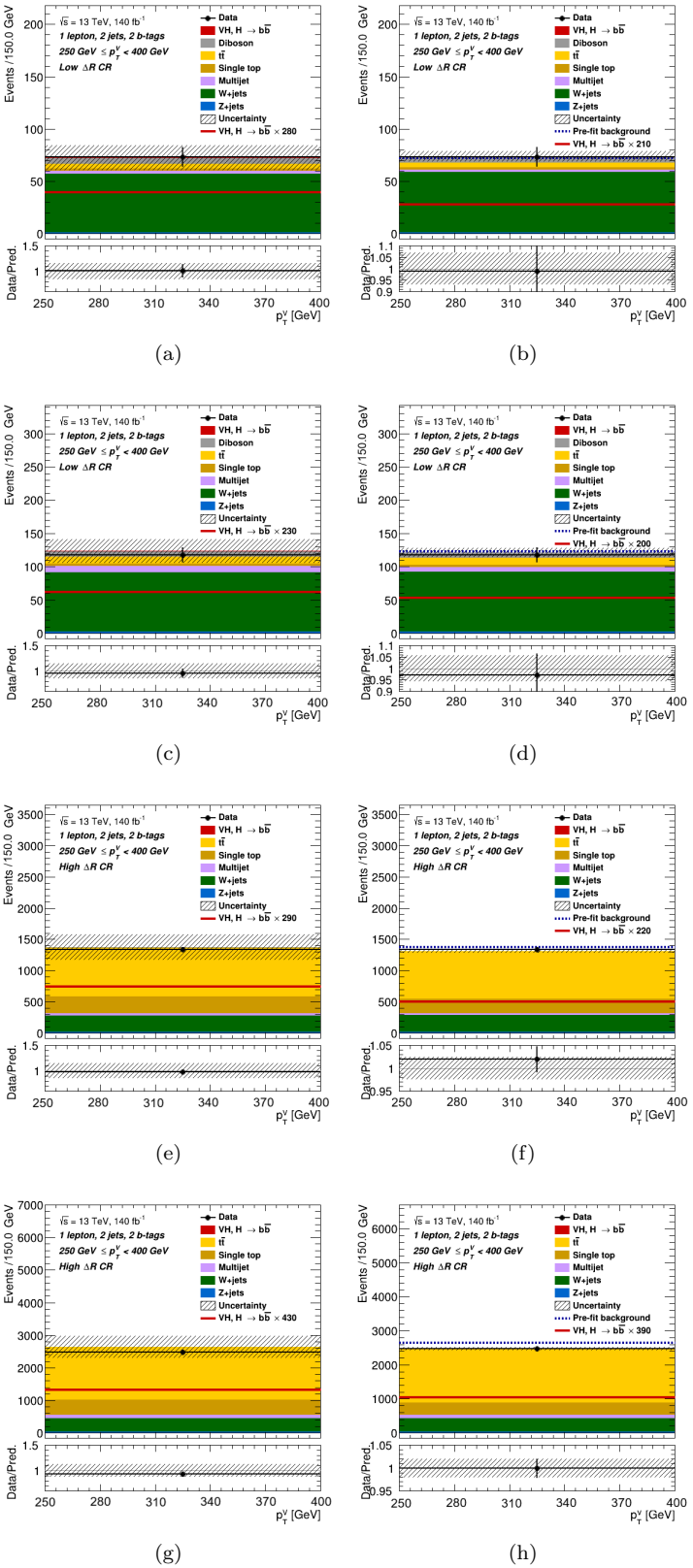

FIGURE A.14: The data-MC plots of the BDT distribution for the 1-lepton, 2-jet, 250 $< p_T^V <$ 400 GeV control regions. The left column has the pre-fit plots, while the right column has the post-fit plots. The top row shows the CRLow jet p_T selection of 20 GeV, the second row shows 30 GeV CRLow, the third row shows the 20 GeV CRHigh and the fourth row shows the 30 GeV CRHigh. The red line is the signal (filled red histogram) scaled by the factor given in the legend so that the shape of the signal is easier to see, and the dashed blue line is the total pre-fit background. The bottom sub-plot shows the ratio of the data to the theory prediction, along with the relative post-fit error given by the shaded band.

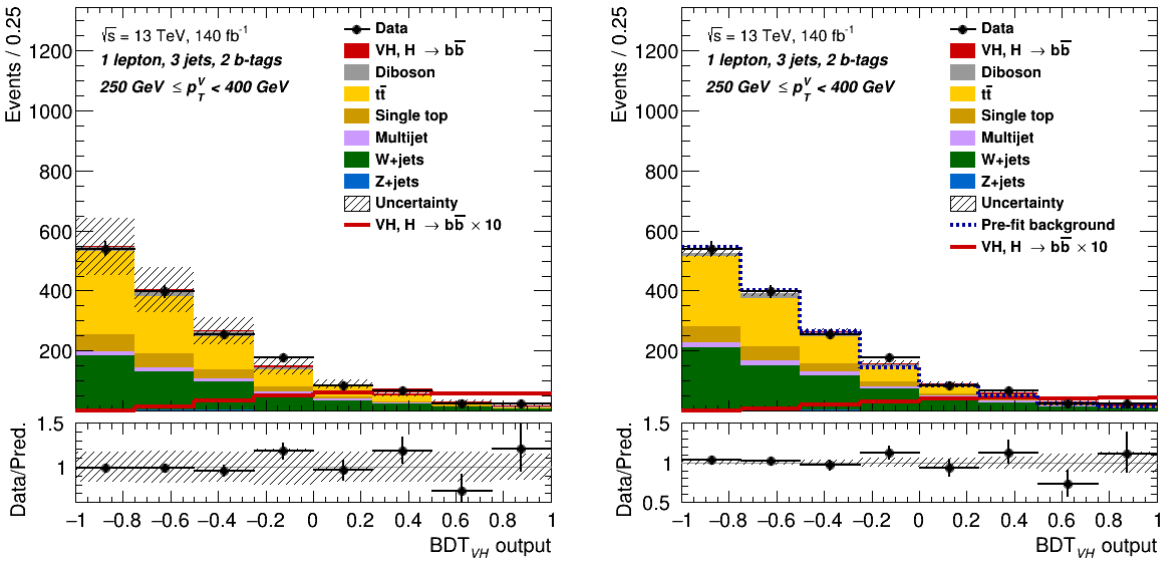

(a)

(b)

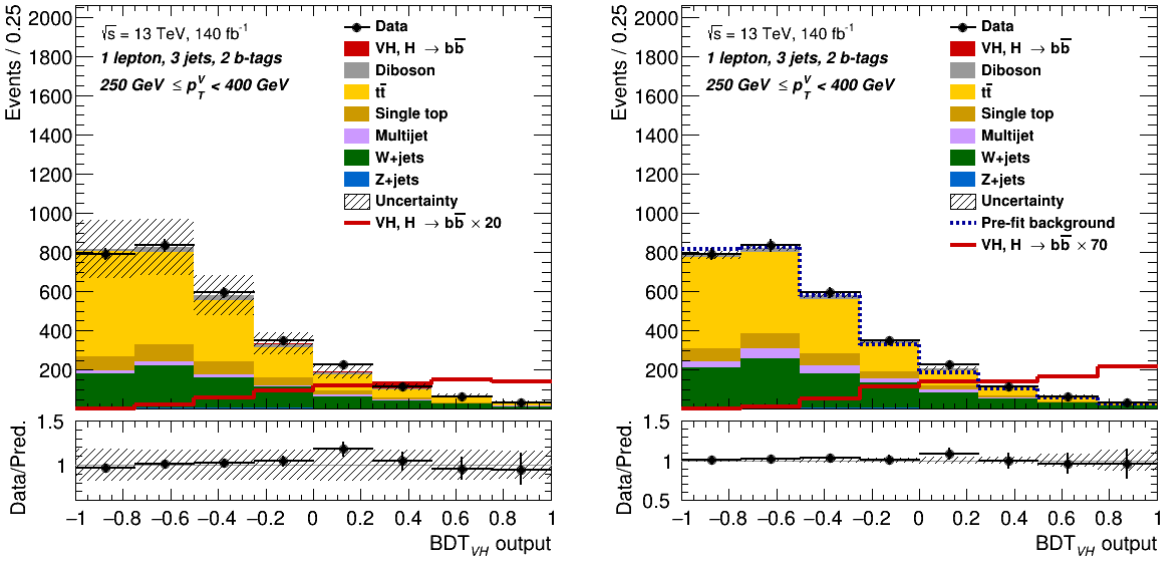

(c)

(d)

FIGURE A.15: The data-MC plots of the BDT distribution for the 1-lepton, 3-jet, 250 $< p_T^V <$ 400 GeV, signal regions. The top row shows the jet p_T selection of 20 GeV, while the bottom row shows 30 GeV. The left column has the pre-fit plots, while the right column has the post-fit plots. The red line is the signal (filled red histogram) scaled by the factor given in the legend so that the shape of the signal is easier to see, and the dashed blue line is the total pre-fit background. The bottom sub-plot shows the ratio of the data to the theory prediction, along with the relative post-fit error given by the shaded band.

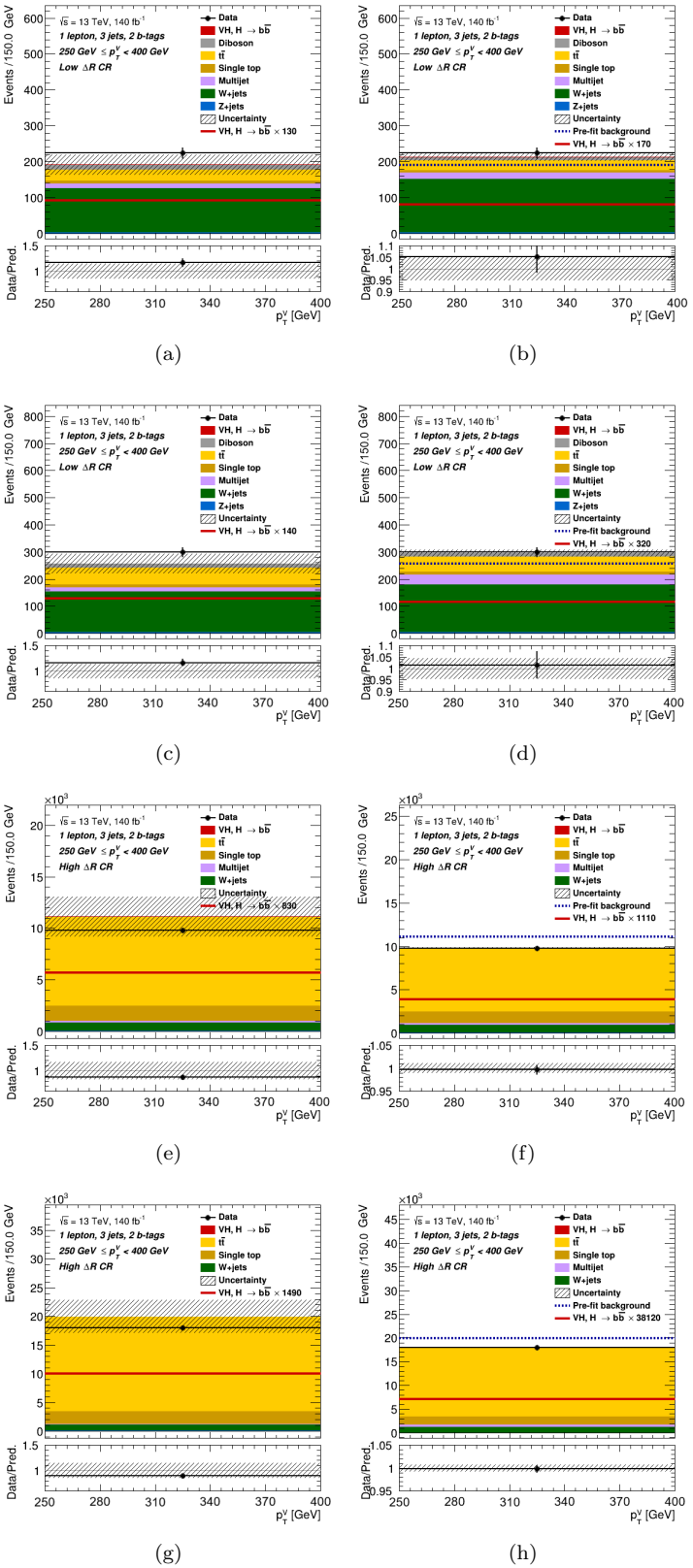

FIGURE A.16: The data-MC plots of the BDT distribution for the 1-lepton, 3-jet, 250 $< p_T^V <$ 400 GeV control regions. The left column has the pre-fit plots, while the right column has the post-fit plots. The top row shows the CRLow jet p_T selection of 20 GeV, the second row shows 30 GeV CRLow, the third row shows the 20 GeV CRHigh and the fourth row shows the 30 GeV CRHigh. The red line is the signal (filled red histogram) scaled by the factor given in the legend so that the shape of the signal is easier to see, and the dashed blue line is the total pre-fit background. The bottom sub-plot shows the ratio of the data to the theory prediction, along with the relative post-fit error given by the shaded band.

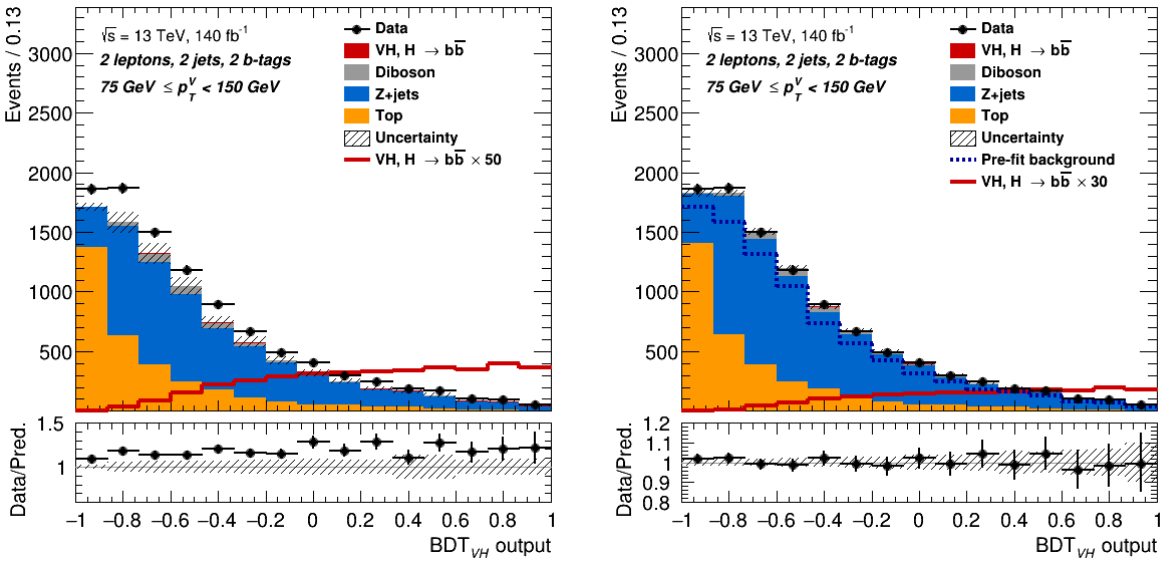

(a)

(b)

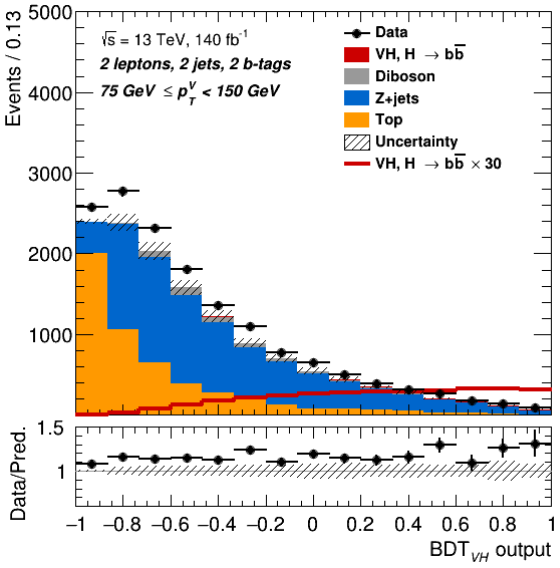

(c)

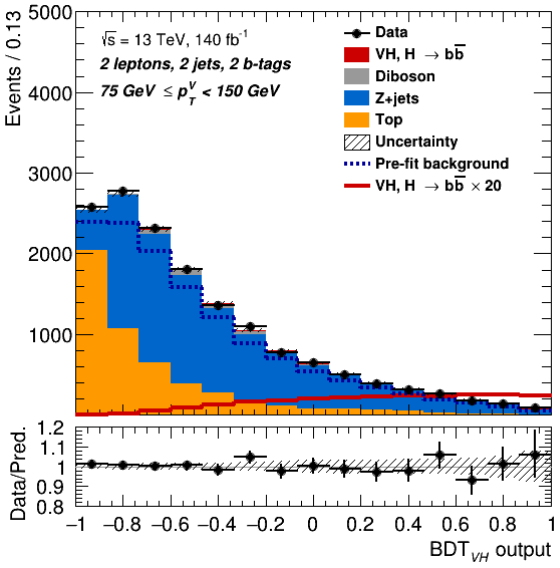

(d)

FIGURE A.17: The data-MC plots of the BDT distribution for the 2-lepton, 2-jet, 75 $< p_T^V <$ 150 GeV, signal regions. The top row shows the jet p_T selection of 20 GeV, while the bottom row shows 30 GeV. The left column has the pre-fit plots, while the right column has the post-fit plots. The red line is the signal (filled red histogram) scaled by the factor given in the legend so that the shape of the signal is easier to see, and the dashed blue line is the total pre-fit background. The bottom sub-plot shows the ratio of the data to the theory prediction, along with the relative post-fit error given by the shaded band.

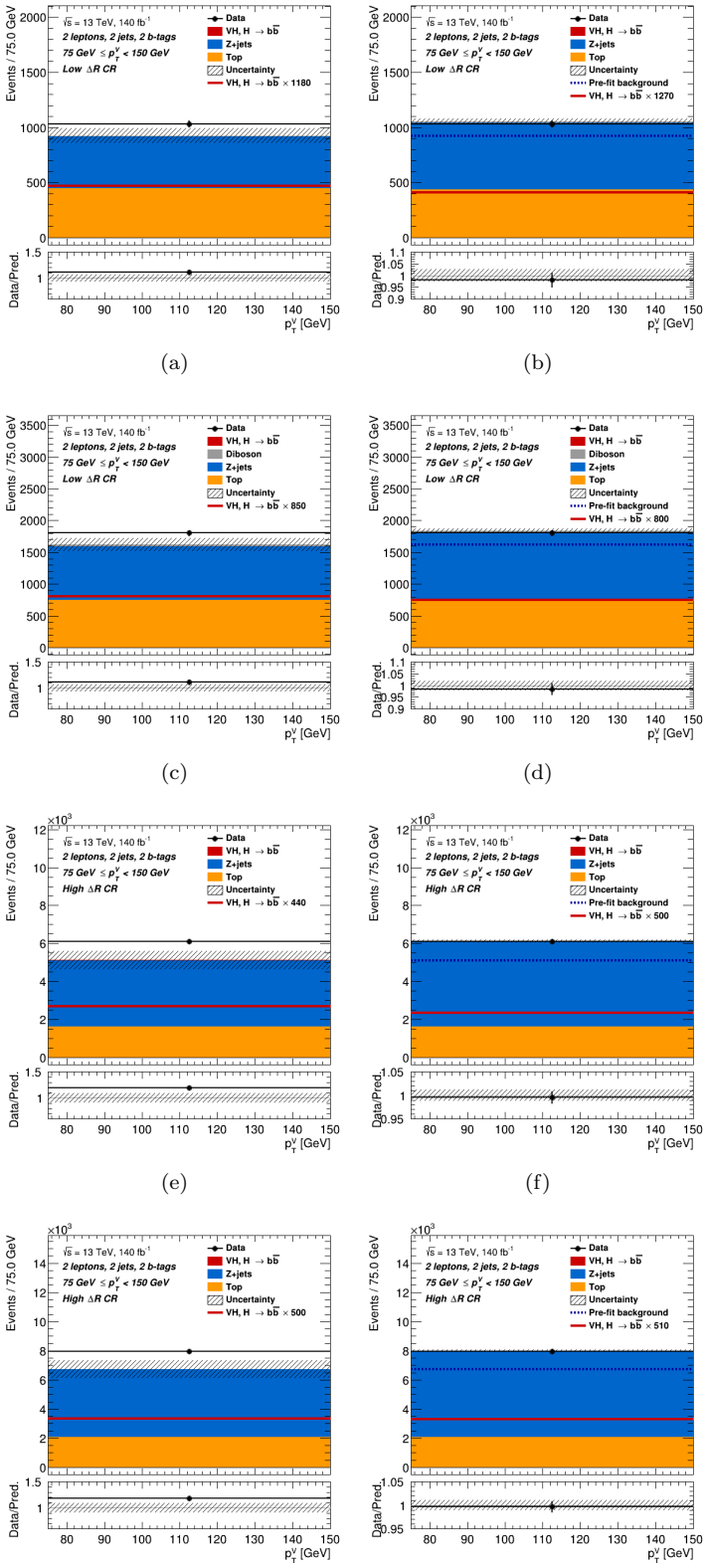

FIGURE A.18: The data-MC plots of the BDT distribution for the 2-lepton, 2-jet, 75 $< p_T^V <$ 150 GeV control regions. The left column has the pre-fit plots, while the right column has the post-fit plots. The top row shows the CRLow jet p_T selection of 20 GeV, the second row shows 30 GeV CRLow, the third row shows the 20 GeV CRHigh and the fourth row shows the 30 GeV CRHigh. The red line is the signal (filled red histogram) scaled by the factor given in the legend so that the shape of the signal is easier to see, and the dashed blue line is the total pre-fit background. The bottom sub-plot shows the ratio of the data to the theory prediction, along with the relative post-fit error given by the shaded band.

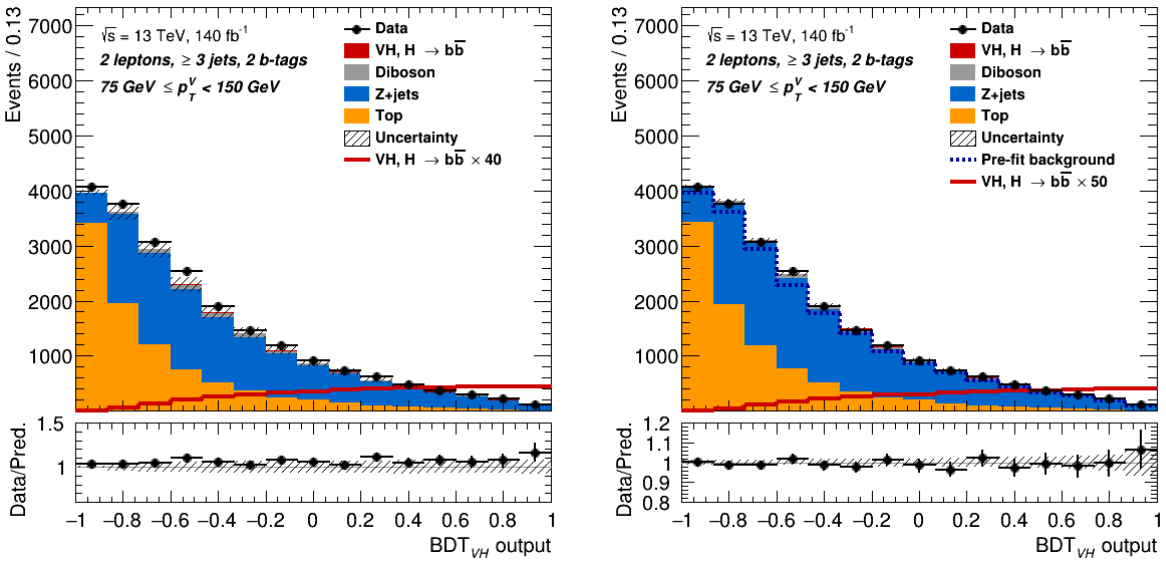

(a)

(b)

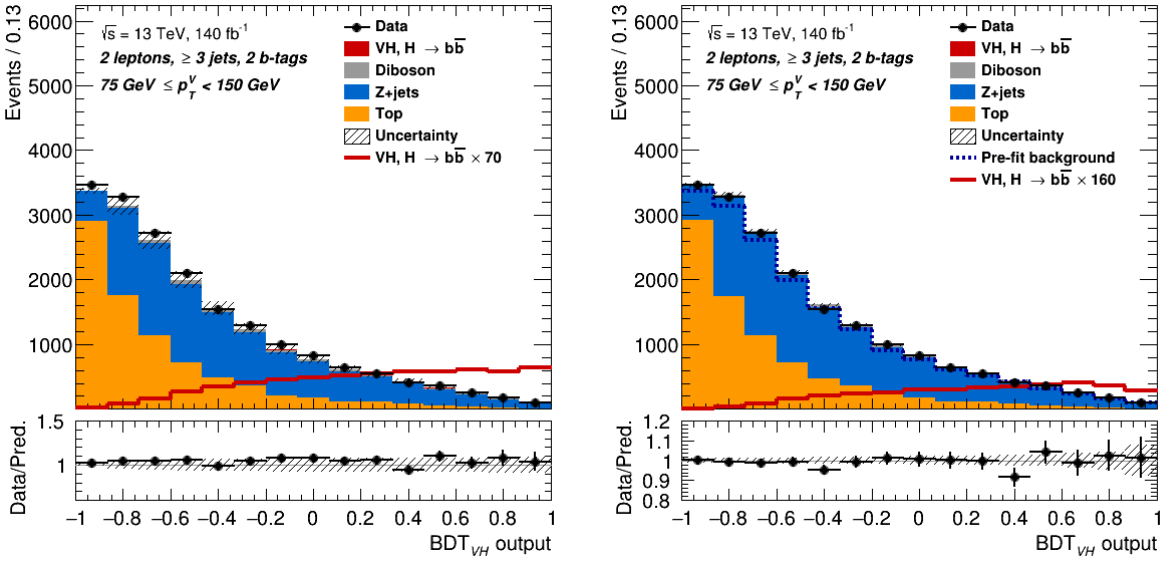

(c)

(d)

FIGURE A.19: The data-MC plots of the BDT distribution for the 2-lepton, ≥ 3-jet, 75 $< p_T^V <$ 150 GeV, signal regions. The top row shows the jet p_T selection of 20 GeV, while the bottom row shows 30 GeV. The left column has the pre-fit plots, while the right column has the post-fit plots. The red line is the signal (filled red histogram) scaled by the factor given in the legend so that the shape of the signal is easier to see, and the dashed blue line is the total pre-fit background. The bottom sub-plot shows the ratio of the data to the theory prediction, along with the relative post-fit error given by the shaded band.

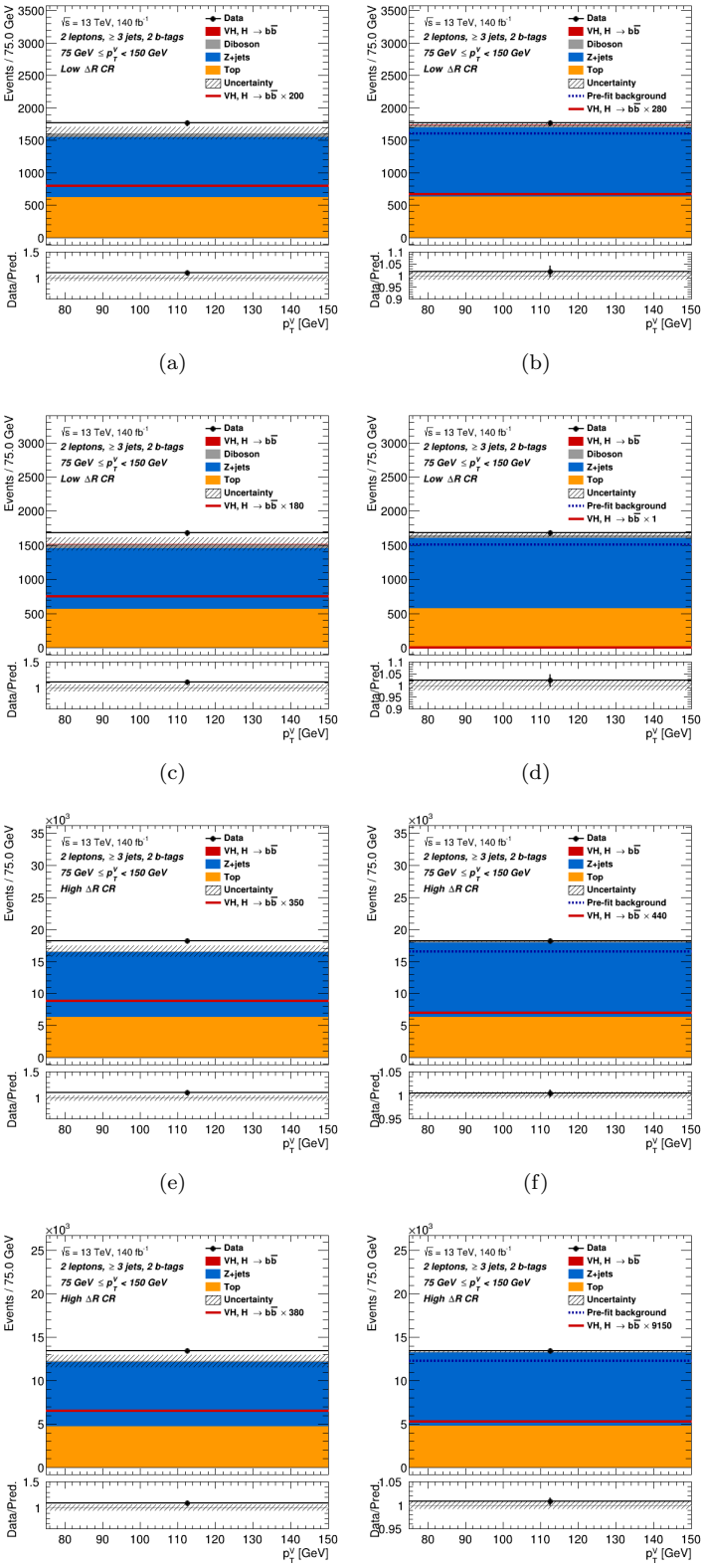

FIGURE A.20: The data-MC plots of the BDT distribution for the 2-lepton, $\geq$ 3-jet, 75 $< p_T^V <$ 150 GeV control regions. The left column has the pre-fit plots, while the right column has the post-fit plots. The top row shows the CRLow jet p_T selection of 20 GeV, the second row shows 30 GeV CRLow, the third row shows the 20 GeV CRHigh and the fourth row shows the 30 GeV CRHigh. The red line is the signal (filled red histogram) scaled by the factor given in the legend so that the shape of the signal is easier to see, and the dashed blue line is the total pre-fit background. The bottom sub-plot shows the ratio of the data to the theory prediction, along with the relative post-fit error given by the shaded band.

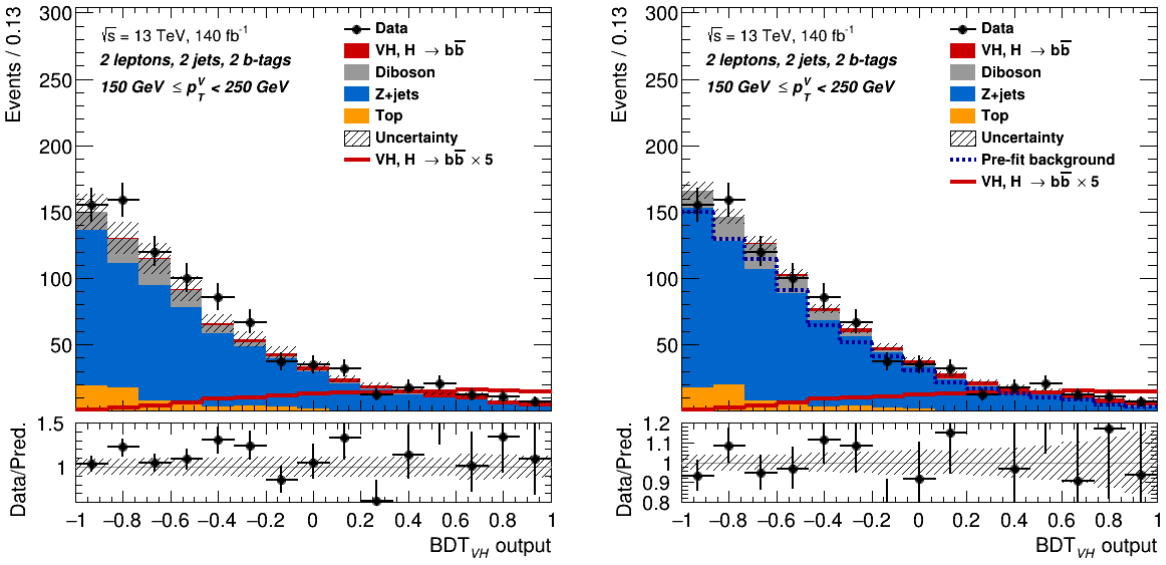

(a)

(b)

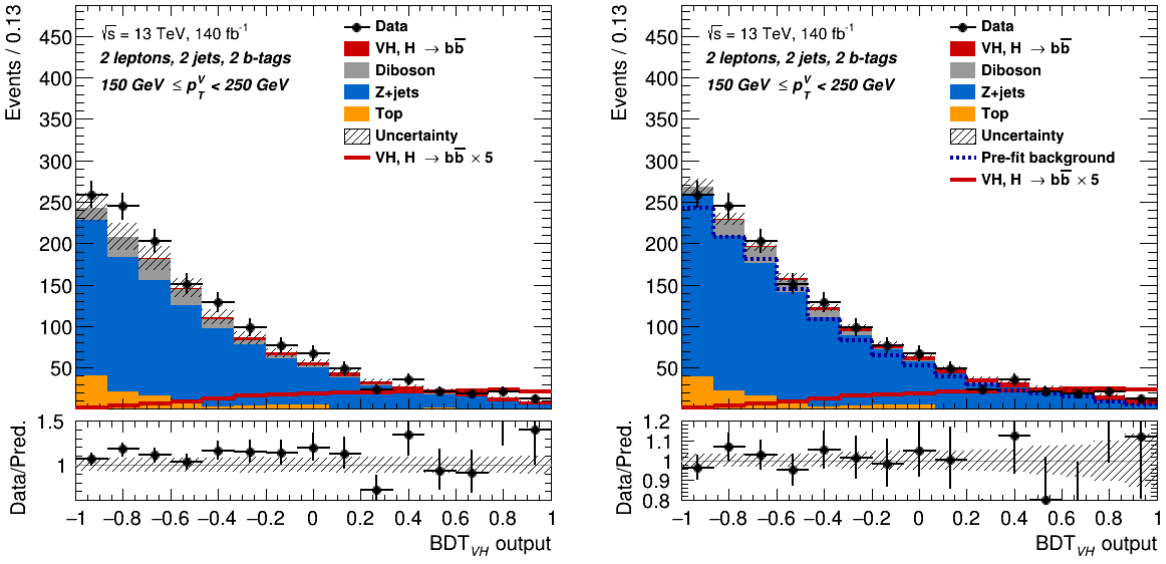

(c)

(d)

FIGURE A.21: The data-MC plots of the BDT distribution for the 2-lepton, 2-jet, 150 $< p_T^V <$ 250 GeV, signal regions. The top row shows the jet p_T selection of 20 GeV, while the bottom row shows 30 GeV. The left column has the pre-fit plots, while the right column has the post-fit plots. The red line is the signal (filled red histogram) scaled by the factor given in the legend so that the shape of the signal is easier to see, and the dashed blue line is the total pre-fit background. The bottom sub-plot shows the ratio of the data to the theory prediction, along with the relative post-fit error given by the shaded band.

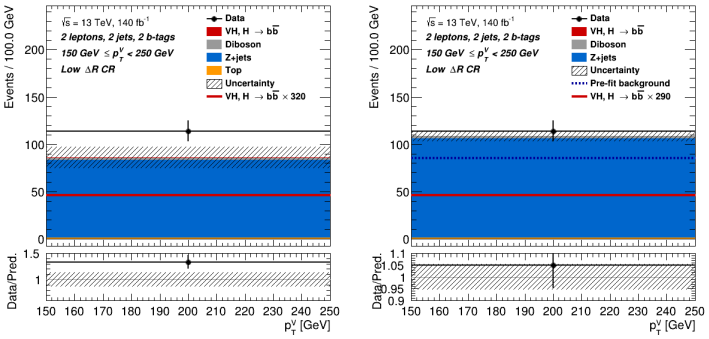

(a) (b)

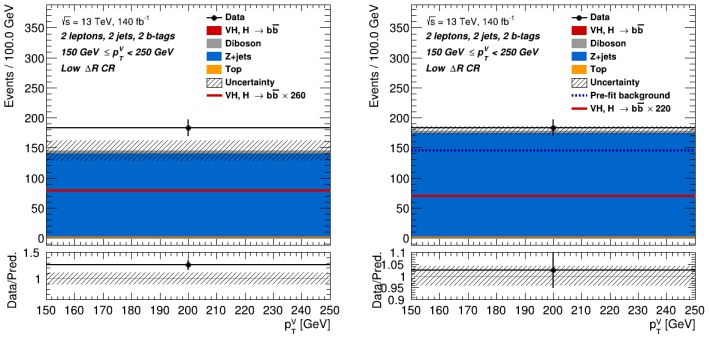

(c) (d)

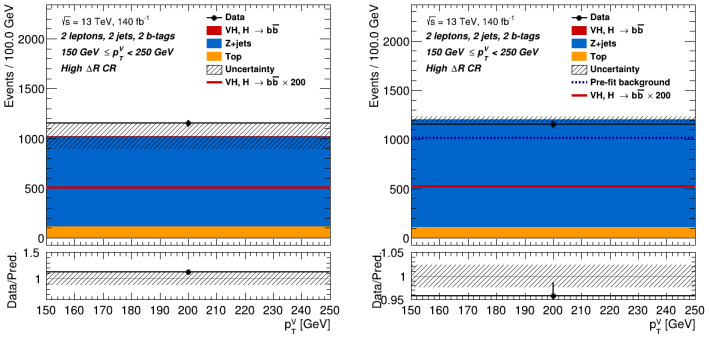

(e) (f)

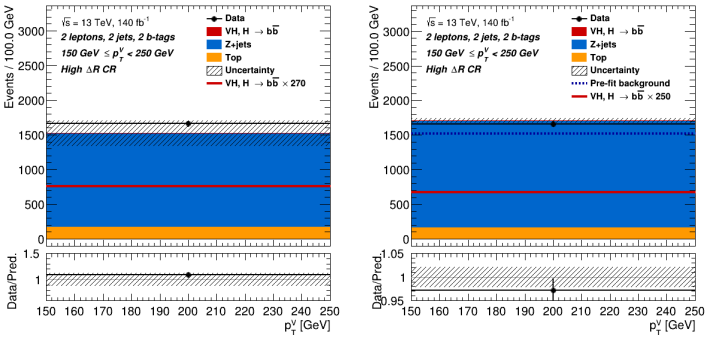

(g) (h)

FIGURE A.22: The data-MC plots of the BDT distribution for the 2-lepton, 2-jet, 150 $< p_T^V <$ 250 GeV control regions. The left column has the pre-fit plots, while the right column has the post-fit plots. The top row shows the CRLow jet p_T selection of 20 GeV, the second row shows 30 GeV CRLow, the third row shows the 20 GeV CRHigh and the fourth row shows the 30 GeV CRHigh. The red line is the signal (filled red histogram) scaled by the factor given in the legend so that the shape of the signal is easier to see, and the dashed blue line is the total pre-fit background. The bottom sub-plot shows the ratio of the data to the theory prediction, along with the relative post-fit error given by the shaded band.

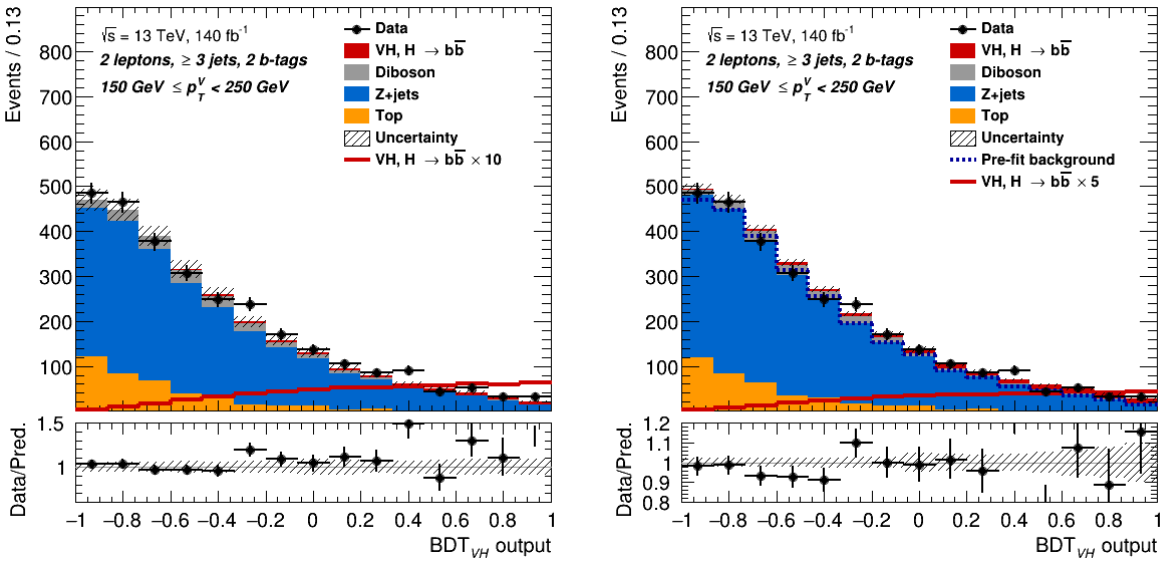

(a)

(b)

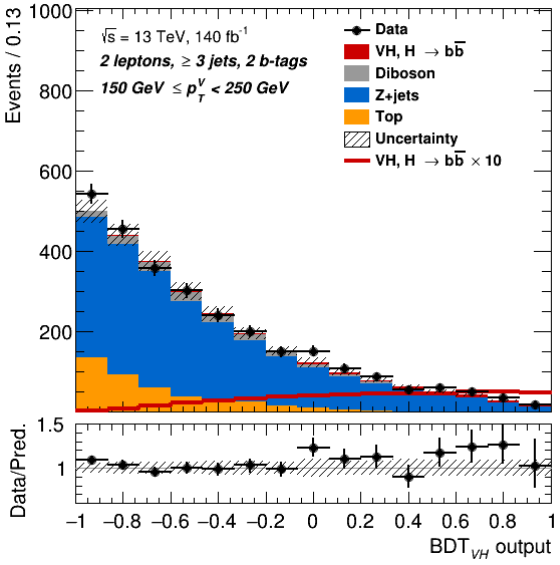

(c)

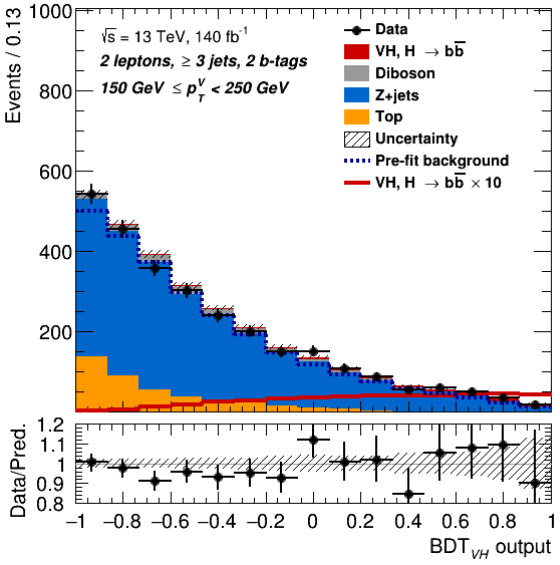

(d)

FIGURE A.23: The data-MC plots of the BDT distribution for the 2-lepton, $\geq$ 3-jet, 150 $< p_T^V <$ 250 GeV, signal regions. The top row shows the jet p_T selection of 20 GeV, while the bottom row shows 30 GeV. The left column has the pre-fit plots, while the right column has the post-fit plots. The red line is the signal (filled red histogram) scaled by the factor given in the legend so that the shape of the signal is easier to see, and the dashed blue line is the total pre-fit background. The bottom sub-plot shows the ratio of the data to the theory prediction, along with the relative post-fit error given by the shaded band.

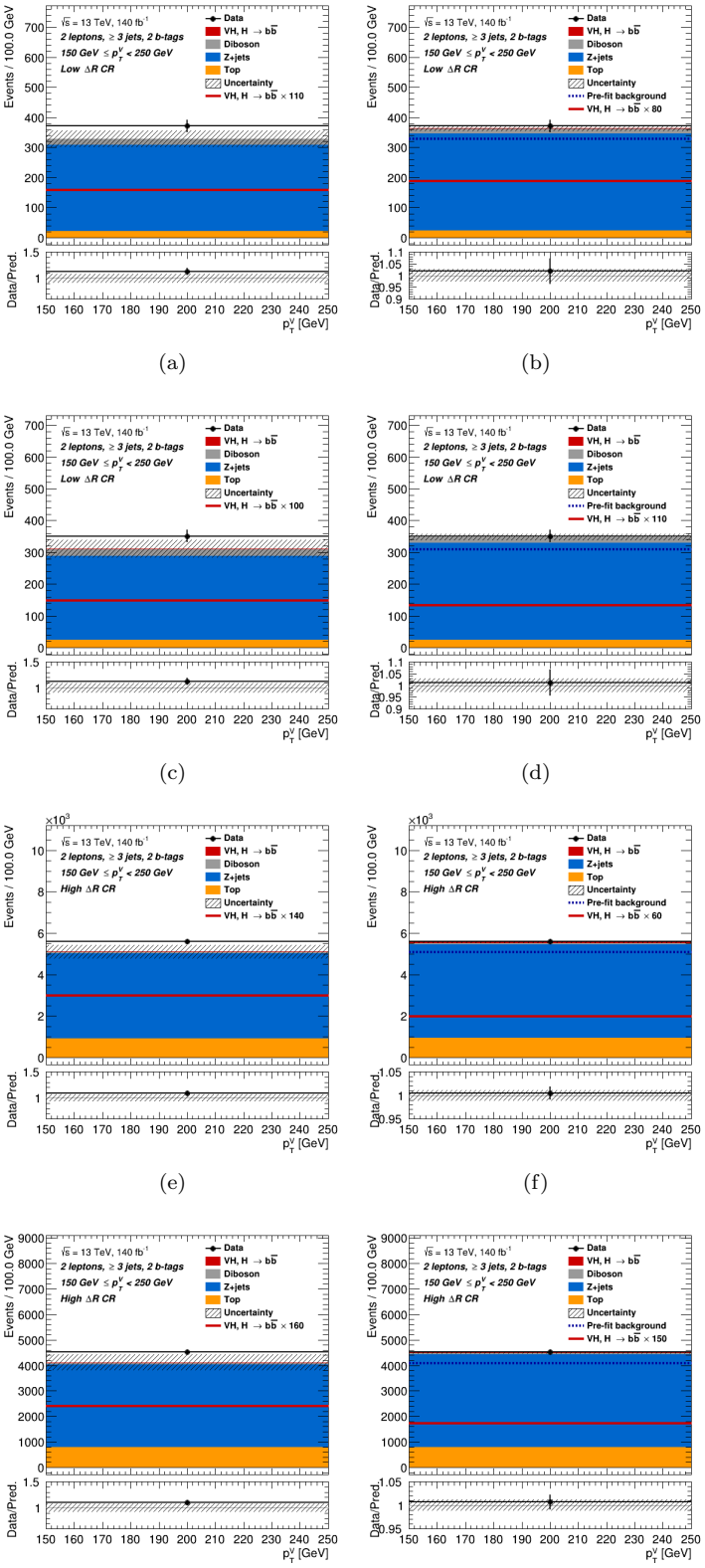

FIGURE A.24: The data-MC plots of the BDT distribution for the 2-lepton, $\geq$ 3-jet, 150 $< p_T^V <$ 250 GeV control regions. The left column has the pre-fit plots, while the right column has the post-fit plots. The top row shows the CRLow jet p_T selection of 20 GeV, the second row shows 30 GeV CRLow, the third row shows the 20 GeV CRHigh and the fourth row shows the 30 GeV CRHigh. The red line is the signal (filled red histogram) scaled by the factor given in the legend so that the shape of the signal is easier to see, and the dashed blue line is the total pre-fit background. The bottom sub-plot shows the ratio of the data to the theory prediction, along with the relative post-fit error given by the shaded band.

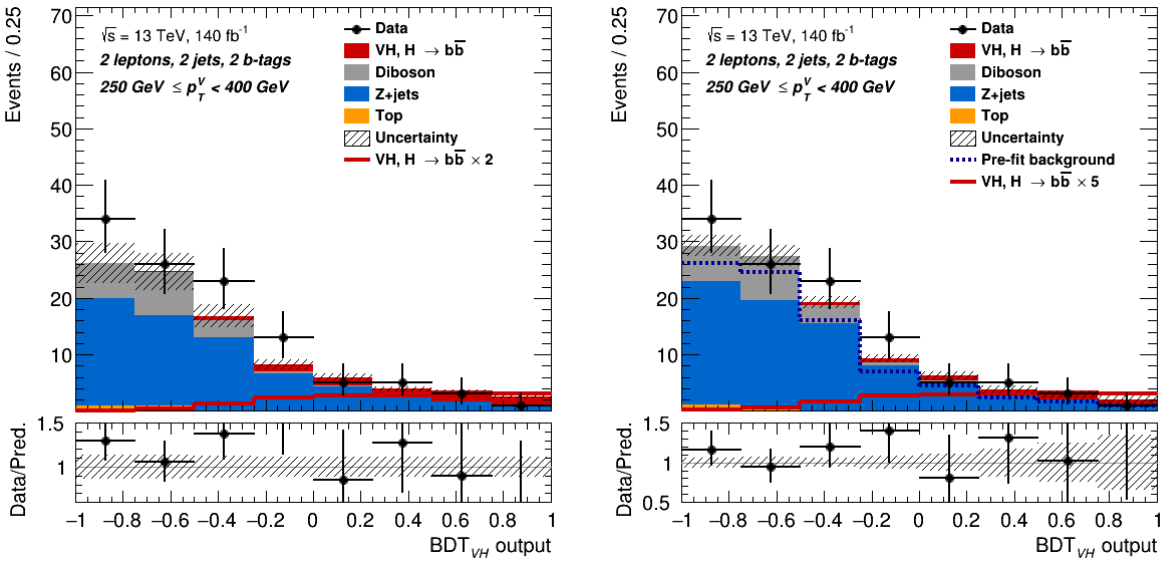

(a)

(b)

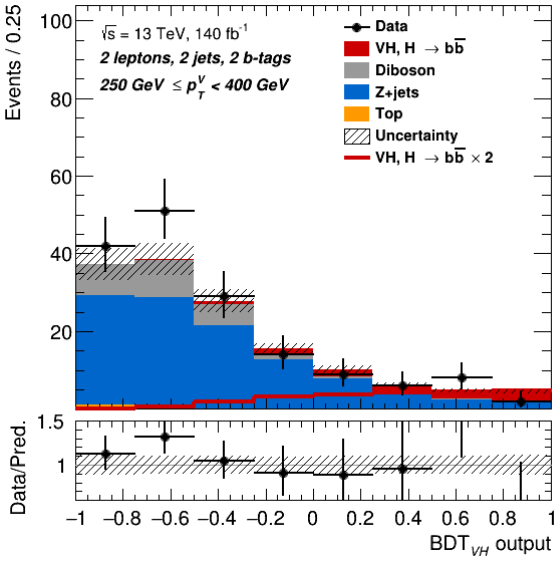

(c)

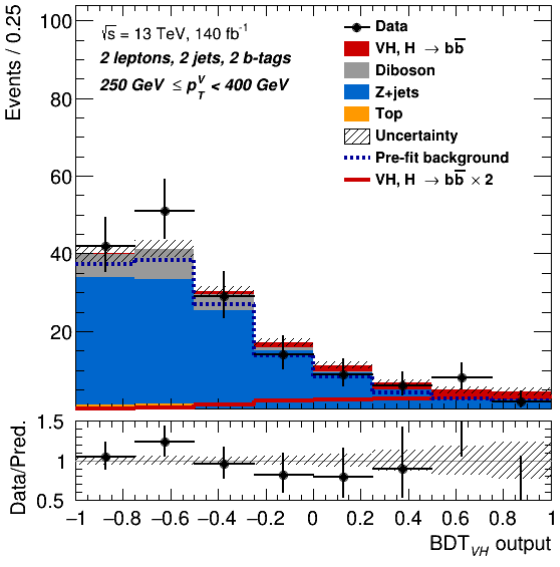

(d)

FIGURE A.25: The data-MC plots of the BDT distribution for the 2-lepton, 2-jet, 250 $< p_T^V <$ 400 GeV, signal regions. The top row shows the jet p_T selection of 20 GeV, while the bottom row shows 30 GeV. The left column has the pre-fit plots, while the right column has the post-fit plots. The red line is the signal (filled red histogram) scaled by the factor given in the legend so that the shape of the signal is easier to see, and the dashed blue line is the total pre-fit background. The bottom sub-plot shows the ratio of the data to the theory prediction, along with the relative post-fit error given by the shaded band.

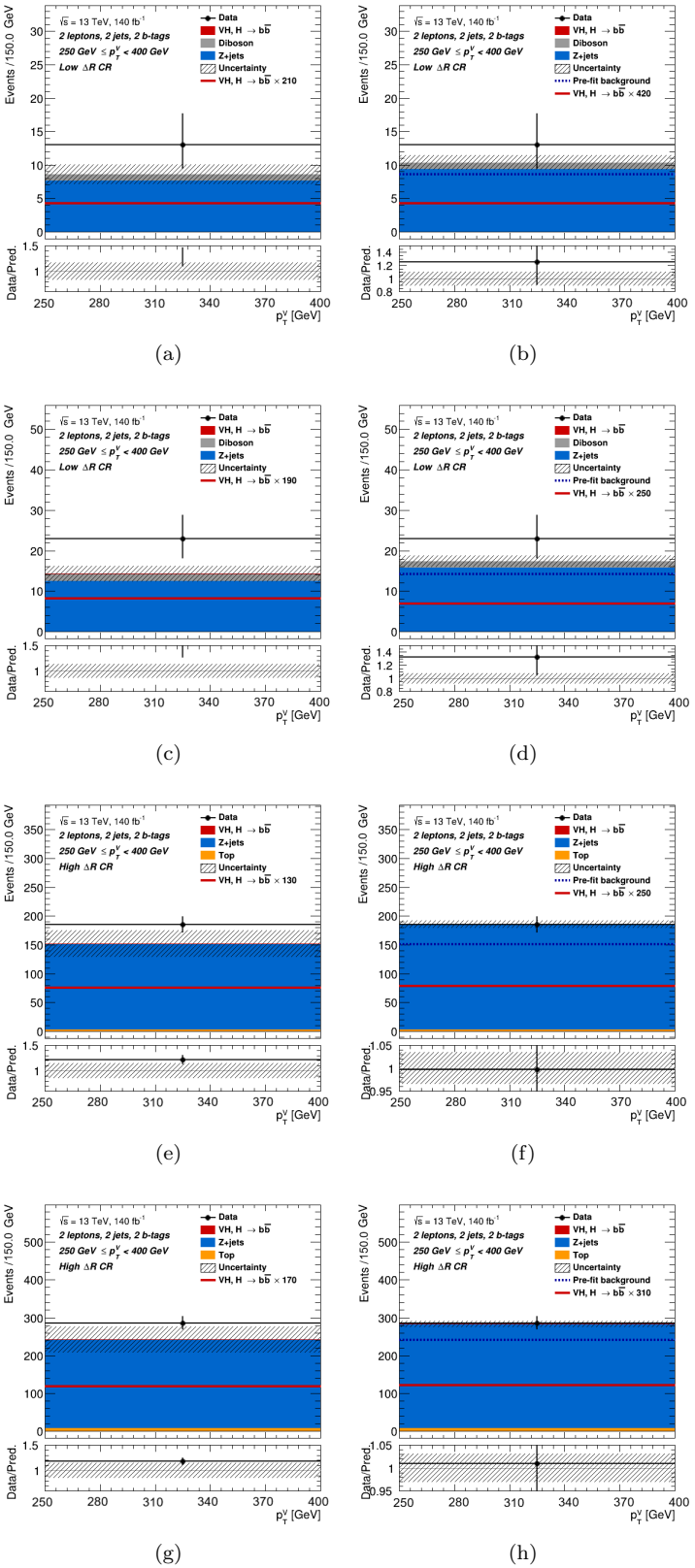

FIGURE A.26: The data-MC plots of the BDT distribution for the 2-lepton, 2-jet, 250 $< p_T^V <$ 400 GeV control regions. The left column has the pre-fit plots, while the right column has the post-fit plots. The top row shows the CRLow jet p_T selection of 20 GeV, the second row shows 30 GeV CRLow, the third row shows the 20 GeV CRHigh and the fourth row shows the 30 GeV CRHigh. The red line is the signal (filled red histogram) scaled by the factor given in the legend so that the shape of the signal is easier to see, and the dashed blue line is the total pre-fit background. The bottom sub-plot shows the ratio of the data to the theory prediction, along with the relative post-fit error given by the shaded band.

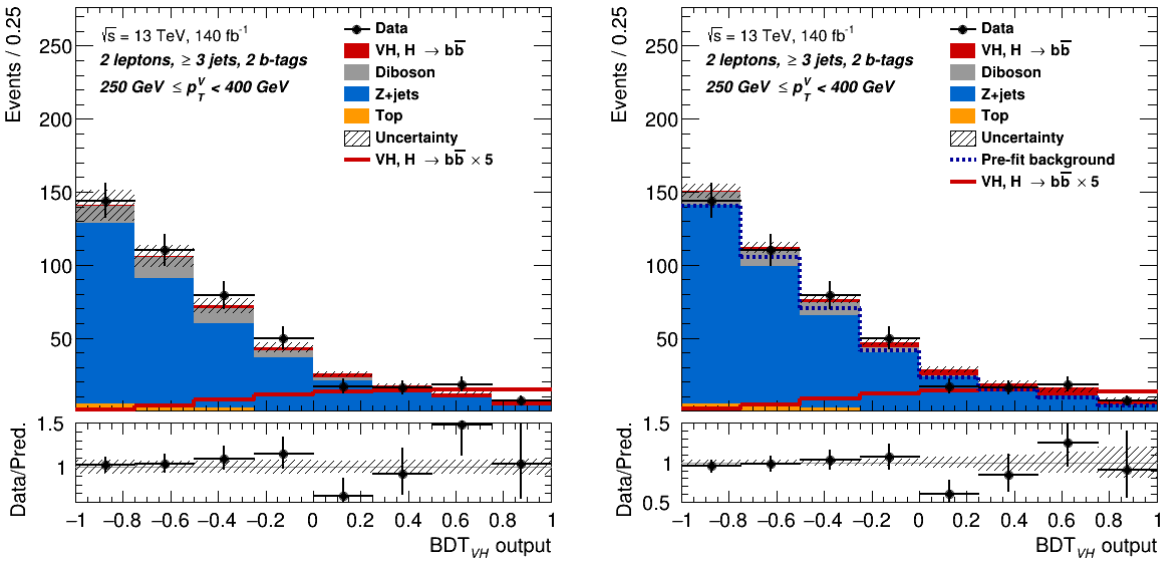

(a)

(b)

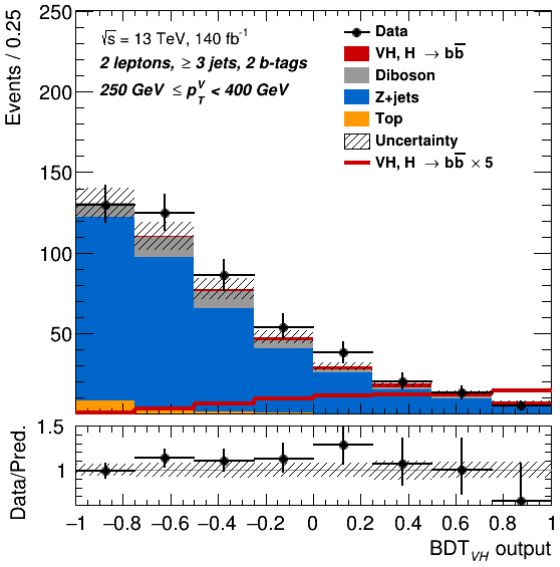

(c)

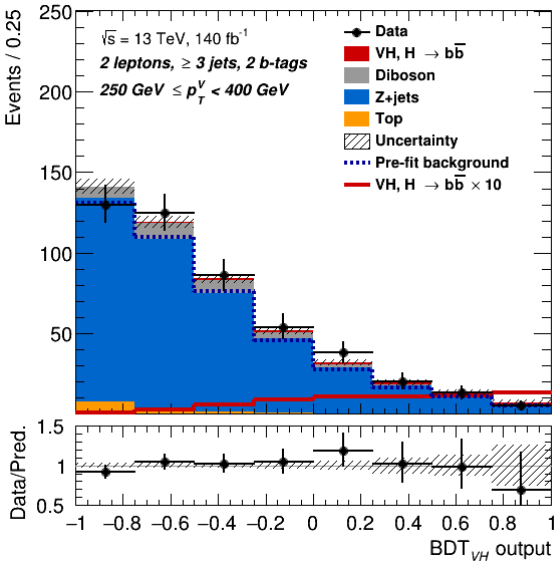

(d)

FIGURE A.27: The data-MC plots of the BDT distribution for the 2-lepton, $\geq$ 3-jet, 250 $< p_T^V <$ 400 GeV, signal regions. The top row shows the jet p_T selection of 20 GeV, while the bottom row shows 30 GeV. The left column has the pre-fit plots, while the right column has the post-fit plots. The red line is the signal (filled red histogram) scaled by the factor given in the legend so that the shape of the signal is easier to see, and the dashed blue line is the total pre-fit background. The bottom sub-plot shows the ratio of the data to the theory prediction, along with the relative post-fit error given by the shaded band.

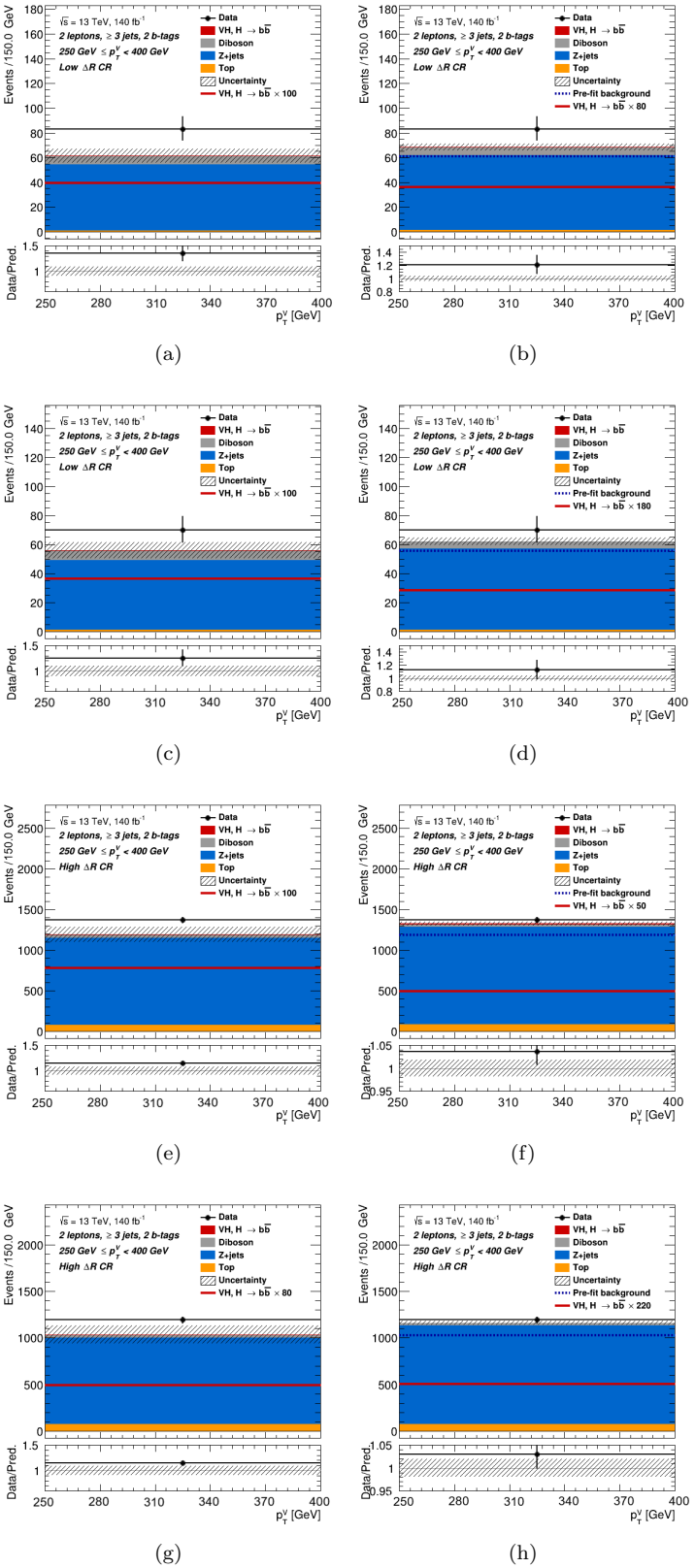

FIGURE A.28: The data-MC plots of the BDT distribution for the 2-lepton, $\geq$ 3-jet, 250 $< p_T^V <$ 400 GeV control regions. The left column has the pre-fit plots, while the right column has the post-fit plots. The top row shows the CRLow jet p_T selection of 20 GeV, the second row shows 30 GeV CRLow, the third row shows the 20 GeV CRHigh and the fourth row shows the 30 GeV CRHigh. The red line is the signal (filled red histogram) scaled by the factor given in the legend so that the shape of the signal is easier to see, and the dashed blue line is the total pre-fit background. The bottom sub-plot shows the ratio of the data to the theory prediction, along with the relative post-fit error given by the shaded band.

Appendix B

Rankings and breakdowns of the 10 POI fit uncertainties

This appendix contains extra information on the 10 POI STXS fit described in Chapter 7. In particular, the ranking of the 15 most impactful nuisance parameters per POI is shown, as well as the breakdown of how the different uncertainties contribute to the uncertainty on the POIs. For an explanation of the rankings and breakdowns, refer to Section 7.3.2.

B.1 Uncertainty rankings

This section contains the ranking plots of the 15 most impactful parameters on the signal strength of each of the 10 different POIs. The results of both the 20 GeV and 30 GeV jet p_T selections are shown. The plots are shown as follows:

- The n_{jets}^{add}=0 and $n_{jets}^{add}\geq$1, $WH, 150 < p_T^W < 250$ GeV signal strengths: Figure B.1
- The n_{jets}^{add}=0 and $n_{jets}^{add}\geq$1, $WH, 250 < p_T^W < 400$ GeV signal strengths: Figure B.2
- The n_{jets}^{add}=0 and $n_{jets}^{add}\geq$1, $ZH, 75 < p_T^Z < 150$ GeV signal strengths: Figure B.3
- The n_{jets}^{add}=0 and $n_{jets}^{add}\geq$1, $ZH, 150 < p_T^Z < 250$ GeV signal strengths: Figure B.4
- The n_{jets}^{add}=0 and $n_{jets}^{add}\geq$1, $ZH, 250 < p_T^Z < 400$ GeV signal strengths: Figure B.5

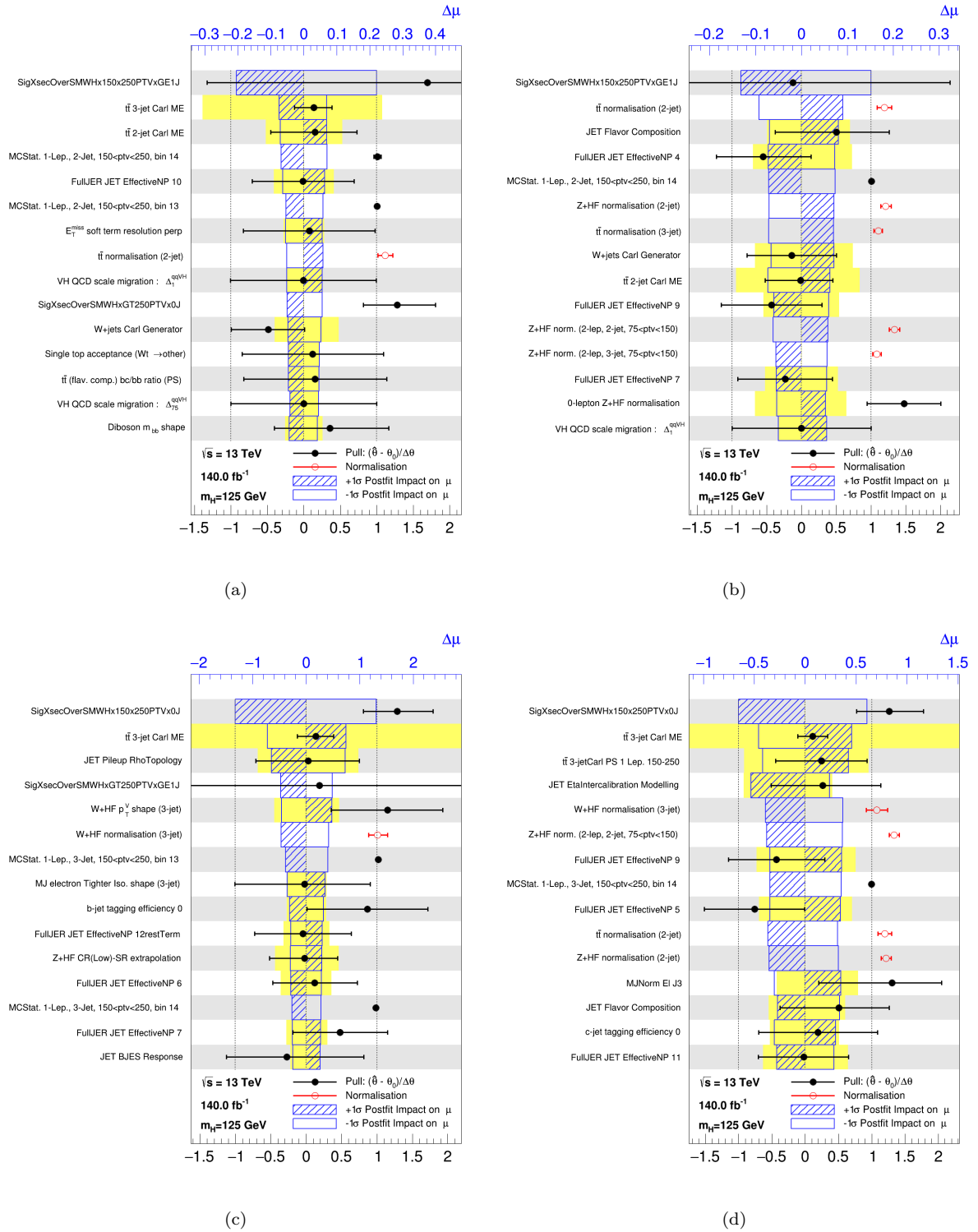

(a) (b)

(c) (d)

FIGURE B.1: The ranking of the nuisance parameters, in descending order, in terms of their impact on the $WH, 150 < p_T^W < 250$ GeV signal strengths $\hat{\mu}$. The top row is for the $n_{jets}^{add} = 0$ signal strengths while the bottom row has the $n_{jets}^{add} \geq 1$ signal strengths. The left column is for the jet p_T selection of 20 GeV and the right column is for 30 GeV. The blue boxes, relating to the top x-axis, show the post-fit impact on $\hat{\mu}$ after fixing the nuisance parameter to the $\pm 1\sigma$ post-fit uncertainty, and re-running the fit. The solid yellow box shows the pre-fit impact. The black points, relating to the bottom x-axis, are the pulls, illustrating how much the parameter deviates from its pre-fit value, with the error bands showing post-fit error, and both normalised by the pre-fit error. The red points are the free floating normalisations, with the pre-fit values set to unity. MCStat is the total statistical uncertainty, per bin, of all the non-data samples, while "DDt stat" is the statistical uncertainty, per bin, for just the data-driven top estimate.

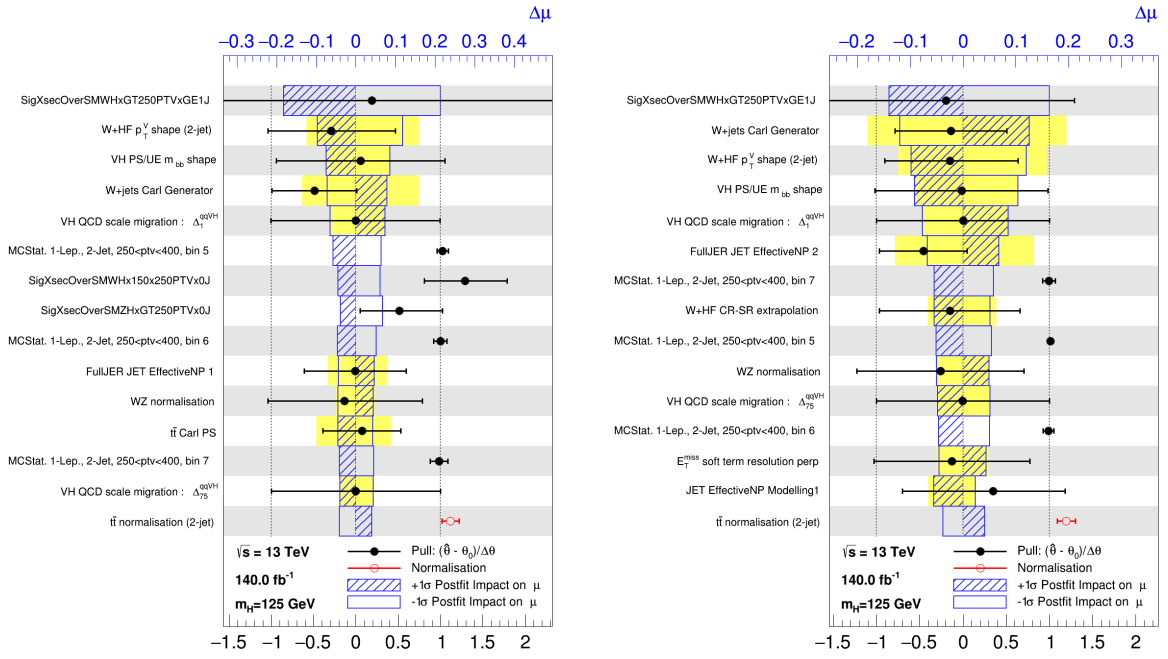

(a) (b)

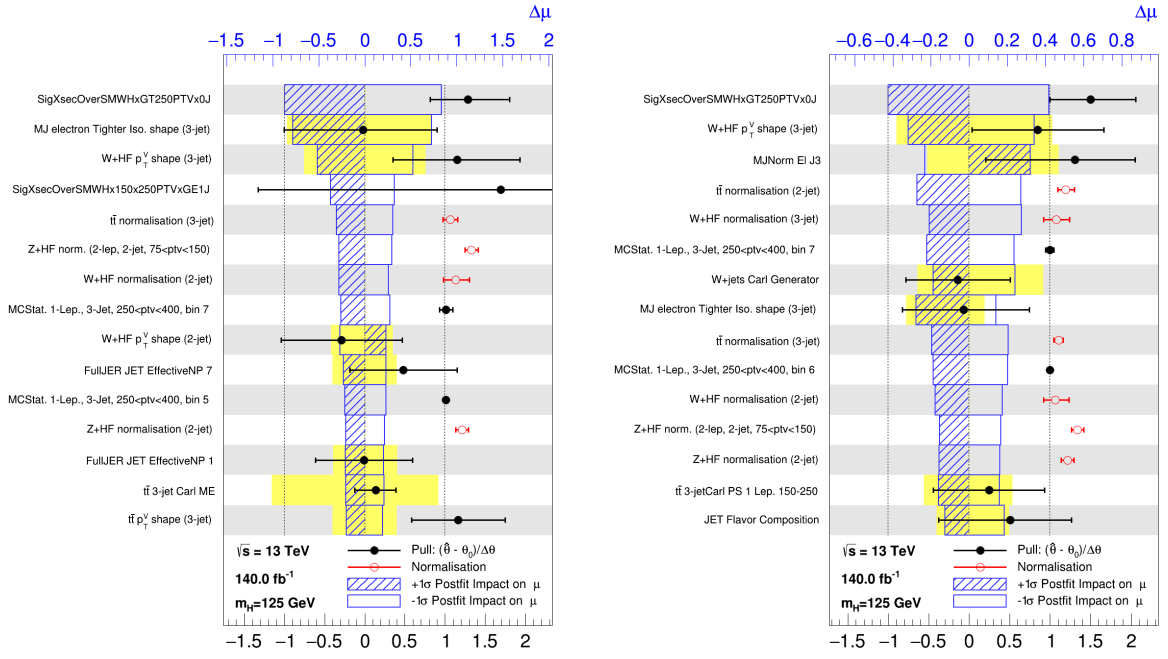

(c) (d)

FIGURE B.2: The ranking of the nuisance parameters, in descending order, in terms of their impact on the $WH, 250 < p_T^W < 400$ GeV signal strengths $\hat{\mu}$. The top row is for the $n_{jets}^{add} = 0$ signal strengths while the bottom row has the $n_{jets}^{add} \geq 1$ signal strengths. The left column is for the jet p_T selection of 20 GeV and the right column is for 30 GeV. The blue boxes, relating to the top x-axis, show the post-fit impact on $\hat{\mu}$ after fixing the nuisance parameter to the $\pm 1\sigma$ post-fit uncertainty, and re-running the fit. The solid yellow box shows the pre-fit impact. The black points, relating to the bottom x-axis, are the pulls, illustrating how much the parameter deviates from its pre-fit value, with the error bands showing post-fit error, and both normalised by the pre-fit error. The red points are the free floating normalisations, with the pre-fit values set to unity. MCStat is the total statistical uncertainty, per bin, of all the non-data samples, while "DDt stat" is the statistical uncertainty, per bin, for just the data-driven top estimate.

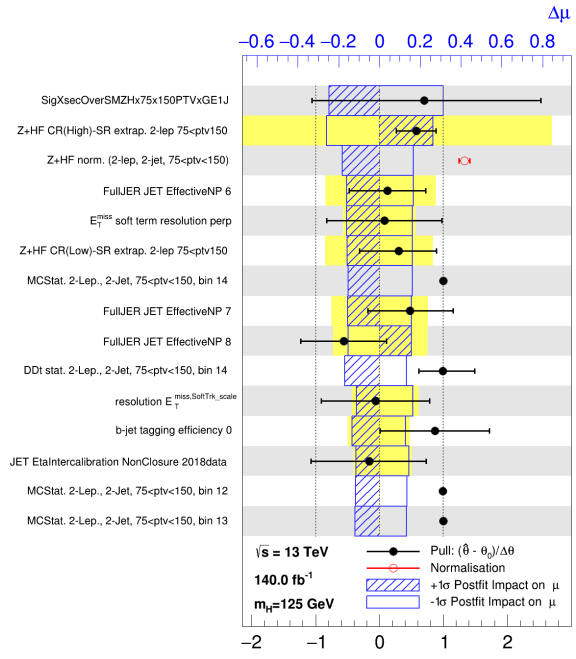

(a)

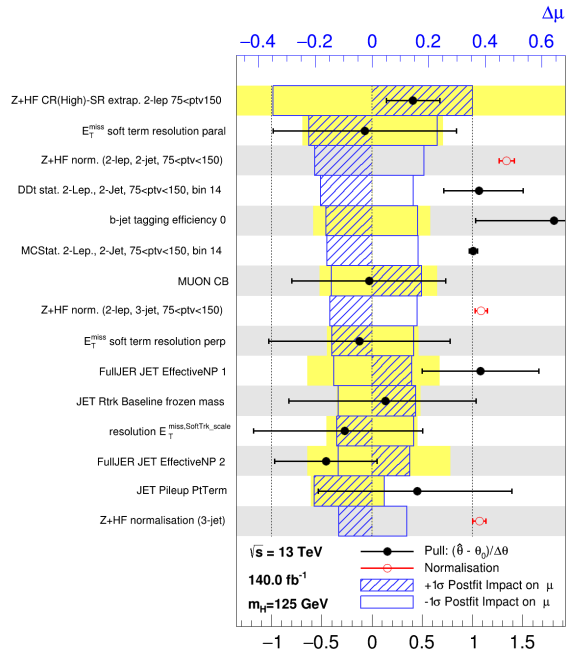

(b)

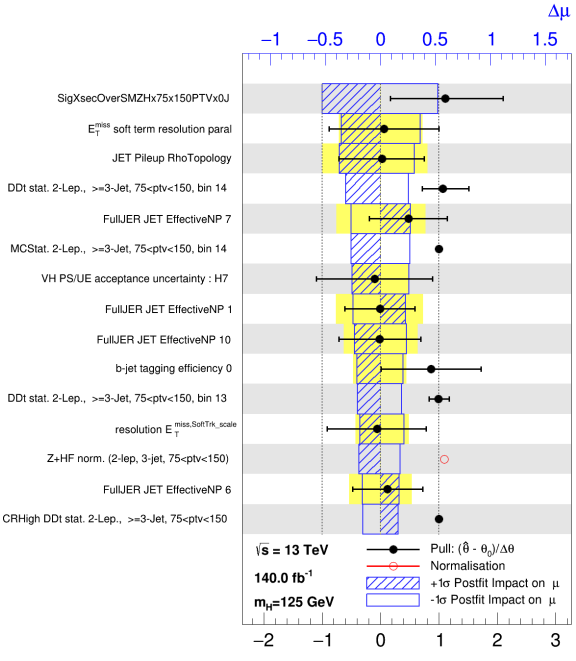

(c)

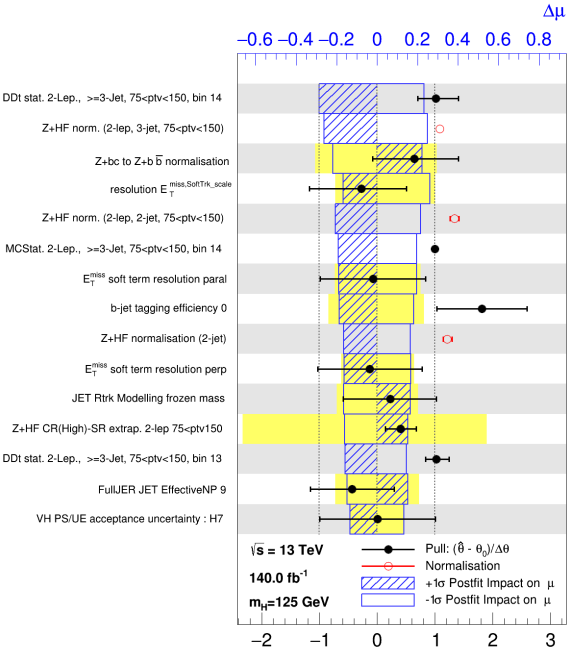

(d)

FIGURE B.3: The ranking of the nuisance parameters, in descending order, in terms of their impact on the $ZH, 75 < p_T^Z < 150$ GeV signal strengths $\hat{\mu}$. The top row is for the $n_{jets}^{add} = 0$ signal strengths while the bottom row has the $n_{jets}^{add} \geq 1$ signal strengths. The left column is for the jet p_T selection of 20 GeV and the right column is for 30 GeV. The blue boxes, relating to the top x-axis, show the post-fit impact on $\hat{\mu}$ after fixing the nuisance parameter to the $\pm 1\sigma$ post-fit uncertainty, and re-running the fit. The solid yellow box shows the pre-fit impact. The black points, relating to the bottom x-axis, are the pulls, illustrating how much the parameter deviates from its pre-fit value, with the error bands showing post-fit error, and both normalised by the pre-fit error. The red points are the free floating normalisations, with the pre-fit values set to unity. MCStat is the total statistical uncertainty, per bin, of all the non-data samples, while "DDt stat" is the statistical uncertainty, per bin, for just the data-driven top estimate.

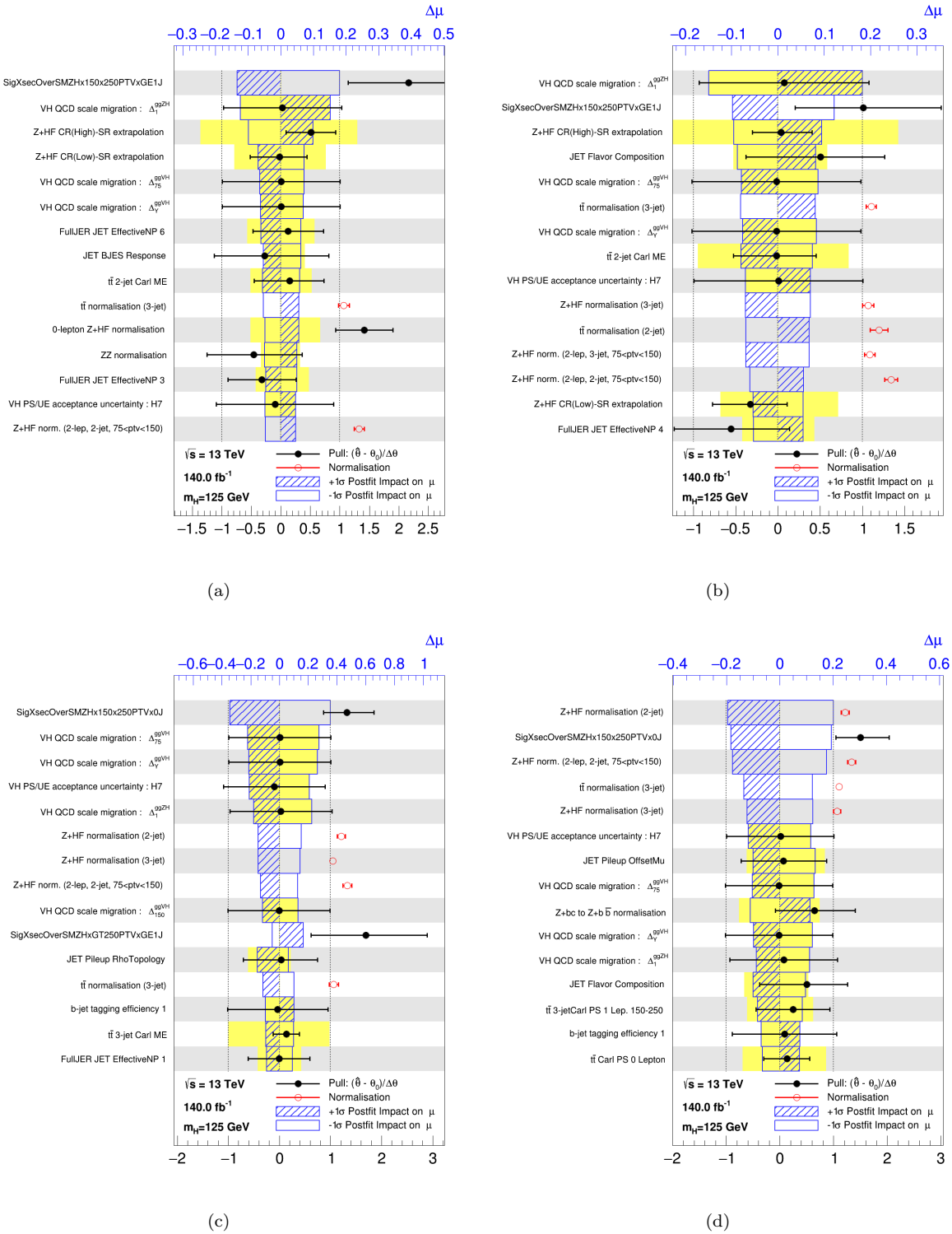

FIGURE B.4: The ranking of the nuisance parameters, in descending order, in terms of their impact on the $ZH, 150 < p_T^Z < 250$ GeV signal strengths $\hat{\mu}$. The top row is for the $n_{jets}^{add} = 0$ signal strengths while the bottom row has the $n_{jets}^{add} \geq 1$ signal strengths. The left column is for the jet p_T selection of 20 GeV and the right column is for 30 GeV. The blue boxes, relating to the top x-axis, show the post-fit impact on $\hat{\mu}$ after fixing the nuisance parameter to the $\pm 1\sigma$ post-fit uncertainty, and re-running the fit. The solid yellow box shows the pre-fit impact. The black points, relating to the bottom x-axis, are the pulls, illustrating how much the parameter deviates from its pre-fit value, with the error bands showing post-fit error, and both normalised by the pre-fit error. The red points are the free floating normalisations, with the pre-fit values set to unity. MCStat is the total statistical uncertainty, per bin, of all the non-data samples, while "DDt stat" is the statistical uncertainty, per bin, for just the data-driven top estimate.

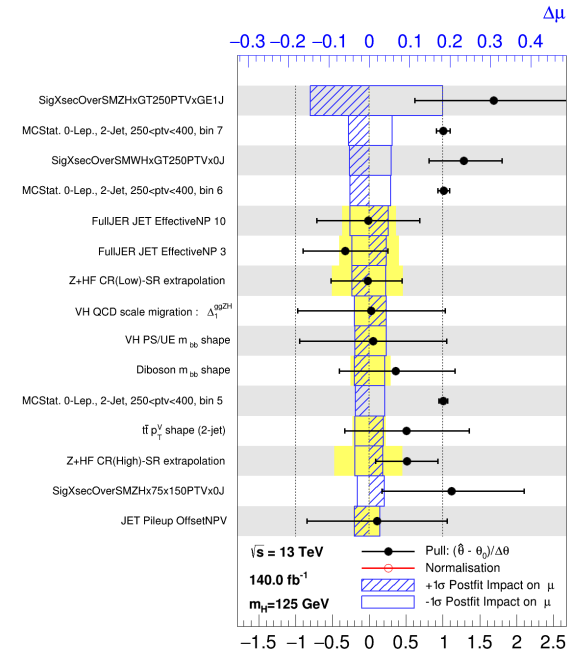

(a)

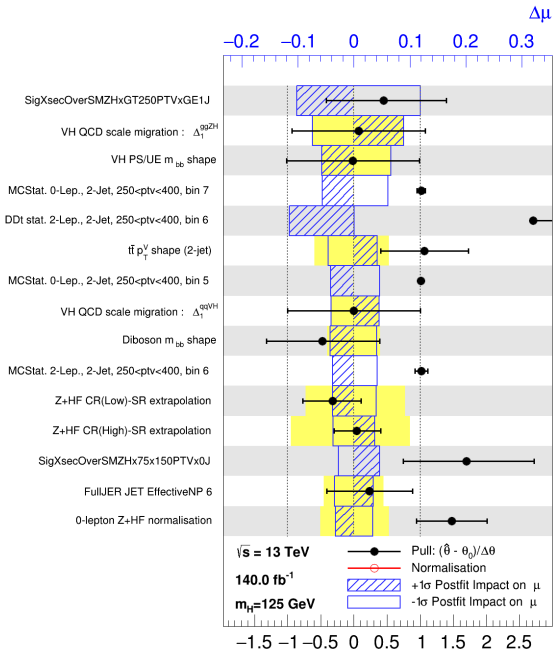

(b)

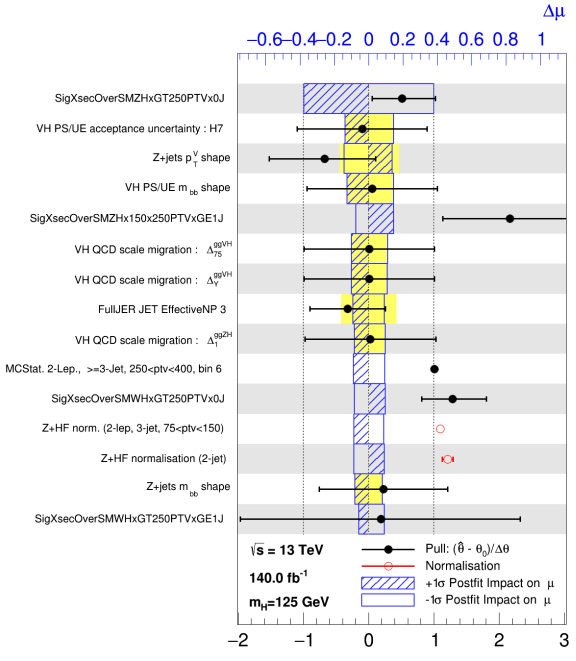

(c)

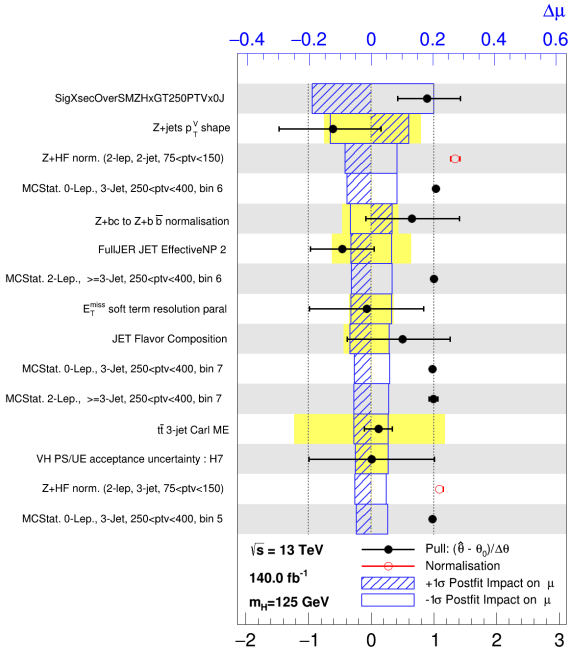

(d)

FIGURE B.5: The ranking of the nuisance parameters, in descending order, in terms of their impact on the $ZH, 250 < p_T^Z < 400$ GeV signal strengths $\hat{\mu}$. The top row is for the $n_{jets}^{add} = 0$ signal strengths while the bottom row has the $n_{jets}^{add} \geq 1$ signal strengths. The left column is for the jet p_T selection of 20 GeV and the right column is for 30 GeV. The blue boxes, relating to the top x-axis, show the post-fit impact on $\hat{\mu}$ after fixing the nuisance parameter to the $\pm 1\sigma$ post-fit uncertainty, and re-running the fit. The solid yellow box shows the pre-fit impact. The black points, relating to the bottom x-axis, are the pulls, illustrating how much the parameter deviates from its pre-fit value, with the error bands showing post-fit error, and both normalised by the pre-fit error. The red points are the free floating normalisations, with the pre-fit values set to unity. MCStat is the total statistical uncertainty, per bin, of all the non-data samples, while "DDt stat" is the statistical uncertainty, per bin, for just the data-driven top estimate.

B.2 Uncertainty breakdowns

This section presents the breakdowns of how the different sources of uncertainties contribute to the uncertainty on the signal strength of each POI. A direct comparison between the 20 GeV and 30 GeV jet p_T selections is also made. The breakdowns are set out as follows:

- The n_{jets}^{add}=0 and n_{jets}^{add}≥1, $WH, 150 < p_T^W < 250$ GeV signal strengths: Table B.1
- The n_{jets}^{add}=0 and n_{jets}^{add}≥1, $WH, 250 < p_T^W < 400$ GeV signal strengths: Table B.2
- The n_{jets}^{add}=0 and n_{jets}^{add}≥1, $ZH, 75 < p_T^Z < 150$ GeV signal strengths: Table B.3
- The n_{jets}^{add}=0 and n_{jets}^{add}≥1, $ZH, 150 < p_T^Z < 250$ GeV signal strengths: Table B.4
- The n_{jets}^{add}=0 and n_{jets}^{add}≥1, $ZH, 250 < p_T^Z < 400$ GeV signal strengths: Table B.5

TABLE B.1: Breakdown of the actual contributions to the total uncertainty on the $WH, 150 < p_T^W < 250$ GeV signal strengths, with $n_{jets}^{add} = 0$ on the left and $n_{jets}^{add} \geq 1$ on the right. The row below the column headings show the value of the signal strength, along with the total uncertainty on that signal strength.

	20 GeV	**30 GeV**	**Ratio**
Signal Strength	1.29	1.26	0.979
Total	0.491	0.503	1.024
DataStat	0.390	0.376	0.964
FullSyst	0.297	0.334	1.125
Data stat only	0.315	0.324	1.029
MC stat	0.117	0.115	0.983
Top-emu CR stat	0.018	0.024	1.333
Floating normalizations	0.238	0.193	0.811
Modelling: VH	0.092	0.091	0.989
Modelling: Background	0.173	0.200	1.156
Multi Jet	0.035	0.052	1.486
Modelling: single top	0.064	0.061	0.953
Modelling: ttbar	0.137	0.152	1.109
Modelling: W+jets	0.069	0.093	1.348
Modelling: Z+jets	0.043	0.077	1.791
Modelling: Diboson	0.064	0.068	1.062
Experimental Syst	0.129	0.164	1.271
Detector: lepton	0.007	0.005	0.714
Detector: MET	0.061	0.042	0.689
Detector: JET	0.084	0.132	1.571
Detector: FTAG (b-jet)	0.042	0.039	0.929
Detector: FTAG (c-jet)	0.045	0.057	1.267
Detector: FTAG (l-jet)	0.004	0.005	1.250
Detector: PU	0.029	0.047	1.621
Lumi	0.018	0.008	0.444

	20 GeV	**30 GeV**	**Ratio**
Signal Strength	1.7	-0.13	-0.075
Total	3.030	2.275	0.751
DataStat	2.126	1.486	0.699
FullSyst	2.159	1.723	0.798
Data stat only	1.657	1.250	0.754
MC stat	0.763	0.543	0.712
Top-emu CR stat	0.195	0.167	0.856
Floating normalisations	1.542	0.910	0.590
Modelling: VH	0.388	0.224	0.577
Modelling: Background	1.171	0.849	0.725
Multi Jet	0.370	0.399	1.078
Modelling: single top	0.379	0.281	0.741
Modelling: ttbar	0.928	0.709	0.764
Modelling: W+jets	0.582	0.241	0.414
Modelling: Z+jets	0.345	0.161	0.467
Modelling: Diboson	0.244	0.168	0.689
Experimental Syst	1.228	1.021	0.831
Detector: lepton	0.038	0.031	0.816
Detector: MET	0.350	0.244	0.697
Detector: JET	0.986	0.755	0.766
Detector: FTAG (b-jet)	0.338	0.289	0.855
Detector: FTAG (c-jet)	0.334	0.425	1.272
Detector: FTAG (l-jet)	0.098	0.100	1.020
Detector: PU	0.062	0.134	2.161
Lumi	0.053	0.018	0.340

TABLE B.2: Breakdown of the actual contributions to the total uncertainty on the $WH, 250 < p_T^W < 400$ GeV signal strengths, with $n_{jets}^{add} = 0$ on the left and $n_{jets}^{add} \geq 1$ on the right. The row below the column headings show the value of the signal strength, along with the total uncertainty on that signal strength.

	20 GeV	**30 GeV**	**Ratio**
Signal Strength	1.28	1.5	1.17
Total	0.494	0.530	1.073
DataStat	0.422	0.424	1.005
FullSyst	0.257	0.318	1.237
Data stat only	0.353	0.374	1.059
MC stat	0.108	0.108	1.000
Top-emu CR stat	0.014	0.020	1.429
Floating normalisations	0.216	0.167	0.773
Modelling: VH	0.127	0.152	1.197
Modelling: Background	0.186	0.204	1.097
Multi Jet	0.015	0.066	4.400
Modelling: single top	0.029	0.023	0.793
Modelling: ttbar	0.061	0.053	0.869
Modelling: W+jets	0.150	0.187	1.247
Modelling: Z+jets	0.036	0.042	1.167
Modelling: Diboson	0.067	0.074	1.104
Experimental Syst	0.064	0.112	1.750
Detector: lepton	0.002	0.004	2.000
Detector: MET	0.016	0.058	3.625
Detector: JET	0.045	0.076	1.689
Detector: FTAG (b-jet)	0.019	0.031	1.632
Detector: FTAG (c-jet)	0.022	0.038	1.727
Detector: FTAG (l-jet)	0.003	0.015	5.000
Detector: PU	0.025	0.026	1.040
Lumi	0.019	0.011	0.579

	20 GeV	**30 GeV**	**Ratio**
Signal Strength	0.18	-0.19	-1.048
Total	2.144	1.477	0.689
DataStat	1.654	1.182	0.715
FullSyst	1.363	0.884	0.649
Data stat only	1.360	1.035	0.761
MC stat	0.515	0.364	0.707
Top-emu CR stat	0.116	0.044	0.379
Floating normalisations	0.985	0.568	0.577
Modelling: VH	0.305	0.195	0.639
Modelling: Background	1.151	0.666	0.579
Multi Jet	0.808	0.384	0.475
Modelling: single top	0.139	0.163	1.173
Modelling: ttbar	0.373	0.275	0.737
Modelling: W+jets	0.634	0.445	0.702
Modelling: Z+jets	0.126	0.135	1.071
Modelling: Diboson	0.203	0.102	0.502
Experimental Syst	0.441	0.359	0.814
Detector: lepton	0.013	0.007	0.538
Detector: MET	0.116	0.089	0.767
Detector: JET	0.360	0.288	0.800
Detector: FTAG (b-jet)	0.142	0.057	0.401
Detector: FTAG (c-jet)	0.129	0.141	1.093
Detector: FTAG (l-jet)	0.025	0.007	0.280
Detector: PU	0.138	0.113	0.819
Lumi	0.037	0.012	0.324

TABLE B.3: Breakdown of the actual contributions to the total uncertainty on the $ZH, 75 < p_T^Z < 150$ GeV signal strengths, with $n_{jets}^{add} = 0$ on the left and $n_{jets}^{add} \geq 1$ on the right. The row below the column headings show the value of the signal strength, along with the total uncertainty on that signal strength.

	20 GeV	**30 GeV**	**Ratio**
Signal Strength	1.12	1.7	1.524
Total	0.965	0.990	1.026
DataStat	0.714	0.671	0.940
FullSyst	0.649	0.728	1.122
Data stat only	0.555	0.560	1.009
MC stat	0.303	0.275	0.908
Top-emu CR stat	0.254	0.243	0.957
Floating normalisations	0.418	0.424	1.014
Modelling: VH	0.126	0.202	1.603
Modelling: Background	0.439	0.487	1.109
Multi Jet	0.008	0.016	2.000
Modelling: single top	0.034	0.037	1.088
Modelling: ttbar	0.094	0.118	1.255
Modelling: W+jets	0.036	0.094	2.611
Modelling: Z+jets	0.303	0.370	1.221
Modelling: Diboson	0.097	0.094	0.969
Experimental Syst	0.354	0.506	1.429
Detector: lepton	0.008	0.148	18.500
Detector: MET	0.222	0.324	1.459
Detector: JET	0.236	0.321	1.360
Detector: FTAG (b-jet)	0.158	0.199	1.259
Detector: FTAG (c-jet)	0.041	0.018	0.439
Detector: FTAG (l-jet)	0.002	0.014	7.000
Detector: PU	0.012	0.000	0.000
Lumi	0.017	0.014	0.824

	20 GeV	**30 GeV**	**Ratio**
Signal Strength	0.7	-0.2	-0.285
Total	1.791	1.391	0.777
DataStat	1.431	1.146	0.801
FullSyst	1.076	0.787	0.731
Data stat only	1.026	0.901	0.878
MC stat	0.463	0.308	0.665
Top-emu CR stat	0.490	0.401	0.818
Floating normalisations	0.734	0.414	0.564
Modelling: VH	0.425	0.302	0.711
Modelling: Background	0.573	0.499	0.871
Multi Jet	0.018	0.059	3.278
Modelling: single top	0.083	0.036	0.434
Modelling: ttbar	0.141	0.196	1.390
Modelling: W+jets	0.061	0.068	1.115
Modelling: Z+jets	0.237	0.335	1.414
Modelling: Diboson	0.159	0.097	0.610
Experimental Syst	0.700	0.501	0.716
Detector: lepton	0.010	0.051	5.100
Detector: MET	0.454	0.371	0.817
Detector: JET	0.586	0.317	0.541
Detector: FTAG (b-jet)	0.247	0.188	0.761
Detector: FTAG (c-jet)	0.118	0.011	0.093
Detector: FTAG (l-jet)	0.011	0.036	3.273
Detector: PU	0.026	0.015	0.577
Lumi	0.031	0.011	0.355

TABLE B.4: Breakdown of the actual contributions to the total uncertainty on the $ZH, 150 < p_T^Z < 250$ GeV signal strengths, with $n_{jets}^{add} = 0$ on the left and $n_{jets}^{add} \geq 1$ on the right. The row below the column headings show the value of the signal strength, along with the total uncertainty on that signal strength.

	20 GeV	**30 GeV**	**Ratio**
Signal Strength	1.33	1.5	1.134
Total	0.493	0.495	1.004
DataStat	0.376	0.360	0.957
FullSyst	0.318	0.338	1.063
Data stat only	0.315	0.320	1.016
MC stat	0.104	0.095	0.913
Top-emu CR stat	0.033	0.035	1.061
Floating normalisations	0.213	0.199	0.934
Modelling: VH	0.191	0.235	1.230
Modelling: Background	0.183	0.175	0.956
Multi Jet	0.007	0.024	3.429
Modelling: single top	0.017	0.015	0.882
Modelling: ttbar	0.080	0.120	1.500
Modelling: W+jets	0.024	0.032	1.333
Modelling: Z+jets	0.125	0.115	0.920
Modelling: Diboson	0.075	0.073	0.973
Experimental Syst	0.144	0.149	1.035
Detector: lepton	0.039	0.029	0.744
Detector: MET	0.062	0.048	0.774
Detector: JET	0.106	0.128	1.208
Detector: FTAG (b-jet)	0.045	0.021	0.467
Detector: FTAG (c-jet)	0.017	0.033	1.941
Detector: FTAG (l-jet)	0.002	0.009	4.500
Detector: PU	0.005	0.022	4.400
Lumi	0.020	0.011	0.550

	20 GeV	**30 GeV**	**Ratio**
Signal Strength	2.17	1.01	0.466
Total	1.118	0.863	0.772
DataStat	0.893	0.707	0.792
FullSyst	0.666	0.492	0.739
Data stat only	0.718	0.610	0.850
MC stat	0.193	0.151	0.782
Top-emu CR stat	0.119	0.109	0.916
Floating normalisations	0.512	0.357	0.697
Modelling: VH	0.499	0.258	0.517
Modelling: Background	0.258	0.227	0.880
Multi Jet	0.010	0.017	1.700
Modelling: single top	0.020	0.032	1.600
Modelling: ttbar	0.167	0.156	0.934
Modelling: W+jets	0.039	0.034	0.872
Modelling: Z+jets	0.150	0.151	1.007
Modelling: Diboson	0.048	0.053	1.104
Experimental Syst	0.264	0.248	0.939
Detector: lepton	0.057	0.056	0.982
Detector: MET	0.120	0.037	0.308
Detector: JET	0.208	0.223	1.072
Detector: FTAG (b-jet)	0.122	0.101	0.828
Detector: FTAG (c-jet)	0.030	0.018	0.600
Detector: FTAG (l-jet)	0.021	0.013	0.619
Detector: PU	0.006	0.024	4.000
Lumi	0.038	0.009	0.237

TABLE B.5: Breakdown of the actual contributions to the total uncertainty on the $ZH, 250 < p_T^Z < 400$ GeV signal strengths, with $n_{jets}^{add} = 0$ on the left and $n_{jets}^{add} \geq 1$ on the right. The row below the column headings show the value of the signal strength, along with the total uncertainty on that signal strength.

	20 GeV	**30 GeV**	**Ratio**
Signal Strength	0.51	0.89	1.746
Total	0.485	0.499	1.029
DataStat	0.445	0.447	1.004
FullSyst	0.192	0.219	1.141
Data stat only	0.399	0.419	1.050
MC stat	0.106	0.103	0.972
Top-emu CR stat	0.018	0.019	1.056
Floating normalisations	0.183	0.139	0.760
Modelling: VH	0.088	0.132	1.500
Modelling: Background	0.136	0.143	1.051
Multi Jet	0.010	0.030	3.000
Modelling: single top	0.006	0.005	0.833
Modelling: ttbar	0.053	0.073	1.377
Modelling: W+jets	0.016	0.019	1.188
Modelling: Z+jets	0.060	0.071	1.183
Modelling: Diboson	0.043	0.047	1.093
Experimental Syst	0.067	0.068	1.015
Detector: lepton	0.004	0.013	3.250
Detector: MET	0.031	0.035	1.129
Detector: JET	0.054	0.044	0.815
Detector: FTAG (b-jet)	0.019	0.020	1.053
Detector: FTAG (c-jet)	0.003	0.009	3.000
Detector: FTAG (l-jet)	0.002	0.005	2.500
Detector: PU	0.006	0.026	4.333
Lumi	0.008	0.007	0.875

	20 GeV	**30 GeV**	**Ratio**
Signal Strength	1.69	0.45	0.267
Total	1.138	0.909	0.799
DataStat	1.014	0.827	0.816
FullSyst	0.510	0.377	0.739
Data stat only	0.908	0.771	0.849
MC stat	0.202	0.174	0.861
Top-emu CR stat	0.055	0.048	0.873
Floating normalisations	0.454	0.249	0.548
Modelling: VH	0.324	0.168	0.519
Modelling: Background	0.289	0.261	0.903
Multi Jet	0.033	0.040	1.212
Modelling: single top	0.023	0.027	1.174
Modelling: ttbar	0.106	0.073	0.689
Modelling: W+jets	0.033	0.062	1.879
Modelling: Z+jets	0.179	0.163	0.911
Modelling: Diboson	0.066	0.024	0.364
Experimental Syst	0.146	0.147	1.007
Detector: lepton	0.034	0.034	1.000
Detector: MET	0.045	0.067	1.489
Detector: JET	0.105	0.109	1.038
Detector: FTAG (b-jet)	0.066	0.040	0.606
Detector: FTAG (c-jet)	0.015	0.020	1.333
Detector: FTAG (l-jet)	0.006	0.020	3.333
Detector: PU	0.010	0.007	0.700
Lumi	0.029	0.007	0.241

Bibliography

[1] Glashow, S.L. Partial-symmetries of weak interactions. *Nucl. Phys.*, 22:579–588, 1961. doi: 10.1016/0029-5582(61)90469-2.

[2] Abdus Salam. Weak and Electromagnetic Interactions. *Conf. Proc. C*, 680519:367–377, 1968. doi: 10.1142/9789812795915_0034.

[3] Steven Weinberg. A Model of Leptons. *Phys. Rev. Lett.*, 19:1264–1266, 1967. doi: 10.1103/PhysRevLett.19.1264. URL https://inspirehep.net/literature/51188.

[4] Peter W. Higgs. Broken Symmetries and the Masses of Gauge Bosons. *Phys. Rev. Lett.*, 13:508–509, 1964. doi: 10.1103/PhysRevLett.13.508.

[5] S. Tomonaga. On a relativistically invariant formulation of the quantum theory of wave fields. *Prog. Theor. Phys.*, 1:27–42, 1946. doi: 10.1143/PTP.1.27.

[6] Julian S. Schwinger. On Quantum electrodynamics and the magnetic moment of the electron. *Phys. Rev.*, 73:416–417, 1948. doi: 10.1103/PhysRev.73.416.

[7] R. P. Feynman. Space-time approach to quantum electrodynamics. *Phys. Rev.*, 76:769–789, Sep 1949. doi: 10.1103/PhysRev.76.769. URL https://link.aps.org/doi/10.1103/PhysRev.76.769.

[8] ATLAS Collaboration. Observation of a New Particle in the Search for the Standard Model Higgs Boson with the ATLAS Detector at the LHC. *Phys. Lett. B*, **716**:1–29, 2012. arXiv:1207.7214 [hep-ex].

[9] CMS Collaboration. Observation of a New Boson at a Mass of 125 GeV with the CMS Experiment at the LHC. *Phys. Lett. B*, **716**:30–61, 2012. arXiv:1207.7235 [hep-ex].

[10] Lyndon Evans and Philip Bryant. LHC Machine. *Journal of Instrumentation*, **3**(08): S08001, 2008. URL http://stacks.iop.org/1748-0221/3/i=08/a=S08001.

[11] S. Navas et al. Review of particle physics. *Phys. Rev. D*, 110(3):030001, 2024. doi: 10.1103/PhysRevD.110.030001.

[12] Steven Weinberg. On the development of effective field theory. *The European Physical Journal H*, 46(1), March 2021. ISSN 2102-6467. doi: 10.1140/epjh/s13129-021-00004-x. URL http://dx.doi.org/10.1140/epjh/s13129-021-00004-x.

[13] Gianfranco Bertone, Dan Hooper, and Joseph Silk. Particle dark matter: evidence, candidates and constraints. *Physics Reports*, 405(5-6):279–390, jan 2005. doi: 10.1016/j.physrep.2004.08.031. URL https://doi.org/10.1016%2Fj.physrep.2004.08.031.

[14] A. D. Sakharov. Violation of CP Invariance, C asymmetry, and baryon asymmetry of the universe. *Pisma Zh. Eksp. Teor. Fiz.*, 5:32–35, 1967. doi: 10.1070/PU1991v034n05ABEH002497.

[15] C. Rovelli. *Quantum Gravity*. Cambridge Monographs on Mathematical Physics. Cambridge University Press, 2004. ISBN 9780521837330. URL https://books.google.co.za/books?id=HrAzTmXdssQC.

[16] vttoth. The parameters of the standard model, 2014. URL https://spinor.info/weblog/?p=6355. Accessed: 02 March 2023.

[17] Michael Krämer. The standard model of particle physics. CERN Summer School, CERN, Geneva, July 2017, 2017. URL https://indico.cern.ch/event/632201/attachments/1491025/2317647/mkraemer_CERN_2017_SM4.pdf.

[18] Sidney Coleman and Jeffrey Mandula. All possible symmetries of the s matrix. *Phys. Rev.*, 159:1251–1256, Jul 1967. doi: 10.1103/PhysRev.159.1251. URL https://link.aps.org/doi/10.1103/PhysRev.159.1251.

[19] Rudolf Haag, Jan T. Lopuszanski, and Martin Sohnius. All Possible Generators of Supersymmetries of the s Matrix. *Nucl. Phys.*, B88:257, 1975. doi: 10.1016/0550-3213(75)90279-5. [,257(1974)].

[20] T. D. Lee. A theory of spontaneous t violation. *Phys. Rev. D*, 8:1226–1239, Aug 1973. doi: 10.1103/PhysRevD.8.1226. URL https://link.aps.org/doi/10.1103/PhysRevD.8.1226.

[21] S. Badger et al. Les houches 2015: Physics at tev colliders standard model working group report, 2016. arXiv:1605.04692 [hep-ph].

[22] Nicolas Berger, Claudia Bertella, Thomas P. Calvet, Milene Calvetti, Valerio Dao, Marco Delmastro, Michael Duehrssen-Debling, Paolo Francavilla, Yacine Haddad, Oleh Kivernyk, Jonathon M. Langford, Changqiao Li, Giovanni Marchiori, Predrag Milenovic, Carlo E. Pandini, Edward Scott, Frank J. Tackmann, Kerstin Tackmann, Lorenzo Viliani, and Meng Xiao. Simplified template cross sections - stage 1.1, 2019. arXiv:1906.02754 [hep-ph].

[23] ATLAS Collaboration. Measurements of WH and ZH production with Higgs boson decays into bottom quarks and direct constraints on the charm Yukawa coupling in 13 TeV pp collisions with the ATLAS detector, 2024. URL https://arxiv.org/abs/2410.19611.

[24] ATLAS Collaboration. Measurements of WH and ZH production in the $H \to b\bar{b}$ decay channel in pp collisions at 13 TeV with the ATLAS detector. *Eur. Phys. J. C*, 81(2):178, 2021. doi: 10.1140/epjc/s10052-020-08677-2.

[25] ATLAS Collaboration. Measurement of the associated production of a higgs boson decaying into b-quarks with a vector boson at high transverse momentum in pp collisions at $\sqrt{s} = 13$ tev with the ATLAS detector. *Physics Letters B*, 816:136204, may 2021. doi: 10.1016/j.physletb.2021.136204. URL https://doi.org/10.1016%2Fj.physletb.2021.136204.

[26] ATLAS Collaboration. Direct constraint on the Higgs-charm coupling from a search for Higgs boson decays into charm quarks with the ATLAS detector. *Eur. Phys. J. C*, 82: 717, 2022. doi: 10.1140/epjc/s10052-022-10588-3.

[27] Mark Thomson. *Modern particle physics*. Cambridge University Press, New York, 2013. ISBN 978-1-107-03426-6. doi: 10.1017/CBO9781139525367.

[28] David J Griffiths. *Introduction to elementary particles; 2nd rev. version*. Physics textbook. Wiley, New York, NY, 2008. URL https://cds.cern.ch/record/111880.

[29] Belle Collaboration. Observation of a Narrow Charmonium-like State in Exclusive $B^{\pm} \to K^{\pm}\pi^{+}\pi^{-}J/\psi$ Decays. *Physical Review Letters*, 91(26), December 2003. ISSN 1079-7114. doi: 10.1103/physrevlett.91.262001. URL http://dx.doi.org/10.1103/PhysRevLett.91.262001.

[30] LHCb Collaboration. Observation of $J/\psi p$ resonances consistent with pentaquark states in $\Lambda_b^0 \to J/\psi K^{-} p$ decays. *Physical Review Letters*, 115(7), August 2015. ISSN 1079-7114. doi: 10.1103/physrevlett.115.072001. URL http://dx.doi.org/10.1103/PhysRevLett.115.072001.

[31] Wikimedia Commons. Standard model of elementary particles, 2019. URL https://upload.wikimedia.org/wikipedia/commons/thumb/0/00/Standard_Model_of_Elementary_Particles.svg/2140px-Standard_Model_of_Elementary_Particles.svg.png.

[32] Paul Adrien Maurice Dirac. *On the theory of quantum mechanics*, volume 112(762). Royal Society, New York, 1926. doi: 10.1098/rspa.1926.0133. URL https://royalsocietypublishing.org/doi/10.1098/rspa.1926.0133.

[33] H. Fritzsch, Murray Gell-Mann, and H. Leutwyler. Advantages of the Color Octet Gluon Picture. *Phys. Lett. B*, 47:365–368, 1973. doi: 10.1016/0370-2693(73)90625-4.

[34] D. J. Gross and Frank Wilczek. Asymptotically Free Gauge Theories - I. *Phys. Rev. D*, 8:3633–3652, 1973. doi: 10.1103/PhysRevD.8.3633.

[35] H. David Politzer. Reliable Perturbative Results for Strong Interactions? *Phys. Rev. Lett.*, 30:1346–1349, 1973. doi: 10.1103/PhysRevLett.30.1346.

[36] Peter W. Higgs. Broken symmetries, massless particles and gauge fields. *Phys. Lett.*, 12: 132–133, 1964. doi: 10.1016/0031-9163(64)91136-9.

[37] Peter W. Higgs. Spontaneous symmetry breakdown without massless bosons. *Phys. Rev.*, 145:1156–1163, May 1966. doi: 10.1103/PhysRev.145.1156. URL https://link.aps.org/doi/10.1103/PhysRev.145.1156.

[38] zer zdal. *The Higgs Boson and Right-Handed Neutrinos in Supersymmetric Models*. PhD thesis, Izmir Institute of Technology, 07 2016.

[39] Steven Weinberg. *The quantum theory of fields. Vol. 2: Modern applications*. Cambridge University Press, 8 2013. ISBN 978-1-139-63247-8, 978-0-521-67054-8, 978-0-521-55002-4. doi: 10.1017/CBO9781139644174.

[40] Nicola Cabibbo. Unitary Symmetry and Leptonic Decays. *Phys. Rev. Lett.*, 10:531–533, 1963. doi: 10.1103/PhysRevLett.10.531.

[41] Makoto Kobayashi and Toshihide Maskawa. CP Violation in the Renormalizable Theory of Weak Interaction. *Prog. Theor. Phys.*, 49:652–657, 1973. doi: 10.1143/PTP.49.652.

[42] Planck Collaboration. Planck2015 results: I. overview of products and scientific results. *Astronomy and Astrophysics*, 594:A1, September 2016. ISSN 1432-0746. doi: 10.1051/0004-6361/201527101. URL http://dx.doi.org/10.1051/0004-6361/201527101.

[43] Vera C. Rubin and Jr. Ford, W. Kent. Rotation of the Andromeda Nebula from a Spectroscopic Survey of Emission Regions. *Astrophysical Journal*, 159:379, February 1970. doi: 10.1086/150317.

[44] Douglas Clowe, Marua Brada, Anthony H. Gonzalez, Maxim Markevitch, Scott W. Randall, Christine Jones, and Dennis Zaritsky. A direct empirical proof of the existence of dark matter. *The Astrophysical Journal*, 648(2):L109L113, August 2006. ISSN 1538-4357. doi: 10.1086/508162. URL http://dx.doi.org/10.1086/508162.

[45] Adam G. et al. Riess. Observational evidence from supernovae for an accelerating universe and a cosmological constant. *The Astronomical Journal*, 116(3):10091038, September 1998. ISSN 0004-6256. doi: 10.1086/300499. URL http://dx.doi.org/10.1086/300499.

[46] M. B. GAVELA, P. HERNNDEZ, J. ORLOFF, and O. PNE. Standard model cp-violation and baryon asymmetry. *Modern Physics Letters A*, 09(09):795809, March 1994. ISSN 1793-6632. doi: 10.1142/s0217732394000629. URL http://dx.doi.org/10.1142/S0217732394000629.

[47] B. Pontecorvo. Mesonium and anti-mesonium. *Sov. Phys. JETP*, 6:429, 1957.

[48] Tsutomu Yanagida. Horizontal Symmetry and Masses of Neutrinos. *Prog. Theor. Phys.*, 64:1103, 1980. doi: 10.1143/PTP.64.1103.

[49] Albert Einstein. On the general theory of relativity. *Sitzungsber. Preuss. Akad. Wiss. Berlin (Math. Phys.)*, pages 778–786, 1915.

[50] G. Veneziano. Construction of a crossing-simmetric, regge-behaved amplitude for linearly rising trajectories. *Il Nuovo Cimento A (1965-1970)*, 57(1):190–197, Sep 1968. ISSN 1826-9869. doi: 10.1007/BF02824451. URL https://doi.org/10.1007/BF02824451.

[51] J. Scherk and J. H. Schwarz. Dual models for non-hadrons. *Nuclear Physics B*, 81:118–144, October 1974. doi: 10.1016/0550-3213(74)90010-8.

[52] Thomas Appelquist and J. Carazzone. Infrared Singularities and Massive Fields. *Phys. Rev. D*, 11:2856, 1975. doi: 10.1103/PhysRevD.11.2856.

[53] Edward Witten. Dynamical Breaking of Supersymmetry. *Nucl. Phys. B*, 188:513, 1981. doi: 10.1016/0550-3213(81)90006-7.

[54] Steven Weinberg. *ULTRAVIOLET DIVERGENCES IN QUANTUM THEORIES OF GRAVITATION*, pages 790–831. 1980.

[55] Steven Weinberg. Baryon and Lepton Nonconserving Processes. *Phys. Rev. Lett.*, 43: 1566–1570, 1979. doi: 10.1103/PhysRevLett.43.1566.

[56] André de Gouvêa, Juan Herrero-García, and Andrew Kobach. Neutrino masses, grand unification, and baryon number violation. *Physical Review D*, 90(1), jul 2014. doi: 10.1103/physrevd.90.016011. URL https://doi.org/10.1103%2Fphysrevd.90.016011.

[57] Jürgen Reuter. Monte carlo event generators for the lhc. LHC Theory Workshop, TRIUMF, Vancouver, 29 April 2009, 2009. URL https://www.desy.de/~reuter/downloads/vancouver_09.pdf.

[58] J. D. Bjorken. Asymptotic Sum Rules at Infinite Momentum. *Phys. Rev.*, 179:1547–1553, 1969. doi: 10.1103/PhysRev.179.1547.

[59] John C. Collins, Davison E. Soper, and George Sterman. Factorization of hard processes in qcd. *Adv. Ser. Direct. High Energy Phys.*, 2004. doi: 10.48550/ARXIV.HEP-PH/0409313. arXiv:0409313 [hep-ph].

[60] Michelangelo L Mangano. Introduction to QCD. 2000. doi: 10.5170/CERN-1999-004.53. URL https://cds.cern.ch/record/454171.

[61] B. R. Webber. Fragmentation and hadronization, 1999. URL https://arxiv.org/abs/hep-ph/9912292.

[62] Zachary Marshall and the Atlas Collaboration. Simulation of Pile-up in the ATLAS Experiment. *Journal of Physics: Conference Series*, 513(2):022024, 2014. URL http://stacks.iop.org/1742-6596/513/i=2/a=022024.

[63] CMS Collaboration. Combined measurements of higgs boson couplings in proton-proton collisions at $\sqrt{s} = 13$ tev. *The European Physical Journal C*, 79(5), may 2019. doi: 10.1140/epjc/s10052-019-6909-y. URL https://doi.org/10.1140%2Fepjc%2Fs10052-019-6909-y.

[64] CERN. Cern yellow reports: Monographs, vol 2 (2017): Handbook of lhc higgs cross sections: 4. deciphering the nature of the higgs sector, 2017. URL https://e-publishing.cern.ch/index.php/CYRM/issue/view/32.

[65] About CERN. Jan 2012. URL http://cds.cern.ch/record/1997225.

[66] UA1 Collaboration. Experimental Observation of Isolated Large Transverse Energy Electrons with Associated Missing Energy at $\sqrt{s} = 540$ GeV. *Phys. Lett. B*, **122**:103–116, 1983.

[67] UA1 Collaboration. Experimental Observation of Lepton Pairs of Invariant Mass Around 95 GeV/c^2 at the CERN SPS Collider. *Phys. Lett. B*, **126**:398–410, 1983.

[68] UA2 Collaboration. Observation of Single Isolated Electrons of High Transverse Momentum in Events with Missing Transverse Energy at the CERN $p\bar{p}$ Collider. *Phys. Lett. B*, **122**:476–485, 1983.

[69] UA2 Collaboration. Evidence for $Z^0 \to e^+e^-$ at the CERN $p\bar{p}$ Collider. *Phys. Lett. B*, **129**:130–140, 1983.

[70] G. Baur et al. Production of anti–hydrogen. *Phys. Lett.*, B368:251–258, 1996. doi: 10.1016/0370-2693(96)00005-6.

[71] ATLAS Collaboration. The ATLAS Experiment at the CERN Large Hadron Collider. *Journal of Instrumentation*, **3**(08):S08003, 2008. URL http://stacks.iop.org/1748-0221/3/i=08/a=S08003.

[72] S. Myers and E. Picasso. The Design, construction and commissioning of the CERN Large Electron Positron collider. *Contemp. Phys.*, 31:387–403, 1990. doi: 10.1080/00107519008213789.

[73] Ewa Lopienska. The CERN accelerator complex, layout in 2022. Complexe des acclrateurs du CERN en janvier 2022. 2022. URL https://cds.cern.ch/record/2800984. General Photo.

[74] ALICE Collaboration. The ALICE Experiment at the CERN Large Hadron Collider. *Journal of Instrumentation*, **3**(08):S08002, 2008. URL http://stacks.iop.org/1748-0221/3/i=08/a=S08002.

[75] CMS Collaboration. The CMS Experiment at the CERN Large Hadron Collider. *Journal of Instrumentation*, **3**(08):S08004, 2008. URL http://stacks.iop.org/1748-0221/3/i=08/a=S08004.

[76] LHCb Collaboration. The LHCb Detector at the CERN Large Hadron Collider. *Journal of Instrumentation*, **3**(08):S08005, 2008. URL http://stacks.iop.org/1748-0221/3/i=08/a=S08005.

[77] Atlas Collaboration. Improved luminosity determination in pp collisions at $\sqrt{s} = 7$ TeV using the ATLAS detector at the LHC. *Eur. Phys J.*, C73(8):2518, 2013. arXiv:1302.4393v2 [hep-ex].

[78] S van der Meer. Calibration of the Effective Beam Height in the ISR. Technical Report CERN-ISR-PO-68-31. ISR-PO-68-31, CERN, Geneva, 1968. URL https://cds.cern.ch/record/296752.

[79] G. Avoni et al. The new lucid-2 detector for luminosity measurement and monitoring in atlas. *Journal of Instrumentation*, 13(07):P07017, jul 2018. doi: 10.1088/1748-0221/13/07/P07017. URL https://dx.doi.org/10.1088/1748-0221/13/07/P07017.

[80] Morad Aaboud et al. Luminosity determination in pp collisions at $\sqrt{s} = 8$ TeV using the ATLAS detector at the LHC. *Eur. Phys. J. C*, 76(12):653, 2016. doi: 10.1140/epjc/s10052-016-4466-1.

[81] ATLAS collaboration. LuminosityPublicResultsRun2, 2018. URL https://twiki.cern.ch/twiki/bin/view/AtlasPublic/LuminosityPublicResultsRun2. Accessed: 22 February 2023.

[82] Claus Grupen and Boris Schwartz. *Particle Detectors*. Cambridge Universty Press, New York, USA, 2 edition, 2008. ISBN 978-0-511-38866-8.

[83] M *et. al.* Capeans. ATLAS Insertable B-Layer Technical Design Report. Technical Report CERN-LHCC-2010-013. ATLAS-TDR-19, Sep 2010. URL https://cds.cern.ch/record/1291633.

[84] Francesca Cavallari. Performance of calorimeters at the LHC. *J. Phys. Conf. Ser.*, 293: 012001, 2011. doi: 10.1088/1742-6596/293/1/012001.

[85] Performance of the ATLAS trigger system in 2015. *The European Physical Journal C*, 77 (5), may 2017. doi: 10.1140/epjc/s10052-017-4852-3. URL https://doi.org/10.1140%2Fepjc%2Fs10052-017-4852-3.

[86] ATLAS Collaboration. Approved plots daq. URL https://twiki.cern.ch/twiki/bin/view/AtlasPublic/ApprovedPlotsDAQ. Accessed: 24 February 2023.

[87] Geant4 Collaboration. GEANT4: A Simulation toolkit. *Nucl. Instrum. Meth.*, A506: 250–303, 2003. doi: 10.1016/S0168-9002(03)01368-8.

[88] ATLAS Collaboration. The ATLAS simulation infrastructure. *The European Physical Journal C*, 70(3):823–874, sep 2010. doi: 10.1140/epjc/s10052-010-1429-9. URL https://doi.org/10.1140%2Fepjc%2Fs10052-010-1429-9.

[89] W Lukas. Fast Simulation for ATLAS: Atlfast-II and ISF. Technical report, CERN, Geneva, 2012. URL https://cds.cern.ch/record/1458503.

[90] Takashi Yamanaka. The ATLAS calorimeter simulation FastCaloSim. *J. Phys. Conf. Ser.*, 331:032053, 2011. doi: 10.1088/1742-6596/331/3/032053.

[91] K Edmonds, S Fleischmann, T Lenz, C Magass, J Mechnich, and A Salzburger. The Fast ATLAS Track Simulation (FATRAS). Technical report, CERN, Geneva, 2008. URL https://cds.cern.ch/record/1091969. All figures including auxiliary figures are available at https://atlas.web.cern.ch/Atlas/GROUPS/PHYSICS/PUBNOTES/ATL-SOFT-PUB-2008-001.

[92] ATLAS Collaboration. Performance of the ATLAS track reconstruction algorithms in dense environments in LHC run 2. *The European Physical Journal C*, 77(10), oct 2017. doi: 10.1140/epjc/s10052-017-5225-7. arXiv:1704.07983 [hep-ex].

[93] ATLAS Collaboration. Reconstruction of primary vertices at the ATLAS experiment in run 1 proton–proton collisions at the LHC. *The European Physical Journal C*, 77(5), may 2017. doi: 10.1140/epjc/s10052-017-4887-5. arXiv:1611.10235 [physics.ins-det].

[94] ATLAS Collaboration. Performance of primary vertex reconstruction in proton-proton collisions at $\sqrt{s}$ =7 TeV in the ATLAS experiment. Technical report, CERN, Geneva, Jul 2010. URL https://cds.cern.ch/record/1281344. All figures including auxiliary figures are available at https://atlas.web.cern.ch/Atlas/GROUPS/PHYSICS/CONFNOTES/ATLAS-CONF-2010-069.

[95] T G Cornelissen, N Van Eldik, M Elsing, W Liebig, E Moyse, N Piacquadio, K Prokofiev, A Salzburger, and A Wildauer. Updates of the ATLAS Tracking Event Data Model (Release 13). Technical report, CERN, Geneva, Jun 2007. URL

https://cds.cern.ch/record/1038095. All figures including auxiliary figures are available at https://atlas.web.cern.ch/Atlas/GROUPS/PHYSICS/PUBNOTES/ATL-SOFT-PUB-2007-003.

[96] W Lampl, S Laplace, D Lelas, P Loch, H Ma, S Menke, S Rajagopalan, D Rousseau, S Snyder, and G Unal. Calorimeter Clustering Algorithms: Description and Performance. Technical report, CERN, Geneva, Apr 2008. URL https://cds.cern.ch/record/1099735. All figures including auxiliary figures are available at https://atlas.web.cern.ch/Atlas/GROUPS/PHYSICS/PUBNOTES/ATL-LARG-PUB-2008-002.

[97] Improved electron reconstruction in ATLAS using the Gaussian Sum Filter-based model for bremsstrahlung. Technical report, CERN, Geneva, 2012. URL https://cds.cern.ch/record/1449796. All figures including auxiliary figures are available at https://atlas.web.cern.ch/Atlas/GROUPS/PHYSICS/CONFNOTES/ATLAS-CONF-2012-047.

[98] ATLAS Collaboration. Electron efficiency measurements with the ATLAS detector using 2012 LHC proton–proton collision data. *The European Physical Journal C*, 77(3), mar 2017. doi: 10.1140/epjc/s10052-017-4756-2. URL https://doi.org/10.1140%2Fepjc%2Fs10052-017-4756-2.

[99] ATLAS Collaboration. Electron reconstruction and identification in the ATLAS experiment using the 2015 and 2016 LHC proton–proton collision data at $sqrts = 13$ tev. *The European Physical Journal C*, 79(8), aug 2019. doi: 10.1140/epjc/s10052-019-7140-6. URL https://doi.org/10.1140%2Fepjc%2Fs10052-019-7140-6.

[100] ATLAS Collaboration. Electron and photon performance measurements with the ATLAS detector using the 2015-2017 LHC proton-proton collision data. *JINST*, 14(12):P12006, 2019. doi: 10.1088/1748-0221/14/12/P12006. arXiv:1908.00005 [hep-ex].

[101] ATLAS Collaboration. Muon reconstruction performance of the ATLAS detector in proton–proton collision data at $\sqrt{s} = 13$ tev. *The European Physical Journal C*, 76(5), may 2016. doi: 10.1140/epjc/s10052-016-4120-y. arXiv:1603.05598 [hep-ex].

[102] ATLAS Collaboration. Muon reconstruction and identification efficiency in ATLAS using the full Run 2 *pp* collision data set at $\sqrt{s} = 13$ TeV. *Eur. Phys. J. C*, 81(7):578, 2021. doi: 10.1140/epjc/s10052-021-09233-2.

[103] Gavin P. Salam. Towards jetography. *The European Physical Journal C*, 67(3-4):637–686, may 2010. doi: 10.1140/epjc/s10052-010-1314-6. arXiv:0906.1833 [hep-ph].

[104] ATLAS Collaboration. Jet reconstruction and performance using particle flow with the ATLAS detector. *The European Physical Journal C*, 77(7), jul 2017. doi: 10.1140/epjc/s10052-017-5031-2. arXiv:1703.10485 [hep-ex].

[105] ATLAS Collaboration. Topological cell clustering in the ATLAS calorimeters and its performance in LHC run 1. *The European Physical Journal C*, 77(7), jul 2017. doi: 10.1140/epjc/s10052-017-5004-5. arXiv:1603.02934 [hep-ex].

[106] M Cacciari, G. P. Salam, and G Soyez. The anti-kt Jet Clustering Algorithm. *JHEP*, 0804(063), 2008. arXiv:0802.1189v2 [hep-ph].

[107] ATLAS Collaboration. Monte Carlo Calibration and Combination of In-situ Measurements of Jet Energy Scale, Jet Energy Resolution and Jet Mass in ATLAS. Technical report, CERN, Geneva, Aug 2015. URL https://cds.cern.ch/record/2044941. All figures including auxiliary figures are available at https://atlas.web.cern.ch/Atlas/GROUPS/PHYSICS/CONFNOTES/ATLAS-CONF-2015-037.

[108] ATLAS Collaboration. Jet energy scale measurements and their systematic uncertainties in proton-proton collisions at $\sqrt{13}$ tev with the ATLAS detector. *Physical Review D*, 96 (7), oct 2017. doi: 10.1103/physrevd.96.072002. arXiv:1703.09665 [hep-ex].

[109] ATLAS Collaboration. Jet energy resolution in proton-proton collisions at $\sqrt{7}$ recorded in 2010 with the ATLAS detector. *The European Physical Journal C*, 73(3), mar 2013. doi: 10.1140/epjc/s10052-013-2306-0. arXiv:1210.6210 [hep-ex].

[110] ATLAS Collaboration. Tagging and suppression of pileup jets with the ATLAS detector. Technical report, CERN, Geneva, May 2014. URL https://cds.cern.ch/record/1700870. All figures including auxiliary figures are available at https://atlas.web.cern.ch/Atlas/GROUPS/PHYSICS/CONFNOTES/ATLAS-CONF-2014-018.

[111] ATLAS Collaboration. Jet energy scale and resolution measured in proton–proton collisions at $\sqrt{s} = 13$ TeV with the ATLAS detector. *Eur. Phys. J. C*, 81(8):689, 2021. doi: 10.1140/epjc/s10052-021-09402-3.

[112] G Piacquadio and C Weiser. A new inclusive secondary vertex algorithm for b-jet tagging in ATLAS. *Journal of Physics: Conference Series*, 119(3):032032, jul 2008. doi: 10.1088/1742-6596/119/3/032032. URL https://inspirehep.net/literature/803051.

[113] Izaak Neutelings. B tagging jets, Mar 2022. URL https://tikz.net/jet_btag/.

[114] ATLAS Collaboration. Commissioning of the ATLAS high-performance b-tagging algorithms in the 7 TeV collision data. Technical Report ATLAS-CONF-2011-102, CERN, Geneva, Jul 2011. URL https://cds.cern.ch/record/1369219.

[115] ATLAS Collaboration. Identification of Jets Containing b-Hadrons with Recurrent Neural Networks at the ATLAS Experiment. Technical report, CERN, Geneva, 2017. URL http://cds.cern.ch/record/2255226.

[116] ATLAS Collaboration. Measurement of the c-jet mistagging efficiency in $t\bar{t}$ events using pp collision data at $\sqrt{s} = 13$ TeV collected with the ATLAS detector. *Eur. Phys. J. C*, 82(1):95, 2022. doi: 10.1140/epjc/s10052-021-09843-w. arXiv:2109.10627 [hep-ex].

[117] ATLAS Collaboration. Optimisation and performance studies of the ATLAS b-tagging algorithms for the 2017-18 LHC run. Technical report, CERN, Geneva, 2017. URL https://cds.cern.ch/record/2273281.

[118] Optimisation of the ATLAS b-tagging performance for the 2016 LHC Run. Technical report, CERN, Geneva, 2016. URL https://cds.cern.ch/record/2160731. All figures including auxiliary figures are available at https://atlas.web.cern.ch/Atlas/GROUPS/PHYSICS/PUBNOTES/ATL-PHYS-PUB-2016-012.

[119] ATLAS Collaboration. Expected performance of the 2019 atlas b-taggers, Sept 2019. URL http://atlas.web.cern.ch/Atlas/GROUPS/PHYSICS/PLOTS/FTAG-2019-005/.

[120] ATLAS Collaboration. Performance of missing transverse momentum reconstruction with the ATLAS detector using proton-proton collisions at $\sqrt{s} = 13$ TeV. *Eur. Phys. J. C*, 78 (11):903, 2018. doi: 10.1140/epjc/s10052-018-6288-9.

[121] Faig Ahmadov et al. Search for the Standard Model Higgs boson produced in association with a vector boson and decaying to a pair of b-quarks. Technical report, CERN, Geneva, 2018. URL https://cds.cern.ch/record/2317111.

[122] Leo Breiman. *Classification and Regression Trees*. Routledge, New York, 1984. doi: https://doi.org/10.1201/9781315139470.

[123] A. Hoecker et al. TMVA - Toolkit for Multivariate Data Analysis, 2007. arXiv:physics/0703039 [physics.data-an].

[124] Jerome Friedman. Greedy function approximation: A gradient boosting machine. *The Annals of Statistics*, 29, 11 2000. doi: 10.1214/aos/1013203451.

[125] Haowen Deng, Youyou Zhou, Lin Wang, and Cheng Zhang. Ensemble learning for the early prediction of neonatal jaundice with genetic features. *BMC Medical Informatics and Decision Making*, 21, 12 2021. doi: 10.1186/s12911-021-01701-9.

[126] Vinod Nair and Geoffrey Hinton. Rectified linear units improve restricted boltzmann machines vinod nair. volume 27, pages 807–814, 06 2010.

[127] Kunal Banerjee, Vishak Prasad C, Rishi Raj Gupta, Karthik Vyas, Anushree H, and Biswajit Mishra. Exploring alternatives to softmax function, 2020. URL https://arxiv.org/abs/2011.11538.

[128] ATLAS Collaboration. Luminosity determination in pp collisions at $\sqrt{s} = 13$ tev using the atlas detector at the lhc. *Eur. Phys. J. C 83 (2023) 982*, 2022. doi: https://doi.org/10.1140/epjc/s10052-023-11747-w. arXiv:2212.09379 [hep-ex].

[129] Simone Alioli, Paolo Nason, Carlo Oleari, and Emanuele Re. A general framework for implementing NLO calculations in shower monte carlo programs: the POWHEG BOX. *Journal of High Energy Physics*, 2010(6), jun 2010. doi: 10.1007/jhep06(2010)043. URL https://doi.org/10.1007%2Fjhep06%282010%29043.

[130] Keith Hamilton, Paolo Nason, and Giulia Zanderighi. Minlo: multi-scale improved nlo. *Journal of High Energy Physics*, 2012(10), October 2012. ISSN 1029-8479. doi: 10.1007/jhep10(2012)155. URL http://dx.doi.org/10.1007/JHEP10(2012)155.

[131] NNPDF Collaboration. Parton distributions for the lhc run ii. *Journal of High Energy Physics*, 2015(4), April 2015. ISSN 1029-8479. doi: 10.1007/jhep04(2015)040. URL http://dx.doi.org/10.1007/JHEP04(2015)040.

[132] ATLAS Collaboration. Measurement of the z/ * boson transverse momentum distribution in pp collisions at s = 7

$$\sqrt{s} = 7$$

tev with the atlas detector. *Journal of High Energy Physics*, 2014(9), September 2014. ISSN 1029-8479. doi: 10.1007/jhep09(2014)145. URL http://dx.doi.org/10.1007/JHEP09(2014)145.

[133] Torbjrn Sjstrand, Stephen Mrenna, and Peter Skands. A brief introduction to PYTHIA 8.1. *Computer Physics Communications*, 178(11):852–867, jun 2008. doi: 10.1016/j.cpc.2008.01.036. URL https://doi.org/10.1016%2Fj.cpc.2008.01.036.

[134] ATLAS Pythia 8 tunes to 7 TeV data. Technical report, CERN, Geneva, 2014. URL https://cds.cern.ch/record/1966419. All figures including auxiliary figures are available at https://atlas.web.cern.ch/Atlas/GROUPS/PHYSICS/PUBNOTES/ATL-PHYS-PUB-2014-021.

[135] Stefano Frixione, Eric Laenen, Patrick Motylinski, Chris White, and Bryan R Webber. Single-top hadroproduction in association with a w boson. *Journal of High Energy Physics*, 2008(07):029–029, jul 2008. doi: 10.1088/1126-6708/2008/07/029. URL https://doi.org/10.1088%2F1126-6708%2F2008%2F07%2F029.

[136] T. Gleisberg, Stefan. Hoeche, F. Krauss, M. Schonherr, S. Schumann, F. Siegert, and J. Winter. Event generation with SHERPA 1.1. *JHEP*, 02:007, 2009. doi: 10.1088/1126-6708/2009/02/007.

[137] ATLAS Collaboration. The Pythia 8 A3 tune description of ATLAS minimum bias and inelastic measurements incorporating the Donnachie-Landshoff diffractive model. Technical report, CERN, Geneva, 2016. URL https://cds.cern.ch/record/2206965. All figures including auxiliary figures are available at https://atlas.web.cern.ch/Atlas/GROUPS/PHYSICS/PUBNOTES/ATL-PHYS-PUB-2016-017.

[138] Richard D. Ball, Valerio Bertone, Stefano Carrazza, Christopher S. Deans, Luigi Del Debbio, Stefano Forte, Alberto Guffanti, Nathan P. Hartland, José I. Latorre, Juan Rojo, and Maria Ubiali. Parton distributions with LHC data. *Nuclear Physics B*, 867(2):244–289, feb 2013. doi: 10.1016/j.nuclphysb.2012.10.003. URL https://doi.org/10.1016%2Fj.nuclphysb.2012.10.003.

[139] D. J. Lange. The EvtGen particle decay simulation package. *Nucl. Instrum. Meth. A*, 462:152–155, 2001. doi: 10.1016/S0168-9002(01)00089-4.

[140] Jon Butterworth, Stefano Carrazza, Amanda Cooper-Sarkar, Albert De Roeck, Jol Feltesse, Stefano Forte, Jun Gao, Sasha Glazov, Joey Huston, Zahari Kassabov, Ronan McNulty, Andreas Morsch, Pavel Nadolsky, Voica Radescu, Juan Rojo, and Robert Thorne. PDF4lhc recommendations for LHC run II. *Journal of Physics G: Nuclear and Particle Physics*, 43(2):023001, jan 2016. doi: 10.1088/0954-3899/43/2/023001. URL https://doi.org/10.1088%2F0954-3899%2F43%2F2%2F023001.

[141] R Barlow and C Beeston. Fitting using finite Monte Carlo samples. *Comput. Phys. Commun.*, 77(2):219–228, 1993. URL https://cds.cern.ch/record/249779.

[142] Glen Cowan, Kyle Cranmer, Eilam Gross, and Ofer Vitells. Asymptotic formulae for likelihood-based tests of new physics. *The European Physical Journal C*, 71(2), feb 2011. doi: 10.1140/epjc/s10052-011-1554-0. URL https://doi.org/10.1140%2Fepjc%2Fs10052-011-1554-0.

[143] A L Read. Presentation of search results: the cls technique. *Journal of Physics G: Nuclear and Particle Physics*, 28(10):2693, sep 2002. doi: 10.1088/0954-3899/28/10/313. URL https://dx.doi.org/10.1088/0954-3899/28/10/313.

[144] S. S. Wilks. The Large-Sample Distribution of the Likelihood Ratio for Testing Composite Hypotheses. *The Annals of Mathematical Statistics*, 9(1):60 – 62, 1938. doi: 10.1214/aoms/1177732360. URL https://doi.org/10.1214/aoms/1177732360.

[145] ATLAS Collaboration. Measurement of the inelastic proton-proton cross section at $\sqrt(s) =$ 13 tev with the atlas detector at the lhc. *Physical Review Letters*, 117(18), October 2016. ISSN 1079-7114. doi: 10.1103/physrevlett.117.182002. URL https://arxiv.org/abs/1606.02625.

[146] Ian Jolliffe and Jorge Cadima. Principal component analysis: A review and recent developments. *Philosophical Transactions of the Royal Society A: Mathematical, Physical and Engineering Sciences*, 374:20150202, 04 2016. doi: 10.1098/rsta.2015.0202.

[147] ATLAS Collaboration. Atlas b-jet identification performance and efficiency measurement with $t\bar{t}$ events in pp collisions at $\sqrt{s} = 13$ tev. *The European Physical Journal C*, 79(11), November 2019. ISSN 1434-6052. doi: 10.1140/epjc/s10052-019-7450-8. URL http://dx.doi.org/10.1140/epjc/s10052-019-7450-8.

[148] Gordon Watts, Frank Filthaut, and Giacinto Piacquadio. Extrapolating Errors for b-tagging. Technical report, CERN, Geneva, 2015. URL https://cds.cern.ch/record/2034234. This is for internal information only, no approval to ever be seen outside of ATLAS.

[149] ATLAS Collaboration. Data/MC Carlo Modelling for the VH($b\bar{b}/c\bar{c}$) Analysis. Technical report, CERN, Geneva, 2022. URL https://cds.cern.ch/record/2843072.

[150] Johannes Bellm et al. Herwig 7.0/herwig ++ 3.0 release note. *The European Physical Journal C*, 76(4), apr 2016. doi: 10.1140/epjc/s10052-016-4018-8. URL https://doi.org/10.1140%2Fepjc%2Fs10052-016-4018-8.

[151] C T Potter et al. Handbook of lhc higgs cross sections: 3. higgs properties: Report of the lhc higgs cross section working group, 2013. URL http://cds.cern.ch/record/1559921.

[152] al. Calvet, Thomas Philippe et. Simplified Template Cross-Section measurements for the $VH(H \to bb)$ process with the ATLAS detector. Technical report, CERN, Geneva, 2018. URL https://cds.cern.ch/record/2636121.

[153] ATLAS Collaboration. Evaluation of theoretical uncertainties for simplified template cross section measurements of V-associated production of the Higgs boson. Technical report, CERN, Geneva, 2018. URL https://cds.cern.ch/record/2649241. All figures including auxiliary figures are available at https://atlas.web.cern.ch/Atlas/GROUPS/PHYSICS/PUBNOTES/ATL-PHYS-PUB-2018-035.

[154] J. Butterworth et al. Pdf4lhc recommendations for lhc run ii. *Journal of Physics G: Nuclear and Particle Physics*, 43(2):023001, January 2016. ISSN 1361-6471. doi: 10.1088/0954-3899/43/2/023001. URL http://dx.doi.org/10.1088/0954-3899/43/2/023001.

[155] L. A. Harland-Lang, A. D. Martin, P. Motylinski, and R. S. Thorne. Parton distributions in the LHC era: MMHT 2014 PDFs. *The European Physical Journal C*, 75(5), May 2015. ISSN 1434-6052. doi: 10.1140/epjc/s10052-015-3397-6. URL http://dx.doi.org/10.1140/epjc/s10052-015-3397-6.

[156] Sayipjamal Dulat, Tie-Jiun Hou, Jun Gao, Marco Guzzi, Joey Huston, Pavel Nadolsky, Jon Pumplin, Carl Schmidt, Daniel Stump, and C.-P. Yuan. New parton distribution functions from a global analysis of quantum chromodynamics. *Physical Review D*, 93 (3), February 2016. ISSN 2470-0029. doi: 10.1103/physrevd.93.033006. URL http://dx.doi.org/10.1103/PhysRevD.93.033006.

[157] J. Alwall, R. Frederix, S. Frixione, V. Hirschi, F. Maltoni, O. Mattelaer, H.-S. Shao, T. Stelzer, P. Torrielli, and M. Zaro. The automated computation of tree-level and next-to-leading order differential cross sections, and their matching to parton shower simulations. *Journal of High Energy Physics*, 2014(7), jul 2014. doi: 10.1007/jhep07(2014)079. URL https://doi.org/10.1007%2Fjhep07%282014%29079.

[158] Kyle Cranmer, Juan Pavez, and Gilles Louppe. Approximating likelihood ratios with calibrated discriminative classifiers. 2016. arXiv:1506.02169 [stat.AP].

[159] Adam Paszke et al. Pytorch: An imperative style, high-performance deep learning library, 2019. arXiv:1912.01703 [cs.LG].

[160] M. Bahr et al. Herwig++ Physics and Manual. *Eur. Phys. J.*, C58:639–707, 2008. doi: 10.1140/epjc/s10052-008-0798-9.

[161] CMS Collaboration. Measurement of simplified template cross sections of the higgs boson produced in association with w or z bosons in the h $\to$ b$\bar{\text{b}}$ decay channel in proton-proton collisions at $\sqrt{s}$ =13 tev, 2023. arXiv:2312.07562 [hep-ex].